DISCOVERY OF LOCALIZED TEV GAMMA-RAY SOURCES AND DIFFUSE TEV GAMMA-RAY EMISSION FROM THE GALACTIC PLANE WITH MILAGRO USING A NEW BACKGROUND REJECTION TECHNIQUE

By

Aous Ahmad Abdo

A DISSERTATION

Submitted to
Michigan State University
in partial fulfillment of the requirements
for the degree of

DOCTOR OF PHILOSOPHY

Department of Physics and Astronomy

2007

ABSTRACT

DISCOVERY OF LOCALIZED TEV GAMMA-RAY SOURCES AND DIFFUSE TEV GAMMA-RAY EMISSION FROM THE GALACTIC PLANE WITH MILAGRO USING A NEW BACKGROUND REJECTION TECHNIQUE

By

Aous Ahmad Abdo

Very high energy gamma-rays can be used to probe some of the most powerful astrophysical objects in the universe, such as active galactic nuclei, supernova remnants and pulsar-powered nebulae. The diffuse gamma radiation arising from the interaction of cosmic-ray particles with matter and radiation in the Galaxy is one of the few probes available to study the origin of cosmic-rays. Milagro is a water Cherenkov detector that continuously views the entire overhead sky. The large field-of-view combined with the long observation time makes Milagro the most sensitive instrument available for the study of large, low surface brightness sources such as the diffuse gamma radiation arising from interactions of cosmic radiation with interstellar matter. In this thesis I present a new background rejection technique for the Milagro detector through the development of a new gamma hadron separation variable. The Abdo variable, A_4, coupled with the weighting analysis technique significantly improves the sensitivity of the Milagro detector. This new analysis technique resulted in the first discoveries in Milagro. Four localized sources of TeV gamma-ray emission have been discovered, three of which are in the Cygnus region of the Galaxy and one closer to the Galactic center. In addition to these localized sources, a diffuse emission of TeV gamma-rays has been discovered from the Cygnus region of the Galaxy as well. However, the TeV gamma-ray flux as measured at $\sim$12 TeV from the Cygnus region exceeds that predicted from a conventional model of cosmic-ray production and propagation. This observation indicates the existence of either hard-spectrum

cosmic-ray sources and/or other sources of TeV gamma rays in the region. Other TeV gamma-ray source candidates with post-trial statistical significances of $> 4\sigma$ have also been observed in the Galactic plane.

I dedicate this work to my mother Muna Al-Qaisi and to the memory of my father Ahmad Abdo

ACKNOWLEDGMENTS

First of all I would like to thank my parents, Ahmad Abdo and Muna Al-Qaisi. Their continuous caring, support, and encouragement to me throughout my life made me the man I am today and helped me face all obstacles in my life with ease and determination.

I would like to thank my wife, Callista, for her continuous and limitless support during my days at grad school. Without her my life would have been much harder.

As a student of Milagro, I was lucky to have more than one advisor, each an expert in his field. I would like to thank my Michigan State University advisor, Professor James Linnemann, for offering me the opportunity to work on Milagro, for his kindness, and for his continuous support. I would like to thank my advisor from Los Alamos National Laboratory, Dr. Gus Sinnis, for all his support and kindheartedness, for believing in me, and for helping me become the scientist that I am today. His invaluable comments, ideas, and guidance helped shape this thesis in the best way possible. Dr. Andrew Smith of the University of Maryland deserves very special thanks. I am not exaggerating when I say that I owe most of what I learned while working on Milagro to him. I would like to thank him for his patience and for answering my endless questions about Milagro and about the field in general. I am also grateful for all the long hours we spent in his office in Maryland working on this analysis. I would like to thank Dr. Brenda Dingus of Los Alamos National Laboratory for all her invaluable input and comments on my work. I am also greatful to her for going out of her way in helping me to find a job. I would also like to thank the Maryland group, Prof. Jordan Goodman, Prof. Robert Ellsworth, and Prof. David Berley for their comments on my work and for their support. I would like to thank Dr. Curtis Lansdell for helping me during my first days at Los Alamos and for being a good friend. I would like to thank the Los Alamos postdocs Dr. Gary Walker, Dr. Sabrina Casanova, and Dr. Petra Huentemeyer for their help and benevolence.

My Milagro friends deserve special thanks for making my life as a grad student much more enjoyable. I would like to thank Dr. David Noyes for all the intellectual conversations I had with him. I would like to thank him for being open minded, for being interested in my culture, and for all the good vegan food he cooked for me. He is a great friend. My fellow student and friend, Vlasios Vasileiou, deserves thanks for creating all the Monte Carlo simulations needed for the completion of this work. The times I spent with him and David in Maryland make some of the best memories I have. Iris Gebauer deserves special thanks for her continuous support and for being such a good friend.

I am grateful to Michael Schneider for his kindness, support, and for being a good friend. I am also grateful to Scott Delay for helping me while on shift and for all the interesting discussions I had with him. I am grateful to Prof. Allen Mincer from NYU for all the intellectual exchanges I had with him.

I am sincerely grateful to Brenda Wenzlick the HEP secretary at MSU for her help and kindheartedness. I am also grateful to Pam Marteniz from Los Alamos for her benevolence and for helping me in all the paperwork needed there.

Contents

List of Tables

List of Figures

Chapter 1

Introduction To Very High Energy Gamma-Ray Astrophysics

1.1 The Relativistic Universe

Our knowledge of the universe comes from the study of the radiation we detect from different sources in the sky. Most of this radiation is emitted by thermal processes. Such processes include the Cosmic Microwave Background (CMB), thermal emissions from the stars, or from the accretion disks around neutron stars and other massive objects. Beyond this Ordinary Universe there exists a non-thermal relativistic universe. This universe is of particular interest to particle physicists, this is because it involves physical processes that are impossible to emulate in our laboratories. One example of these non-thermal processes is the cosmic radiation, whose origin, after 90 years of its discovery, is still largely a mystery. cosmic-rays are remarkable for many reasons:

- cosmic-ray particles represents the largest source of material reaching Earth from outside our Solar System. The chemical composition of these particles reflects the nucleosynthetic processes occurring at their origin.

- cosmic-rays span a very large range of energies, from 1 MeV (10^6 eV) to 100 EeV (10^{20} eV). The very high energies involved are evidence for powerful astrophysical accelerators.

- cosmic-rays are abundant and serve an important role in the energy balance of the Galaxy. Their energy density ~ 1 eV cm^{-3} is comparable to that contained in the CMB.

The study of sources of very high energy cosmic radiation involves the study of astrophysical situations in which conventional physics operates under extreme conditions (e.g. intense magnetic and gravitational fields). It may also involve new physical phenomena (e.g. annihilation of Dark Matter (DM) particles.)

Observing the non-thermal universe is difficult. One reason for this is the dominance of the radiation from thermal processes. This can be overcome by making use of the hard power-law spectrum of many of the non-thermal emissions by using the highest radiation detectors to probe such processes. Thus, hard x-ray and gamma-ray observational techniques are widely used to study this non-thermal universe.

1.2 Gamma-Ray Astronomy

Gamma-ray astronomy is relatively a new field compared to other branches of astronomy. The energy domain of gamma-ray astronomy spans from approximately $E = m_e c^2 \backsimeq 0.5 \times 10^6$ eV to $\geq 10^{20}$ eV[1]. Covering more than 14 decades in frequency, this is more than the rest of the observed electromagnetic spectrum. It is thus not surprising that a wide variety of different objects and phenomena can be studied using γ-rays. The lower bound of this range characterizes the region of nuclear γ-ray lines, as well as electron-positron annihilation lines. The higher bound characterizes the energy of the highest energy cosmic-ray particles detected. This enormous

[1]Gamma rays have been detected with energies up to 10^{14} eV. However, gamma rays with higher energies are possible.

range in energies is divided in bands according to the interaction phenomena and detection techniques [72]. Table 1.1 lists these γ-ray bands.

Gamma-ray photons represent the most energetic part of the electromagnetic spectrum. They therefore provide information about the most energetic processes and phenomena in the universe.

Unlike cosmic-rays, gamma-rays are neutrally charged particles and thus will not be deflected in the interstellar magnetic fields and will point back to their sources of origin.

Gamma-rays are emitted from the most compact and energetic objects in the universe: neutron stars, stellar and massive black holes, supernova remnants, and cosmic-rays via the interactions with matter and fields. Gamma-ray astronomy has become an integral part of astronomy and astrophysics. It is now recognized that objects exist in the universe, such as pulsars, quasars, blazars, and γ-ray burst sources, which have their peak luminosities at γ-ray energies. It is impossible to understand these objects without knowing and understanding their γ-rays properties.

Band	Low/Medium	High	Very High	Ultra High
Shorthand	LE/ME	HE	VHE	UHE
Range	0.1-30 MeV	0.3-100 GeV	0.1-100 TeV	>100 TeV
Environment	Space	Space	Ground-based	Ground-based

Table 1.1: Gamma-Ray Bands[72]

1.3 Gamma-Ray Detection

There are two broad categories of cosmic γ-rays detectors: space-based, and ground-based, each of which uses different detection techniques.

1.3.1 Space-based Detectors

Space-based detectors are flown on satellites and high altitude balloons. Space-based detectors have three basic components: a tracking chamber, a calorimeter, and an anti-coincidence counter. The tracking chamber is used to record the path of charged particles in the detector. The tracks are used to reconstruct the direction of the incident γ-ray photon through the identification of the electron positron pair that resulted from the annihilation of this γ-ray photon. The calorimeter determines the energy of the incident photon by measuring the integrated path length of particles in the electromagnetic cascade produced by the incident photon. The anti-coincidence counter rejects triggers caused by charged particles which are usually protons, heavier nuclei, and electrons. Space-based detectors have excellent background rejection which allows them to unambiguously identify γ-rays. They also have high duty cycle which allows continuous monitoring of transient sources all year around. One more advantage of space-based detectors over ground-based ones is the high exposure. They can view the whole sky in matter of hours unlike ground-based detectors that can only view half of the sky since the other half is always obscured by earth. Despite all these advantages, satellite detectors have limited angular resolution, usually on the order of a degree. This made it hard to correlate observed sources with satellite detectors to those observed in other wavelengths. Unlike ground-based detectors, space-based detectors have small detection area, on the order of 0.1 m^2. This limits the energy range of these detectors to be in the range of several MeV to several GeV. This is because the flux of γ-rays from a γ-ray source follows a rapidly falling power-law spectrum in energy and is given by:

$$\frac{dN}{dE} \propto E^{-\alpha} \tag{1.1}$$

where α is the differential spectral index of the energy spectrum. That is, the higher the energy, the lower the flux, requiring very large detection area for VHE and UHE observations. A typical range of α is 2.0-3.0.

The most successful satellite experiment to date was the Compton Gamma Ray Observatory (CGRO) project. It operated from 1991 to 2000. CGRO had four instruments that covered an unprecedented six decades of the electromagnetic spectrum, from 30 keV to 30 GeV. In order of increasing spectral energy coverage, these instruments were the Burst And Transient Source Experiment (BATSE), the Oriented Scintillation Spectrometer Experiment (OSSE), the Imaging Compton Telescope (COMPTEL), and the Energetic Gamma Ray Experiment Telescope (EGRET).

EGRET covered an energy range between 20 MeV to 30 GeV. One of EGRET's major achievements was the production of the third EGRET catalog. This catalog contained 271 new γ-ray sources with energies above 100 MeV [32]. Figure 1.1 shows the third EGRET source catalog in galactic coordinates. The 271 sources in the catalog include the single 1991 solar flare, the Large Magellanic Cloud, five pulsars, one radio galaxy, and 66 high-confidence identifications of blazars. In addition, 27 lower confidence potential blazar identifications are noted. The rest of the sources, 170 out of 271, have not yet been identified with known objects. Many of these unidentified sources are located near the galactic plane which suggests a galactic origin of these sources. The spectra of the identified sources are flat ($\alpha \sim 2.0$) with luminosities that peak in the high-energy region of the spectrum which indicate that they may be sources of VHE photons.

A next-generation telescope, the Gamma Ray Large Area Space Telescope (GLAST), is scheduled for launch in fall of 2007. GLAST is a major space mission to explore the high energy γ-ray universe. There are two instruments on board. The primary instrument is the GLAST Large Area Telescope (LAT), which is sensitive at energies from 20 MeV to 300 GeV. The secondary instrument is the GLAST Burst Monitor

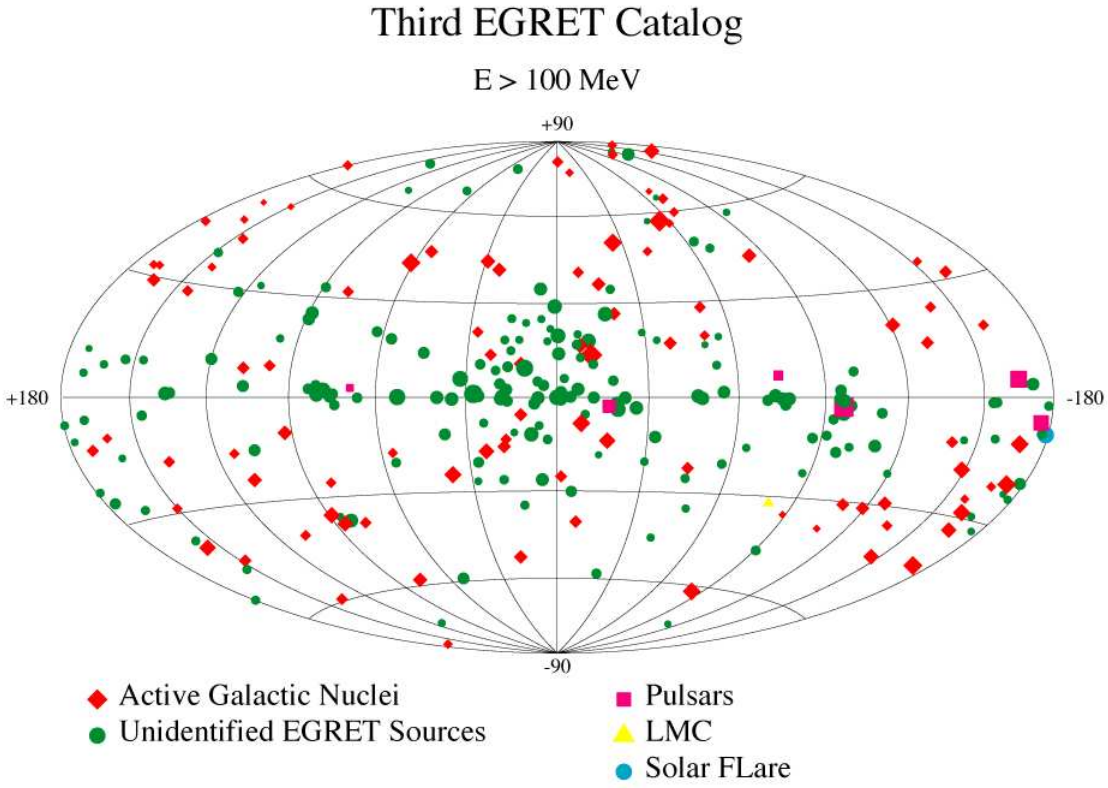

Figure 1.1: Third EGRET source catalog, shown in Galactic coordinates. The size of each symbol is proportional to the highest intensity seen for the corresponding source. Out of the 271 sources 170 have not yet been identified with known objects. Taken from [73]. Images in this thesis are presented in colors.

(GBM) to detect γ-ray bursts and provide broad band spectral coverage of this important phenomenon. The LAT instrument will have many advantages over EGRET. The improvement in its angular resolution ($< 0.15^\circ$ for $E > 1$ GeV) is expected to reduce the source location error box by as much as a factor of 100 depending on the energy spectrum of photons detected and the local γ-ray background[49]. The large collection area of LAT , ~ 1 m^2, will allow for the galactic γ-ray spectra to be derived for much smaller area bins than was possible with EGRET[49]. The extension of the energy reach from 30 GeV for EGRET to 300 GeV for LAT will allow for direct comparisons with results from ground based γ-ray detectors that operate at energies above 100 GeV, like Milagro.

1.3.2 Ground-based Detectors

The flux of γ-rays from celestial γ-ray sources is low and decreases rapidly with energy. As a result, very large detector area is required to do VHE γ-ray astronomy. The large detector area required limits the detection of VHE photons to be done from the ground. However, the atmosphere is opaque to VHE photons. Therefore the by-products[2] of the interaction of the VHE photon with the atmosphere are used to determine the direction and energy of the initial photon. This is done by either detecting the secondary particles in the Extensive Air Shower (EAS) that reaches the ground or by detecting the Cherenkov light produced by these secondary particles as they propagate through the atmosphere. One main disadvantage for ground based γ-ray detectors is the large background from cosmic-rays. Cosmic-rays, consisting of protons and heavier nuclei, are constantly striking the atmosphere. These cosmic rays produce EAS that are superficially similar to those produced by photons, and are $\sim$ 10,000 more numerous for a given incident photon energy. This large hadronic background limits the sensitivity of ground based detectors and makes it very hard to

[2]See next section

observe a statistically significant signal from a celestial γ-ray source. To minimize the effect of this large hadronic background, differences in the EAS initiated by hadronic particles and photons have to be detected.

1.3.3 Extensive Air Showers

The development of an EAS begins with the interaction of the primary particle in the upper atmosphere. The physics of the interaction of the primary γ-ray photon with the earth's atmosphere is fairly well understood. The total cross section for photon-proton collisions has been measured for center-of-mass energies up to 200 GeV [8], which is equivalent to a 20-TeV photon colliding with a proton at rest. VHE γ-ray photons interact with the molecules in the atmosphere through electromagnetic and hadronic interactions.

In the electromagnetic case, VHE γ-ray photons interact with the electromagnetic field of a nitrogen or oxygen nucleus and produces an electron-positron pair moving at ultra-relativistic speeds. This first interaction typically occurs after the photon has traversed one radiation length of the atmosphere, i.e. at an altitude of about 20 km. The resultant electron and positron form more high energy photons via bremsstrahlung radiation which in turn form more electron-positron pairs, and so on. The resulting electromagnetic cascade grows nearly exponentially as it propagates through the atmosphere. The energy of the primary particle is divided among more and more particles until the mean energy of the electrons and positrons approaches the critical energy for bremsstrahlung interaction (80 MeV in air). At this point energy loss through ionization mechanism, which does not produce additional shower particles, becomes more important than bremsstrahlung, while Compton scattering and photoelectric absorption begin to dominate over pair production for the γ-rays. This point in the shower development is referred to as the shower maximum since this is when the shower contains the greatest number of particles. After the shower

maximum is reached, energy is lost from the shower and the number of particles in the shower decreases rapidly as the shower continues to propagate. This makes it important for ground-based detectors to be located at high altitude with the exception of Air Cherenkov Telescopes (IACTs)[3] which detect Cherenkov light in the shower, and since the attenuation length of light in the atmosphere is large, ACTs are not required to be placed at high altitudes.

The cross sections for the production of hadrons and muon pairs are several orders of magnitude lower than that for pair production and thus the predominant interaction for a γ-ray primary is electromagnetic.

Since the particles in the EAS are ultra-relativistic and the dominant physical processes are sharply peaked forward, the EAS arrives at ground level in a thin front only a few meters thick. While the front is only a few meters thick, the lateral extent of the showers, primarily the result of multiple Coulomb scattering of the electrons and positrons in the EAS, is of order one hundred meters.

The passage of cosmic-rays through the atmosphere follows similar, but more complicated process. The interaction of the primary cosmic particle with the molecules in the atmosphere generates a hadronic cascade. This hadronic cascade includes neutral and charged pions. The neutral pions decay into two γ-rays, which in turn produce electromagnetic cascades. The charged pions decay into muons and neutrinos. The low energy muons can decay into electrons and positrons, while the high energy muons typically reach ground level. As a result, particles reaching the ground level in a hadronically initiated air shower are mostly muons, electrons, positrons, neutrinos, and photons. Figure 1.2 shows a simulated development of a 1 PeV (1000 TeV) hadronic air shower. Only a small fraction of particles is shown. The right hand plot shows the evolution of the total particle number with depth. The lower figure shows the distribution of particles at ground level.

[3]See next section

Except for the presence of muons, a cosmic-ray shower at ground level is not very dissimilar to a γ-ray shower. The muon lateral distribution is considerably wider than that of the electromagnetic particles. There are roughly 20 times more muons in a hadron-initiated EAS than in a photon-initiated EAS of the same energy. Figure 1.3 shows the development of the cascades of three different primaries through the atmosphere [74].

1.3.4 Imaging Air Cherenkov Telescopes

In addition to shower particles in an EAS, Cherenkov photons are also produced. Cherenkov light is produced in a medium when a charged particle is traveling faster than the speed of light in that medium. This emission is governed by the refractive index of the medium, n. For air, the refractive index is proportional to the atmospheric density which decreases exponentially with height, with a scale height[4] of $\sim$ 8 km. The radiation is emitted by atoms and molecules polarized by the moving charged particle. This radiation is emitted as a light cone with a fixed angle with respect to the direction of the particle's motion, this angle is given by:

$$\cos\,\theta_c = \frac{c}{nv} \tag{1.2}$$

where c is the speed of light in vacuum, and v is the speed of the charged particle in the medium.

The condition for this radiation to occur is $\frac{c}{nv} < 1$, which can be expressed in terms of the particle's energy:

$$E_{th} = \frac{m_\circ c^2}{\sqrt{1-\frac{1}{n^2}}} \tag{1.3}$$

[4]Scale height is the vertical distance upwards, over which the pressure of the atmosphere decreases by a factor of e

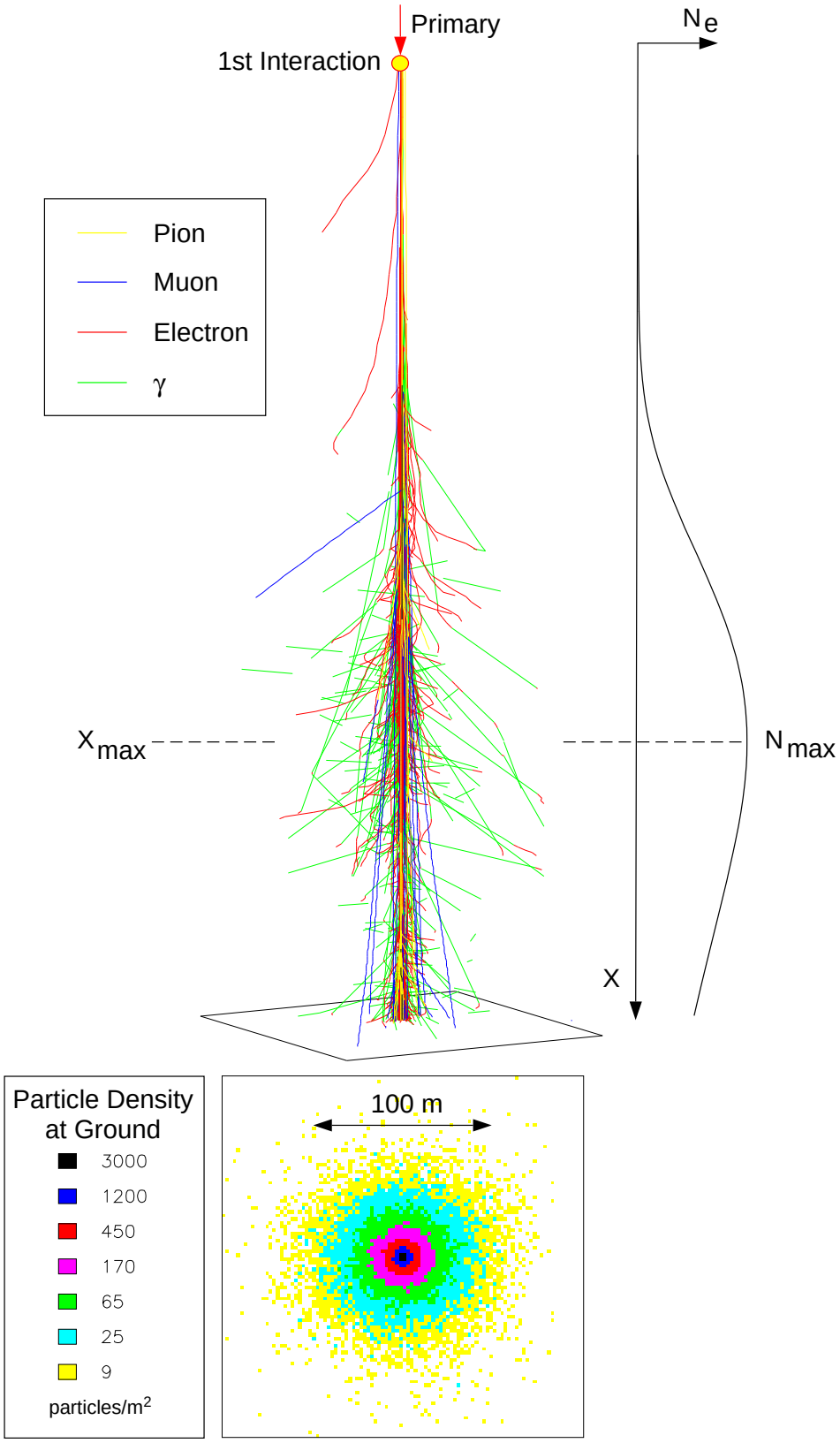

Figure 1.2: Simulated development of a 1 PeV hadronic air shower. Only a small fraction of particles is shown. The right hand plot shows the evolution of the total particle number with depth. The lower figure shows the distribution of particles at ground level. Taken from [36]

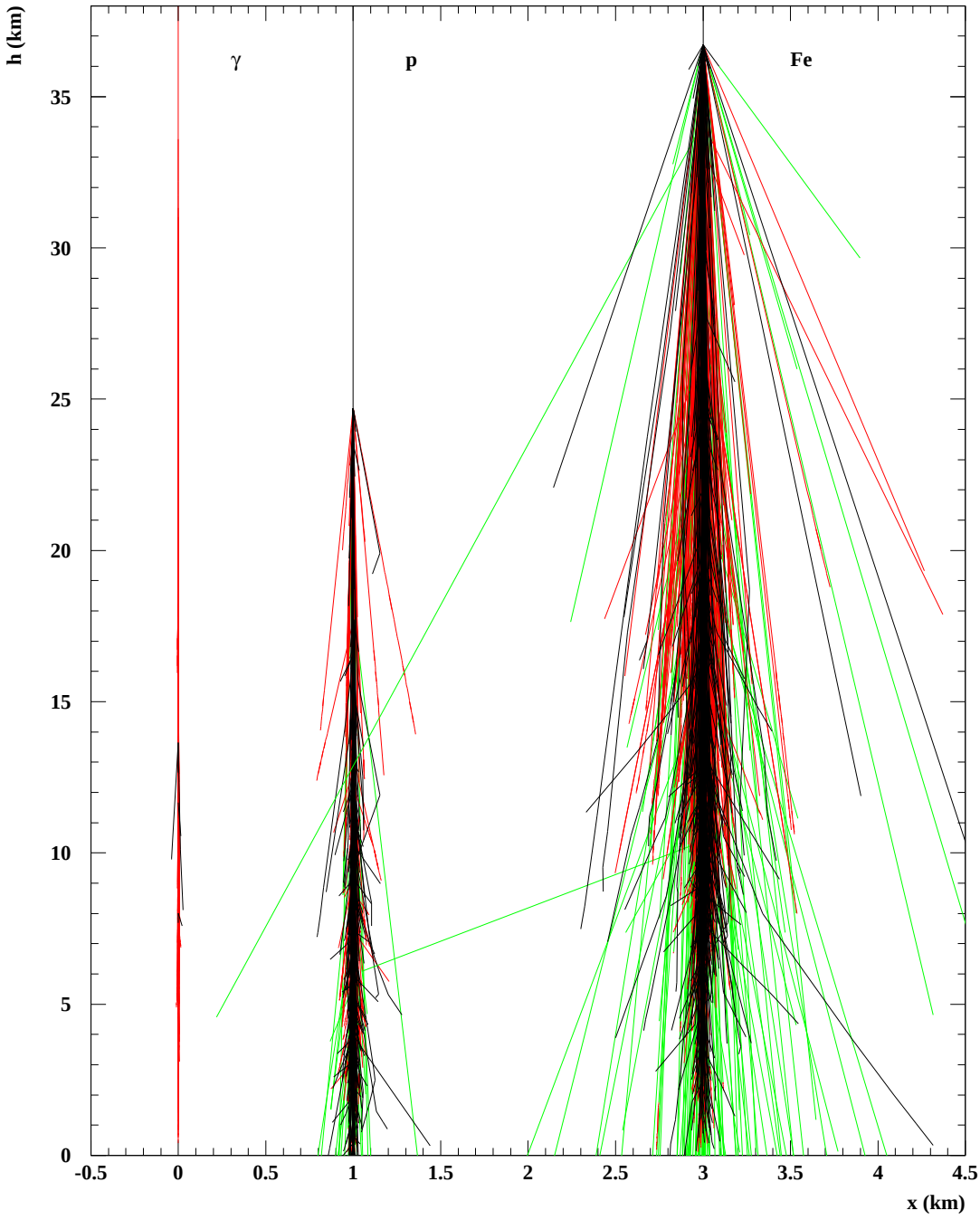

Figure 1.3: Development of the cascades of three different primaries through the atmosphere. Taken from[74]

where $m_\circ$ is the rest mass of the particle. For example, at sea level, the threshold energy for Cherenkov emission to occur is 21 MeV for electrons [or 35 MeV at 8 km above sea level (a.s.l.)], 4.4 GeV for muons, and 39 GeV for protons. The maximum angle of Cherenkov emission is 1.3° at sea level, or 1° at 8 km a.s.l., independent of the mass of the emitting particle.

Observations with Imaging Air Cherenkov Telescopes (IACTs) are done through the detection of the Cherenkov light produced in an EAS [72]. One or more mirrors are used to concentrate the Cherenkov light onto a camera of photomultiplier tubes (PMTs). Observations with IACTs faces two problems; the night-sky background and the large isotropic background from cosmic-ray showers. Cherenkov light in an EAS is very faint compared to moonlight or even bright stars within the field of view. Observations can only be made on clear, moonless nights. This limits the duty cycle of these detectors to ∼10% and restricts them to viewing sources for the part of the year that they are above the horizon at night. An effective background rejection technique has been developed which is based on the image characteristics of the Cherenkov light cone. cosmic-ray showers are more chaotic than γ-ray showers, since their development is governed by a relatively small number of particles in the hadronic core. The larger transverse momentum of hadronic interactions gives a broader lateral distribution. Therefore, measurements of the angular distribution of the Cherenkov light cone on the sky for each shower allow for the separation between hadronic showers and γ-ray showers. In addition to this imaging technique, accurate measurement of the shower arrival direction improves the separation between γ-ray showers from point sources and isotropic cosmic-ray showers. The imaging technique can achieve high angular resolution ($< 0.1°$), especially when individual telescopes are combined into arrays. In addition to the low duty cycle, IACTs are pointed instruments and this make it inefficient to use them as survey instruments. The Whipple 10m γ-ray telescope made the first successful detection of a TeV γ-

Figure 1.4: The HESS telescope array in Namibia.

ray source, the Crab Nebula. A next generation of IACTs arrays are already making significant progress in the field of TeV γ-ray astronomy. The High Energy Stereoscopic System (H.E.S.S) telescope in Namibia had detected point sources of TeV γ-rays from the galactic plane. The Very Energetic Radiation Imaging Telescope Array System (VERITAS) is currently under construction in Arizona. Figure 1.4 shows the H.E.S.S telescope array.

1.3.5 Extensive Air Shower Arrays

Another way to detect EAS is to directly detect secondary charged particles in the shower that reach the ground at the detector level. Extensive Air Shower Arrays (EASA) are used to detect EASs produced by UHE primaries. Fluxes of UHE γ-rays are expected to be small, so a large detection area in excess of 10^4 m^2 is needed[37]. The cost of having a uniformly sensitive detector over such large areas is prohibitive. However, one doesn't need to observe all the particles in an EAS to make a successful detection of this shower, this is because the number of particles in an EAS that reaches the ground is large. A typical EAS initiated by a 100-TeV photon has roughly 50,000 electrons and positrons and about five times as many γ-rays, spread out over an area in excess of 10^4 m^2 at mountain altitudes[37]. Because there are so many particles reaching the ground, an EASA need to sample only a relatively small fraction of these

particles to make a successful detection of the shower. However, this partial sampling of the shower causes the energy threshold of these instruments to be large, on the order of 50 TeV. A typical EASA has between 50 and 1000 scintillation counters, each with an area of ~ 1 m^2. These are usually spread over an area of $10^4 - 10^5$ m^2 and cover only 1% of the total area of the array. The performance of the array can be improved by placing lead, roughly one radiation-length thick, above each counter to convert the more plentiful shower photons into charged particles.

The individual scintillation counters in the array are used to measure the relative arrival times of charged particles in the shower. These times are then used to reconstruct the direction of the shower. The angular resolution resulting from this method of reconstruction is $\sim 0.5^\circ$. This angular resolution depends upon properties of both the EAS and the detector. To obtain good angular resolution with an EASA, one must perform a fit to a shower front that is curved by an amount that is a function of position from the shower core. To separate γ-ray-initiated air showers from cosmic-ray-initiated air showers, EASA use muon detectors to look for muons which are mostly presented in cosmic-ray-initiated showers. These muon detectors are usually placed around the scintillation counters. This technique is limited by the partial sampling of the shower. Scintillation counters measure the energy deposited by charged particles in the shower.

EASA have two advantages over IACTs; large duty cycle ($> 90\%$), and large field of view (~ 2 sr). These two factors provide the ability for continuously monitoring the over-head sky, study of transient sources, and performing sky surveys. Despite all of this, no new γ-ray sources have been discovered and only upper limits exist using EAS arrays. Figure 1.5 shows the Tibet air shower array.

Figure 1.5: The Tibet air shower array

1.3.6 Water Cherenkov Technique

The large field of view and large duty cycle of an EAS array make it an ideal survey instrument. However, the low sensitivity, high energy threshold (> 50 TeV), and the difficulty of discriminating γ-ray showers from hadron showers limited the results from these instruments to only setting upper limits and no new γ-ray sources have been discovered using these instruments.

The Milagro gamma-ray detector near Los Alamos, New Mexico is a new type of detectors that uses the water Cherenkov technique to detect extensive air showers. The water Cherenkov technique is widely used in particle physics experiments but is new to air shower detection. The use of water as a detection medium has the advantage of lowering the energy threshold of the detector to energies comparable to those of IACT's. The lower energy threshold is achieved through the detection of nearly every relativistic particle in an extensive air shower. At ground level, gamma-rays in an EAS outnumber electrons and positrons by a factor of ~ 5. In a conventional air shower array these photons are undetected. Upon their entrance into the water, these

gamma-ray photons convert to electron-positron pair or Compton scatter electrons which will in turn produce Cherenkov radiation that can be detected.

A detailed description of the water Cherenkov technique and the Milagro detector and its performance are given in chapter 3.

Chapter 2

Galactic Gamma-Ray Emission

The Milky Way Galaxy is a bright, diffuse source of high energy γ-rays. About 90% of the total luminosity of the galaxy at high energies (>1 GeV) comes from processes in the interstellar medium (ISM)[52]. Diffuse γ-rays are produced in the galaxy via the interaction of Cosmic-Rays (CR) with the interstellar gas and with the interstellar radiation field. Therefore, the study of this emission may provide information about the properties of CR and their production sites. The main part in this diffuse emission is believed to originate by CR processes but some part is certainly contributed to by two other components; the extragalactic background, and the contribution from unresolved and faint Galactic point sources.

Observations of the diffuse γ-ray emission by the Energetic Gamma Ray Experiment Telescope (EGRET), with its high sensitivity and spatial and energy resolution, resulted in high quality data over three decades of energy in γ-rays (Figure 2.1). The first detailed analysis of this diffuse emission for Galactic latitudes $|b| \leq 10^{\circ}$ came in 1997 [39]. The basic assumptions of this analysis were :

1. cosmic-rays are Galactic in origin.

2. cosmic-ray density is related to the gas column density of the interstellar medium.

3. The spectra of cosmic-rays are the same in all parts of the Galaxy and are equal to those measured locally.

Gamma-rays are produced in the galaxy through hadronic and leptonic interactions (sec 2.2). These different types of interactions will give different γ-ray spectra. The fact that the overall observed spectrum of γ-rays does not significantly vary as a function of Galactic longitude and latitude, indicates that the cosmic ray electron/proton ratio is more or less constant throughout the galaxy.

In their analysis Hunter et. al. [39] used a three dimensional model to describe the spatial and spectral distribution of the diffuse γ-ray emission. This analysis revealed an excess above model predictions in the diffuse γ-ray emission for energies > 1 GeV in all directions of the sky as shown in Figure 2.2. Although many explanations for this GeV excess have been proposed[67, 28, 15, 12], there is still no definitive answer for this observed excess. These explanations include a varying CR spectrum and intensity across the galaxy[67, 28], a hard electron injection spectrum leading to an increase in the ICS component[67], the existence of unresolved point sources with hard spectra[20], the annihilation of relic dark matter particles[24], inverse Compton scattering of cosmic microwave background (CMB) and star light photons by the CR electrons produced in our galaxy and in external galaxies[12], and a miscalibration of the EGRET telescope[53].

In an attempt to solve this "GeV Excess" puzzle, attempts had been made to re-evaluate the reaction of π^0-production in proton-proton-interactions. However, a calculation made using modern Monte Carlo event generators to simulate high energy proton-proton-collisions has shown[50] that the γ-ray flux agrees rather well with previous calculations.

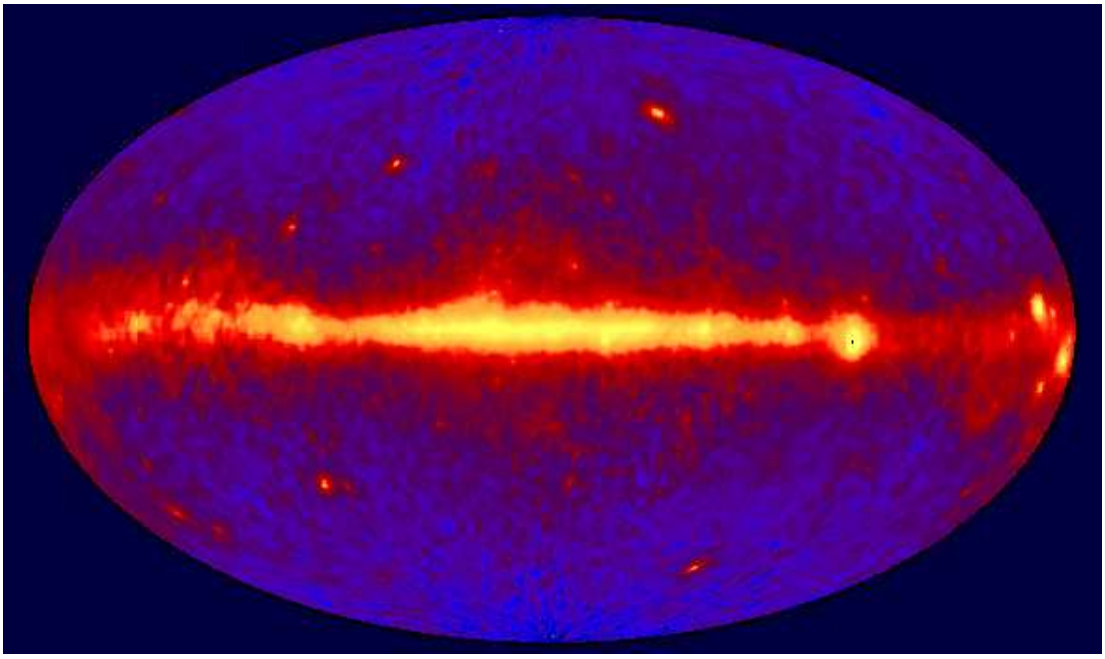

Figure 2.1: EGRET all-sky γ-ray map above 100 MeV in Galactic coordinates[75].

2.1 Cosmic-Rays

Cosmic-Rays are observed with energies from a few MeV up to more than 10^{20} eV. Electrons in the MeV-TeV energy range and protons and α particles in the GeV-TeV energy range are relevant to the production of the diffuse γ-ray emission. The spectra of CR are measured using balloons and satellites. These measured spectra represent the spectra of CR in the local region of the galaxy. For energies below $\sim$ 10 GeV, the heliospheric modulation [1] is large. This heliospheric modulation hinders the study of the truly interstellar spectrum and the locally measured CR spectra may not be representative of the CR spectra in the rest of the Galaxy.

Galactic CR are an important part of the interstellar medium. The average energy density of CR is about 1 eV cm^{-3} and is comparable to the energy density of the interstellar radiation and magnetic fields. Thus, CR are one of the essential factors determining the dynamics and processes in the interstellar medium. The EGRET

[1]Heliospheric modulation is the interaction of cosmic-rays with protons from the sun. This may alter the spectra of the cosmic-rays observed at Earth.

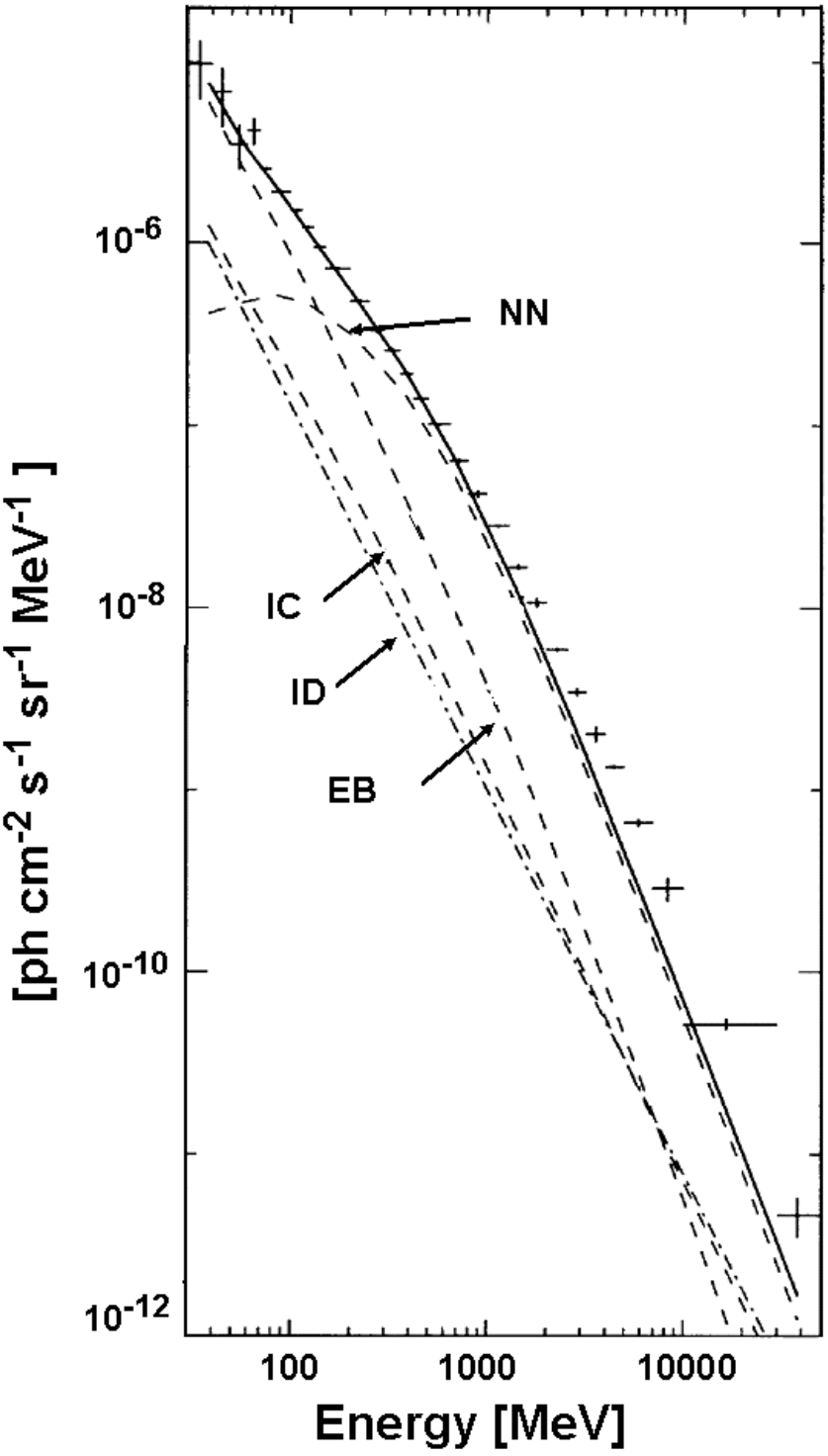

Figure 2.2: The average spectrum of diffuse γ-rays detected by EGRET from the inner galaxy (Galactic Longitude, $300^\circ < l < 60^\circ$, and Galactic Latitude, $|b| \leq 10^\circ$). Contributions from point sources detected with more than 5σ significance have been removed. The data are represented by the points and the solid line represents the prediction of the diffuse γ-ray model. The model incorporates electron bremsstrahlung (EB), inverse Compton (IC), and nucleon-nucleon (NN) processes, as indicated by the various lines.

observations of the Small Magellanic Cloud [65] have shown that CR are a Galactic and not a extra galactic phenomenon. The flux of gamma-ray emission (> 100 MeV) measured was $0.5 \times 10^{-7}\ cm^{-2}\ s^{-1}$, a third of the expected value of $(2.4 \pm 0.5) \times 10^{-7}$ $cm^{-2}\ s^{-1}$ if cosmic-rays were universal in origin.

Sources of CR are not yet known but are believed to be supernovae, supernova remnants, pulsars, compact objects in close binary systems, and stellar wind. To sustain the observed CR density of 1 eV cm^{-3}, the total power of Galactic CR sources needed is of the order $\sim 10^{40}$ erg s^{-1}. If the supernova rate in the Galaxy is 1 every 30 years, a release of energy in the form of CR of 10^{49} erg per supernovae is required. This value comes to about 5% of the kinetic energy of the ejecta, which is in agreement with the prediction of the theory of diffusive shock acceleration [41]. These shock accelerated CR propagate further in the Galaxy where they are contained for at least 10 million years before escaping into intergalactic space. Before escaping into the intergalactic space, CR spend most of the time in a region several kpc wide around the Galactic disk. Direct evidence for this wide confinement region comes from observations of synchrotron emission from CR electrons, which indicates a scale height that is much larger than that of the Galactic disc [22].

During their propagation, the initial spectra and composition of CR change due to energy gain and loss processes. These processes include the production of secondary particles and γ-rays. Secondary nuclei and isotopes that are rare in nature are produced in spallation processes (e.g. $^{12}\mathrm{C} \rightarrow ^{11}\mathrm{B}$). Because secondary antiprotons, positrons, and diffuse γ-rays are all products of the same proton-proton-interactions, accurate measurements of the antiproton and positron fluxes, especially at high energies, could provide a diagnostic of the interstellar nucleon spectrum complementary to that provided by γ-rays [51, 66]

2.2 Basic Processes of Gamma-Ray Production

Gamma-rays are produced in the galaxy through three main processes:

1. Decay of π^0 mesons produced through the interaction of CR nucleons with the interstellar gas.

2. Bremsstrahlung from relativistic CR electrons interacting with the interstellar gas.

3. Inverse Compton scattering from relativistic CR electrons with the interstellar optical, infrared, and microwave radiation field.

2.2.1 Pion Decay

The interaction of CR nucleons, predominantly protons and α particles, produce neutral and charged pions via $N + N \rightarrow \pi^{(\pm,\circ)} + X$. Neutral pions in turn decay into γ-rays ($\pi^0 \rightarrow \gamma + \gamma$). The production spectrum of secondary γ-rays can be obtained if one knows the distribution of pions $F_{\pi^0}(\epsilon_{\pi^0}, \epsilon_p)$ from a collision of a proton of energy ϵ_p, and the distribution of γ-rays $F_\gamma(\epsilon_\gamma, \epsilon_{\pi^0})$ from the decay of a pion of energy ϵ_{π^0}:

$$\frac{df_\gamma}{d\epsilon_\gamma} = n_H \int_{\epsilon_p^{min}}^{\infty} d\epsilon_P J_p(\epsilon_p) \langle \eta \sigma_{\pi^0}(\epsilon_p) \rangle \int_{\epsilon_{\pi^0}^{min}}^{\infty} d\epsilon_{\pi^0} F_\gamma(\epsilon_\gamma, \epsilon_{\pi^0}) F_{\pi^0}(\epsilon_{\pi^0}, \epsilon_p) \qquad (2.1)$$

where n_H is the atomic hydrogen number density, $J_p(\epsilon_p)$ is the proton flux, $\langle \eta \sigma_{\pi^0}(\epsilon_p) \rangle$ is the inclusive cross section of π^0 production, and $\epsilon_{\pi^0}^{min} = \epsilon_\gamma + m_{\pi^0}/4\epsilon_\gamma$ is the minimum energy a pion should have to contribute to the production of γ-rays with energy ϵ_γ.

For elements heavier than hydrogen, the inclusive cross section of π^0 production should be scaled with a factor $\sim (A_1^{3/8} + A_2^{3/8} - 1)^2$, where $A_{1,2}$ are the atomic

numbers of the target and CR nuclei. Besides hydrogen, the main contributor is helium, with a ratio in the interstellar medium of He/H ~ 0.1 by number.

The distribution of γ-rays from π^0 decay is given by:

$$F_\gamma(\epsilon_\gamma, \epsilon_{\pi^0}) = \frac{2}{m_{\pi^0}\Gamma_{\pi^0}\beta_{\pi^0}} \tag{2.2}$$

with

$$\frac{m_{\pi^0}}{2}\Gamma_{\pi^0}(1-\beta_{\pi^0}) \leq \epsilon_\gamma \leq \frac{m_{\pi^0}}{2}\Gamma_{\pi^0}(1+\beta_{\pi^0}) \tag{2.3}$$

where Γ_{π^0} and β_{π^0} are the pion Lorentz factor and velocity.

The γ-ray spectrum (equation 2.1) obtained after integration over the CR nucleon spectrum peaks at 70 MeV and is symmetric about the maximum on a logarithmic energy scale. For CRs with a power law spectral distribution of index α_{cr}, the spectral distribution for high energy γ-rays will also be a power law spectrum with $\alpha_\gamma = 4/3(\alpha_{cr} - 1/2)$[72].

2.2.2 Bremsstrahlung

Bremsstrahlung, or braking radiation, happens when a charged particle is deflected in the electric field of another charged particle. In the interstellar medium consisting of atomic hydrogen, helium, and the ionized medium, electron-nucleon bremsstrahlung is the most important.

In the case of a nucleus as a target, the nucleus is screened by the bound electrons. The screening factor[2] is defined as[66]:

$$\delta = \frac{\epsilon_\gamma}{2\Gamma_\circ\Gamma} \tag{2.4}$$

[2]For units $\hbar = c = m_e = 1$.

where ϵ_γ is the energy of the emitted photon, $\Gamma_\circ$ and Γ are the initial and final Lorentz factor of the electron in the collision. In the case where $\delta \to 0$, the distance between the electron and the atom is large compared to the atomic radius. In this case the screening of the nucleus by the bound electrons is important. For low-energy electrons only the contribution of the nucleus is significant, while at high energies the atomic electrons can be treated as unbound targets in the same way as the nucleus[66].

The contribution to the Galactic diffuse emission from bremsstrahlung is important for energies < 200 MeV. For electron energies ≥ 2 MeV, the production cross section is given by:

$$\frac{d\sigma_b}{d\epsilon_\gamma} = r_e^2 \alpha_f \frac{1}{\epsilon_\gamma} \left[\left(1 + \frac{\Gamma^2}{\Gamma_\circ^2} \right) \phi_1 - \frac{2}{3} \frac{\Gamma}{\Gamma_\circ} \phi_2 \right] \tag{2.5}$$

where r_e is the classical electron radius, α_f is the fine structure constant, and for an unshielded charge, $\phi_1 = \phi_2 = \phi_u$ which is given by:

$$\phi_u = 4Z^2 \left[\ln \left(\frac{2\Gamma_\circ \Gamma}{\epsilon_\gamma} - \frac{1}{2} \right) \right] \tag{2.6}$$

where Z is the nucleus charge.

Approximate expressions for σ_b have been derived for different energy ranges of T, the kinetic energy of the electron:

- Non-relativistic case; $T < m_e c^2$:

$$\sigma_b = \frac{16}{3} \sigma_\circ Z^2 \tag{2.7}$$

- Highly relativistic case; $T > m_e c^2$:

$$\sigma_b = 4\sigma_\circ Z^2 \left[\ln \left(\frac{2(T + m_e c^2)}{m_e c^2} \right) - \frac{1}{3} \right] \tag{2.8}$$

- Extreme relativistic case; $T > 137 m_e c^2 Z^{-1/3}$:

$$\sigma_b = 4\sigma_\circ Z^2 \left[\ln\left(183 Z^{-1/3}\right)\right] \tag{2.9}$$

where $\sigma_\circ = 4(1/137)(e^2/m_e c^2)^2 Z^2 = 0.58$ millibarn/nucleus.

To obtain the production spectrum of electron bremsstrahlung for a distribution of electrons we integrate over the spectrum of CR electrons and sum over the species of the ISM:

$$\frac{df_\gamma}{d\epsilon_\gamma} = \sum_{i=H,HI,HII,He} cn_i \int d\gamma f_e(\gamma) \frac{d\sigma_i}{d\epsilon_\gamma} \tag{2.10}$$

where c is the speed of light, n_i is the number density of the corresponding species, and $f_e(\gamma)$ is the spectrum of CR electrons.

The γ-rays that result from bremsstrahlung have energies that are comparable to those of the incident electron. Thus, if the population of the electrons is characterized by a power law with spectral index α_e, the resulting γ-ray spectrum has an index $\alpha_\gamma \approx \alpha_e$[72].

2.2.3 Inverse Compton Scattering

Inverse Compton scattering is a process in which a high energy electron interacts with a low energy photon, transferring some of its energy to the photon.

For photons with energies, in the electron rest frame system (ERS), $\epsilon_\circ \Gamma(1 - \beta\cos\theta) \ll m_e c^2$, where $\epsilon_\circ$ is the energy of the background photon, θ is the angle between the momenta of the electron and the photon, and Γ is the Lorentz factor of the electron in the rest frame of the photon, the scattering cross section is that given by the classical Thomson cross section:

$$\sigma_T = \frac{8\pi}{3} r_e^2 \tag{2.11}$$

where r_e is the classical electron radius. In this nonrelativistic region, the cross section is independent of the photon energy. As soon as the energy of the electron is high enough that the up-scattered photon has an ERS energy that is comparable with the electron rest mass, the cross section is given by the Klein-Nishina formula:

$$\sigma = 2\pi r_e^2 \left[\frac{1+\alpha}{\alpha^2} \left(\frac{2(1+\alpha)}{(1+2\alpha)} - \frac{1}{\alpha} \ln(1+2\alpha) \right) + \frac{1}{2\alpha} \ln(1+2\alpha) - \frac{(1+3\alpha)}{(1+2\alpha)^2} \right] \tag{2.12}$$

where $\alpha = \epsilon_\circ / m_e c^2$.

The average energy of the scattered photons is given by:

$$\langle \epsilon_\gamma \rangle \sim \Gamma^2 \epsilon_\circ \tag{2.13}$$

This allows for the estimate of the contribution of different background radiation fields to the resulting spectrum of γ-rays.

If the electron is energetic enough, the incoming photons can be considered as a unidirectional beam in the ERS since the angular distribution of the photons in that system is confined to angles $\sim 1/\Gamma$ radians. In this case, for an isotropic distribution of monoenergetic electrons and photons the spectrum of the up-scattered photons is given by:

$$\frac{dR(\Gamma, \epsilon_\circ)}{d\epsilon_\gamma} = \frac{2\pi r_e^2}{\epsilon_\circ \Gamma^2} \left[2q \ln q + (1+2q)(1-q) + \frac{1}{2} \frac{(4\epsilon_\circ \Gamma q)^2}{(1+4\epsilon_\circ \Gamma q)} (1-q) \right] \tag{2.14}$$

where ϵ_γ is the energy of the photon after scattering, $q = \epsilon_\gamma / [4\epsilon_\circ \Gamma^2 (1 - \epsilon_\circ / \Gamma)]$ and $1/4\Gamma^2 < q \leq 1$.

The resulting spectrum for a distribution of electrons can be obtained by integrating over the spectra of electrons and the background radiation:

$$\frac{df_\gamma}{d\epsilon_\gamma} = c \int d\epsilon_\circ \int d\gamma f_\nu(\epsilon_\circ) f_e(\gamma) \frac{dR(\Gamma, \epsilon_\circ)}{d\epsilon_\gamma} \tag{2.15}$$

where $f_{\nu,e}$ are the spectra of the interstellar radiation field and the CR electrons.

2.3 Galactic Structure

The Galaxy is a barred spiral with a radius of ~ 30 kpc. For the γ-ray diffuse emission the important components are the interstellar gas and the interstellar radiation field [22].

2.3.1 Interstellar Gas

The gas content in the Galaxy is dominated by atomic (HI) and molecular (H_2) hydrogen. Although present in approximately equal amounts in the inner Galaxy ($\sim 10^9$ $M_\odot$), atomic and molecular hydrogen have very different radial distributions. In addition, low density ionized hydrogen (HII) and heavier elements make a small fraction of the interstellar gas. Helium has a ratio of $10 \sim \%$ by number relative to hydrogen. This makes it an important contributor to the gas-related γ-ray emission.

Atomic hydrogen extends out to 30 kpc, with a rather uniform density and a scale height of 200 pc [61]. The atomic hydrogen disk is asymmetric, with warping in the outer disk, and it extends to about 1.5 kpc above the Galactic plane in the northern hemisphere and down to about 1 kpc in the southern hemisphere [22]. The gas density is roughly uniform at 1 atom cm^{-3}. HI gas is mapped directly via its 21 cm radio line, which gives both distance (from the Doppler-shifted velocity and Galactic rotation models) and density information.

Molecular hydrogen is concentrated within R $<$ 10 kpc, with a peak around 5

kpc and a scale height of 70 pc. It is mainly concentrated in dense clouds of typical density of 10^4 atom cm^{-3}. Unlike atomic hydrogen, H_2 cannot be detected directly on large scales. However, the 115 GHz emission of the abundant molecule ^{12}CO is a good tracer, since it forms in the dense clouds where the H_2 resides. Molecular hydrogen column densities N_{H_2} have been found to be approximately proportional to W_{CO}, the integrated density of CO line, where the constant of proportionality is $X \equiv N_{H_2}/W_{CO}$. A recent result of the H_2 density obtained from a complete CO survey and infrared and HI maps gives an average $X \equiv N_{H_2}/W_{CO} = 1.8 \times 10^{20}$ cm^{-2} K^{-1} km^{-1} s [23]. Observations of particular local clouds [25, 26, 27, 38] yield somewhat lower values $X = (0.9 - 1.65) \times 10^{20}$ cm^{-2} K^{-1} km^{-1} s (with error bars of 15-20%), but still close to the average.

Ionized hydrogen is present in the interstellar medium at lower densities $\sim 10^{-3}$ atom cm^{-3} and has a large scale height of 1 kpc. Although this gas makes a small contribution to the γ-ray emission, it is of interest because it produces a much broader latitude distribution than the neutral gas.

2.3.2 Interstellar Radiation Field

The interstellar radiation field (ISRF) is made up of contributions from starlight, cosmic microwave background (CMB), and emission from dust [22]. It is important for γ-ray production through inverse Compton scattering of CR electrons.

Stellar emission dominates from 0.1 μm to 10 μm, and emission from very small dust grains contributes from 10 μm to 30 μm. Emission from dust at T $\sim$20 K dominates from 20 μm to 300 μm. The 2.7 K microwave background is the main radiation field above 1000 μm. The ISRF has a vertical extent of several kpc, where the Galaxy acts as a disk-like source of radius $\sim$10 kpc. The radial distribution of the stellar component is also centrally peaked, since the stellar density increases exponentially inwards with a scale-length of $\sim$2.5 kpc until the bar is reached. The dust

component is related to that of the atomic and molecular hydrogen and is therefore distributed more uniformly in radius than the stellar component.

Chapter 3

The Milagro Detector

The Milagro observatory is a ground-based TeV detector that utilizes a large water Cherenkov detector to observe extensive air showers produced by high energy particles impacting the Earth's atmosphere. Milagro's distinct advantage compared to other ground-based TeV gamma-ray detectors is its wide field of view (2 steradian overhead sky) and its high duty cycle ($> 90\%$ live time). These factors give Milagro the potential for discovery of new sources with unknown positions and times, such as gamma-ray bursts, flaring AGNs, and observation of diffuse extended sources like the Galactic plane or large supernova remnants.

The Milagro detector configuration, its electronics and data acquisition system, trigger conditions, event reconstruction algorithms, and simulations are described in this chapter.

3.1 Detector Description

3.1.1 Location

The Milagro detector is located near Los Alamos, NM, in the Jemez mountains at latitude 35° 52' 45" and longitude 106° 40' 37" West. Since the number of particles

Figure 3.1: An aerial view of the Milagro detector. The pond is visible in the center of the photo. The red circles mark locations of the outrigger tanks.

in an EAS decreases after a height known as shower maximum ($\sim$ 7-10 km above sea level) is reached, the detector is located at high altitude in order to sample as many particles as possible. The altitude of the detector is 2630 m which translates into 750 g cm^{-2} of atmospheric overburden. The detector consist of a 24 million liters artificial pond sealed with a light tight cover and instrumented with 723 photomultiplier tubes (PMTs) arranged in two layers. The pond has dimensions of 80 m $\times$ 60 m $\times$ 8 m (depth). The sides of the pond are sloping, leading to an area of 30$\times$50 m^2 on the bottom. A schematic diagram of the pond is shown in Figure 3.2. In addition to the central pond, Milagro is surrounded by an outrigger array of 175 tanks, each containing a single PMT. The outrigger array extends the physical area of the detector from 5,000 m^2 to 40,000 m^2. Figure 3.1 shows an aerial view of Milagro. The pond is visible in the center of the photo. The red circles mark locations of the outrigger tanks.

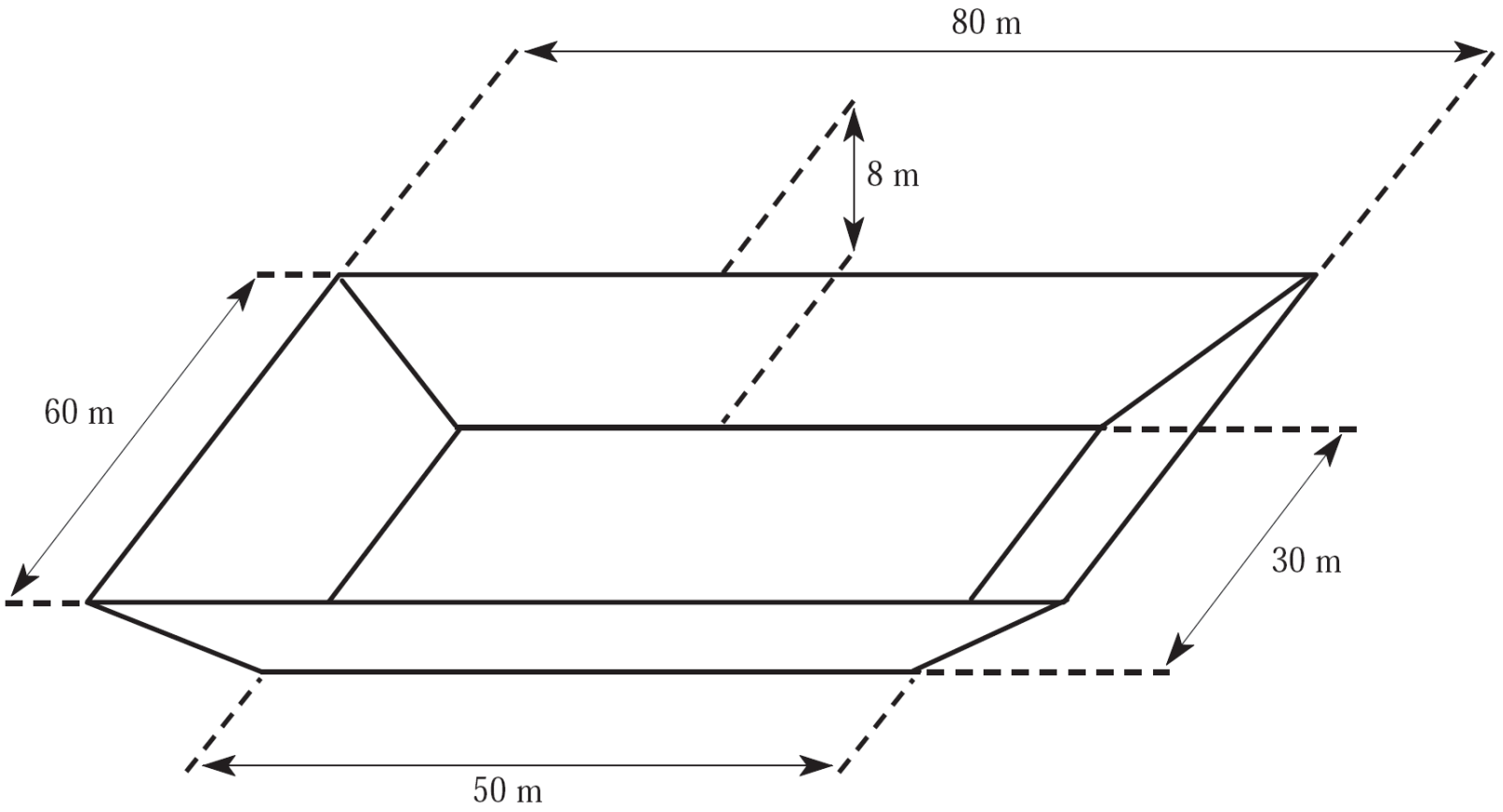

Figure 3.2: A schematic diagram of the Milagro pond (not to scale). Figure taken from [45]

3.1.2 The Pond

The pond PMTs are arranged in two layers. The top layer, called the air shower (AS) layer, consists of 450 PMTs and is under 1.5 m of water. This layer is used primarily for triggering and event reconstruction. The bottom layer, called the muon layer (MU), consists of 273 PMTs and is placed under 6 m of water. It is used for background rejection and energy imaging. In each of these layers the PMTs are arranged on a 2.8 m $\times$ 2.8 m grid. The MU layer PMTs are horizontally offset from the AS layer PMTs by half the grid spacing. Figure 3.3 shows a schematic diagram of the PMT placement in the pond [34]. Figure 3.4 shows the inside of the pond. The AS layer PMTs can be seen attached to the grid crossing, while the MU layer PMTs are tied between grid crossing. This photo was taken with the cover inflated during one of the tube repair operations.

The pond densely samples the EAS particles that reach the detector level. Since the Cherenkov angle in water is $\sim 41^{\circ}$, the AS layer PMTs detects the Cherenkov radiation from the relativistic charged particles in the air shower with high efficiency. Roughly 50% of all electromagnetic particles that enter the pond are detected. In addition, at ground level gamma-rays in an EAS outnumber electrons and positrons by a factor of ~ 5. Since the AS PMTs are placed under 4 radiation lengths of water, these gamma-rays convert to electrons and positrons before reaching this layer. These electrons and positrons in turn Cherenkov radiate in water and will be detected. The depth of the Muon layer corresponds to 16 radiation lengths of water. This means that all electromagnetic particles in an air shower will be absorbed before reaching this layer and that only muons and hadrons can penetrate and shower near this layer. Thus, the MU layer is used to detect muons and hadrons which are mostly present in hadronic showers. Muons of energies as low as 1.2 GeV reach the muon layer in Milagro. Monte Carlo simulations estimate that 80 % of cosmic-ray-initiated air showers and 6 % of gamma-ray-initiated air showers that trigger Milagro contain a

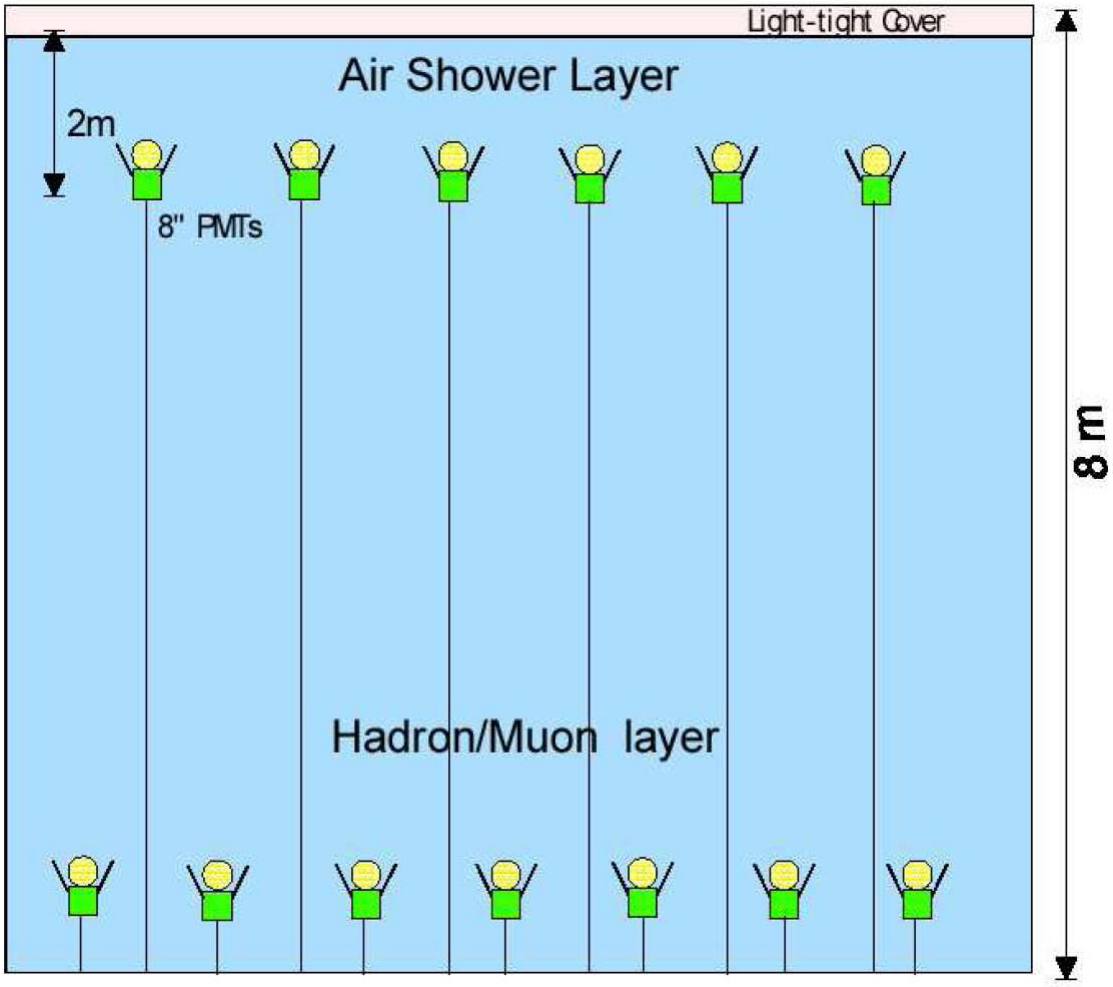

Figure 3.3: Schematic of PMT placement in the pond (not to scale). Figure taken from [34].

Figure 3.4: An inside view of the Milagro pond.

muon or a hadron that enters the pond[1].

The combination of high altitude and high particle detection efficiency gives Milagro a lower energy threshold compared to other air shower arrays. Milagro is sensitive to gamma-rays with energies above $\sim$ 100 GeV.

The PMTs used in Milagro are 20 cm in diameter (Hamamatsu #R5912SEL). A waterproof polyvinyl chloride (PVC) casing protects the electronic base of each PMT. A single RG-59 coaxial cable carries the high voltage to the tube and the AC signal from the tube back to the electronic system. The initial high-voltage Fisher connector used when all of the PMTs were installed had a high failure rate when submerged in water. This was the cause of many PMT failures and led to the development of an improved connector which had reduced strain and was sealed in heat shrink and glue. Each PMT is surrounded by a conical collar baffle. These baffles were installed for two reasons: blocking out light traveling horizontally (from muons at large zenith angles) and increasing the collection area of each PMT. The baffles were originally made of anodized aluminum on the inside with black polypropylene on the outside. Aluminum was originally chosen because its good reflectivity increases the collection area of the PMT. However, due to corrosion of the aluminum in water, the aluminum baffles were replaced by new baffles made of polypropylene with a white interior and black exterior.

3.1.3 The Outrigger Array

The outrigger array covers a 40,000 m^2 area around the central Milagro pond (Figure 3.1). An outrigger is an individual Cherenkov counter that consists of a 5,680 liter tank of water, measuring 2.4 m in diameter and 1 m in height. Each outrigger is instrumented with a single PMT facing the bottom of the tank. The inside of each

[1]The rate of production of muons and hadrons in a gamma-ray initiated air shower is much less than this. However muons and hadrons generated in the shower have a much higher survival probability than electrons and positrons and can reach the ground level.

tank is lined with Tyvek to reflect light inside the tank.

By extending the physical area of the detector from 5,000 m^2 to 40,000 m^2, the outrigger array allows a more accurate determination of the location of the shower core. It also improves the angular reconstruction of the air shower by providing a longer lever arm across the shower front to reconstruct the shower direction.

3.2 Water System

The central Milagro pond holds 24 million liter of water. The water is constantly recirculated at a rate of 200 GPM. During recirculation the water is filtered through a charcoal filter, a 10 μm filter, a 1 μm filter , a carbon filter, and a 0.2 μm filter [2] to maintain transparency. In addition, the water passes through a UV filter before returning to the pond to prevent any biological growth. To ensure good quality of the water, measurements of the attenuation length of the water are made periodically. Recent tests have shown an attenuation length of 17 m at 325 nm. The bottom of the pond is lined to keep contaminants out of the filtered water.

3.3 Pond Cover

In order to keep external light out of the pond, the pond is covered with a 1 mm thick polypropylene cover. The top of the cover is painted with highly reflective roofing paint in order to reduce the temperature inside the pond. The cover is normally kept in contact with the water by adjustable nylon straps as seen in figure 3.1. During repair operations, the cover is inflated through vents and fans that are placed in the pond utility building (PUB). When fully inflated the internal pressure keeps the cover approximately 20 feet from the surface of the water. This allows people to enter the

[2]The 0.2 μm filters have been removed due to clogging with the aluminum oxide from corroding baffles.

pond and conduct repair operations.

3.4 Electronic System

The main function of the electronic system is to provide timing and pulse height information from each PMT. In addition, selection of showers for digitization must be made using a trigger decision. The accurate time-of-arrival of the selected showers must be recorded. Custom made electronics boards distribute high voltage to the PMTs and processes the PMT signals prior to readout using commercial FASTBUS modules.

3.4.1 Signal Extraction

The PMTs are divided into patches of sixteen tubes that operate at the same high voltage level. Each patch is first processed by a custom 16 channel front end board (FEB). The FEB reads in the AC signal from each PMT, and distributes the high voltage (HV) to each tube. The FEB then processes the signal from each PMT and sends it to the digital boards where timing and pulse height information is prepared for digitization.

To determine the arrival time and charge of a signal in a PMT, the time-over-threshold (TOT) technique is used. A more straight-forward way of doing this would be to employ analog-to-digital converters (ADCs), but due to high cost and high event rate in Milagro the TOT method was used instead.

In the FEB, the signal from each PMT is split and sent to high gain ($\sim \times 7$) and low gain ($\sim \times 1$) amplifiers [13]. The amplified signals are then sent to a discriminator with a preset photo-electron (PE) thresholds. The signal from the high gain amplifier is sent to a low threshold discriminator with a $\sim 1/4$ PE threshold. The signal from the low gain amplifier is split in two, one part goes to a high threshold discriminator

with a $\sim$ 5 PE threshold, while the other goes to an output which can be connected to an external ADC for calibration purposes. Whenever the PMT pulse crosses either of the low or high thresholds, an edge is generated as illustrated in fig 3.5. For a small pulse which crosses only the low threshold, two edges are generated. For a pulse that crosses both the low and high thresholds, four edges are generated. The time spent over the threshold can then be calibrated to get the charge, under the assumption that all signals have the same shape.

The output of the low and high threshold discriminators are sent to the digital boards. The digital boards multiplex the signals from the low and high threshold discriminators, and also provide triggering and monitoring information. The edges are then digitized in LeCroy FASTBUS time-to-digital converters (TDCs). The FASTBUS TDCs can record up to 16 edges per event with a 0.5 ns resolution. A FASTBUS latch connected to a GPS clock encodes the common stop time for each event.

3.4.2 Triggering

Over the course of running Milagro, different trigger conditions have been used. From the time Milagro began taking data in January 1999 until March 2002, the Milagro trigger consisted of a simple multiplicity count of the number of PMTs hit in the AS layer (N_{top}). A threshold on this number was set to be between 50 and 70 PMTs hit within a 200 ns time window. The threshold was set by the maximum data rate the data acquisition system (DAQ) could handle ($\sim$ 2000 Hz). A lower trigger threshold would increase the number of low energy (hundreds of GeV) showers detected. This would increase Milagro's sensitivity to gamma-rays at these energies. One obstacle to doing so are events generated by single muons traveling nearly horizontally across the pond. A muon entering the pond at high angle and crossing the pond horizontally causes a cone of light that produces signals in a large number of PMTs. Such an event can satisfy the multiplicity trigger condition. On the other hand, these events have

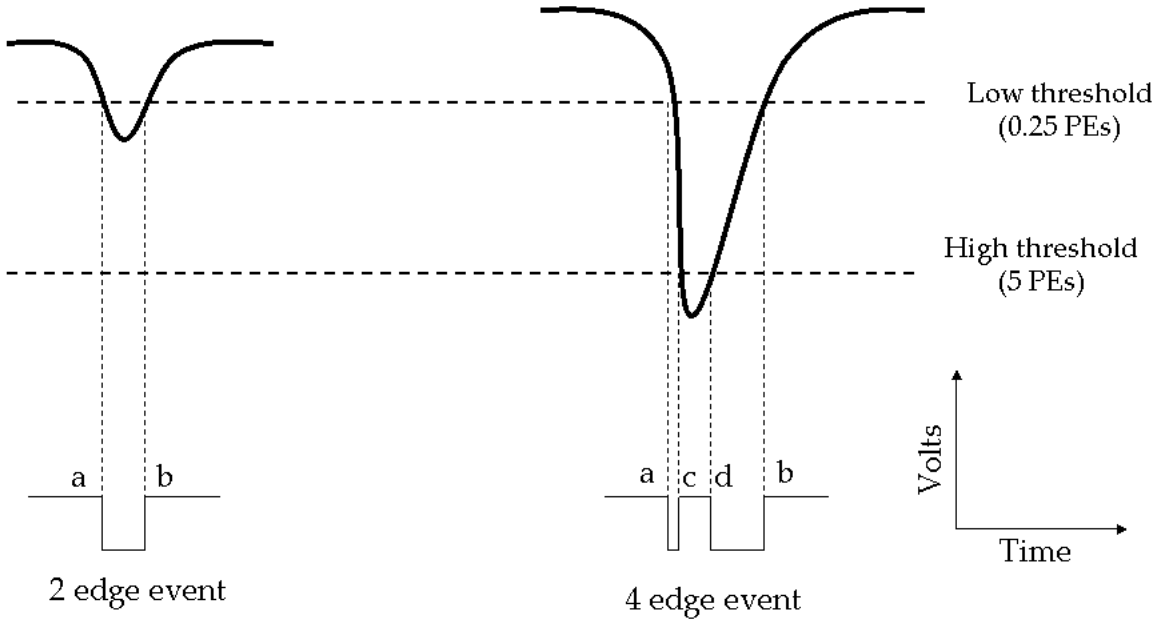

Figure 3.5: Time-over-threshold (TOT) method.

different time profiles in the PMT arrival times than that of an air shower. While particles in an air shower travel nearly at the speed of light, c, the light cone from a horizontal muon travels at the speed of light in water, c/n, where n is the index of refraction of light in water. Thus, hits from a high angle muon will occur over a longer period of time than those from an air shower, and by making a cut on the time development of the event, it is possible to reject these muon events. Although such events can be removed after the angle reconstruction, since the resulting angles are unphysical, removing these events at the trigger level will allow for the trigger threshold to be lowered without a large increase in the event rate.

The arrival time profile of an event is characterized by the risetime parameter. The risetime of an event is defined as the time interval within which 10% to 90% of the hits occur in that event. The risetime distributions for data events which were fit, data events which failed the fit, and simulated gamma-ray showers are shown in Figure 3.6 [33]. It is clear from this figure that data events that failed the fit have longer risetimes. The risetime is calculated and applied at the trigger level to bias triggers at low multiplicities toward gamma-ray showers while keeping the trigger rate below the 2000 Hz limit of the DAQ system.

A custom made VME (Versa Module Europa) trigger card was built that allowed the risetime of the event to be included in the trigger decision. In addition, the card is reprogrammable allowing the implementation of multiple trigger conditions and external triggering. These trigger conditions could be changed to keep the trigger rate below the maximum the DAQ system could handle. The set of trigger conditions that were used when the VME trigger was first installed are as follows:

1. $N_{top} > 20$ & risetime < 50 ns.

2. $N_{top} > 53$ & risetime < 87.5 ns.

3. $N_{top} > 74$.

These values were selected to maximize the number of low energy showers, while keeping the trigger rate at a manageable level of $\sim$ 1800 Hz with $\sim$ 8% dead time. The trigger conditions have been modified over time to keep the trigger rate below the DAQ limit. The simple multiplicity trigger was brought back online on April 1st, 2006 after the VME trigger card failure on the same day.

3.5 Data Acquisition System

When a trigger condition is met, information from the TDCs is read out using a FASTBUS Smart Crate Controller (FSCC). A GPS clock is used to determine the time of the event. The TDC information from all the channels are transferred to a VME memory module. This data are then read and processed by the DAQ computer. The DAQ computer system consists of a master PC and several PC workers. The DAQ system operates using a client-server architecture in which the master controls the assignments of data blocks to workers on several PCs.

The raw data are broken into runs and subruns. A new subrun is started every 5 minutes. A new run started at 0:00 UT every day and will last for a whole day unless the DAQ system is shut down by a user, for maintenance, or by external factors like power outage. The raw data consists of the TOT information from each tube and the time of the event. Storing all the raw data would be prohibitively expensive since in one day it will require more than 230 GB of disk space which translates into $\sim$ 82 TB/year. Instead raw data are saved only for selected sources, such as the Crab Nebula, the active galaxies Mrk 421 and Mrk 501 when they are flaring, the sun, and the moon. The raw data are also saved when there is a notification, by other experiments, of a GRB that occurred in the field of view of Milagro. All the raw data are calibrated and reconstructed in real time. All of these reconstructed data are saved. The reconstructed data contain information about each reconstructed event

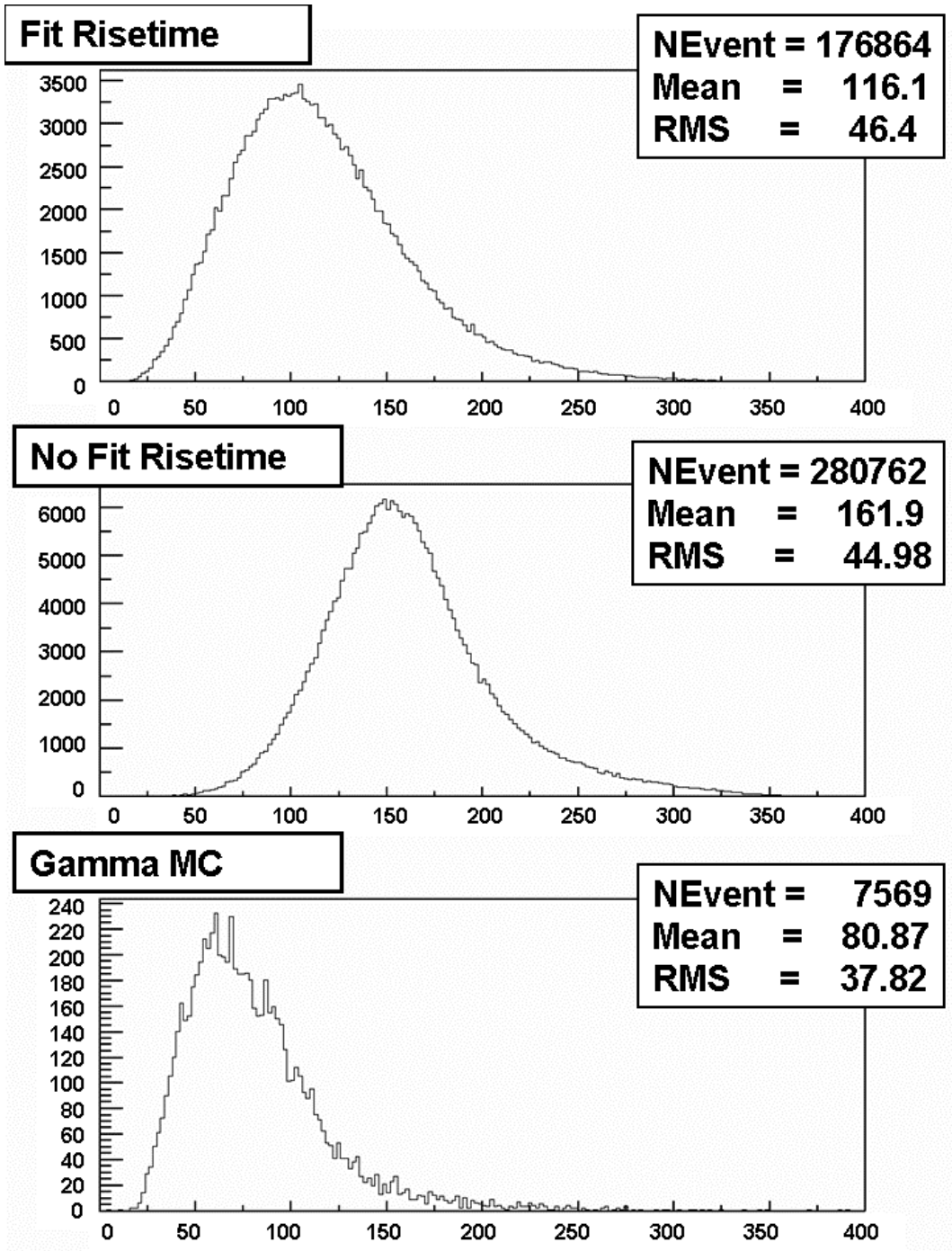

Figure 3.6: Distributions of the risetime parameter [33]. From top to bottom: data events that could be fit, data events that failed the fit, and simulated gamma-ray showers.

which include, the reconstructed direction of the event, core position, event time, the modified Julian date (MJD) (see section 4.1.3), and timing error information from the GPS clock. The size of disk space required to store all the reconstructed data for one day is $\sim$ 5 GB. The reconstructed data are stored on a DLT (Digital Linear Tape) tapes at the site , and more recently on portable disk arrays, which are then physically transferred for storage in Los Alamos National Laboratory. The reconstructed data are also piped through the network to large redundant disks arrays (RAID) in Los Alamos National Laboratory and University of Maryland.

3.6 Calibration

As was discussed above, the raw data from Milagro consist of a series of edge times. This raw edge information must be converted to relative arrival times of the Cherenkov photons at the PMTs and to the number of PEs in each hit PMT. Although the hit time of each PMT is known, it must be corrected for two effects. The first correction involves timing corrections. This correction is required because the analog PMT pulses have finite risetime. A large pulse will cross a threshold more quickly than a smaller pulse. This correction is referred to as electronic slewing and is corrected for by measuring the change in start time as a function of TOT. The second correction applied accounts for differences in travel times of the PMT pulses through the signal cables and electronics. These corrections are done with a laser calibration system which consists of a pulsed laser, a filter wheel, and optical fibers that carry the light to a system of diffusing balls placed throughout the pond. The laser fires a set number of pulses of fixed amplitude through a filter wheel which go through optical fiber that connects to an optical switch, allowing the light to be sent to any of the thirty laser balls in the pond. A laser ball is an optical fiber with a sphere of epoxy at the end which diffuses the light out isotropically from the fiber. The filter wheel allows the

intensity of the light sent to the pond to be varied. Laser calibration data are taken periodically to produce new calibration constants [34].

In addition to the timing calibrations, the calibration of the PMT charge is carried out. As discussed above, in the TOT method an edge is generated whenever the PMT signal crosses one of the high or low discriminator thresholds. The TOT is proportional to the logarithm of the number of photo-electrons. This relation is determined using the occupancy method, which is based on the fact that, at low light levels, the number of photon-electrons created by the PMT obeys a Poisson distribution. This produces a logarithmic relation between TOT and the number of PEs. The exact relation is determined by the laser calibration.

3.7 Event Reconstruction

Next, each event has to be reconstructed to determine the direction of the incident primary particle and the core location of the air shower on the ground. During the development of an air shower, the swarm of particles spreads out laterally forming what is known as the shower front. The relative arrival times of the shower particles in the pond are used to reconstruct the direction of the incident primary particle. Figure 3.7 shows a conceptual drawing of the primary particle direction reconstruction in Milagro. The reconstruction of an event proceeds in the following steps:

3.7.1 Core Position Reconstruction

The core position of an EAS is the point on the ground at which the primary particle would hit if it were to experience no interaction in the atmosphere. Over the course of running Milagro, different algorithms have been used to determine the location of the shower core. The core of an air shower contains the highest energy particles in the shower. The particle density near the shower core is also at its maximum. Thus,

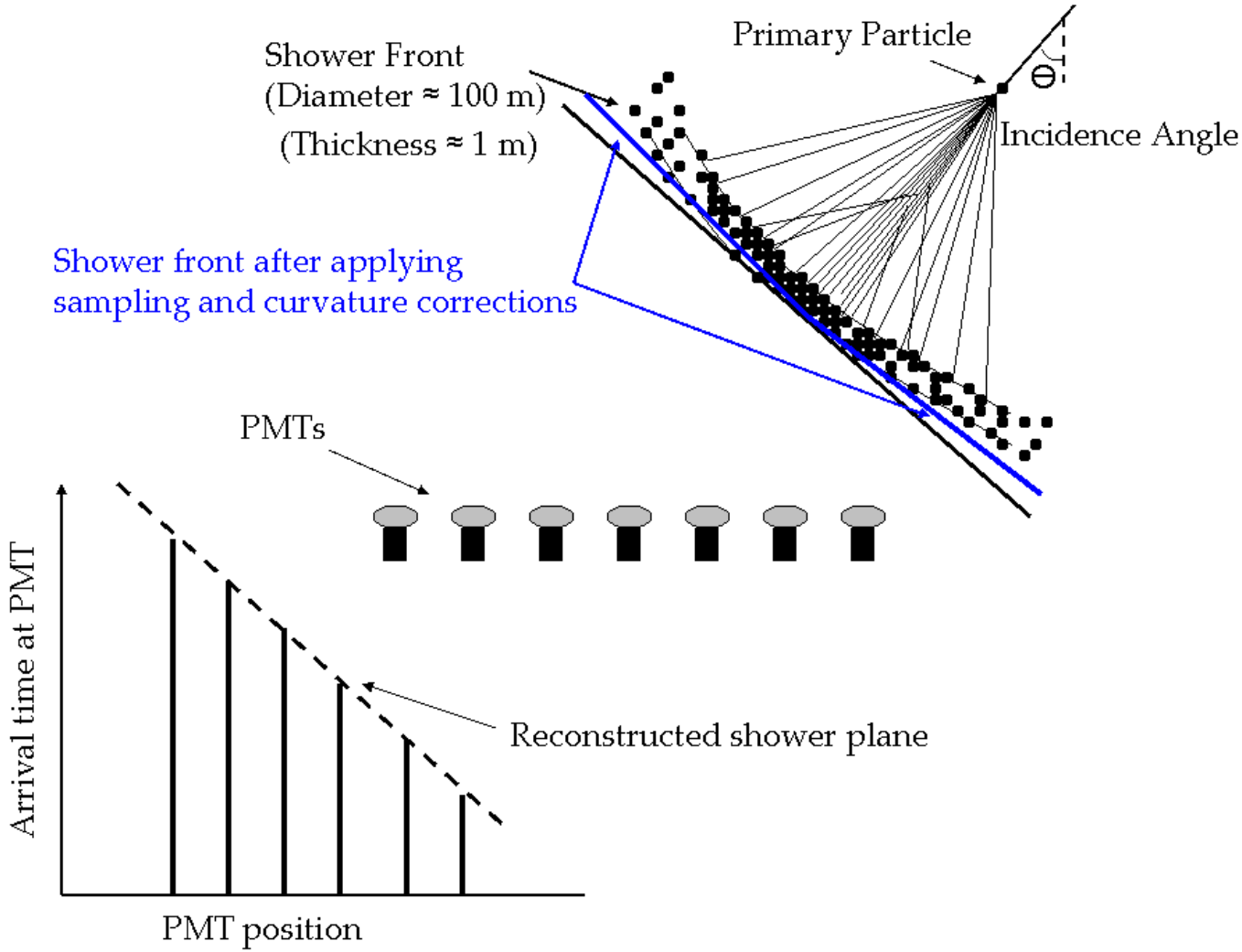

Figure 3.7: Conceptual diagram of the primary particle direction reconstruction in Milagro.

the shower core should be associated with the largest number of PEs detected and with the location of the largest number of PMTs hit in an event.

The first core fitter used in Milagro was a simple center of mass fitter which put all the cores on the pond. This algorithm used a weighted sum of the locations of all the hit PMTs in the AS layer. The core location in this case is given by:

$$x_{core} = \frac{\Sigma_i \sqrt{PE_i} \times x_i}{\Sigma_i \sqrt{PE_i}} \tag{3.1}$$

$$y_{core} = \frac{\Sigma_i \sqrt{PE_i} \times y_i}{\Sigma_i \sqrt{PE_i}} \tag{3.2}$$

where PE_i is the number of PEs detected by the PMT with coordinates x_i and y_i. The weight assigned for each hit PMT was taken as $\sqrt{PE_i}$ to keep the big hits from completely dominating the fit.

To improve the core fitter, several methods were used to to determine if the shower core was likely to be located off the pond. If the core was likely to be on the pond, the center of mass core fitter was used; otherwise the reconstructed core location is placed 50 meters from the center of the pond in the direction determined by the center of mass fitter. The value of 50 meters was used because Monte Carlo simulations indicate that this value results in the best agreement, on average, with the true core location.

After the installation of the outriggers, they were used in the core fitter to determine if the core was located on or off the pond. The ratio of the number of outriggers hit to the number of the AS layer PMTs hit provides a good measure of whether the core was on or off the pond. If the core was determined to be off the pond, the center of mass of the outriggers was used to determine the location of the shower core. If the core was determined to be on the pond, the center of mass of the AS layer tubes was used to determine the location of the shower core.

The current core fitter algorithm performs a least square fit to a 2-D Gaussian

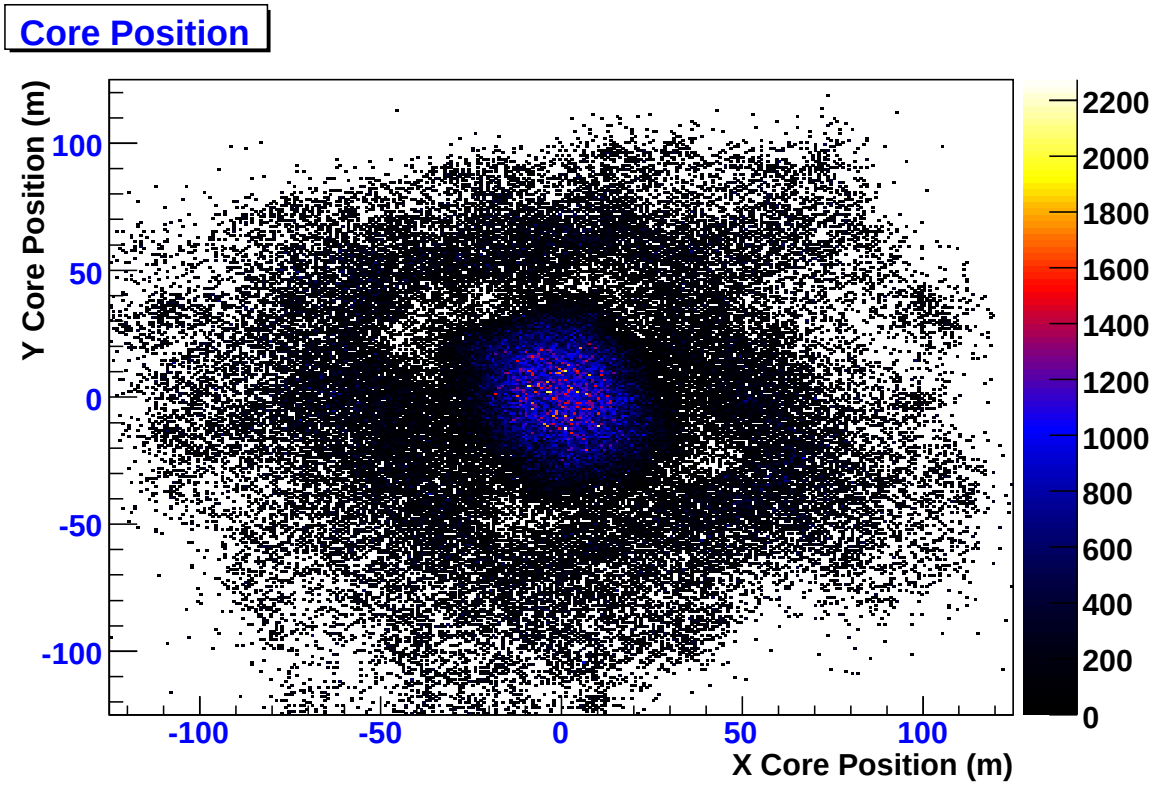

Figure 3.8: Reconstructed core positions for simulated gamma-ray events that triggered the detector using the current 2-D Gaussian fitter. In the figure, the y- and x-axes point north and east, respectively. The Milagro pond is inclined by angle of 24.4° from the north-south direction.

using the AS layer PMTs and the outriggers. Figure 3.8 shows the distribution of core locations for simulated gamma-ray events that triggered the detector using this core fitter. Figure 3.9 shows the fit core location versus true core location for simulated gamma ray events. The core resolution, the distribution of the errors in the fitted core location, is shown in figure 3.10. The error is determined by comparing the fitted core location to the true core location from the Monte Carlo simulations.

3.7.2 Shower Front Sampling Correction

The shower front of an extensive air shower has a finite thickness. It is thinner near the shower core and thicker near the edge of the shower (Figure 3.7). This thickness

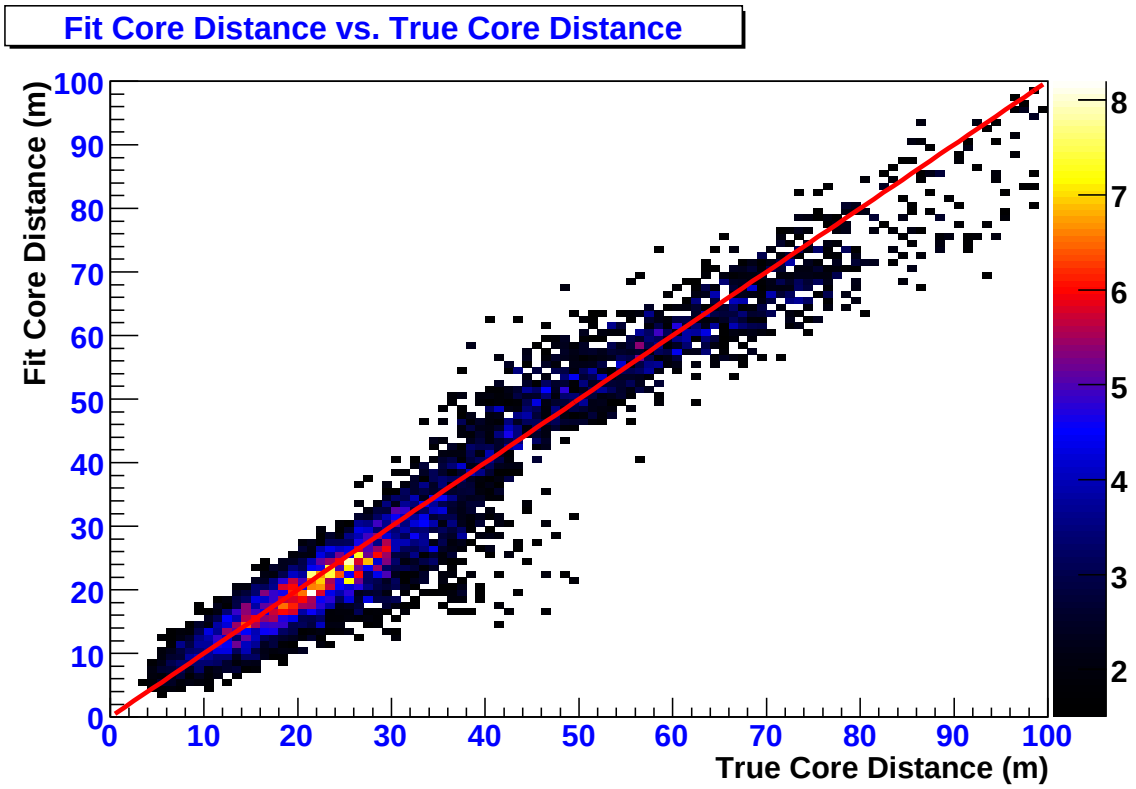

Figure 3.9: Reconstructed (fit) core position versus true core position for simulated gamma-ray events.

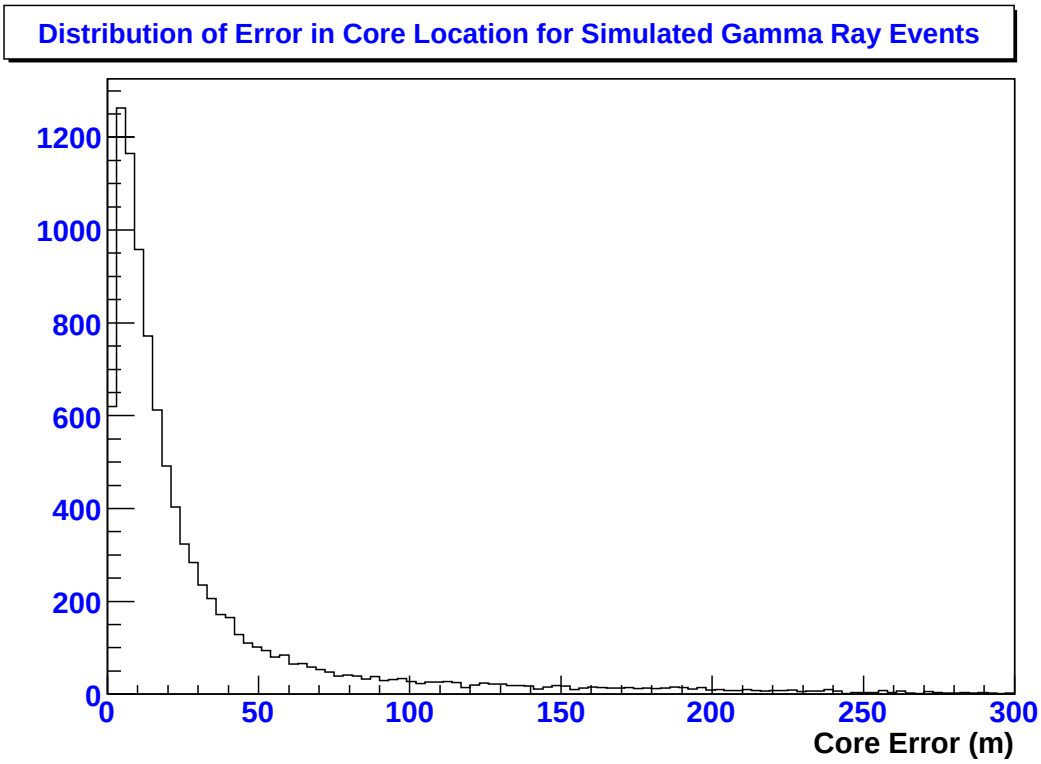

Figure 3.10: Distribution of error in core location for the simulated gamma-ray events shown in figure 3.9.

in the shower front is due to the lower energy secondary particles, which are present near the shower edge, suffering more scattering than the higher energy ones that are present near the shower core. Since the arrival time of the first photoelectron is measured by the TDC, the larger the number of particles (and thus more PE's), the earlier the measured arrival time, therefore a correction must be applied. Sampling correction corrects for the time difference between PMTs hit by one photon as opposed to many photons and is determined as a function of PEs from Monte Carlo simulations and data optimization. The sampling correction is relatively smaller around the core position, where each PMT collects more photons, and bigger away from the core, where each PMT collects fewer photons.

3.7.3 Shower Front Curvature Correction

For an extensive air shower, the shower front is actually not a plane, but is approximately a apherical cap with apex at the primary interaction location as shown in figure 3.7. One could fit a parabola to the shower front but the equations to be solved in such a fit are not of closed form and the algorithms to solve such equations will be slow and hard to implement in the reconstruction code. Therefore, instead of fitting the shower front to a parabola, a curvature correction is applied to the shower front and the resulting shower front is fit to a plane. The curvature of the shower front is defined as the slope of the cone measured from the shower core. The curvature correction accounts for this shower curvature and is 0.07 ns per meter from the core. The time information of each PMT used in the core reconstruction is corrected by this amount. The value of the curvature correction is found using Monte Carlo simulations. Monte Carlo simulations show an improvement in the angular resolution of Milagro when using this correction [13].

3.7.4 Direction Reconstruction

To reconstruct the direction of the primary particle, the shower front is fit to a plane using an iterative least squares (χ^2) fit (figure 3.7). These iterative fits are applied after the sampling and curvature corrections have been applied. Each hit PMT is assigned a weight depending on its pulse height. In each of these iterations, PMTs with poor residuals are removed from the fit, and the PE threshold cut is relaxed to allow more PMTs to enter in the fit in the next iteration. This process is repeated five times. Using this method $\sim 90\%$ of triggered data is successfully fit. The remaining 10% of the triggers are due to single muons passing through the detector at nearly horizontal angles and single hadrons.

Originally, only the AS layer was used in the angular reconstruction but after the addition of the outriggers they were used as well. The addition of the outriggers improved the angular resolution of the detector by giving a longer lever arm to reconstruct the shower.

A measure of the angular resolution of the detector is given by the Δ_{angle} variable. Δ_{angle} is defined as the space angle difference between the true direction of an air shower (from Monte Carlo simulations) and the reconstructed direction:

$$\Delta_{angle} = |\Omega_{true} - \Omega_{fit}| \tag{3.3}$$

If $\hat{n}_t$ represents a normal vector in the true direction of the air shower, from the Monte Carlo, and $\hat{n}_f$ represents a normal vector in the fitted air shower direction, then $\hat{n}_t$ and $\hat{n}_f$ are given by:

$$\hat{n}_t = \sin\theta_t \cos\phi_t \ \hat{x} + \sin\theta_t \sin\phi_t \ \hat{y} + \cos\theta_t \ \hat{z} \tag{3.4}$$

$$\hat{n}_f = \sin\theta_f \cos\phi_f \ \hat{x} + \sin\theta_f \sin\phi_f \ \hat{y} + \cos\theta_f \ \hat{z} \tag{3.5}$$

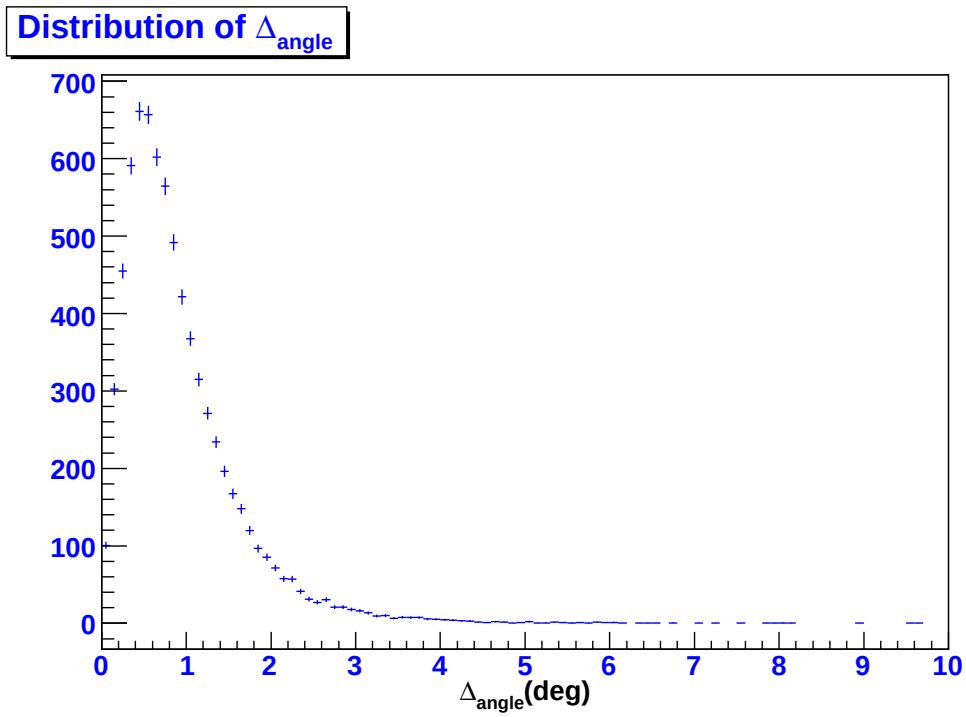

Figure 3.11: Distribution of Δ_{angle} for triggered gamma-ray events that passed the $N_{fit} \geq 40$ cut. The median of the Δ_{angle} distribution of $\sim 0.85^{\circ}$ is roughly the angular resolution of the detector for this N_{fit} cut.

The Δ_{angle} is then given by:

$$\Delta_{angle} = \arccos\left[\sin\theta_t \sin\theta_f \sin\left(\phi_t + \phi_f\right) + \cos\theta_t \cos\theta_f\right] \tag{3.6}$$

where θ and ϕ are the zenith and azimuth angles, respectively.

The distribution of Δ_{angle} is shown in figure 3.11 for triggered gamma-ray events with 40 or more PMTs participating in the fit ($N_{fit} \geq 40$). The median of the Δ_{angle} distribution of $\sim 0.85^{\circ}$ is roughly the angular resolution of the detector for this N_{fit} cut. In general the angular resolution improves with increasing the N_{fit} cut. The angular resolution is also a function of the background rejection cut applied. Angular resolutions as good as 0.3° can be achieved. More detailed discussions of the angular resolution and its dependencies are given in chapter 6.

3.8 Energy Dependence

Milagro has a rather broad energy response as can be seen in figure 3.12 [3]. This figure shows the distribution of detected gamma-ray events as a function of energy for a power law spectrum of $dN/dE \propto E^{-2.4}$. Air showers initiated by low energy primaries are hard to detect since fewer particles in the air shower will survive to the ground. At higher primary particle energies there are simply fewer primary particles (for a power law spectrum). Milagro has no well defined energy threshold below which no events are detected. The median triggered energy is useful as it usually illustrates the peak of the energy distribution, in logarithmic space, and above which fluxes and upper limits are usually quoted. The median energy for gamma-ray events that trigger Milagro is $\sim$ 3.5 TeV. For triggered gamma-ray events, 90% of the events from a source with this spectrum fall between $\sim$ 400 GeV and $\sim$ 70 TeV.

The median energy is a function of the zenith angle. At larger zenith angles particles in the shower have to traverse more of the atmosphere and hence fewer shower particles survive to ground level. This means that higher energy showers have a higher chance of triggering the detector at larger zenith angles than lower energy ones. This is illustrated in figure 3.13 which shows the relation between the median energy of detected gamma-ray events as a function of the zenith angle of the shower. The median energy is roughly constant for small zenith angles ($< 20^\circ$), but increases for larger zenith angles. For evens with zenith angles greater than 40°, the median energy is roughly 5 times that for events with small zenith angles.

3.9 Effective Area

The effective area is a parameter used to characterize the energy response of a detector. The effective area is a measure of the efficiency for the successful detection of a

[3] Figure for epoch 7, see section 7.2 for details.

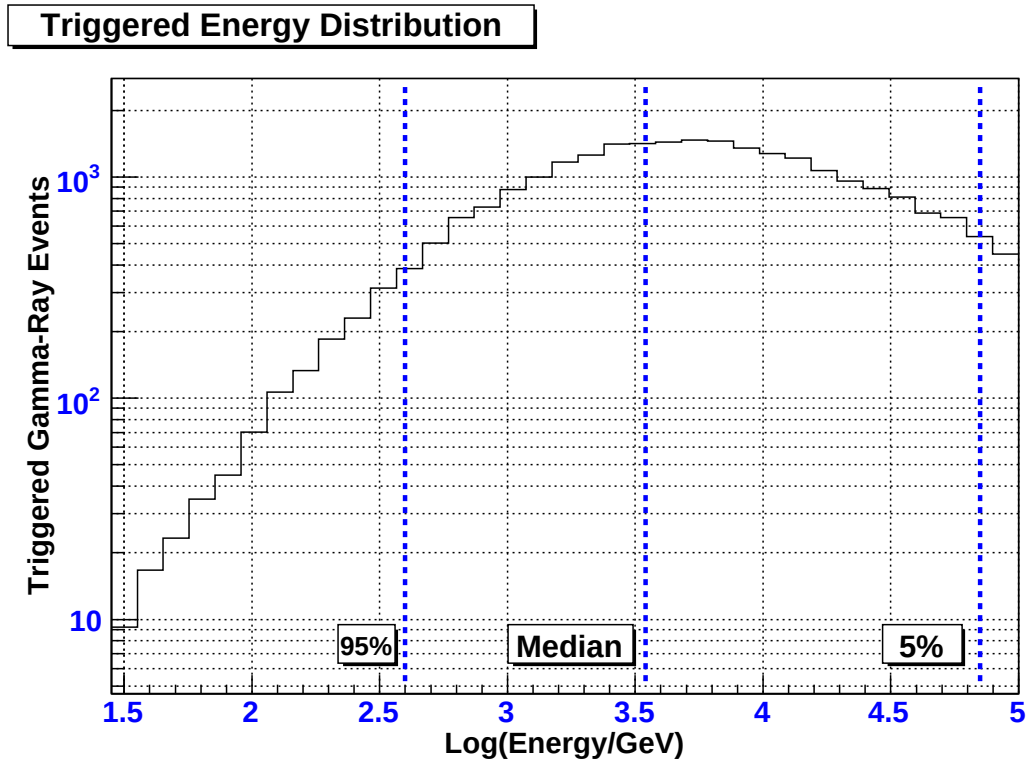

Figure 3.12: Distribution of gamma-ray events that triggered the detector for a power law spectrum of $dN/dE \propto E^{-2.4}$. The median energy (3.5 TeV) is indicated by the middle dotted line. The two other dotted lines indicate the energies above which 95% and 5 % of the detected gamma-rays fall.

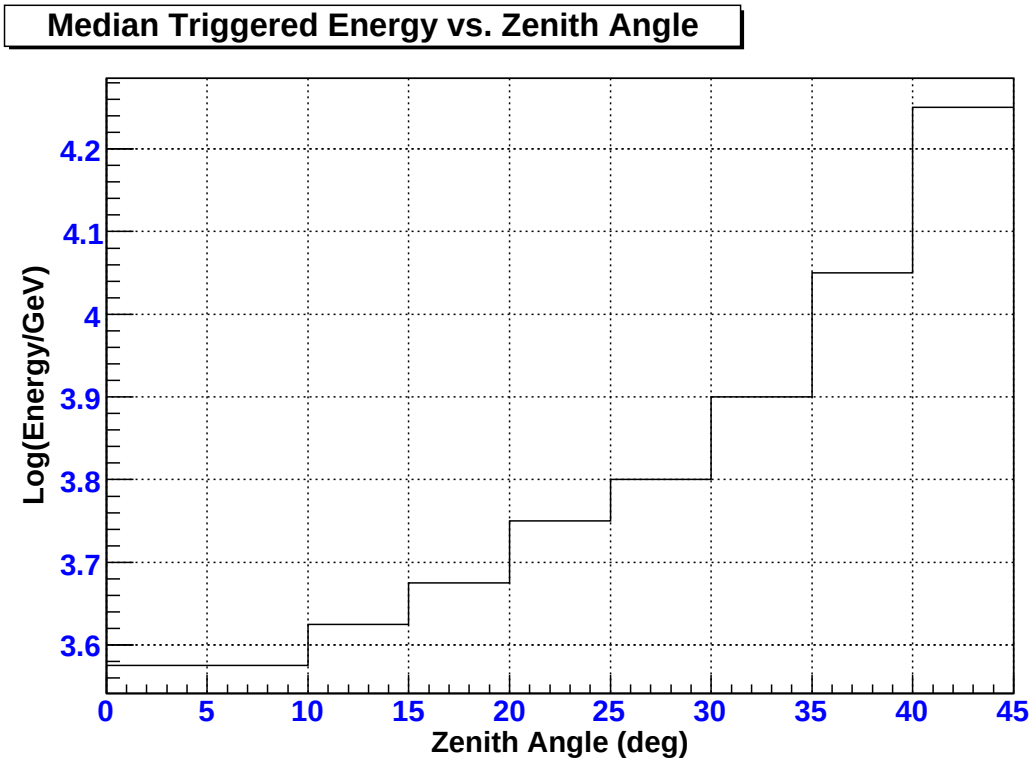

Figure 3.13: Median triggered energy as a function of zenith angle for simulated gamma-ray events with a power law spectrum of $dN/dE \propto E^{-2.4}$

gamma-ray-induced air shower based on the energy and zenith angle of the primary particle. The effective area is defined as:

$$A_{eff}(E,\theta) = \frac{N_{trig}(E,\theta)}{N_{throw}(E,\theta)} \times A_{throw} \tag{3.7}$$

where $N_{trig}(E,\theta)$ is the number of events that triggered the detector at a given energy and zenith angle, $N_{throw}(E,\theta)$ is the number of events that were thrown, from the Monte Carlo, at that energy and zenith angle, and A_{throw} is the area over which the simulated gamma-rays were thrown. This area is equal to 1 km^2 (see next section).

Figure 3.14 shows the effective area as a function of energy for three different zenith angle ranges. As can be seen the effective area increases dramatically, from almost zero at 30 GeV, to about 10,000 m^2 at 10 TeV. The physical area of the detector is marked by the dashed horizontal line and is equal to (4.8 $\times 10^3$ m^2). For energies above several TeVs, the effective area exceeds the physical area of the detector. This is because a successful detection of a gamma-ray shower does not require that the initial trajectory of the primary gamma-ray intersects the physical area of the detector. All that is needed for a successful detection is the satisfaction of the trigger condition and direction reconstruction which may be achieved by high energy primaries landing off the detector.

The effective area as a function of zenith angle is given by:

$$A_{eff}(\theta) = \frac{\int_{E_{min}}^{E_{max}} A_{eff}(E,\theta)\frac{dN}{dE}dE}{\int_{E_{min}}^{E_{max}} \frac{dN}{dE}dE} \tag{3.8}$$

This is shown in figure 3.15 for an $E^{-2.4}$ spectrum. This figure shows that Milagro is most sensitive to showers near zenith, and that its sensitivity decreases dramatically for large zenith angles.

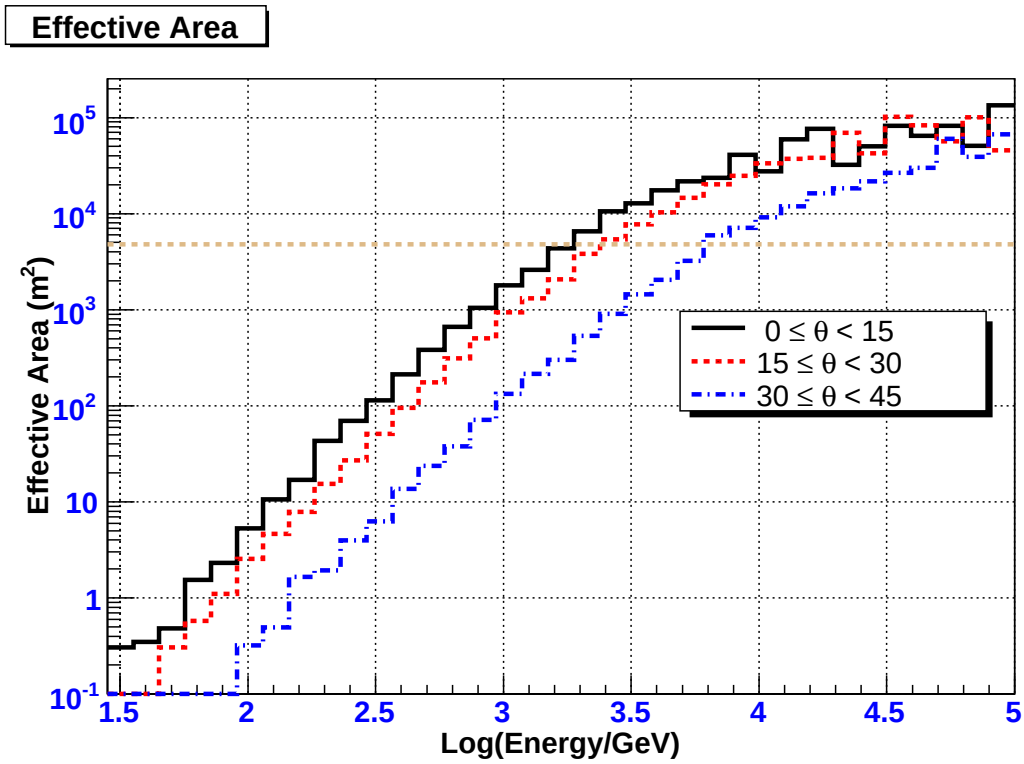

Figure 3.14: The effective area as a function of energy for three different zenith angle ranges for an $E^{-2.4}$ spectrum. The horizontal dashed line represents the physical area of the detector (4.8×10^3 m^2).

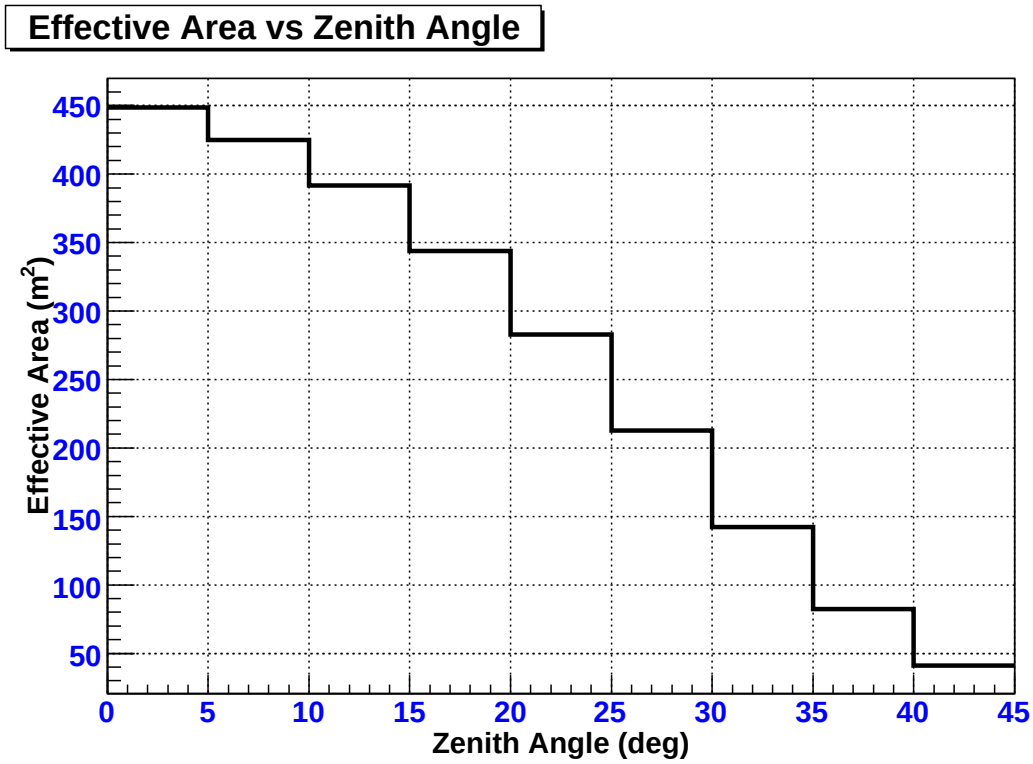

Figure 3.15: The effective area as a function of zenith angle for an $E^{-2.4}$ spectrum.

3.10 Simulations

3.10.1 Monte Carlo Simulations of Extensive Air Showers

The first stage in simulating the response of the Milagro detector to EAS is the simulation of the production and propagation of EAS through the atmosphere. This is done using the CORSIKA (Cosmic-Ray SImulations for KAskade) v6.5021 software package [78]. For hadronic air showers, only the ones created by proton or helium primaries were simulated. Low energy (< 80 GeV) hadronic interactions were simulated with FLUKA v2005.6, higher energy hadronic interactions were simulated with NEXUS v3.975. Electromagnetic interactions were simulated with EGS4[4].

The simulation of an EAS with CORSIKA begins with the first interaction of the primary particle in the atmosphere, followed by the subsequent interactions of the secondary particles in the shower down to ground level. In order to obtain enough statistics, especially at high energies, hundreds of millions of CORSIKA showers were generated. The primaries that were thrown were proton and helium, to simulate the cosmic-ray background, and gamma-ray primaries to simulate cosmic gamma-rays. The gamma-ray showers were thrown over a zenith angle range of 0° to 45°, while the helium and proton showers were thrown over a zenith angle range of 0° to 70°. All the showers had an energy in the range 30 GeV to 100 TeV. The showers were thrown with a falling power law spectrum of $dN/dE \propto E^{-2.0}$. Later, at the analysis stage, the events were properly re-weighted so that the spectral indices for hadrons were $\alpha = -2.75$ for proton and $\alpha = -2.68$ for helium showers. For the Monte Carlo cosmic-ray sample, the helium flux is about 35% of the total flux. These values are the ones measured by the BESS balloon experiment[30].

3.10.2 Monte Carlo Simulations of Detector Response

The simulation of the detector's response to EAS is done using the GEANT4 (GEometry ANd Tracking) software package [79]. The input for this stage of the simulation are the information about the shower particles reaching the ground (from CORSIKA). The GENAT software takes these particles and propagates them through a model of the Milagro detector. The interactions of the secondary particles in the shower, such as Cherenkov light production by relativistically charged particles traveling in water, pair production of electron-positron pairs from gamma-rays, hadronic interactions, and other interactions are simulated with GEANT4. The GEANT4 software redistributes the core positions of the CORSIKA showers randomly over a circle of 1000 m radius centered on the pond. For each PMT hit, the GEANT4 output includes the number of PEs, their arrival times, and the position of detection on the face of the photocathode.

Chapter 4

Data Analysis Techniques

4.1 Coordinate Systems on the Celestial Sphere

The celestial sphere is an imaginary sphere with an infinite radius centered on the earth. Stars, galaxies, and other extraterrestrial objects appear to lie on this celestial sphere. Astronomers use different coordinate systems to describe the positions of objects on the celestial sphere. The most commonly used coordinate system is the equatorial coordinate system.

4.1.1 Equatorial Coordinate System

The earth rotates eastward on its axis once a day, as a consequence, the sky appears to rotate westward about the earth. The extension of the earth's rotation axis to the celestial sphere defines the north and south celestial poles (NCP and SCP). The extension of the earth's equatorial plane to the celestial sphere defines the celestial equator (see figure 4.1).

For an observer on the earth's surface, the direction of gravity fixes the direction of the local vertical. The point at which the local vertical intersects the celestial sphere is the zenith for that observer. The great circle passing through the celestial

poles and the zenith is the meridian. The horizon is the great circle whose pole is the zenith.

As the earth revolves annually around the sun, the sun appears to move from west to east around the celestial sphere on a path called the ecliptic. The earth's rotation axis is inclined from the normal to its orbit by an angle of 23.5 °, hence the ecliptic is also inclined to the celestial equator by the same angle. This angle is called the obliquity of the ecliptic. The celestial equator and the ecliptic intersect at two points separated by 180°, these two points are called the vernal and autumnal equinoxes. The sun passes by through the vernal equinox around March 21 each year. About six months later it passes by the autumnal equinox.

The great circle through the celestial poles (NCP and SCP) and a star's position is that star's hour circle. The star's hour angle is the angle around the celestial equator between the meridian and its hour circle. The star's right ascension α is the arc of the celestial equator from the vernal equinox to the star's hour circle. Right ascension increases from west to east, thus stars with large right ascension rise later than those with small ones. A star's declination δ is the angular distance measured from the celestial equator along the star's hour circle to the star. A declination is positive northward and negative southward. For example the NCP is at $\delta = +90°$, the SCP is at $\delta = -90°$, and the celestial equator is at $\delta = 0°$. In this system α and δ on the celestial sphere are equivalent to longitude and latitude on the earth's surface.

4.1.2 J2000 Reference

The earth is not spherical but flattened near the equator. This flattening allows the sun and the moon to exert torques on the earth, and, since the earth spins like a top, its axis of rotation precesses about the ecliptic pole. The period of this precession is about 26 000 years. In addition to this precession, the shape and orientation of the earth's orbit around the sun is changing on a time scale of millions of years in

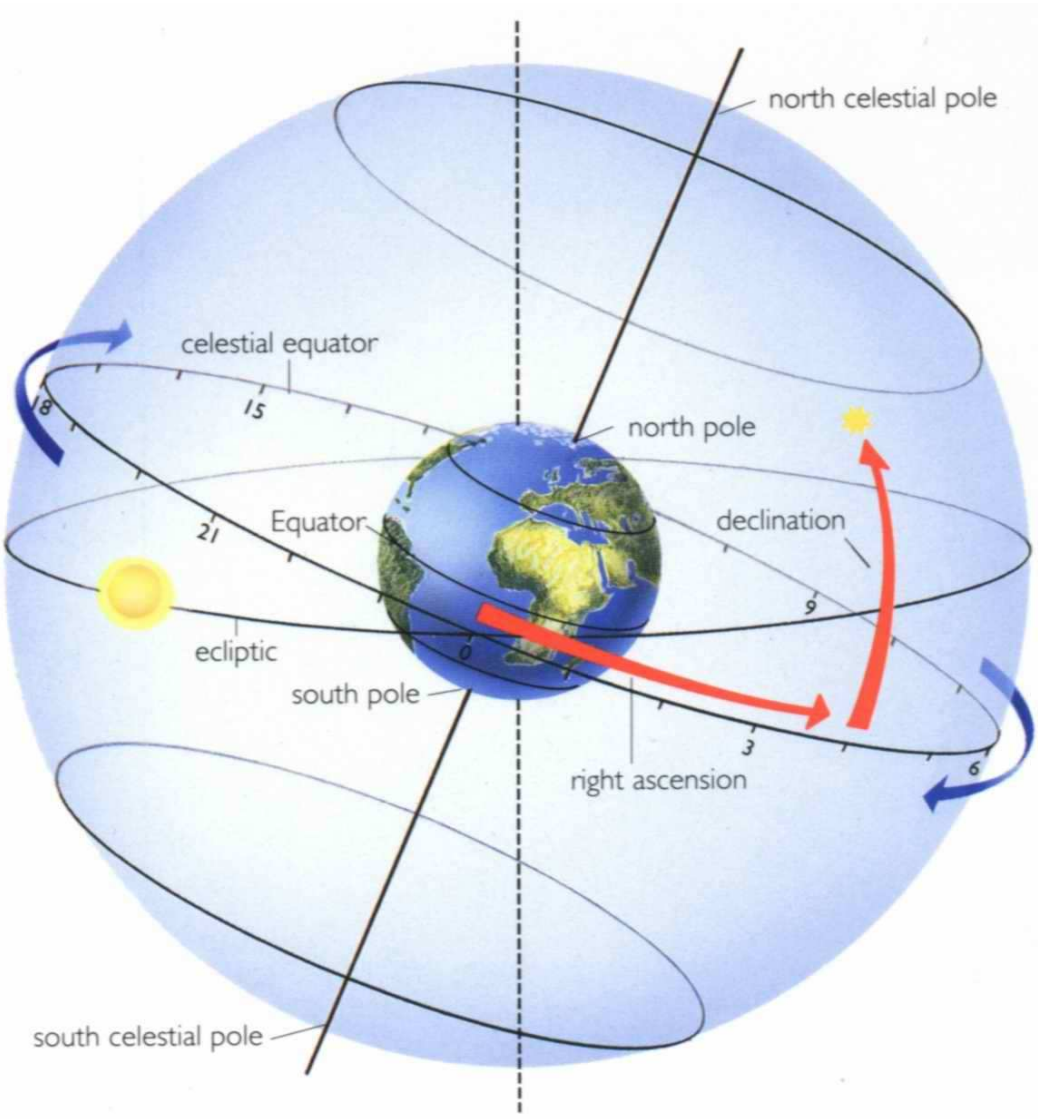

Figure 4.1: Equatorial coordinates on the celestial sphere. Image taken from [76]

response to the forces applied by the planets. Since the vernal equinox is defined as the intersection on the celestial sphere of the great circles of the equator and the ecliptic, any change in the direction of the ecliptic will result in a change in the vernal equinox and hence a change in the equatorial coordinate system. It is, thus, essential to specify an epoch at which the right ascension and declination were measured. Each of these epochs last for 50 years and the current epoch is defined with respect to the position of the earth at noon on January 1, 2000. The reference epoch for all equatorial coordinates in this dissertation is J2000. For example, if a source has the coordinates α= J2019 and δ= 37 in the J2000 epoch, then this means that the source has a right ascension of 20 hours and 19 minutes, and a declination of 37 degrees.

4.1.3 Julian Date and Modified Julian Date

The Julian day (JD) is the integer number of days that passed since noon on January 1, 4713 BC. Almost 2.5 million days have transpired since this date. The use of Julian day omits any dependence on months and years when used as a calendar, thus Julian dates are widely used in astronomy. For reference, Julian day 2450000 began at noon on 1995 October 9. Because Julian dates are so large, astronomers often make use of a "modified Julian date"; MJD = JD - 2400000.5.

4.1.4 Galactic Coordinate System

The Galactic coordinate system is most useful for considerations of objects beyond the solar system, especially for considerations of objects of our Milky Way Galaxy. The reference for the Galactic coordinate system is the disk of our Galaxy. The intersection of this plane with the celestial sphere is known as the Galactic equator and is inclined by 62.87° with respect to the celestial equator. The north pole of the Galactic coordinate system is located at $(\alpha_{GP}, \delta_{GP}) = (192.86°, 27.13°)$. The Galactic latitude b of a star is the angle from the Galactic equator to the star along the great

circle through the start and the Galactic poles. For example, the north Galactic pole (NGP) is at $b = +90^\circ$, and the south Galactic pole (SGP) is at $b = -90^\circ$. The Galactic longitude l of a star is measured with respect to the direction to the Galactic center[1]. The Galactic Center position in the equatorial coordinate system is $(\alpha_{GC}, \delta_{GC}) = (266.4^\circ, -28.94^\circ)$.

Transformations between the equatorial coordinates and Galactic coordinates are given by [40]:

$$\sin b = \sin\delta_{GP}\sin\delta + \cos\delta_{GP}\cos\delta\cos(\alpha - \alpha_{GP}) \quad (4.1)$$

$$\cos b\cos(l_{CP} - l) = \cos\delta_{GP}\sin\delta - \sin\delta_{GP}\cos\delta\cos(\alpha - \alpha_{GP}) \quad (4.2)$$

$$\cos b\sin(l_{CP} - l) = \cos\delta\sin(\alpha - \alpha_{GP}) \quad (4.3)$$

The inverse transformation is given by:

$$\sin\delta = \sin\delta_{GP}\sin b + \cos\delta_{GP}\cos b\cos(l_{CP} - l) \quad (4.4)$$

$$\cos\delta\cos(\alpha - \alpha_{GP}) = \cos\delta_{GP}\sin b - \sin\delta_{GP}\cos b\cos(l_{CP} - l) \quad (4.5)$$

$$\cos\delta\sin(\alpha - \alpha_{GP}) = \cos b\sin(l_{CP} - l) \quad (4.6)$$

where $l_{CP} = 123.93^\circ$ is the longitude of the NCP.

The Galactic coordinate system is shown in figure 4.2. An optical view of the Milky Way Galaxy in Galactic coordinates is shown in figure 4.3. In this figure, the Galactic center ($l = 0$) is in the middle of the map. Galactic longitude increases to the left of the center and decreases to the right. Figure 4.4 shows an artist drawing of what the Milky Way Galaxy might look like from the North Galactic Pole. The

[1]The Galactic Center (GC) lies in the constellation of the Sagittarius. The compact radio source, Sgr A* believed to mark the location of the GC is actually 0.08° away from the GC.

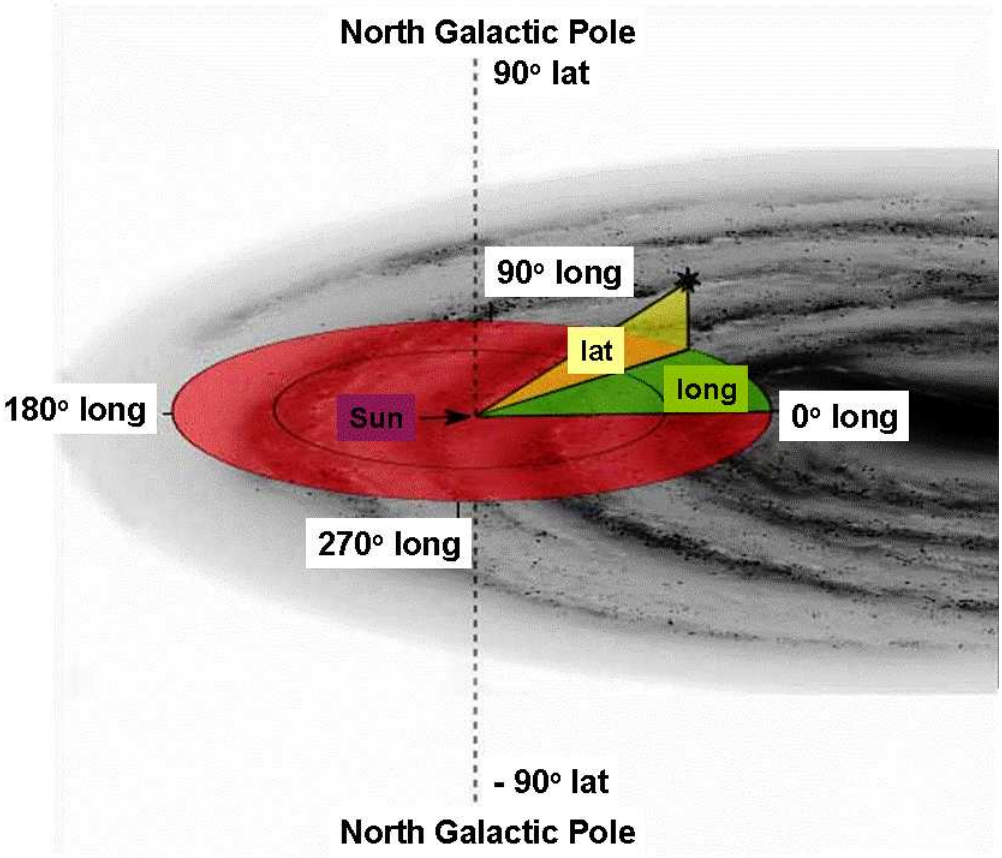

Figure 4.2: Galactic coordinate system. Figure taken from [77].

highlighted region is the region visible from the location of Milagro, the rest of the Galaxy is obscured by the earth.

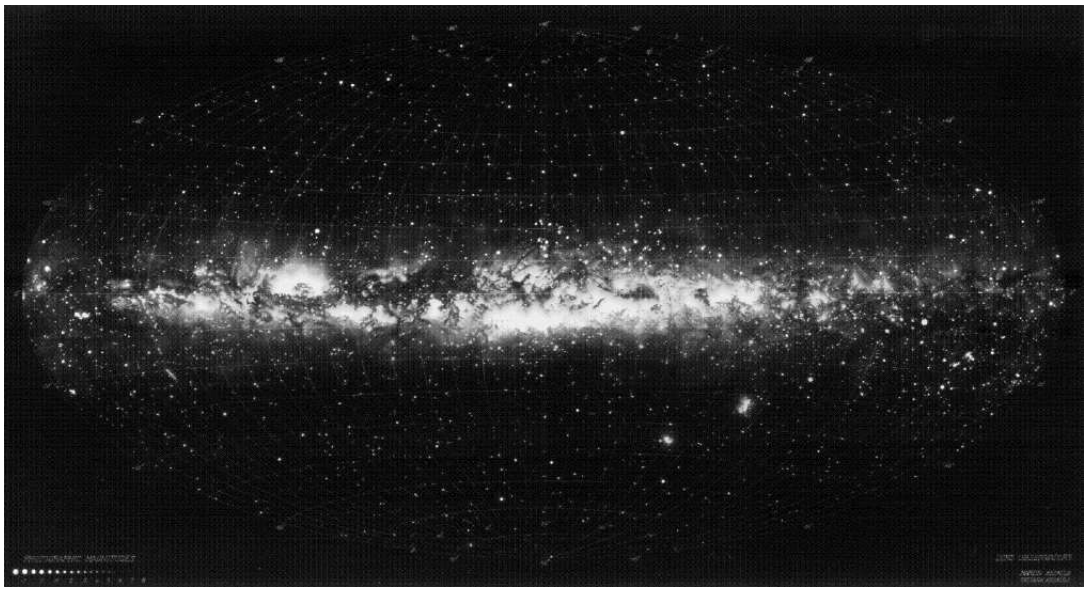

Figure 4.3: Optical view of our Galaxy in Galactic coordinates. The Galactic center ($l = 0$) is in the middle of the map. Galactic longitude increases to the left of the center and decreases to the right.

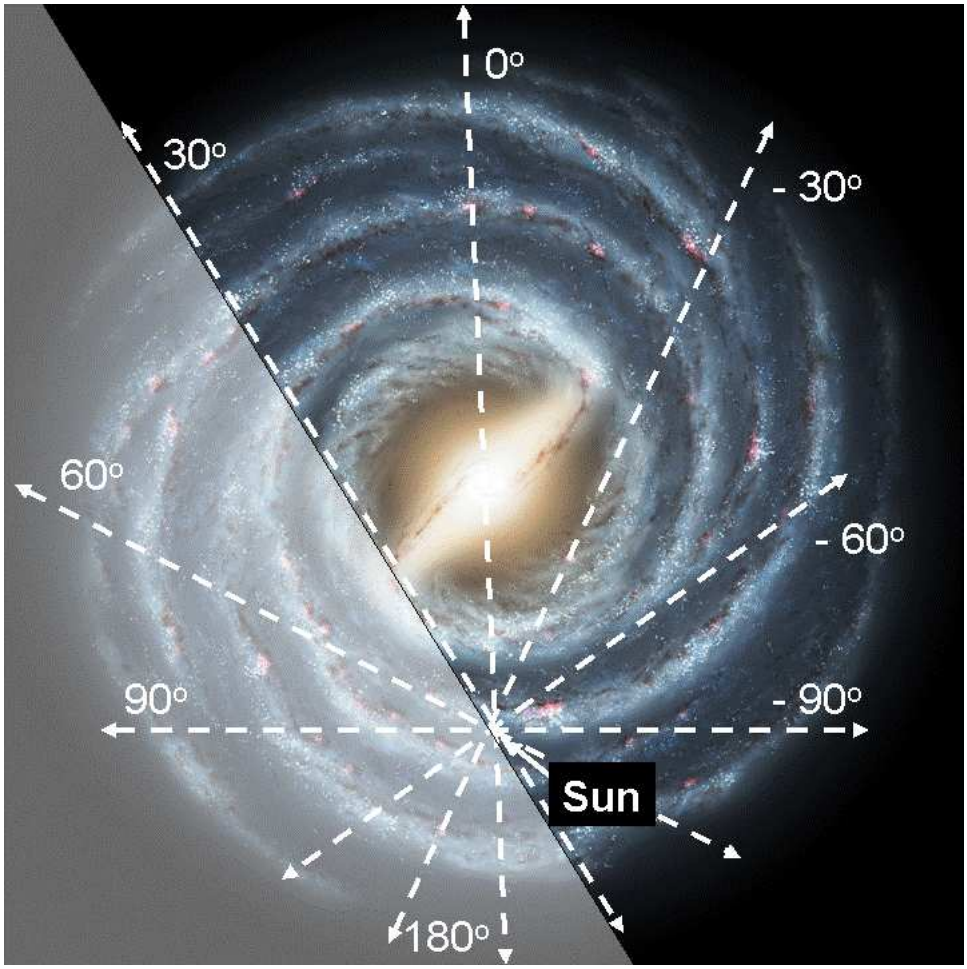

Figure 4.4: Artist conception of the Milky Way Galaxy as seen from the North Galactic Pole. The highlighted region is the region visible from the location of Milagro, the rest of the Galaxy is obscured by the earth.

4.2 Background Estimation

For ground-based gamma-ray detectors, the search for a gamma-ray signal from a celestial gamma-ray source is obscured by a large isotropic background that is due to hadronic-initiated EAS. A crucial step in searching for a gamma-ray signal is the correct estimation of this hadronic background. If the background is overestimated, a real gamma-ray signal could be washed out by this overestimation and could be lost. If the background is underestimated, a fluctuation in the estimation of the background could appear as a signal.

The method used in this analysis for background estimation is the direct integration method [14]. This technique assumes that the efficiency for detecting events is a function of the local coordinates and is independent of the trigger rate for short periods of time. Figure 4.5 shows the all-sky rate for one day. From this figure we see a clear variation of the trigger rate over an entire day. This variation is mainly due to atmospheric effects. For this analysis, an integration period of two hours was selected. This integration time of two hours was selected because the duration needs to be long enough that the source transits a large enough distance so that the background can be well measured, and not so long that the assumption that the local coordinate efficiency is constant is not violated.

In this method the number of background events is obtained by the numerical integration:

$$N_B(\alpha,\delta) = \int\int E(HA(t),\delta)\ R(t)\ \epsilon(HA(t),\alpha,t)\ dt\ d\Omega \tag{4.7}$$

where $N_B(\alpha,\delta)$ is the background estimate within a bin in equatorial coordinates (α,δ), $E(HA(t),\delta)$ is the efficiency or acceptance of the detector at local coordinate $(HA(t),\delta)$ and is simply the probability that an event comes from the differential angular bin $d\Omega = d(HA(t))d(\delta)$. The event rate of the detector as a function of time

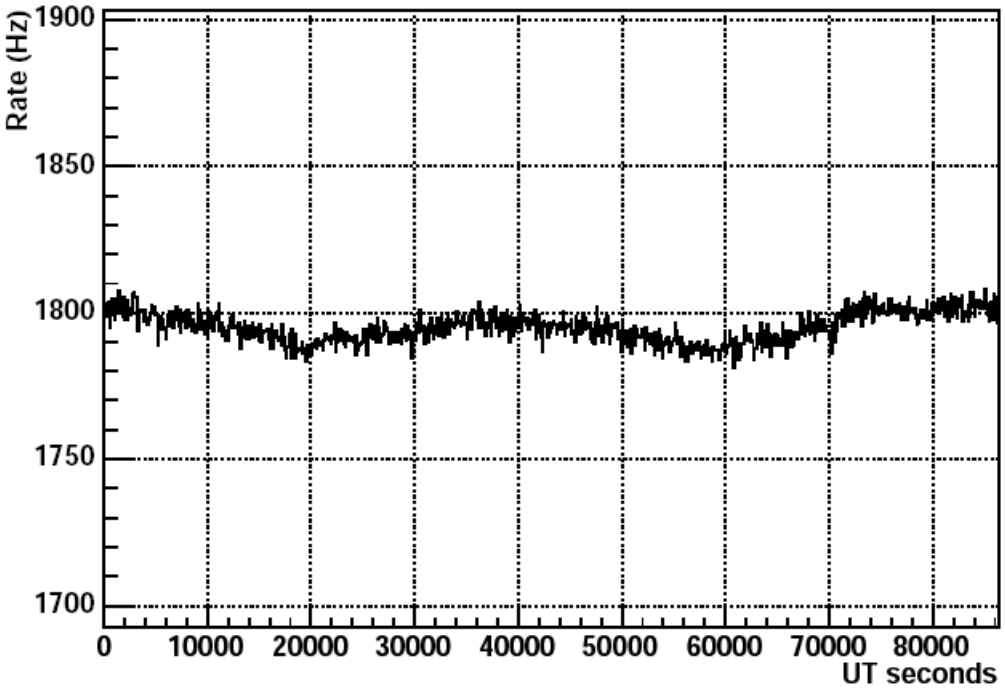

Figure 4.5: An all-sky rate for one day. As can be seen ,the rate varies with time of the day. For a two hour period, 7200 seconds, the rate is essentially constant.

is given by the $R(t)$ term. The $\epsilon(HA(t), \alpha, t)$ term is equal to 1 if an event falls in the (α, δ) bin at sidereal time[2] t and zero otherwise. The hour angle, HA(t), is a function of the sidereal time and is given by:

$$HA(t) = t - \alpha \tag{4.8}$$

The hour angle provides the conversion from the local coordinates to the equatorial coordinates.

To estimate the detector acceptance $E(HA(t), \delta)$, events in the sky are binned in $0.1^\circ \times 0.1^\circ$ bins. The number of events in each of these bins is then normalized by dividing it by the total number of events observed in that integration period. The resulting map is called the efficiency map. Events in the efficiency map have to pass

[2]Sidereal time literally means "star time". A sidereal day is the time it takes for the earth to complete a full revolution around its axis, 360° with respect to distant stars, and is equal to 23 hours and 56 minutes.

any cuts applied on the data. At the end of the two hours background integration period, the efficiency map is converted into background map in equatorial coordinates by multiplying the rate of events collected for each 24 seconds of time by the efficiency for each bin. The size of the time bin is selected to eliminate any appreciable motion of the sky within the angular bin of 0.1°. This ensures that the background events have the same time distribution as the collected data.

The presence of a signal from a gamma-ray source will contaminate the background. This means that the background estimate will be higher in the presence of a gamma-ray signal since these signal events will be included in the efficiency map. This effect is removed by excluding a $3^\circ \times 3^\circ$ region around known sources like the Crab nebula and the active Galaxy Mrk421 from the background estimate. For the Galactic plane, the region defined by $|b| < 2.5$ is also excluded from the background estimate. It should be noticed that a truly diffuse isotropic gamma-ray emission will not be detected, using this background estimation method, and will be counted as background. However, gamma-ray sources with sizes smaller than the integration scale (30 degrees for 2 hours) are detectable.

After the estimation of the background the map is smoothed by the point spread function (PSF) of Milagro. See section 6.3 for more details.

4.3 Significance of a Measurement

The next step in searching for a gamma-ray signal is the calculation of the statistical significance of an excess (or deficit) for each point in the sky. To calculate the statistical significance the method of Li and Ma [47] is used. This method of calculating the significance is based on the likelihood ratio test. In this method the statistical significance, S, of a measurement is given by:

$$S = \sqrt{2}\sqrt{N_{on}\ln\left(\frac{(1+\alpha)}{\alpha}\frac{N_{on}}{(N_{on}+N_{off})}\right) + N_{off}\ln\left((1+\alpha)\frac{N_{off}}{(N_{on}+N_{off})}\right)} \tag{4.9}$$

where N_{on} is the number of events in the signal bin, N_{off} is the number of events in the background bin, and α is the ratio of signal to background exposures and is given by:

$$\alpha(\delta) = \left(\frac{B}{\cos\delta}\right)\left(\frac{1}{T \times 15}\right) \tag{4.10}$$

where B is the bin size, 0.1° in this case, δ is the declination of the bin at which the significance is to be calculated, and T is the integration time in hours, 2 hours in this case. The first part on the left gives the signal exposure in degrees, while the second part gives the reciprocal of the background exposure in degrees. The number 15 in the numerator is the number of degrees the earth rotates in one hour.

Equation 4.9 is valid in the case that the observed counts are not too few ($N_{on} \geq 10$, $N_{off} \geq 10$). The significance distributions obtained with this method are consistent with the Gaussian probabilities [47].

The distribution of significance provides a check of the background estimation. This distribution for the background, in the absence of any signals, should follow a Gaussian distribution with zero mean and sigma of 1.0. Divergence from the background expectation indicates a signal, or a bias in the calculation of significance or of the background estimate. Figure 4.6 shows the distribution of excess (or deficit) significances for the whole sky. The distribution follows a Gaussian distribution with a mean of 0.0005 and sigma of 0.997. Those values are very close to that predicted in the absence of a signal.

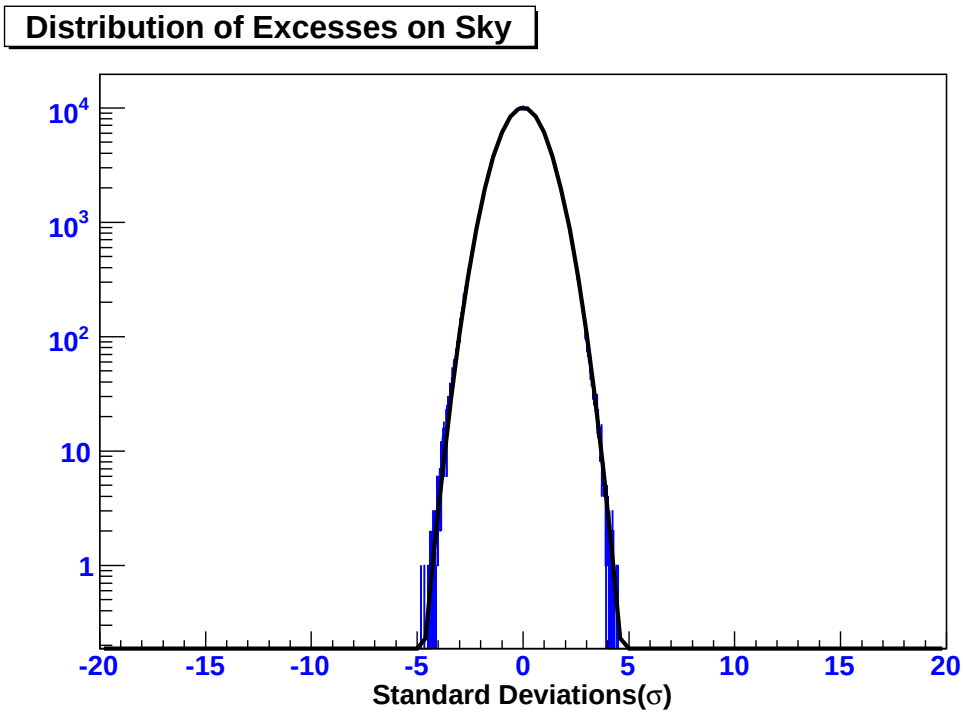

Figure 4.6: Distribution of excess (or deficit) significances. The distribution is well fitted to a Gaussian distribution with a mean of 0.0005 and sigma of 0.997.

Chapter 5

New Gamma-Hadron Separation Technique and Variable

5.1 Gamma-Hadron Separation In Milagro

When a γ-ray enters the atmosphere, its interactions with the nuclei in the air are almost purely electromagnetic, resulting in an air shower that contains mostly lower energy electrons, positrons, and γ-rays. Hadronic cosmic-rays, on the other hand, will undergo hadronic interactions with the nuclei in the air. This will give rise to charged pions that can decay into muons and neutrinos. In addition, multi-GeV hadronic particles may also reach the ground.

A γ-ray initiated EAS at ground level is composed primarily of electrons, positrons, and low-energy γ-rays. The γ-rays outnumber the electrons and positrons in the air shower by a factor of ~ 5. The Top layer in Milagro is placed under ~ 4 radiation lengths ($X_\circ$) and ~ 2 interaction lengths (λ_I). This means that the bulk of the γ-rays that enter the pond will be converted to electron-positron pairs. These relativistic charged particles will Cherenkov radiate in the water and will illuminate the PMTs in the Top layer. Roughly 50% of all electromagnetic particles that enter the pond

are detected.

The muon layer in Milagro is located under 6m of water (corresponding to 17 more radiation lengths and 7.2 interaction lengths). This means that most EM charged particles that enter the pond get absorbed before reaching this layer, although their Cherenkov light does reach the muon layer. On the other hand, muons with energies as low as 1.2 GeV can penetrate and shower near the PMTs of the muon layer. These penetrating muons and hadrons will result in bright compact clusters of light in this layer. This is clearly seen in figure 5.1 which shows images from the muon layer of six Monte Carlo events. The top three events are γ-ray-induced events, and the bottom three are proton-induced events. The area of each square is proportional to the number of photoelectrons (PEs) registered in the corresponding PMT, and the area is saturated at 300 PEs. It can be seen from this figure that the γ-ray events have relatively smooth PE distributions in the muon layer while the hadronic events have well-defined clumps of high intensity regions. Using Monte Carlo simulations it is estimated that 79% of all proton showers that trigger Milagro contain a muon and/or a hadron that enters the pond, while only 6% of gamma ray induced air showers contain a muon and/or a hadron that enters the pond.

5.1.1 The Compactness Parameter

A simple algorithm has been developed [14] to distinguish γ-ray initiated air showers from the overwhelming background of hadron initiated air showers. The compactness parameter [14] is defined as:

$$C = \frac{N_{bot \geq 2PEs}}{PE_{maxB}} \tag{5.1}$$

where $N_{bot \geq 2PEs}$ is the number of PMTs in the bottom layer with more than 2 PEs, and PE_{maxB} is the number of PEs in the bottom layer tube with the maximum

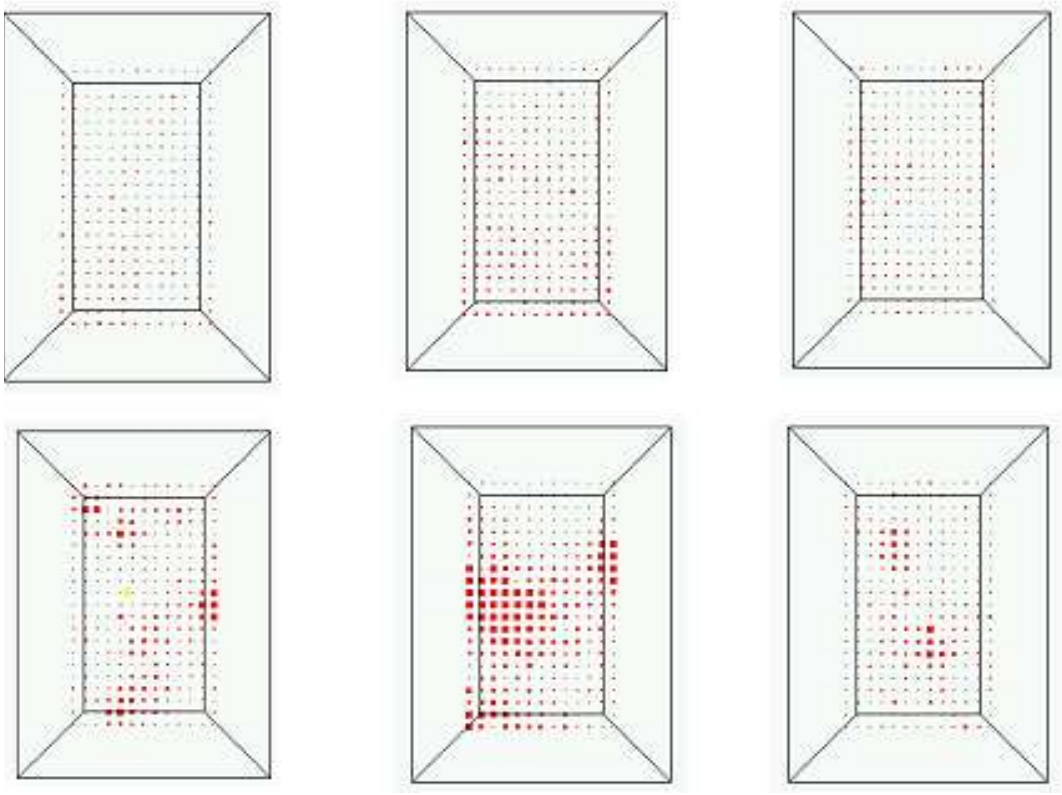

Figure 5.1: Gamma-ray (top row) and proton (bottom row) events imaged in the muon layer of Milagro. The area of each square is proportional to the number of photoelectrons (PEs) registered in the corresponding PMT, and the area is saturated at 300 PEs.

number of PEs. The compactness parameter should yield small values for events where few PMTs in the bottom layer are struck with a large amount of light (large PE_{maxB}) and large values for events where few PMTs are struck with a small amount of light (large $N_{bot \geq 2PEs}$). Therefore, hadronically initiated showers typically have small values of C, while γ-ray initiated showers typically have large values of C.

Figure 5.2 shows the compactness distribution for Monte Carlo γ-ray showers, Monte Carlo cosmic-ray showers, and data[1]. An event selection is made on the Monte Carlo events identical to that made on data: the number of PMTs used in the angular fit must be greater that 20, and, for γ-ray Monte Carlo, the events must be

[1]Epoch 7 is used throughout this chapter. The Monte Carlo gamma-ray sample was thrown with a Crab-like spectrum of $E^{-2.62}$.

reconstructed within 1.2° of their true direction. As can be seen in this figure, there is a clear difference between the Monte Carlo γ-ray showers and the Monte Carlo comic-ray showers. Further, there is a reasonable agreement between the data and the Monte Carlo cosmic-ray showers, as expected, since the data consist mainly of cosmic-ray initiated showers.

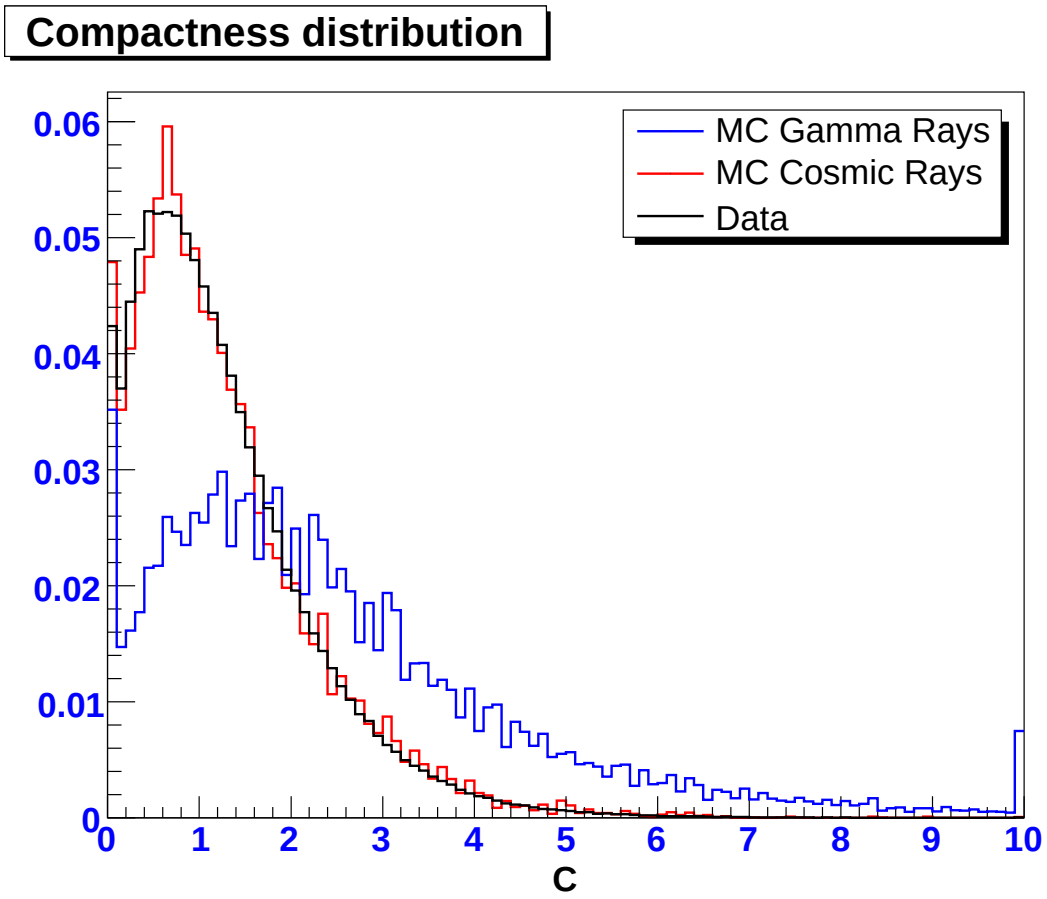

Figure 5.2: The compactness distribution for Monte Carlo γ-ray showers, Monte Carlo cosmic-ray showers, and data. All of the histograms have been normalized to have unit area.

Figure 5.3 shows the efficiencies for retaining data, cosmic-ray Monte Carlo, and γ-ray Monte Carlo showers as a function of the compactness cut.

The relative increase in sensitivity for a given selection criterion is given by the Quality factor (Q) of the cut. For a large number of events, Q is given by:

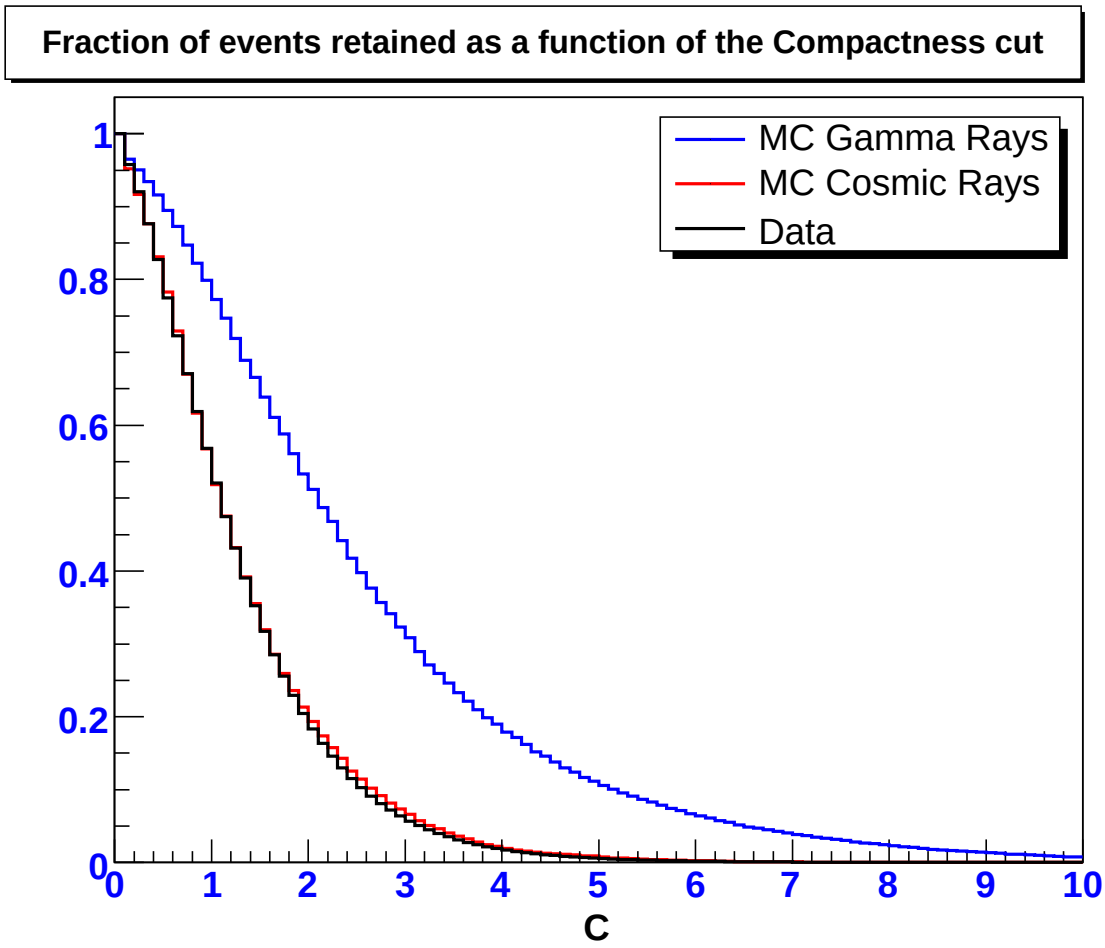

Figure 5.3: Fraction of data, cosmic-ray Monte Carlo, and γ-ray Monte Carlo showers with a compactness value that is greater than the x-axis value.

$$Q = \frac{\epsilon_s}{\sqrt{\epsilon_b}} \tag{5.2}$$

where ϵ_s and ϵ_b are the efficiencies for retaining the signal and background, respectively.

Figure 5.4 shows the Q factor as a function of the minimum value of C required to retain an event. Requiring events to have C $\geq$ 2.5 rejects 89.0 % of the simulated cosmic-ray-induced air showers that trigger Milagro and 90.0 % of the data (for this data sample), and retains 39.0 % of the γ-ray-induced air showers. This results in

a predicted Q-factor of 1.18 comparing Monte Carlo γ-ray events to Monte Carlo cosmic-ray events, and 1.23 comparing Monte Carlo γ-ray events to data. In a previous publication by the Milagro collaboration [14], a different set of Monte Carlo simulations was used to study the compactness parameter which gives a quality factor of 1.6 comparing Monte Carlo γ-ray events to Monte Carlo proton events, and 1.7 comparing Monte Carlo γ-ray events to data. These simulations used GEANT 3.0 to simulate the detector's response to extensive air showers and had different values for the quantum efficiency of the PMTs than the one used in this thesis. The current PMT efficiency adopted in the current simulations were performed at the University of Maryland and seems to give a better agreement with the data [70].

The compactness parameter does not carry information about the size of the air shower, it also does not carry information about how well the shower was fit. Air Cherenkov telescopes, for example, make use of their excellent angular resolution to improve their background rejection. As will be shown in the coming sections, the inclusion of the information about the shower size and how well the shower was fit in a new gamma-hadron separation variable in Milagro lead to a significant increase in the sensitivity of the detector.

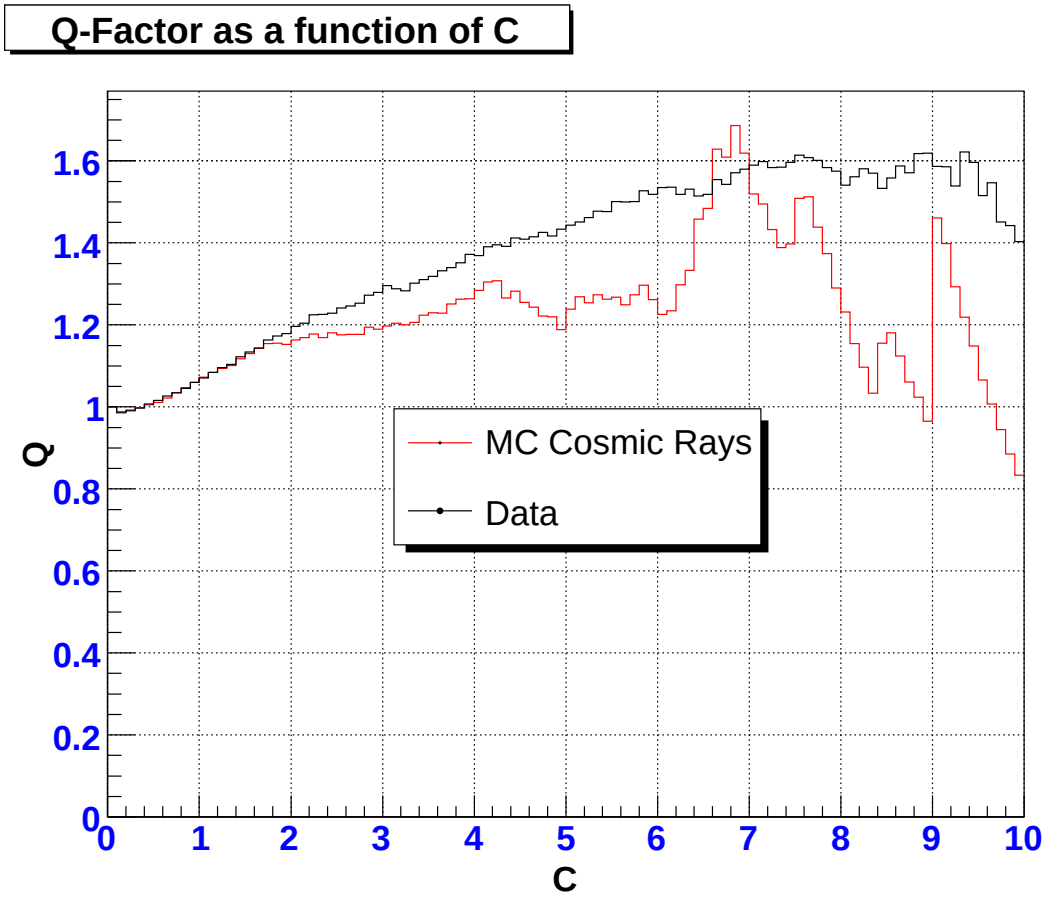

Figure 5.4: Quality factor Q as a function of the minimum value of C required to retain an event. The red line compares Monte Carlo γ-rays to Monte Carlo cosmic-rays, and the black line compares Monte Carlo γ-rays to data.

5.2 A_4, Milagro's New Gamma-Hadron Separation Variable

The denominator of the compactness parameter (equation 5.1) carries the proper information about the clumpiness in the muon layer that is caused by the penetrating muons and hadrons that are mostly present in cosmic-ray-induced air showers. This parameter, however, does not carry information about the size of the air shower or how well this shower was fit.

A_4 is a new γ-hadron separation variable that makes use of the information about the shower size and how well the shower was fit [2, 3]. A_4 is defined as:

$$A_4 = \frac{(f_{top} + f_{out}) \times N_{fit}}{PE_{maxB}} \tag{5.3}$$

where

- f_{top} is the fraction of the air shower layer PMTs hit in an event.
- f_{out} is the fraction of the outriggers hit in an event.
- N_{fit} is the number of PMTs that entered in the angle fit.

The "A" in A_4 stands for "Abdo" and the "4" stands for the number of parameters that make up A_4. Originally A_4 included N_{top} and N_{out} instead of f_{top} and f_{out}, respectively. The reason for using the fraction of the air shower layer and outriggers hit and not the actual numbers of the tubes hit is to give a higher weight for the outriggers in this variable. This is done for many reasons. One of these reasons is that events with cores on the pond seem to be more hadron like, while events with cores off the pond seems to be more γ-ray like. Also, events with large number of outriggers hit have better angular and core resolutions.

The first part in the numerator of A_4 carries information about the size of the

shower, while N_{fit} carries information about how well the shower was reconstructed. PE_{maxB} carries information about the clumpiness in the Muon layer that is due to the penetrating Muons and hadrons which are mostly presented in hadronic air showers.

Figure 5.5 shows the A_4 distribution for γ-ray Monte Carlo, cosmic-ray Monte Carlo, and data. Figure 5.6 shows the efficiencies for retaining data, cosmic-ray Monte Carlo, and γ-ray Monte Carlo as a function of A_4. In both figures we see a clear difference between the Monte Carlo γ-ray showers and the Monte Carlo cosmic-ray showers, while there is a good agreement between the data and the cosmic-ray Monte Carlo showers. Figure 5.7 shows the Q-factor as a function of the minimum value of A_4 required to retain an event. Requiring events to have $A_4 \geq 3.0$ rejects 97.4% of the simulated cosmic-ray-induced air showers that trigger Milagro and 97.2% of the data (for this data sample), and retains 27% of the γ-ray-induced air showers. This results in a predicted Q-factor of 1.62 comparing Monte Carlo cosmic-ray events to Monte Carlo γ-ray events, and 1.59 comparing the data to Monte Carlo γ-ray events. Thus the Monte Carlo predicts an improvement in significance over all triggered data of 1.62, or a factor of $1.62/1.18 = 1.4$ over the present compactness cut.

It can be noted from figures 5.2 through 5.7 that the A_4 distribution for cosmic-ray showers matches the data better than does the compactness distribution of cosmic-ray showers. This is clearly evident in figures 5.4 and 5.7.

5.3 Properties of A_4

5.3.1 Energy Dependence

The efficiency of the A_4 parameter is a function of the energy of the primary gamma-ray. At low gamma-ray energies, few PMTs are hit in the air shower layer and the outrigger array (low $(f_{top} + f_{out})$). This will also mean that few PMTs entered in the

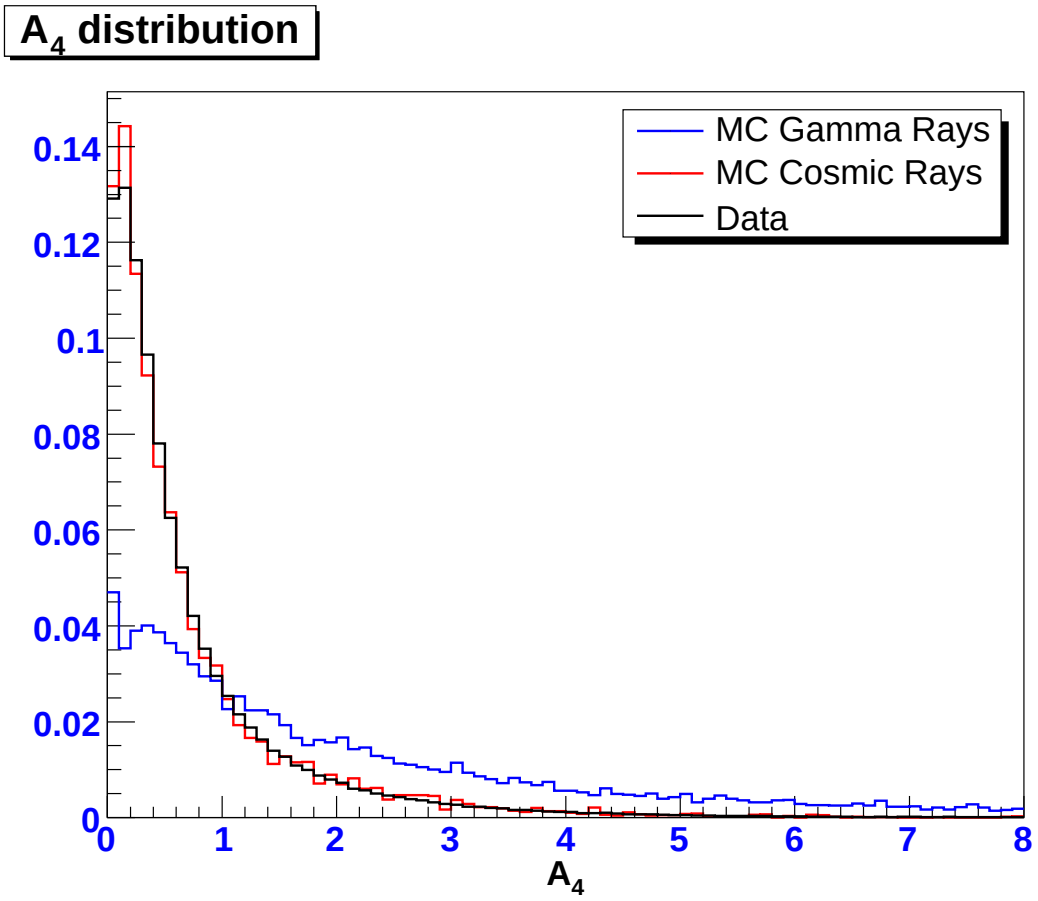

Figure 5.5: A_4 distribution for Monte Carlo γ-ray showers, Monte Carlo cosmic-ray showers, and data. All of the histograms have been normalized to have unit area.

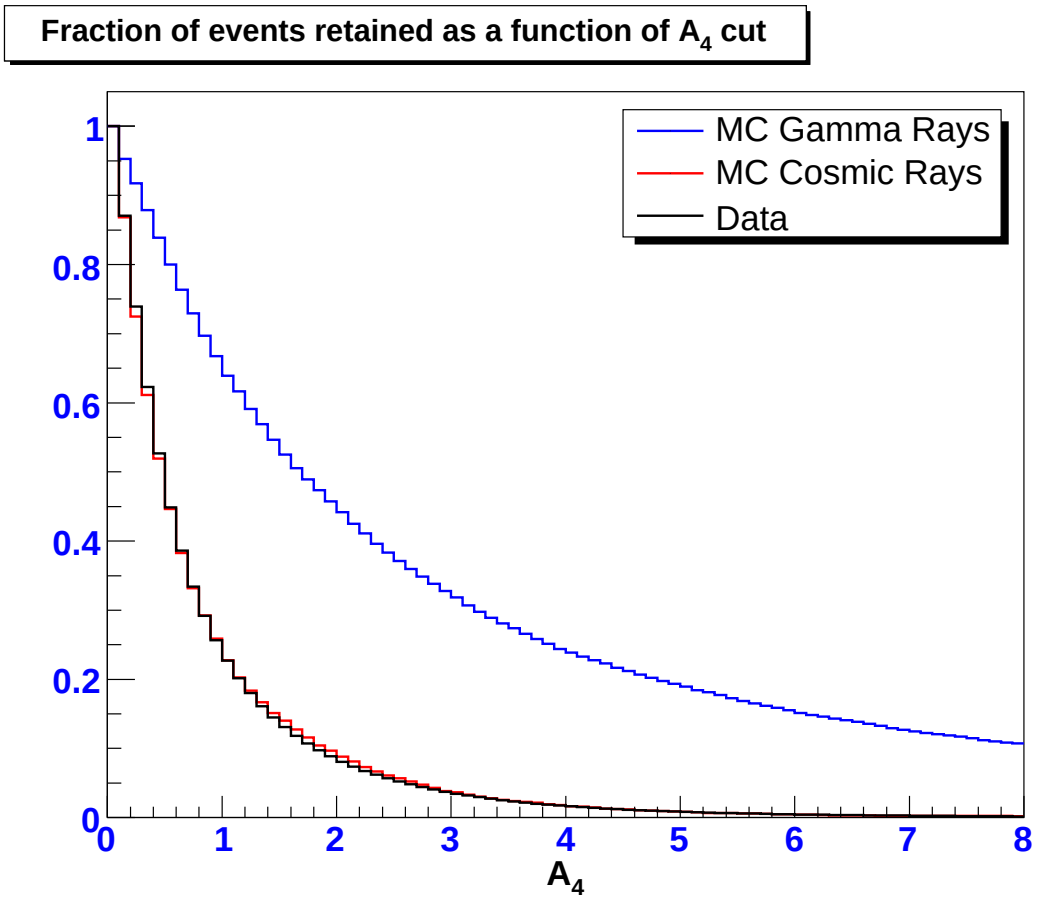

Figure 5.6: Fraction of data, cosmic-ray Monte Carlo, and γ-ray Monte Carlo showers with an A_4 value that is greater than the x-axis value.

angular fitter (low N_{fit}). As a result, events with a low value of PE_{maxB} may have low values of A_4. In addition, low energy gamma-ray events tend to have their cores on the pond. These on-pond events will again have low values of $(f_{top} + f_{out})$ and N_{fit} and high values of PE_{maxB} which will result in smaller values of A_4. Figure 5.8 shows the efficiency of the $A_4 \geq 3.0$ cut as a function of the primary energy for gamma-ray and cosmic-ray showers. From this figure it is seen that the efficiency of gamma-ray-initiated events is dependent on the energy of the primary gamma-ray, while for cosmic-rays the efficiency is nearly independent of energy. It is also noticed that for the $A_4 \geq 3.0$ cut we don't expect to see any gamma-ray-initiated events with primary energy less than 400 GeV, and that the median energy for gamma-ray-

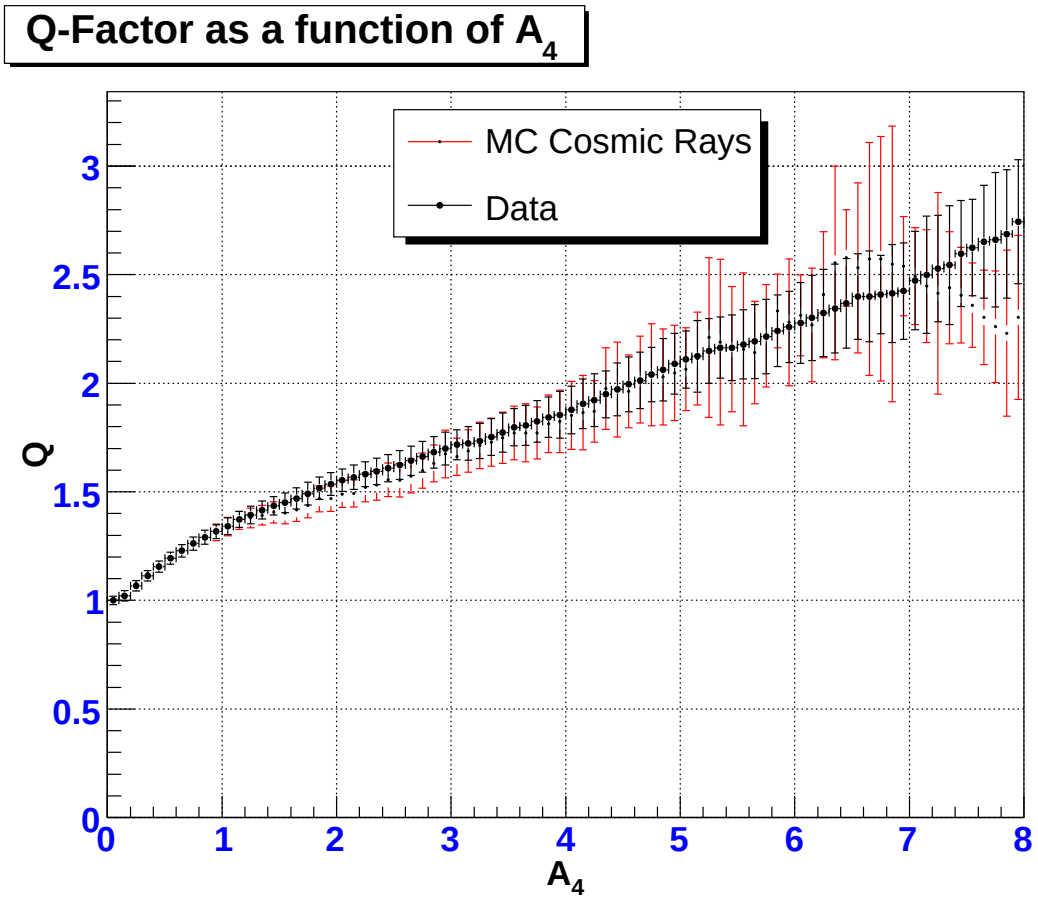

Figure 5.7: Quality factor Q as a function of the minimum value of A_4 required to retain an event. The red line compares Monte Carlo γ-rays to Monte Carlo cosmic-rays, and the black line compares Monte Carlo γ-rays to data.

initiated events passing this cut is around 10 TeV.

The energy of the primary gamma-ray is also a function of the A_4 cut applied. Figure 5.9 shows the median energies as a function of an A_4 cut. Each point represents the median energy for gamma-ray events with an A_4 value greater than the x-axis value. As can be seen from this figure, there is a good correlation between the median energy for a given A_4 value and that value of A_4. One can use this dependence to estimate the energy spectrum of a gamma-ray source. See Appendix A for details.

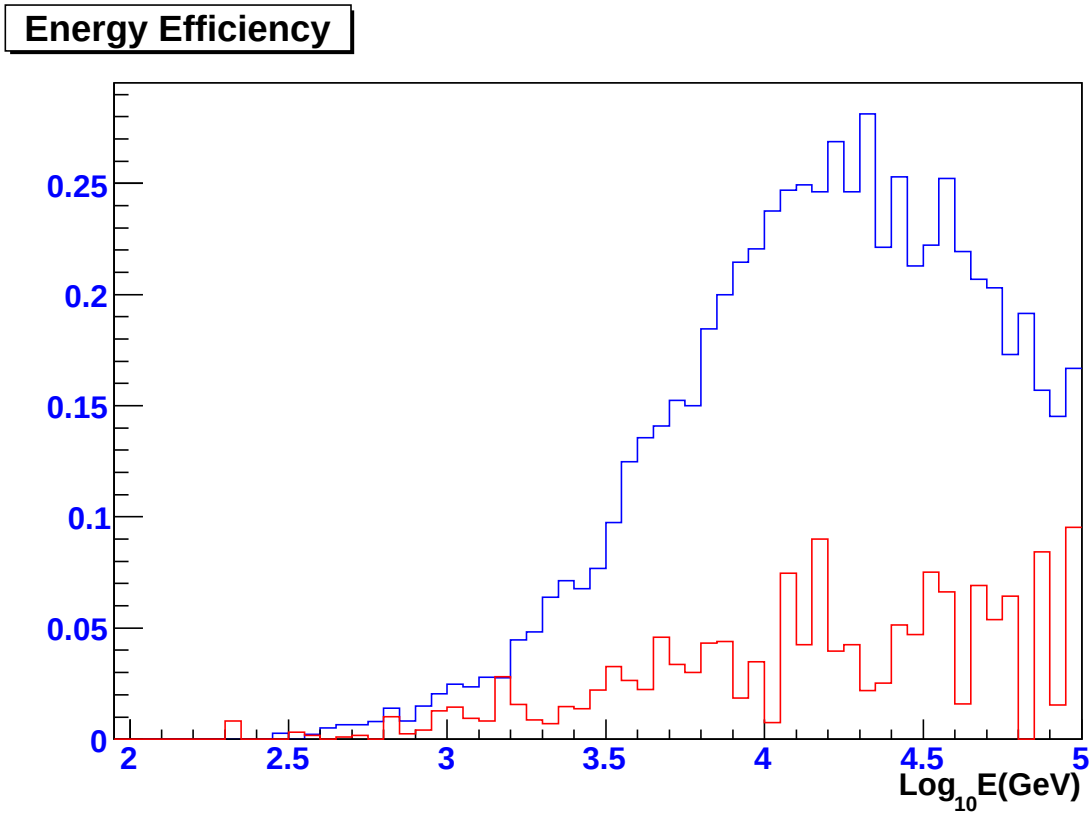

Figure 5.8: Fraction of gamma-rays and cosmic-rays retained by the cut $A_4 \geq 3.0$ as a function of the primary energy. Gamma-ray in blue, cosmic-ray in red.

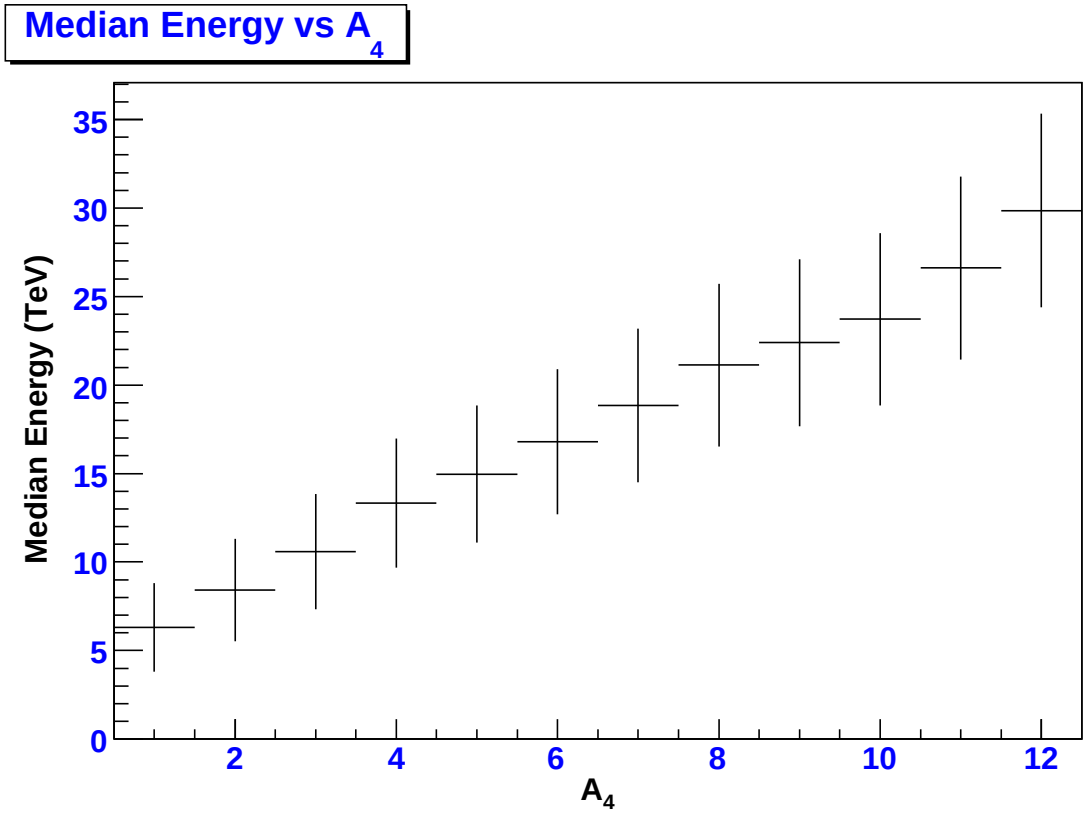

Figure 5.9: Median energies of gamma-ray-initiated air showers as a function of A_4. Each point represents the median energy for gamma-ray events with an A_4 value greater than the x-axis value.

5.3.2 Core Location Dependence

A_4 is a function of the location of the core of the air shower. Events that land on the pond tend to have smaller values of A_4 (i.e. more hadron like) than events with cores off the pond. This is because these events tend to have higher values of PE_{maxB} and lower values of $((f_{top} + f_{out}) \times N_{fit})$ which will result in smaller values of A_4. Low energy events are more likely to trigger the detector if they land on the pond, because a low energy event landing off the pond will have less chance of satisfying the trigger criteria. High energy events, on the other hand, have a good chance of triggering the detector whether they land on or off the pond.

Figures 5.10 and 5.11 show the A_4 distributions for γ-ray Monte Carlo, cosmic-

ray Monte Carlo, and data for on and off the pond showers, respectively. As can be seen from these two figures, there is a clear difference in the A_4 distribution for γ-ray showers in the two cases. More events have lower values of A_4 for on-pond events compared to off-pond events, while more events have higher values of A_4 for off-pond events compared to on-pond events. This will make it harder to distinguish between γ-ray-induced air showers and cosmic-ray-induced air showers when their cores land on the pond. This is clear from figures 5.12 and 5.13 which show the Quality factor distribution for on and off the pond events, respectively. Figure 5.12 compares Monte Carlo γ-rays to Monte Carlo cosmic-rays and figure 5.13 compares Monte Carlo γ-rays to data. The quality factor for events with cores off the pond is $> 50\%$ higher than for the events with cores on the pond. In figures 5.10 through 5.13 there is a good agreement between the data and the cosmic-ray Monte Carlo.

5.3.3 Zenith Angle Dependence

Since the energy threshold of the detector is a function of the zenith angle, and the number of muons generated in a cosmic-ray shower rises with primary energy, it is expected that the performance of A_4, as a background rejection variable, will improve with larger zenith angles. Figures 5.14 through 5.16 show the A_4 distribution for γ-ray Monte Carlo, cosmic-ray Monte Carlo, and data for three different zenith angle ranges, Figure 5.14 shows the A_4 distribution for zenith angles less than 15°, Figure 5.15 for zenith angles between 15° and 30°, and Figure 5.15 for events between 30° and 45°. The distributions look relatively similar. The quality factor as a function of the A_4 cut is shown in Figures 5.17 and 5.18 for the three zenith angle ranges. Figure 5.17 compares Monte Carlo γ-rays to Monte Carlo cosmic-rays and figure 5.18 compares Monte Carlo γ-rays to data. Although in general the higher zenith angle ranges give higher quality factors than lower zenith angle ranges, these differences are insignificant and the three zenith angle ranges give similar quality factors. In figures

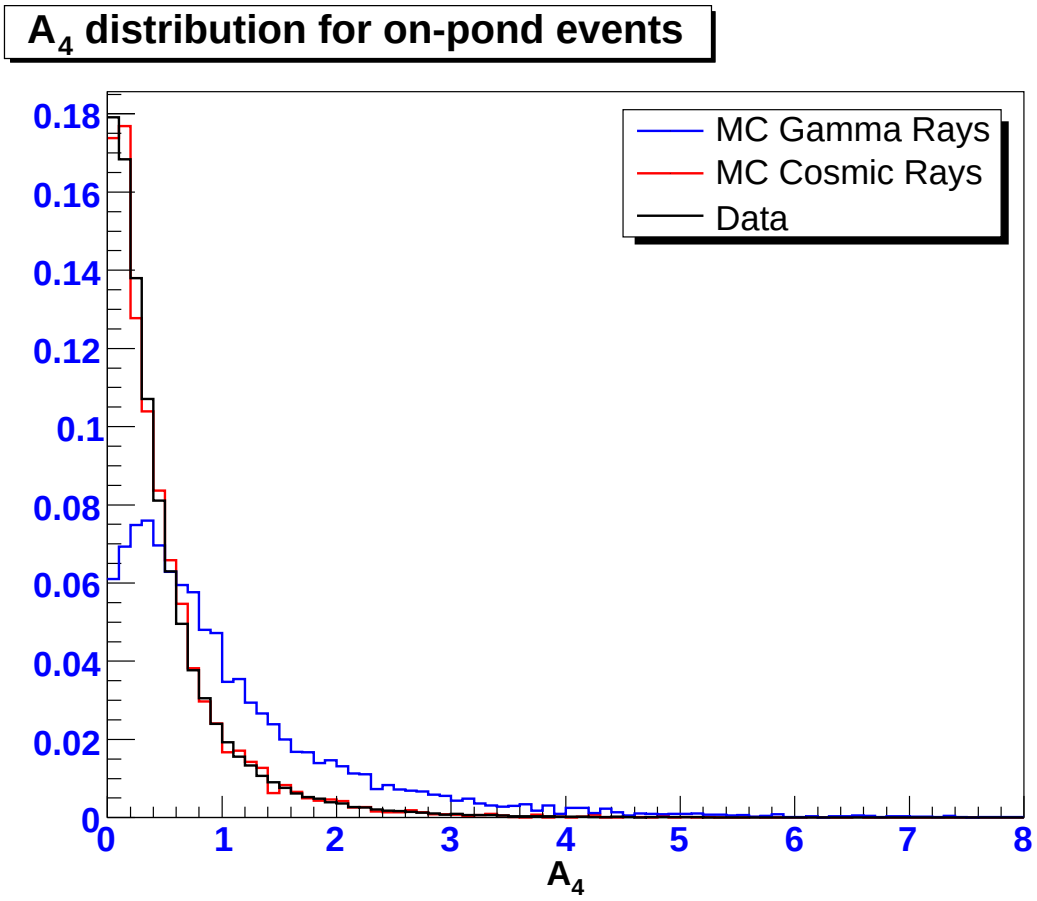

Figure 5.10: A_4 distribution for Monte Carlo γ-ray showers, Monte Carlo cosmic-ray showers, and data for events with their core on the pond. All of the histograms have been normalized to have unit area.

5.14 through 5.18 there is a good agreement between the data and the cosmic-ray Monte Carlo.

5.4 Observations of the Crab Nebula Using A_4

The Crab Nebula acts as a standard candle for gamma-ray astronomy due to its long-term, unchanging energy emission though many wavelengths. A new technique in the field of TeV gamma-ray astronomy is best verified on this source.

To verify the performance of the A_4 parameter a data set of 1.7 years of off-line reconstructed data was searched for gamma-ray signals from the location of the Crab Nebula using A_4. This data set extends from September 2003 to May 2005. Figure 5.19 shows a map of the statistical significance around the Crab Nebula with the $A_4 \geq 3.0$ and $N_{fit} \geq 40$ cuts applied. In this map the Crab Nebula is seen at 8.02

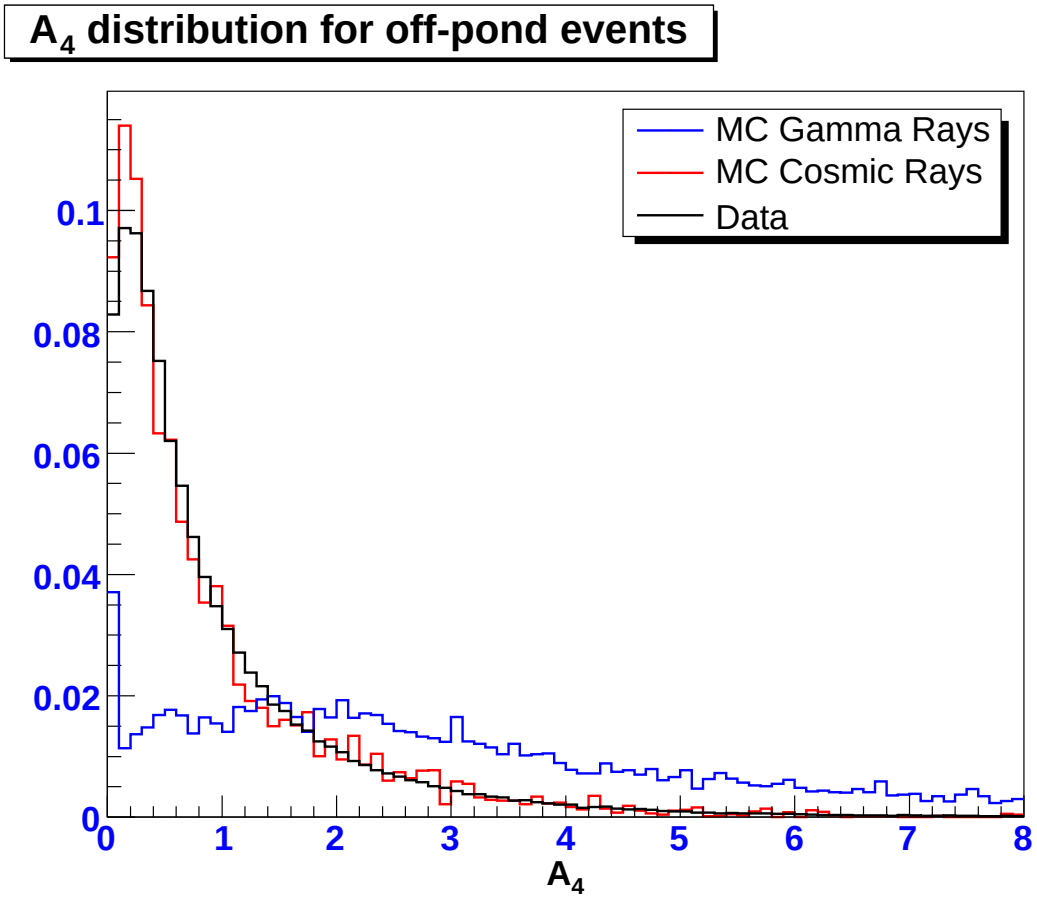

Figure 5.11: A_4 distribution for Monte Carlo γ-ray showers, Monte Carlo cosmic-ray showers, and data for events with their core off the pond. All of the histograms have been normalized to have unit area.

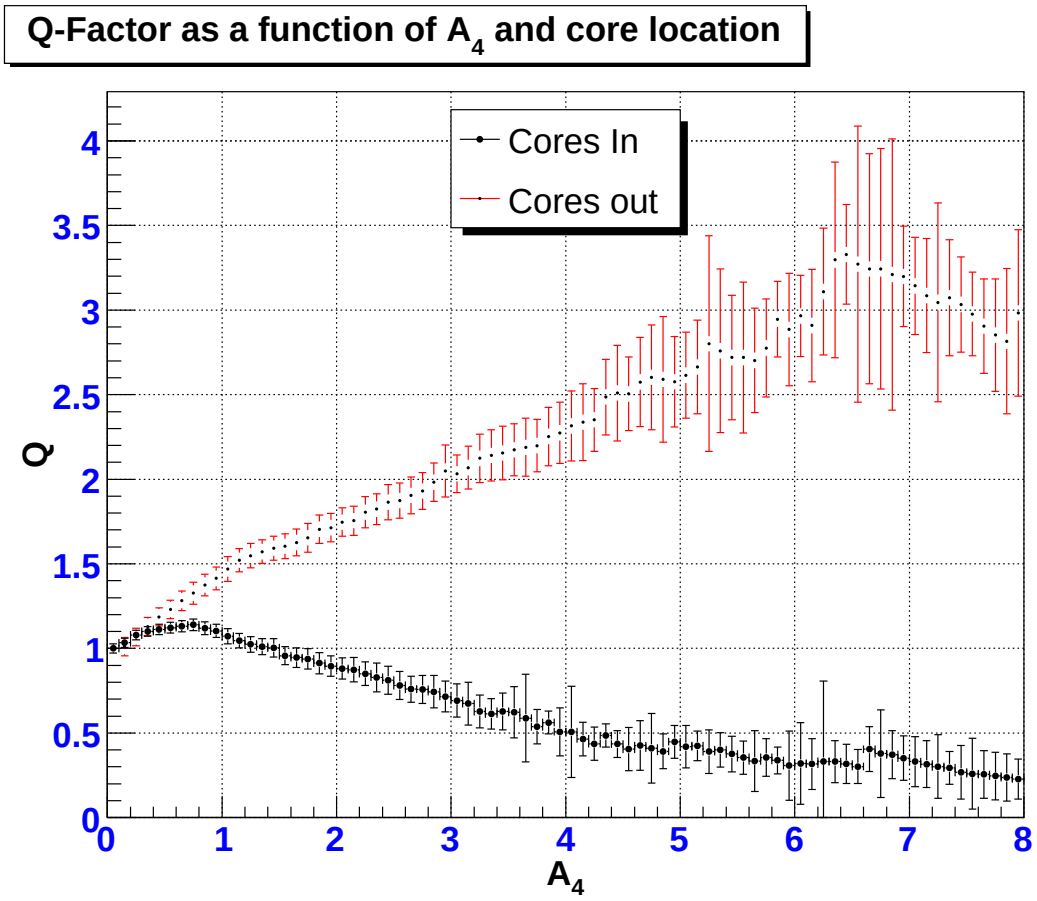

Figure 5.12: Quality factor Q for events with their core on and off the pond. In both cases Monte Carlo γ-rays are compared to Monte Carlo cosmic-rays

σ [2]. To compare the performance of the A_4 parameter to that of the compactness parameter, the same data set was searched using the compactness parameter. Figure 5.20 shows the map of the statistical significance around the Crab Nebula with the $C \geq 2.5$ and $N_{fit} \geq 20$ cuts applied. In this map the statistical significance in the location of the Crab Nebula is 5.34 σ.

The improvement in the detection of a gamma-ray signal from the Crab Nebula using A_4 over the compactness parameter ($Q = 8.02/5.34 = 1.5$) is in good agreement with that predicted by the Monte Carlo ($Q = 1.4$).

Another improvement is the signal-to-background ratio in both cases. The signal-

[2]Changing the cut on N_{fit} from 40 to 20 improves the quality factor for the $A_4 \geq 3.0$ cut by $\sim$10%.

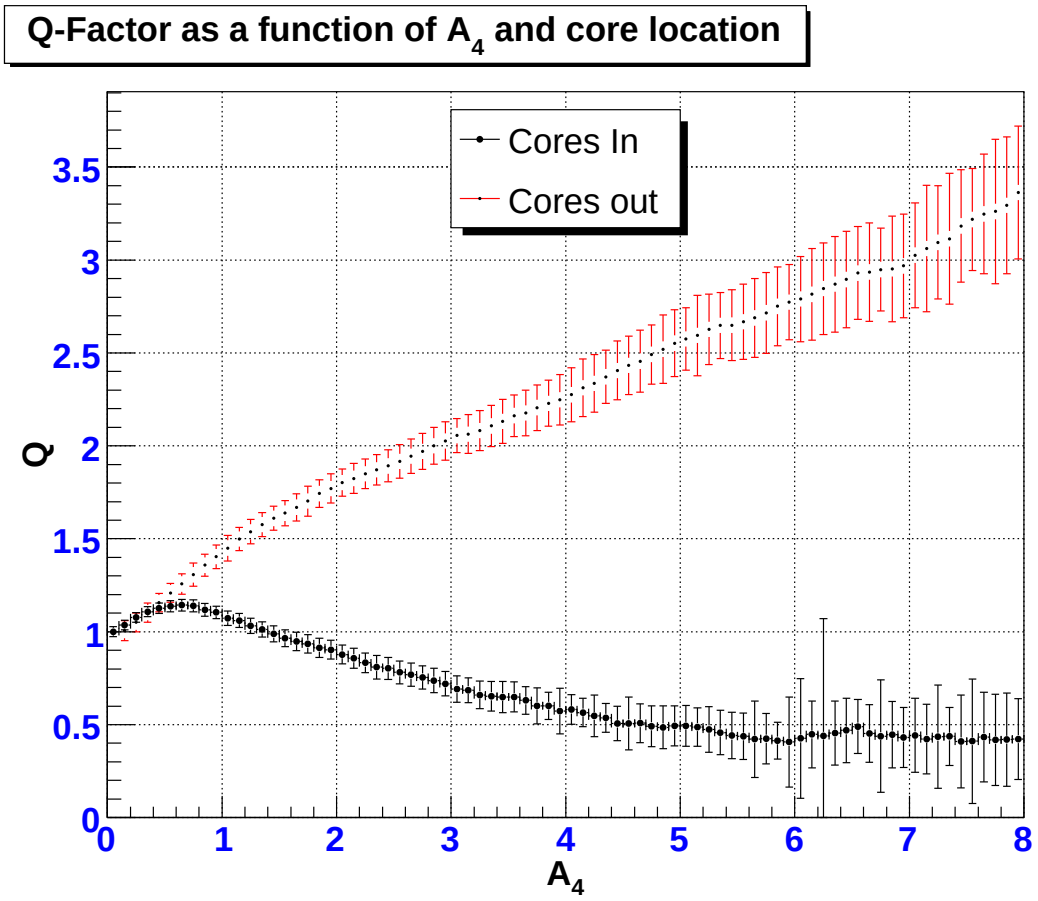

Figure 5.13: Quality factor Q for events with their core on and off the pond. In both cases Monte Carlo γ-rays are compared to data

to-background ratio in the case of A_4 is roughly 7 times that for the compactness. As will be discussed in the next chapter, signal-to-background ratios as high as 60% are achievable with high A_4 cuts.

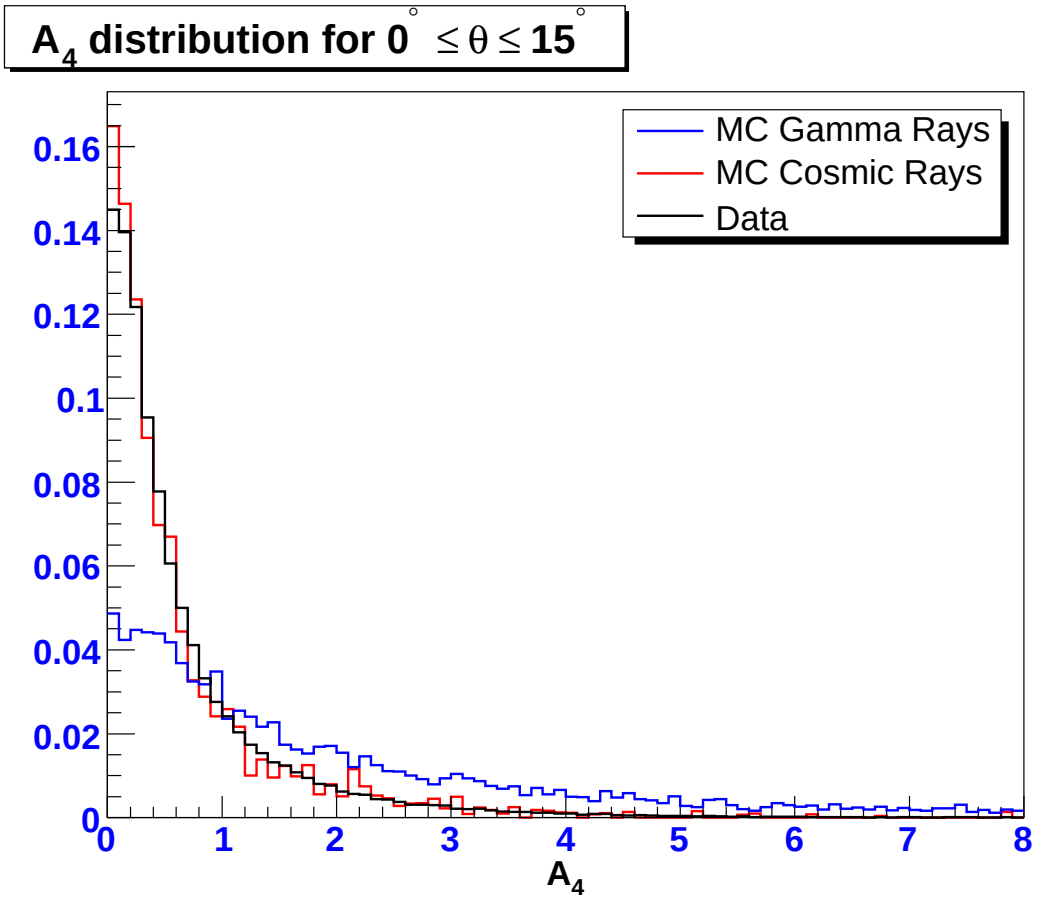

Figure 5.14: A_4 distribution for Monte Carlo γ-ray showers, Monte Carlo cosmic-ray showers, and data for the zenith angle range $0^\circ \leq \theta \leq 15^\circ$. All of the histograms have been normalized to have unit area.

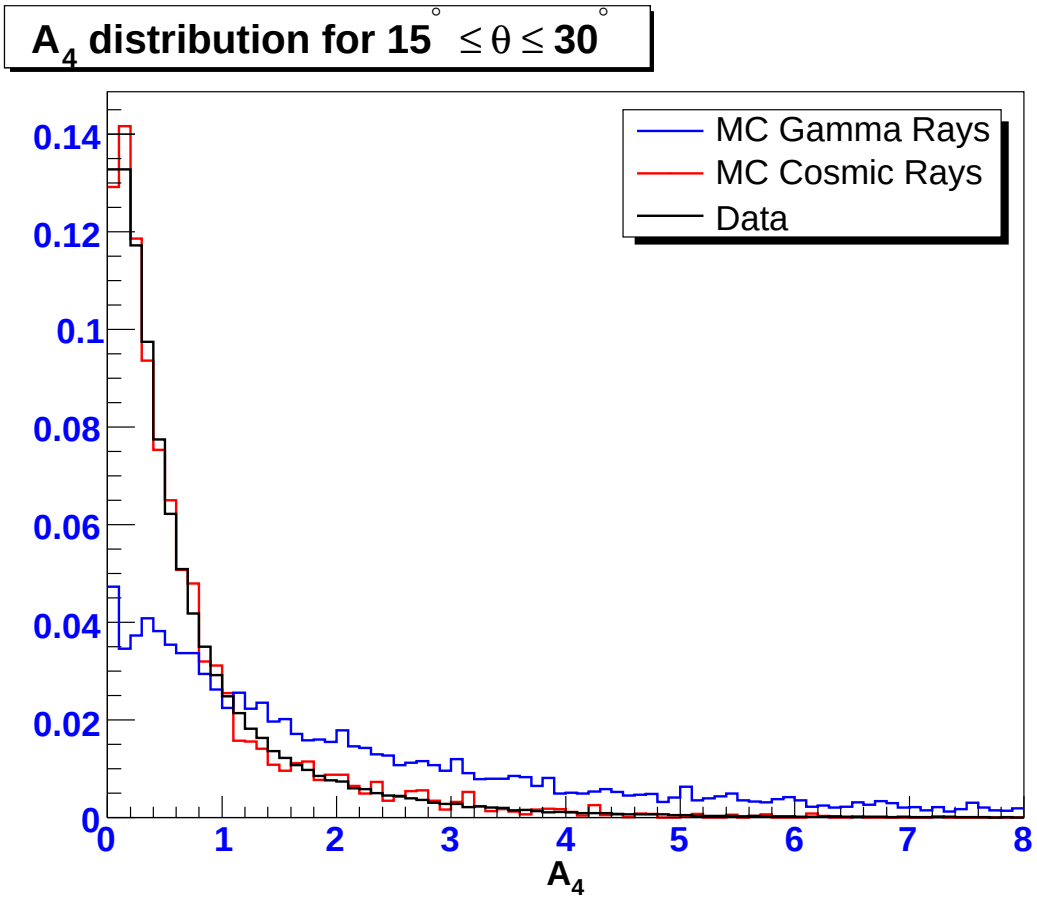

Figure 5.15: A_4 distribution for Monte Carlo γ-ray showers, Monte Carlo cosmic-ray showers, and data for the zenith angle range $15^\circ \leq \theta \leq 30^\circ$. All of the histograms have been normalized to have unit area.

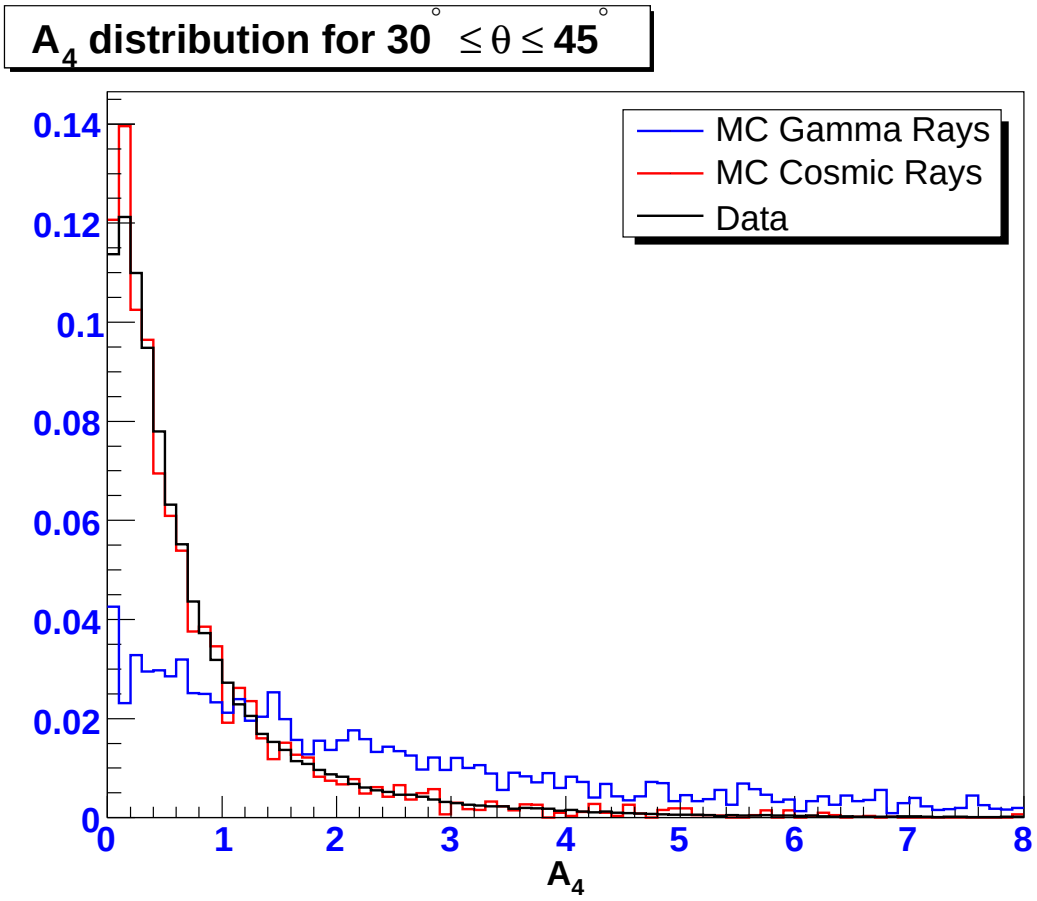

Figure 5.16: A_4 distribution for Monte Carlo γ-ray showers, Monte Carlo cosmic-ray showers, and data for the zenith angle range $30^\circ \leq \theta \leq 45^\circ$. All of the histograms have been normalized to have unit area.

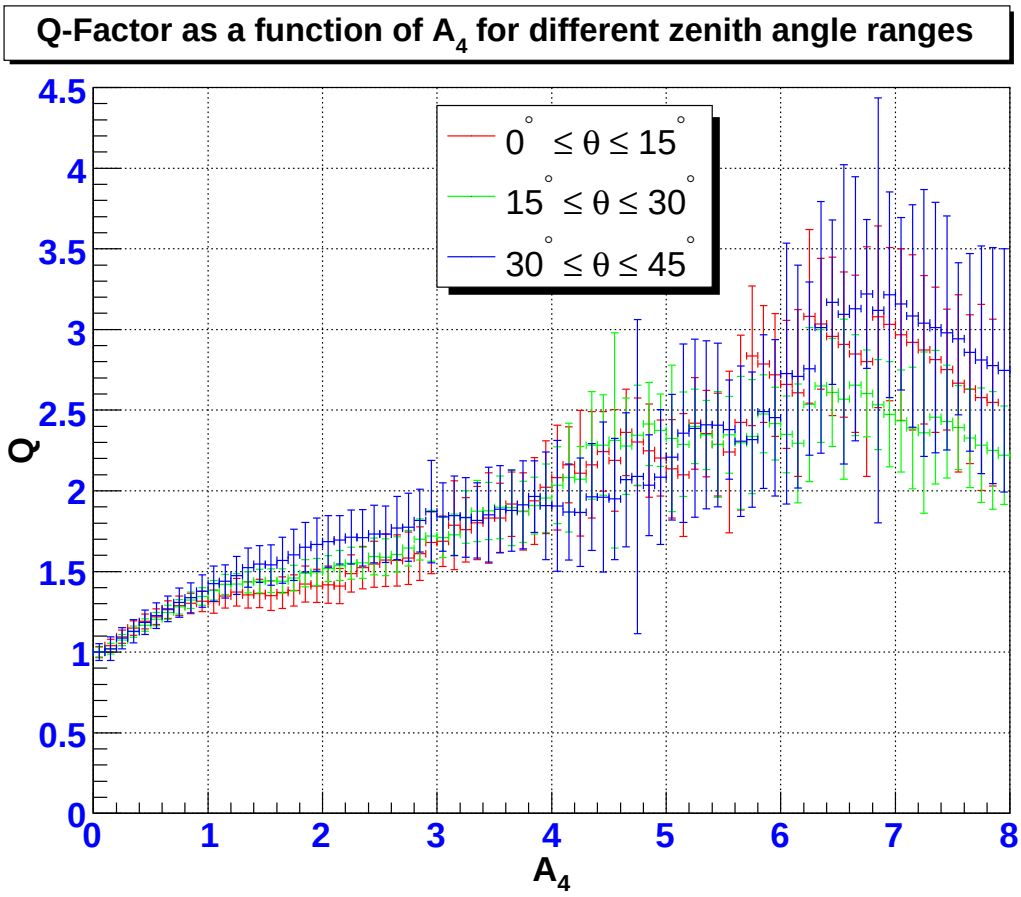

Figure 5.17: Quality factor as a function of the A_4 cut for three different zenith angle ranges. In all three cases Monte Carlo γ-rays is compared to cosmic-rays.

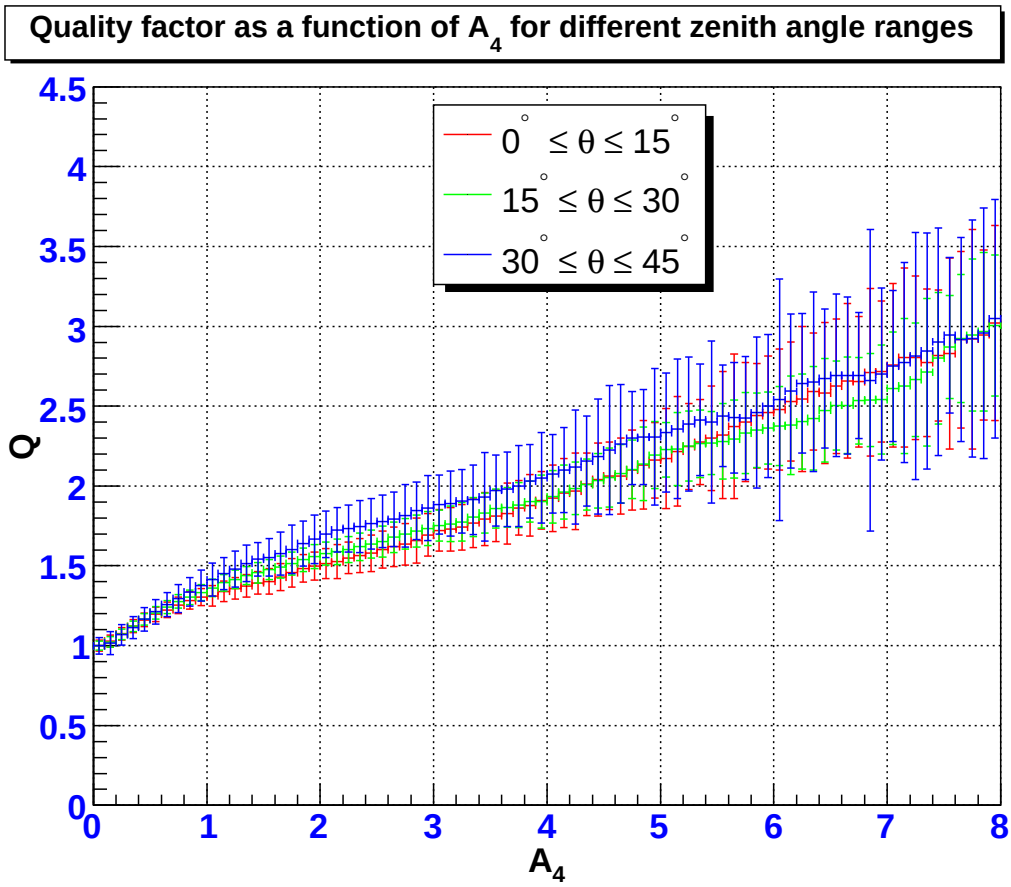

Figure 5.18: Quality factor as a function of the A_4 cut for three different zenith angle ranges. In all three cases Monte Carlo γ-rays is compared to data.

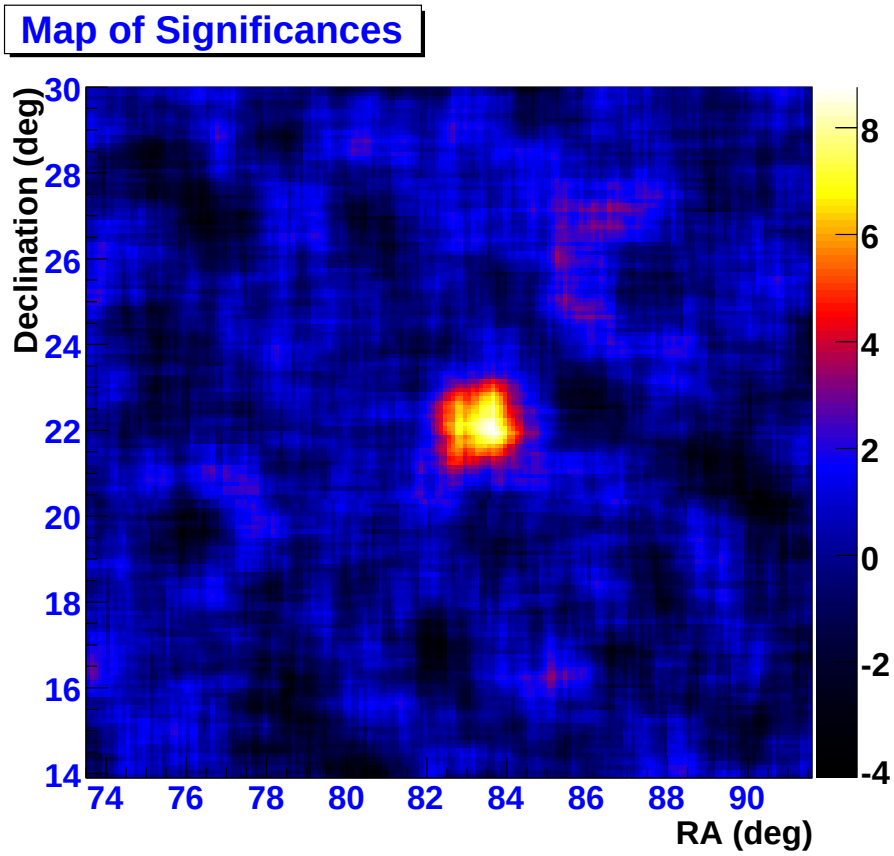

Figure 5.19: Map of the statistical significance around the Crab Nebula with the $A_4 \geq 3.0$ and $N_{fit} \geq 40$ cuts applied.

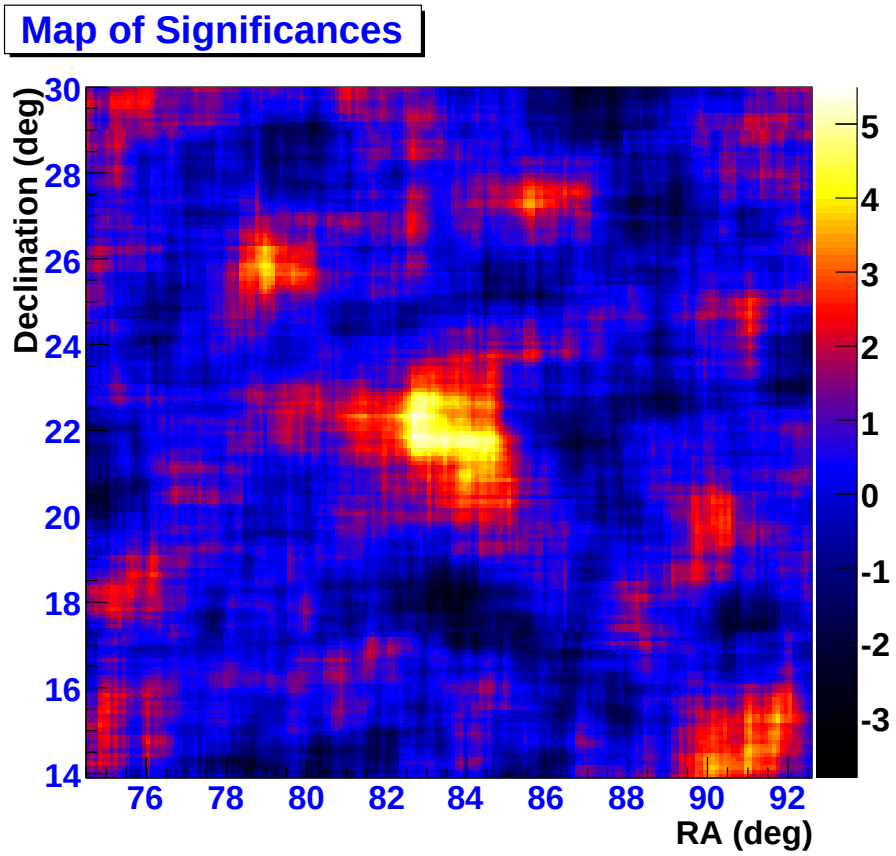

Figure 5.20: Map of the statistical significance around the Crab Nebula with the $C \geq 2.5$ and $N_{fit} \geq 20$ cuts applied.

Chapter 6

A_4 Weighted Analysis Technique

6.1 Motivations for Weighted Analysis Technique

As can be seen from figures 5.5 through 5.7, the Monte Carlo predicts an improvement in the performance of the A_4 parameter when higher values of this parameter are applied. The signal-to-background ratio (S/B) increases with increasing A_4.

Harder A_4 cuts were applied on the same data set as the one used in section 5.4. Figure 6.1 shows the map of statistical significance around the Crab Nebula with the $A_4 \geq 12.0$ and $N_{fit} \geq 40$ applied on this data set. In this map the Crab Nebula is seen at 5.58 σ. Although there was a $\approx 30\%$ loss in statistical significance of the Crab Nebula when the harder A_4 cut was applied, the main advantage of applying the hard A_4 cut is the higher S/B ratio (60.0%) achieved with this cut compared to that with the softer $A_4 \geq 3.0$ cut (3.4%). An increase by a factor of ~ 18.

The fact that one can achieve a higher S/B ratios with no major loss in statistical significance when applying harder A_4 cuts, and the fact that a single cut applied on the A_4 parameter would result in retaining a small fraction of the gamma-ray signal led to the development of the weighting analysis technique. This technique weights events based on the relative probability that the event was due to a gamma-ray, rather

than a cosmic-ray[63]. Events in an angular bin are not counted equally. Instead a weighted sum of events is used where events with higher values of A_4 are assigned higher weights. The same technique was applied to the estimation of the background. Rather than the background event count, a sum of the weights of the background sample was used for the background estimate in the bin.

Because there is a correlation between the gamma-ray energy and the value of A_4 of an event (figure 5.9), this weighting technique enhances the contribution of high energy gamma-rays and increases the median energy of detected events relative to previously published analyses. A source with a Crab-like spectrum will have a median energy of 12 TeV as compared to 3 TeV using a compactness cut[14].

The weighting analysis technique is equivalent to a likelihood ratio method estimation in the limit that the background is large, which is true for the Milagro data.

6.2 Determining the Gamma-Hadron Weights

In order to determine the weights for different values of A_4, the data set is binned in 12 bins in A_4. In each of these bins, events with A_4 value greater than or equal to the lower end of the bin and smaller than the upper end of the bin are kept in that bin. i.e. for the i'th A_4 bin, only events that satisfy the criteria

$$b_i^{min} \leq A_4 < b_i^{max} \tag{6.1}$$

are kept in that bin (with the exception of the last bin, for which the upper end is ∞), b_i^{min} and b_i^{max} being the bin's lower and upper limits, respectively.

Table 6.1 lists the set of cuts applied for each A_4 bin along with the number of Monte Carlo gamma-ray events[1] expected in that bin $\langle S_i \rangle$, the number of measured

[1]The Monte Carlo gamma-ray sample was generated with a Crab-Like spectrum ($E^{-2.6}$)

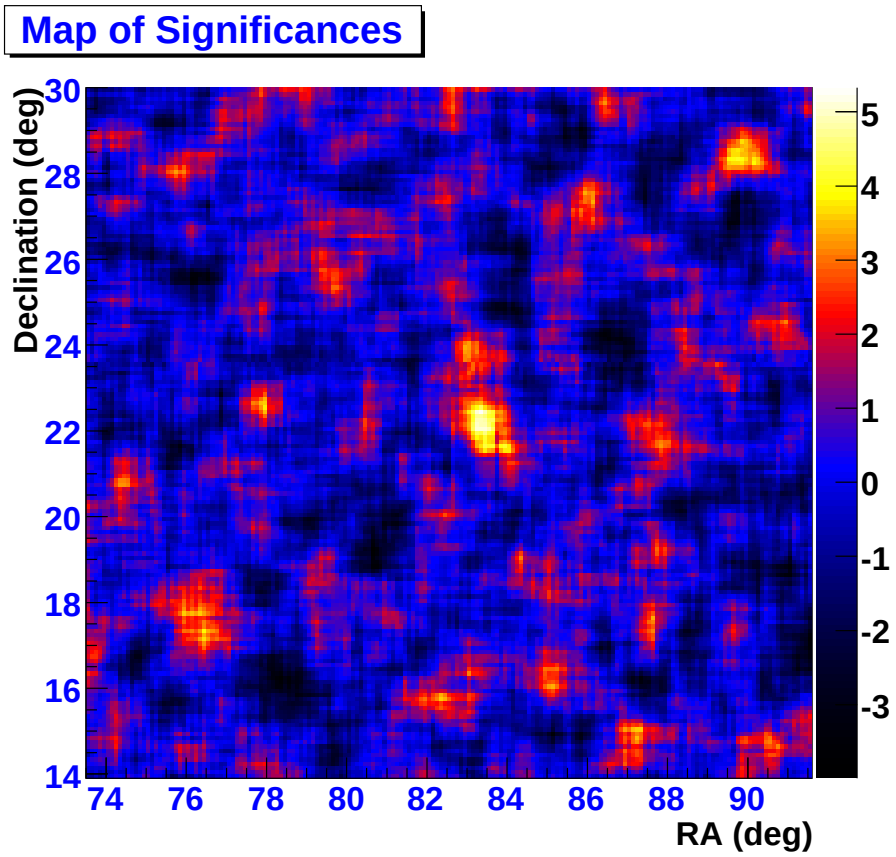

Figure 6.1: Map of the statistical significance around the Crab Nebula with the $A_4 \geq 12.0$ and $N_{fit} \geq 40$ cuts applied.

background events in the same bin $\langle B_i \rangle$, and the weight assigned for that bin ω_i. The weight assigned for the i'th bin is equal to [63, 48]:

$$\omega_i = \frac{\langle S_i \rangle}{\langle B_i \rangle} \tag{6.2}$$

All weights have been normalized to that of the first bin.

Bin No	Cuts	N_γ^{Exp}	$N_B^{Meas}(\times 10^6)$	Weight
1	$1 \leq A_4 < 2$	1262.5	409.314	1.00
2	$2 \leq A_4 < 3$	700.3	126.831	1.79
3	$3 \leq A_4 < 4$	410.1	50.166	2.65
4	$4 \leq A_4 < 5$	254.1	23.601	3.49
5	$5 \leq A_4 < 6$	182.4	13.055	4.53
6	$6 \leq A_4 < 7$	162.2	8.404	6.26
7	$7 \leq A_4 < 8$	161.4	6.186	8.46
8	$8 \leq A_4 < 9$	49.5	1.335	12.03
9	$9 \leq A_4 < 10$	32.2	0.743	14.03
10	$10 \leq A_4 < 11$	27.9	0.479	18.90
11	$11 \leq A_4 < 12$	7.4	0.275	26.93
12	$12 \leq A_4$	5.1	0.159	32.01

Table 6.1: List of the set of cuts applied for each A_4 bin along with the number of gamma Monte Carlo events expected in that bin, the number of measured background events in the same bin, and the weight assigned for each bin. All weights have been normalized to that of the first bin.

6.3 Determining the PSF Fits

For Milagro, the point spread function (angular response) is determined from simulations of the detector response to gamma-ray-initiated air showers, and is given by the distribution of the space angle difference between the simulated primary direction and the reconstructed direction (Δ_{angle}). The point spread function can be characterized by a double 2D Gaussian function of the form:

$$F(r) = A\ r(e^{(-r^2/2\sigma_1^2)} + R\ e^{(-r^2/2\sigma_2^2)}) \tag{6.3}$$

where A is the amplitude, R is the ratio between the two parts of the 2D Gaussian, and r is Δ_{angle}. Figure 6.2 shows the Δ_{angle} distribution of triggered gamma-ray events that passed the $N_{fit} \geq 40$ cut. On the same plot the fit to equation 6.3 is shown (black line). The box on the right side of the figure lists the fit parameters. The median of the distribution is $\sim 0.85^\circ$.

The PSF of Milagro is a function of the A_4 cut applied. It is expected that the angular resolution of the detector will improve with harder A_4 cuts. This is clearly

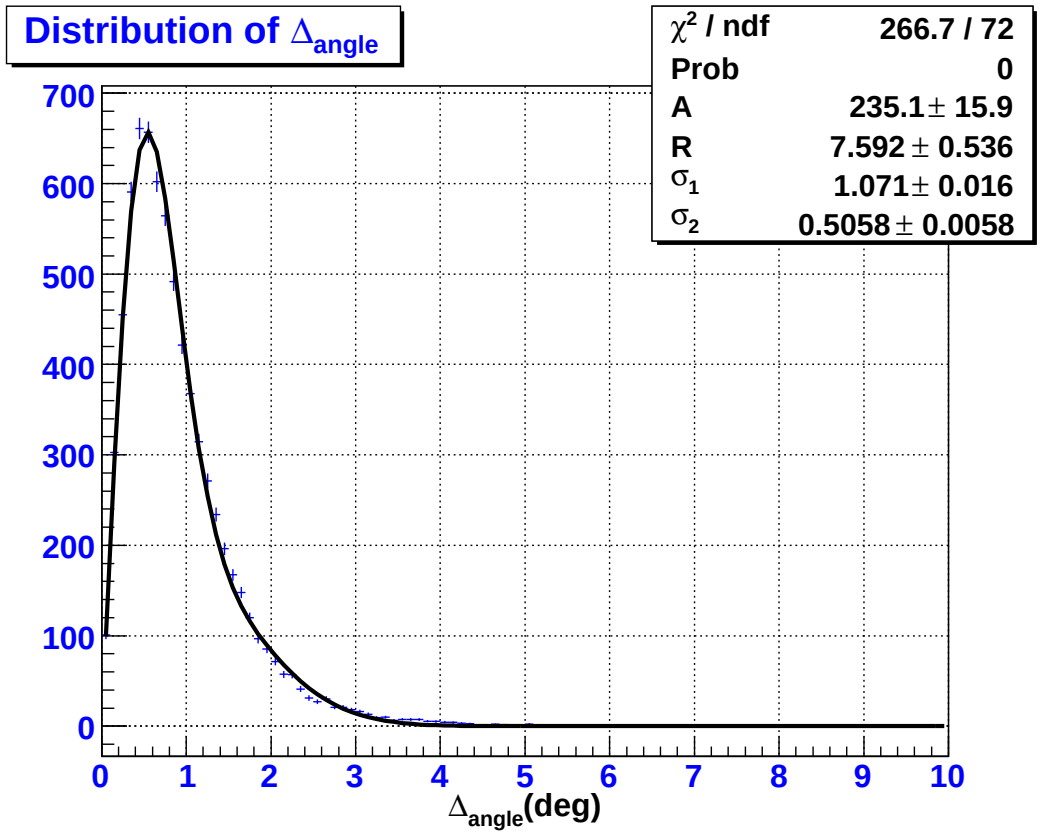

Figure 6.2: Distribution of Δ_{angle} for triggered gamma-ray events that passed the $N_{fit} \geq 40$ cut. The median of the distribution is $\sim 0.85°$.

seen in Figure 6.3 which shows the Δ_{angle} distribution for triggered gamma-ray events that passed the $A_4 \geq 3.0$ (top) and $A_4 \geq 12.0$ cuts (bottom). In the first case the angular response is essentially a 2D Gaussian with $\sigma = 0.44$ and a median of 0.75°, while for the second case the angular response is essentially a 2D Gaussian with $\sigma = 0.36$ and a median of 0.5°.

Since the PSF of Milagro is a function of the A_4 cut applied, it is necessary to determine the PSF for each bin in A_4. The distribution of Δ_{angle} for triggered gamma-ray events in each bin in A_4 was fitted to a function of the form given in equation 6.3. The fit parameters are given in Table 6.2. Each event in an A_4 bin is smoothed by the PSF of the detector for that A_4 bin [9].

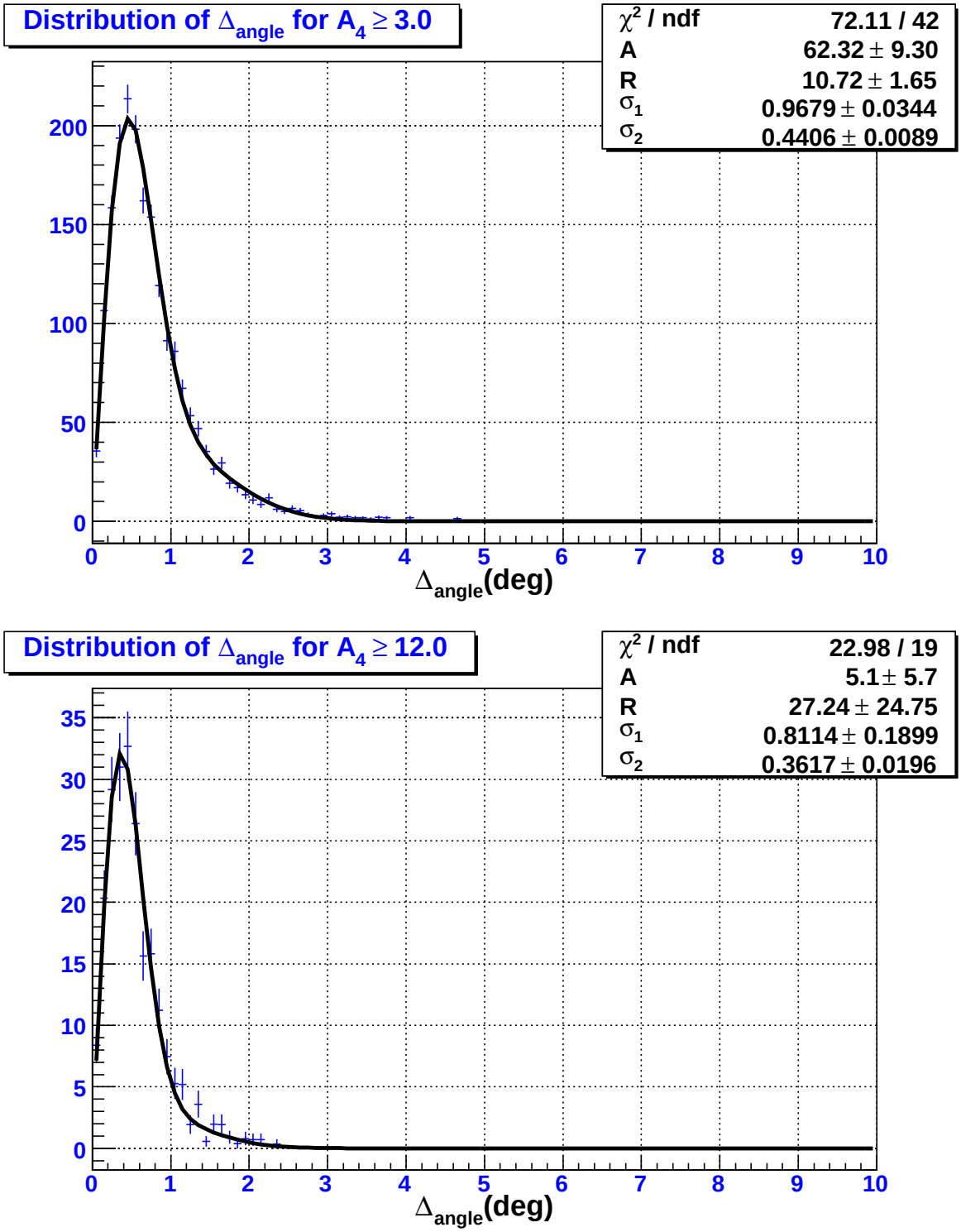

Figure 6.3: Distribution of Δ_{angle} for triggered gamma-ray events that passed the $A_4 \geq 3.0$ (top) and $A_4 \geq 12.0$ cuts (bottom).

Bin No	Cuts	Amplitude (A)	Ratio (R)	σ_1	σ_2
1	$1 \leq A_4 < 2$	59.4± 7.2	5.39±0.73	1.06±0.03	0.54±0.01
2	$2 \leq A_4 < 3$	33.42± 8.09	6.06±1.64	1.04±0.05	0.54±0.02
3	$3 \leq A_4 < 4$	37.64± 8.63	3.32±0.95	0.85±0.03	0.48±0.03
4	$4 \leq A_4 < 5$	15.42± 3.58	6.37±1.60	0.93±0.05	0.43±0.02
5	$5 \leq A_4 < 6$	7.18± 3.29	10.33±5.51	0.92±0.09	0.47±0.02
6	$6 \leq A_4 < 7$	4.39± 3.49	12.49±10.24	0.91±0.16	0.43±0.03
7	$7 \leq A_4 < 8$	0.98± 1.99	42.55±86.05	1.28±1.24	0.48±0.04
8	$8 \leq A_4 < 9$	0.86± 0.76	46.62±53.13	1.23±0.59	0.44±0.02
9	$9 \leq A_4 < 10$	0.56± 0.38	72.40±56.2	1.65±1.25	0.41±0.02
10	$10 \leq A_4 < 11$	0.32± 0.20	106.60±91.4	-2.32±5.20	0.38±0.02
11	$11 \leq A_4 < 12$	0.32± 0.57	68.18±108.96	-1.71±2.12	0.44±0.02
12	$12 \leq A_4$	5.10± 5.70	27.24±24.75	0.81±0.20	0.36±0.02

Table 6.2: A list of the fit parameters for Milagro's PSF for the different A_4 bins used in this analysis.

6.4 Median Energy For the Weighted Analysis Technique

Since the weighting analysis technique assigns higher weights for events with higher values of A_4 and since events with higher values of A_4 have, on average, higher median energies (see Figure 5.9), it is expected that the median energy for gamma-ray events using this technique will be higher than the one for triggered events (Figure 3.12). This is clearly shown in figure 6.4 which shows the energy distribution for gamma-ray events with a power law spectrum of $dN/dE \propto E^{-2.6}$. The blue line represents the energy distribution for the A_4 weighted analysis technique, while the green line represents the energy distribution for triggered events. The median of the distributions are 12 and 3.2 TeV, respectively. Changing the spectrum of the simulated gamma-ray events from $E^{-2.0}$ to $E^{-3.0}$ changes the median energies from ~ 19 TeV to ~ 8 TeV. Table 6.3 lists the median energies for different spectra.

α	Median energy (TeV)
- 2.0	19.0
- 2.2	15.9
- 2.4	14.2
- 2.6	12.0
- 2.8	11.1
- 3.0	8.0

Table 6.3: A list of the fit parameters for Milagro's PSF for the different A_4 bins used in this analysis.

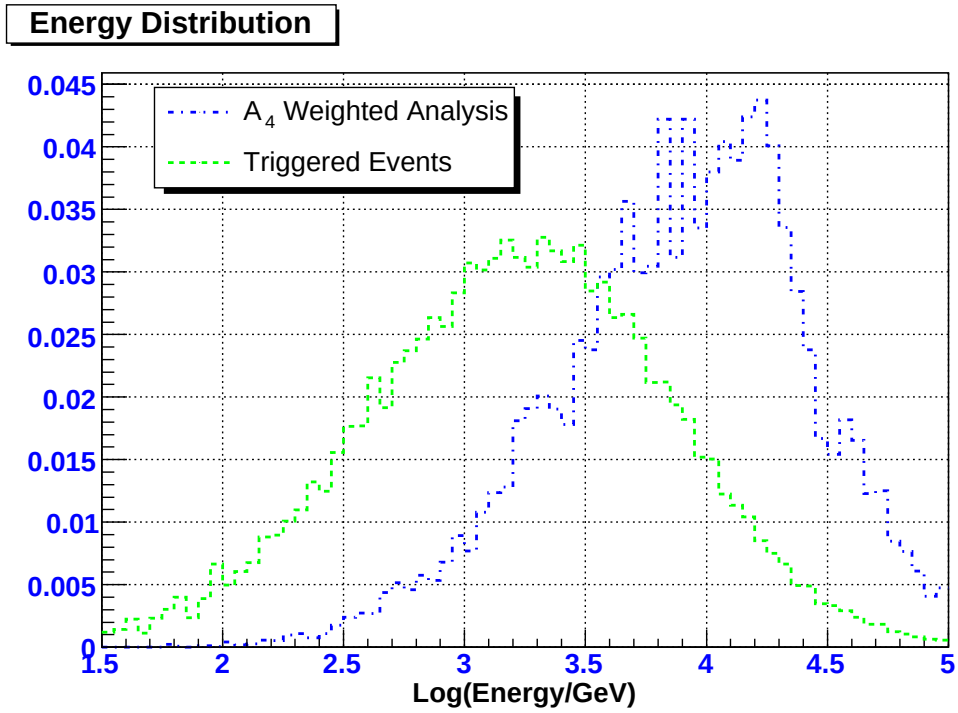

Figure 6.4: Energy distribution for gamma-ray events with a power law spectrum of $dN/dE \propto E^{-2.6}$. The blue line represents the energy distribution for the A_4 weighted analysis technique, while the green line represents the energy distribution for triggered events. The median of the distributions are 12 and 3.2 TeV, respectively.

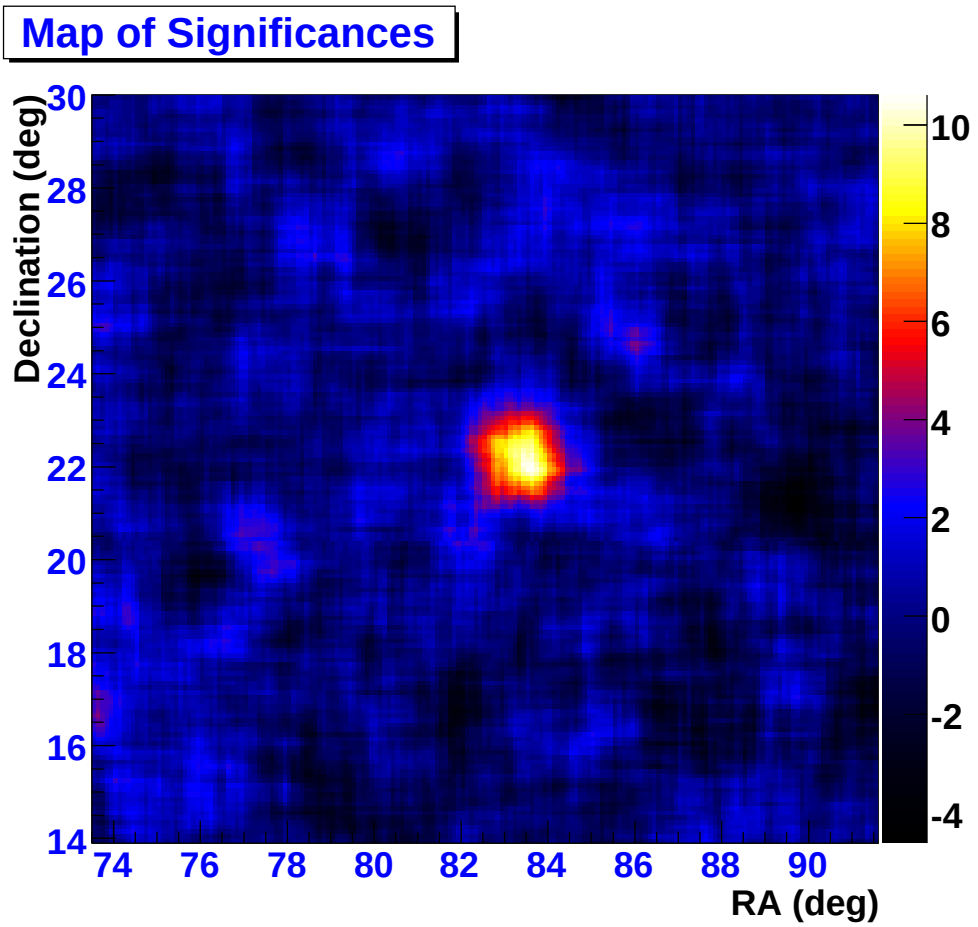

Figure 6.5: Map of the statistical significance around the Crab Nebula with the weighting analysis method applied.

6.5 Results on the Crab Nebula

To test the new weighting analysis technique, this technique was applied to the same data set as the one used in sections 5.4 and 6.1 with the gamma-hadron weights as those given in table 6.1 and PSF weights given by the fit parameters in table 6.2. Figure 6.5 shows the map of statistical significance around the Crab Nebula with the A_4 weighted analysis applied. The significance at the location of the Crab is 10.55 σ. An increase by 32% over the significance achieved with the standard A_4 cut ($A_4 \geq 3.0$).

Chapter 7

All-Sky Survey

7.1 Data Set

After the confirmation of the new A_4 weighting analysis method on the Crab nebula, the next logical step was to apply this analysis method to a bigger data set in search for new TeV gamma-ray sources in the sky. This all-sky survey covered online-reconstructed data collected between MJD51745(July 20, 2000) and MJD54102(January 1, 2007). A total of 2358 days of collected data.

7.1.1 Event Selection Cuts

In performing this analysis two event selection cuts were applied on the whole data set:

1. $N_{fit} > 40$
2. Zenith angle $\theta < 45^{\circ}$

The N_{fit} cut was applied to ensure the selection of good fit showers. The zenith angle cut applied was selected to match the cut applied on the simulated gamma-ray Monte Carlo events generated for this analysis (see section 3.10).

7.1.2 Excluded Data Runs

Some of the runs[1] in the online-reconstructed data set were taken under special conditions such as calibration runs. Some runs show sudden change in the trigger rate and/or zenith angle distribution. Other runs have corrupted data due to buffers with overwrites. Other runs were taken with deep water on cover. These runs make up a small fraction of the entire data set and are excluded from this analysis[2].

7.2 Epochs in Milagro

Milagro is a very dynamic experiment. It is dynamic in, at least, two ways:

1. Human controlled variations. Those include:
   (a) Installation of Outriggers.
   (b) Different reconstruction algorithms.
   (c) Different calibration software.
   (d) Trigger type used.
   (e) Trigger conditions.
2. Weather related variations. Those include:
   (a) Water on top of the cover.
   (b) Snow and ice on top of the cover.
   (c) Air under cover.
   (d) Freezing of a layer of water under the cover.
   (e) Change of atmospheric properties due to daily and seasonal changes.

[1] At 0 UT each day a new run is started by the DAQ system. Each run consists of smaller subruns of 5 minutes each. A new run will also be started if the DAQ system is restarted for any reason.

[2] A full list of all the excluded data runs is available in the Bad Run List file under Milinda, the Milagro software.

Variations due to weather changes have much less effect on the detector than those due to human controlled variations. Although weather variations are hard to keep track of and would require many different sets of Monte Carlo simulations, such weather effects can be minimized by excluding runs with big fluctuations due to weather as mentioned in section 7.1.2.

To take into account the human controlled variations, the data set was split into epochs. Table 7.1 lists epochs in Milagro. For each epoch, the detector was simulated with the exact configurations.

7.2.1 Dead PMTs

During the operation of Milagro, some of the PMTs leak water through their connectors and stop working. An annual repair operation is performed in which these "dead" PMTs are taken out of the pond and are either fixed or replaced with new ones. The percentage of PMTs that are dead can have an effect on the performance of the detector and, thus, should be taken into account in any analysis. The number of "dead" PMTs changes from small numbers after each repair to bigger numbers before the next repair is performed. To study the effect of dead PMTs on the behavior of A_4, three different runs from each epoch were used to compare the A_4 distributions in each case. These runs correspond to the minimum, average, and maximum percentages of "dead" PMTs for the given epoch. In addition to using these data runs, Monte Carlo simulations of the detector for the different percentages of "dead" PMTs, minimum, average, and maximum, were used to study the effect of "dead" PMTs in the Monte Carlo. Figure 7.1 show distributions of A_4 for the different percentage of "dead" PMTs for cosmic-ray Monte Carlo, data, and gamma-ray Monte Carlo for the eighth epoch. It can be seen that the distributions, in all three cases, are indistinguishable. The same distributions are shown in figure 7.2 on a log-scale for the y-axis. Similar behavior is seen in the rest of the epochs. Similar figures for

Epoch No	Core Finder	Angle Fitter	Trigger Type	Special	Run Numbers	Start Date
1	Center Of Mass(COM)	AS Layer	Multiplicity		2360-2700	07/19/00
2	Off Pond	AS Layer	Multiplicity		2701-3767	12/10/00
3	Off Pond	AS Layer	VME	Pre Outriggers	3768-4972	01/11/02
4	Outrigger COM	AS Layer	VME	Post Outriggers	4973-5918	05/18/03
5	Gaussian	(AS+MU+OR) Layers	VME		5919-6232	10/06/04
6	Gaussian	(AS+OR) Layers	VME	High % Dead PMTs	6233-6564	04/01/05
7	Gaussian	(AS+OR) Layers	VME	Low % Dead PMTs	6565-6895	09/20/05
8	Gaussian	(AS+OR) Layers	Multiplicity	Calibration 603	6896-7369	04/01/06

Table 7.1: A list of different epochs in Milagro that are used in this analysis. The end date for the last epoch is January 1, 2007. For the exposure of each epoch see table 7.2.

Epoch No	Exposure (days)	% AS Dead	% MU Dead	% OU Dead
1	131.6	5	5	100
2	382.5	5	5	100
3	430.1	5	5	100
4	471.8	5	5	3
5	169.8	8	5	2
6	164.6	10	5	2
7	174.3	2	4	4
8	280.4	3	6	2

Table 7.2: Percentage of "dead" PMTs in each layer for the different epochs. The second column shows the number of dead PMTs for the air shower layer, the third column for the muon layer, and the fourth column for the outrigger array. For the first three epochs the outrigger array was not yet installed and thus 100% of the outrigger array PMTs were simulated as dead PMTs.

the other epochs are shown in Appendix B.

A more sensitive analysis to the effect of "dead" PMTs was performed[64]. This analysis estimated the number of events from the Crab Nebula per day for different percentage of "dead" PMTs. Again, there were no significant differences in this number for the different percentages.

Since there were no significant differences in the A_4 distributions for the different percentages of "dead" PMTs, the average number of "dead" PMTs in each epoch was taken as input for the simulations. These numbers are shown in table 7.2. For the first three epochs the outrigger array was not yet installed and thus 100% of the outrigger array PMTs were simulated as dead PMTs.

7.3 Determining the Gamma-Hadron Weights

In order to calculate the gamma-hadron weights, the same method used in section 6.2 was applied to each epoch. The only difference is that for the pre outrigger data the A_4 bins were different. Table 7.3 lists the A_4 bins used for the pre outrigger and post outrigger data sets. On average, the contribution from the f_{Out} term in A_4, equation 5.3, is equal to that from the term f_{Top}. So in the absence of this term, for

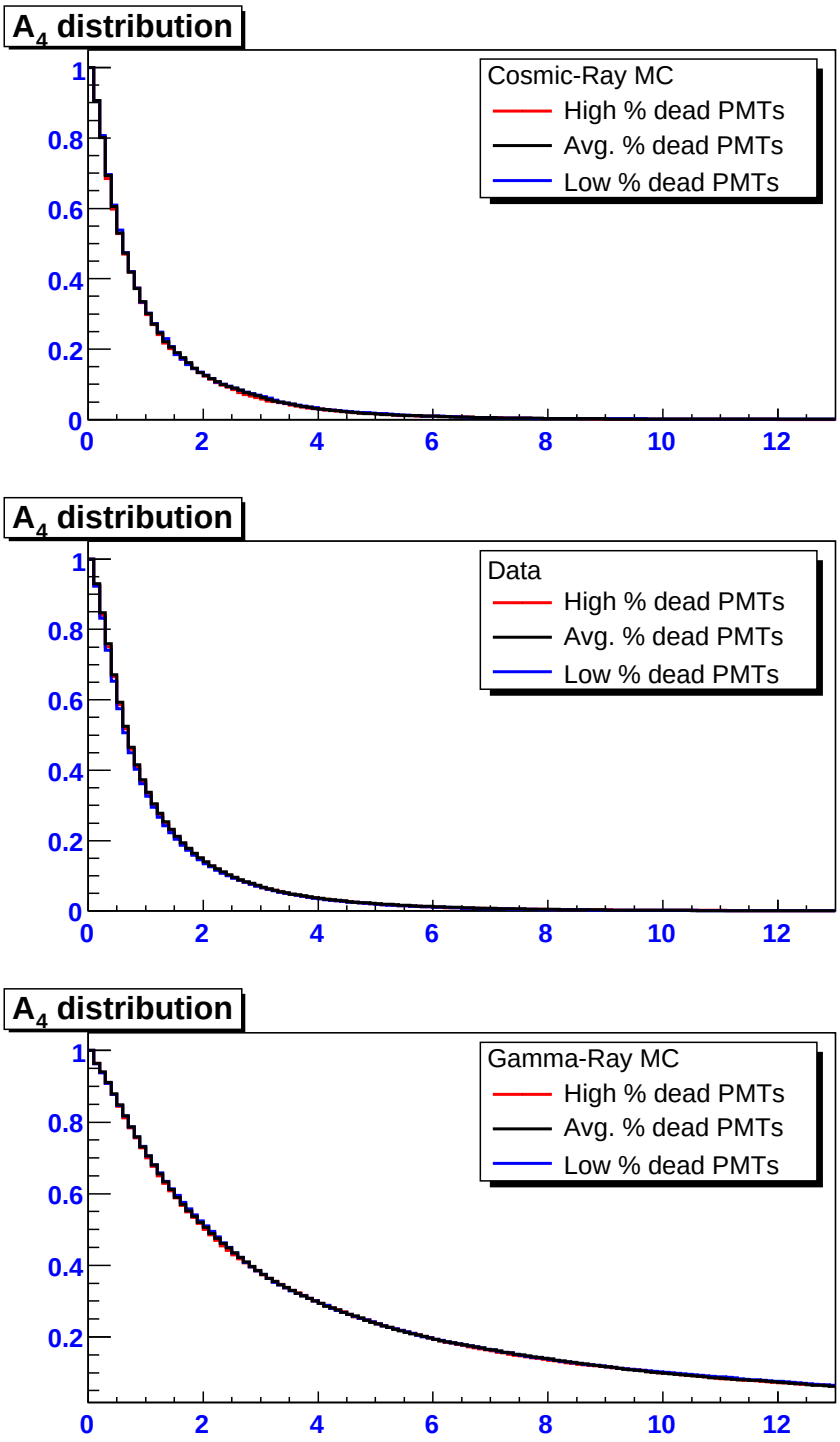

Figure 7.1: Distributions of A_4 for the different percentage of "dead" PMTs for cosmic-ray Monte Carlo, data, and gamma-ray Monte Carlo for the eighth epoch.

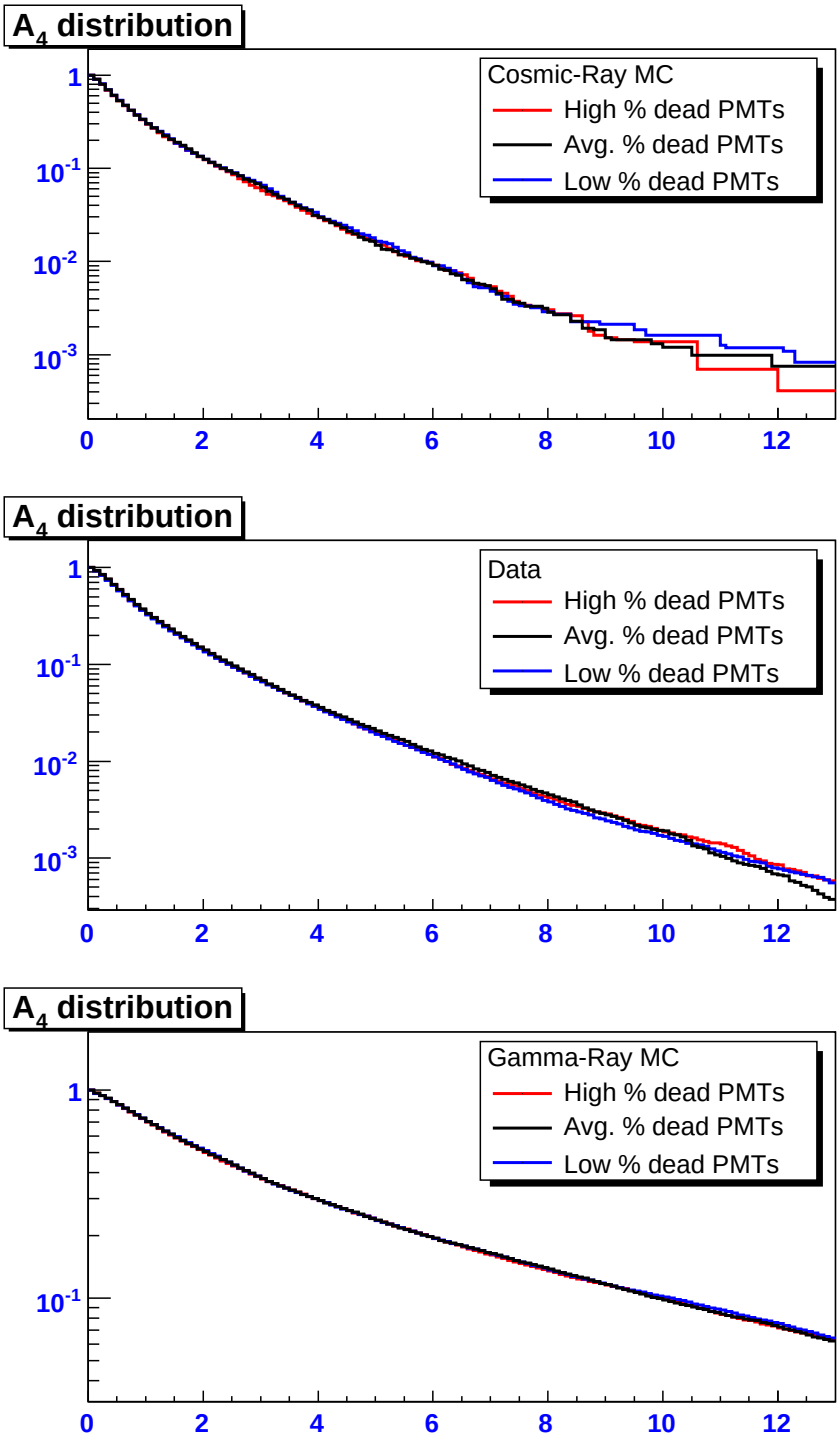

Figure 7.2: Same distributions as in figure 7.1 but with log-scale on the y-axis.

Pre Outrigger. Epochs 1-3												
Bin Number(i)	1	2	3	4	5	6	7	8	9	10	11	12
b_i^{min}	0.5	1.0	1.5	2.0	2.5	3.0	3.5	4.0	4.5	5.0	5.5	6.0
b_i^{max}	1.0	1.5	2.0	2.5	3.0	3.5	4.0	4.5	5.0	5.5	6.0	∞
Post Outrigger. Epochs 4-8												
Bin Number(i)	1	2	3	4	5	6	7	8	9	10	11	12
b_i^{min}	1	2	3	4	5	6	7	8	9	10	11	12
b_i^{max}	2	3	4	5	6	7	8	9	10	11	12	∞

Table 7.3: A_4 Bins. b_i^{min} and b_i^{max} represent the lower and upper edges of the A_4 bin, respectively (see section 6.2 and equation 6.1).

	Weights							
Bin No	E1	E2	E3	E4	E5	E6	E7	E8
1	1.00	1.00	1.00	1.00	1.00	1.00	1.00	1.00
2	2.38	2.25	1.87	2.10	2.07	1.83	1.34	1.47
3	4.60	4.08	2.82	3.69	3.43	2.70	1.62	1.72
4	8.26	7.11	4.12	5.96	5.11	3.98	1.64	2.22
5	13.08	11.23	5.51	10.72	7.17	5.26	2.01	2.43
6	20.28	16.25	6.78	15.32	9.45	6.92	2.08	2.91
7	29.27	22.04	7.76	17.25	15.93	11.13	2.81	3.70
8	42.12	27.18	7.96	21.74	20.15	14.81	3.47	4.88
9	49.72	37.51	8.92	23.88	30.90	20.72	4.56	5.67
10	51.83	35.34	6.66	22.44	45.75	30.91	5.48	6.50
11	72.23	55.35	8.02	23.95	62.71	45.31	6.87	8.54
12	116.17	97.32	10.50	44.22	100.33	116.02	8.24	10.25

Table 7.4: Gamma-hadron weights for the different epochs. In each epoch, the weights have been normalized to that of the first A_4 bin.

the pre outrigger data, A_4 is roughly half that for the post outrigger data, hence the different binning for the pre outrigger data.

Equation 6.2 was used to estimate the gamma-hadron weights for each epoch. As in section 6.2, the simulated gamma-ray Monte Carlo events were used to estimate the expected number of signal events in an A_4 bin ($\langle S_i \rangle$), while the data were used to estimate the number of background events in the same bin ($\langle B_i \rangle$). Table 7.4 lists the gamma-hadron weights for the eight epochs used in this analysis.

Epoch	E1	E2	E3	E4	E5	E6	E7	E8
Relative weight	1.00	1.05	1.04	2.38	2.24	2.33	2.23	2.22

Table 7.5: Relative epoch weights. The weights have been normalized to that of the first epoch (E1). For example, the eighth epoch gets 2.22 times more weight than the first epoch in this analysis.

7.3.1 Relative Epoch Weighting

The efficiency for detecting a gamma-ray event varies from one epoch to another. This efficiency depends on the reconstruction algorithms used, the detector configuration (number of dead PMTs), and the outriggers. It is thus necessary to take this into account when combining the different epochs. To account for this, the gamma-hadron weights in the first A_4 bin for each epoch were calculated and then normalized to that of the first epoch. This is shown in table 7.5

7.4 Determining the PSF Fits

For each A_4 bin in each epoch the PSF fits were calculated using the method described in section 6.3. Figures 7.3 and 7.4 show the Δ_{angle} distribution for the 12 A_4 slices for the last epoch for a Crab-like spectrum. The fit function is shown in black and the fit parameters are shown for each case. Table 7.7 shows the fit parameters for this epoch. Similar plots and tables for the other epochs are shown in Appendices B and C, respectively. For some of the bins in the earlier epochs the fit to a double 2D Gaussian function of the form given in equation 6.3 resulted in a poor fit and thus a one 2D Gaussian function was used:

$$F(r) = A\ r \times e^{(-r^2/2\sigma^2)} \tag{7.1}$$

where A is the amplitude, R is the ratio between the two parts of the 2D Gaussian, and r is Δ_{angle}. Although the error on the ratio R in some cases is of the same order as R itself, the fit to the function given is good as can be seen in the last column (χ^2/ndf) in each table.

To study the effect of different source spectra on the PSF of Milagro, different Δ_{angle} distributions as a function of A_4 for different spectral indices were generated and compared. Such distributions are shown in Appendix B for a -2.2 and -3.0 spectra. As can be seen from these plots, the Δ_{angle} distributions are similar in both cases and the fit parameters to a double 2D-Gaussian are very similar. Table 7.6 lists the fit parameters of Milagro's PSF for the two different source spectra ($\alpha = -2.2$ and $\alpha = -3.0$) for the different A_4 bins for the eighth epoch. The effective angular resolution of Milagro for the weighted analysis takes into account the different weights for different A_4 slices, and since different spectra will have different A_4 distributions, the effective angular resolution of the detector should be studied for different spectra to determine any changes. This has been done for four different source spectra,

	$\alpha = -2.2$			$\alpha = -3.0$		
Bin No	σ_1	σ_2	R	σ_1	σ_2	R
1	1.05 ± 0.03	0.52 ± 0.02	4.85	1.05 ± 0.03	0.56 ± 0.02	5.24
2	1.05 ± 0.04	0.51 ± 0.02	5.18	1.04 ± 0.07	0.57 ± 0.02	7.86
3	0.88 ± 0.04	0.49 ± 0.03	3.53	0.82 ± 0.03	0.48 ± 0.03	3.20
4	0.88 ± 0.04	0.37 ± 0.02	4.17	0.91 ± 0.06	0.45 ± 0.03	7.42
5	0.86 ± 0.07	0.43 ± 0.03	5.80	0.99 ± 0.14	0.49 ± 0.02	19.2
6	0.73 ± 0.06	0.37 ± 0.04	3.58	1.39 ± 0.29	0.45 ± 0.02	58.2

Table 7.6: A list of the fit parameters of Milagro's PSF for two different source spectra for the different A_4 bins for the eighth epoch.

$\alpha = -2.0, -2.4, -2.6,$ and -3.0. The effective angular resolutions for these spectra are shown in figure 7.5 and 7.6. As can be seen, the distributions look very similar and the fit parameters to a 2D Gaussian function are very similar in all cases. Therefore, the PSF of Milagro is independent of the spectral shape of the source for the A_4 weighted analysis.

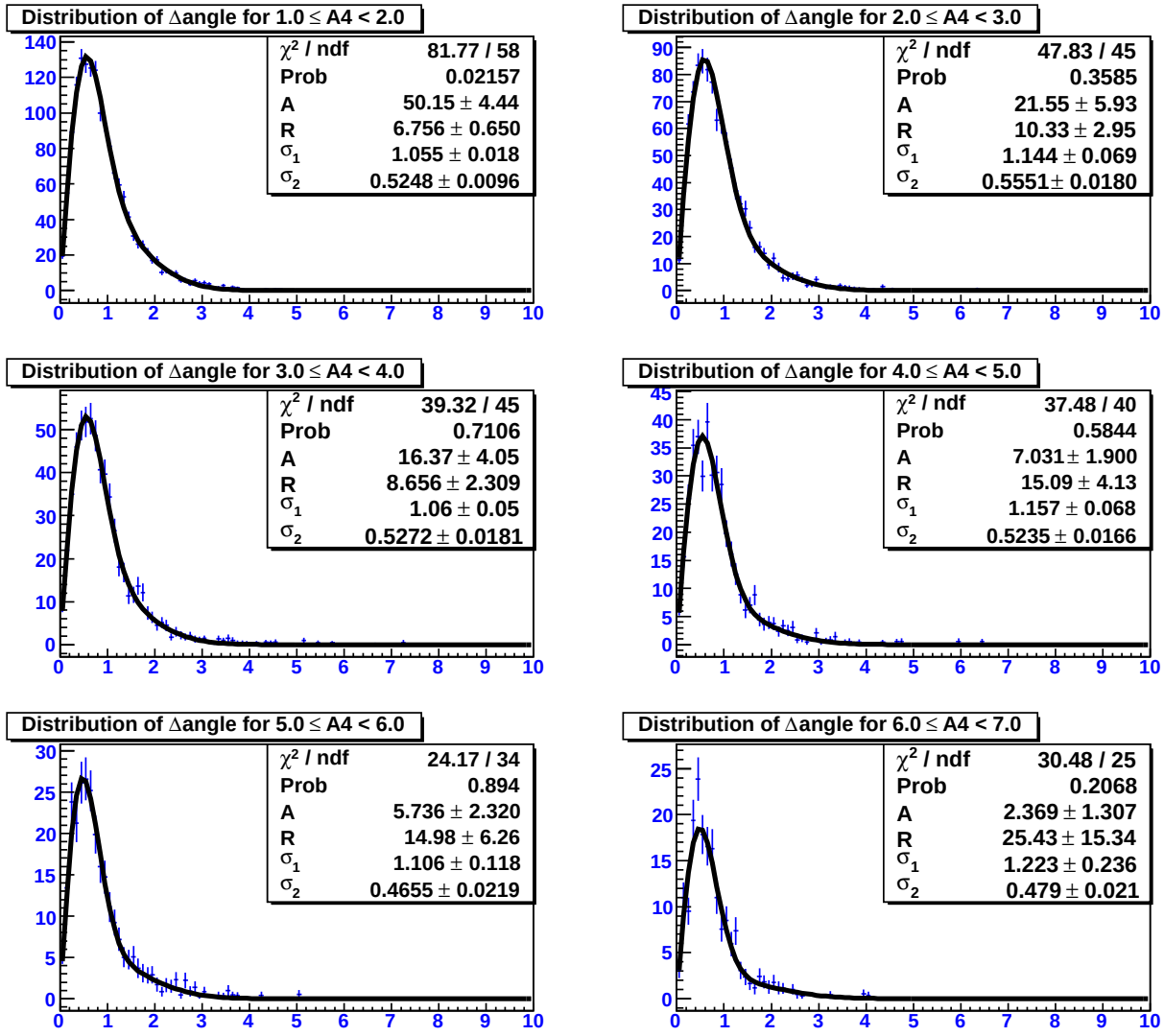

Figure 7.3: Δ_{angle} distributions and the corresponding PSF fits for the first six slices in A_4 for the eighth epoch for a Crab-like spectrum.

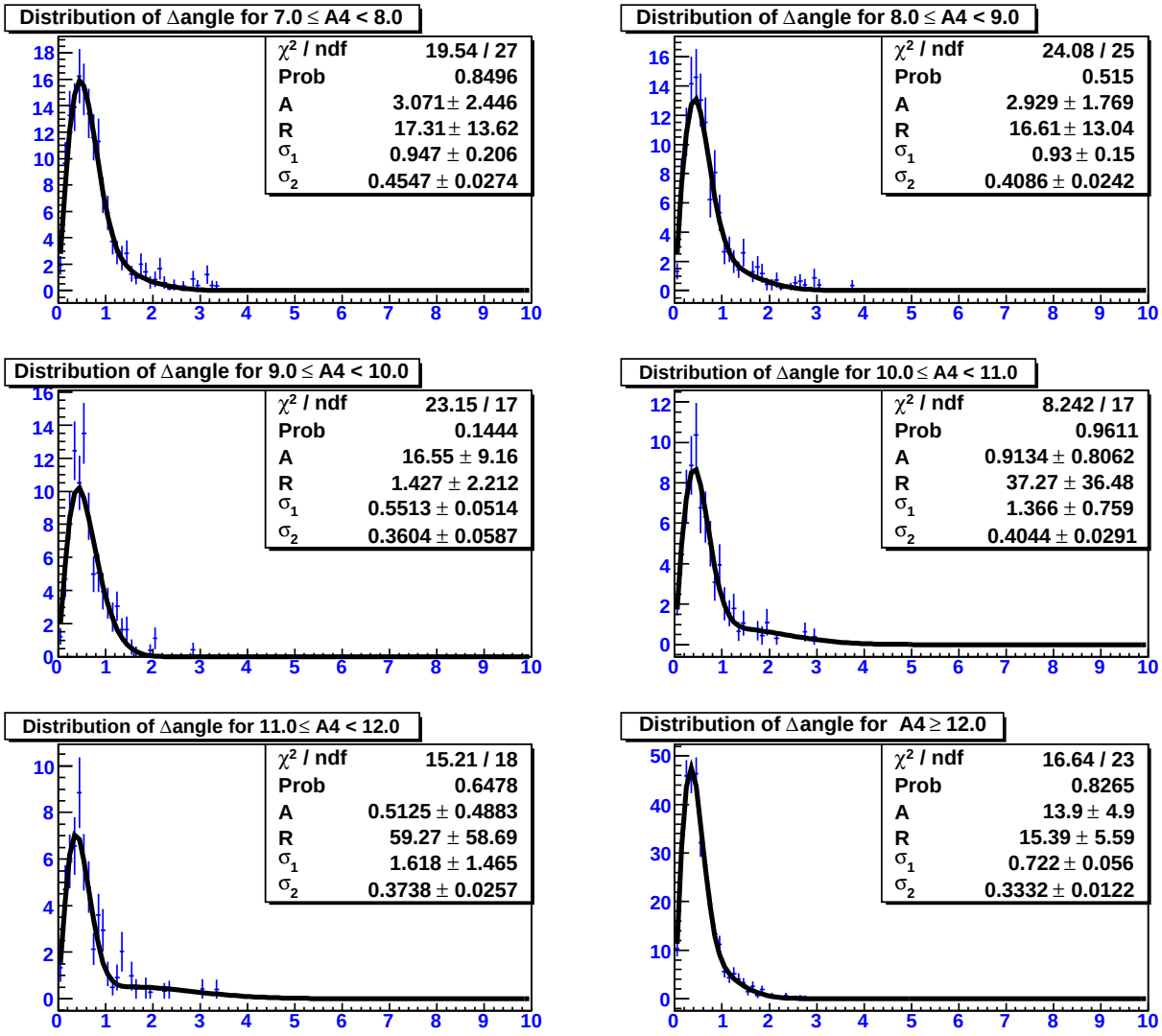

Figure 7.4: Δ_{angle} distributions and the corresponding PSF fits for the last six slices in A_4 for the eighth epoch for a Crab-like spectrum.

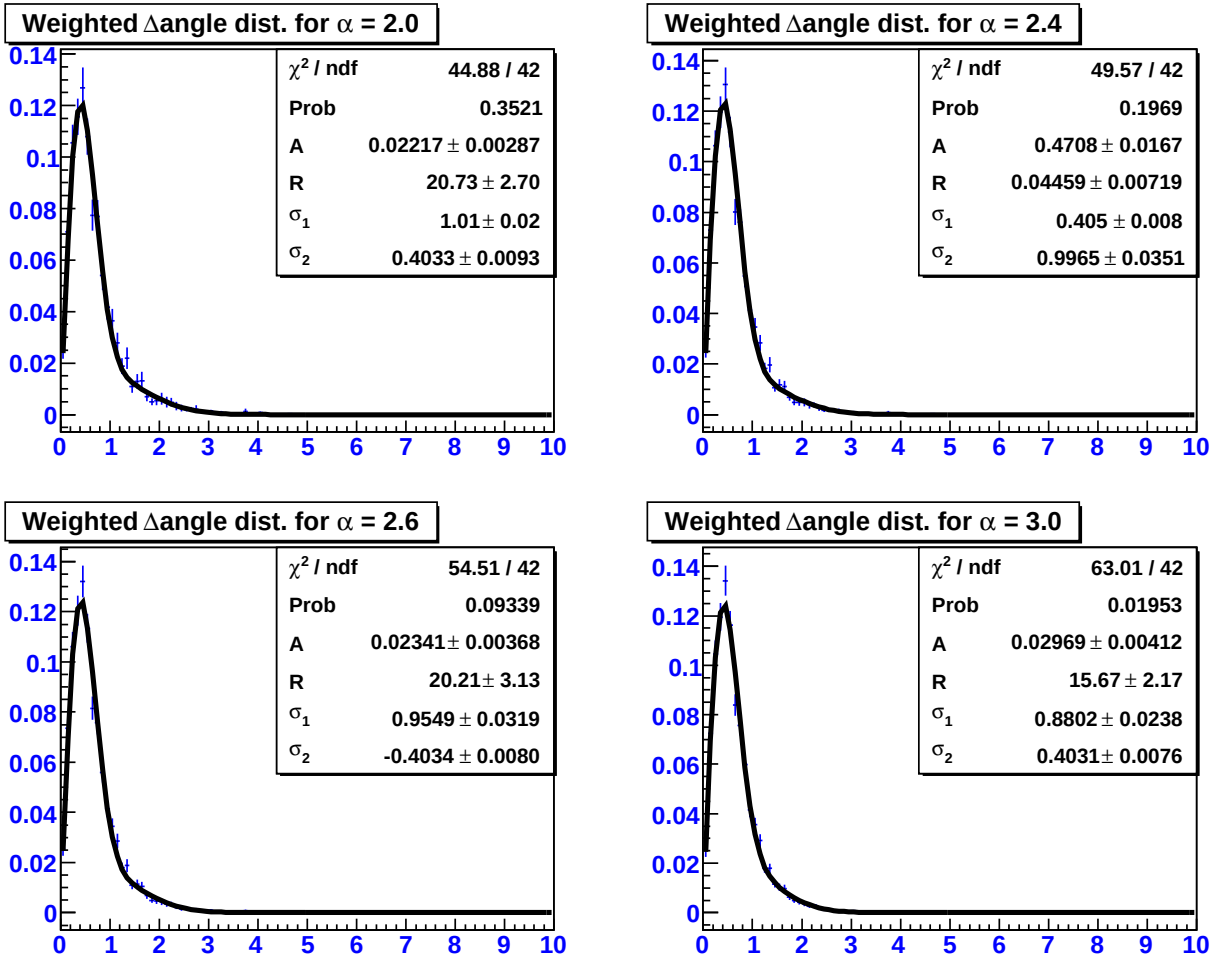

Figure 7.5: The effective Δ_{angle} distributions and the corresponding PSF fits for the weighted analysis for four different source spectra.

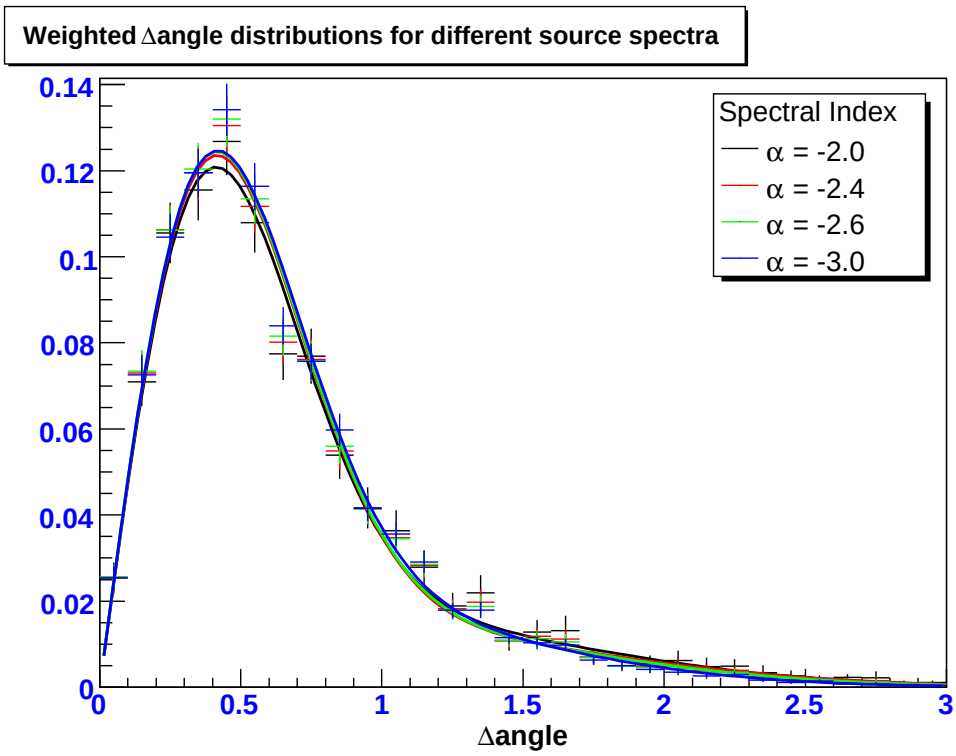

Figure 7.6: Same distributions as in figure 7.5 overlaid on the same plot. The lines represent in each case the fit to a double 2D Gaussian function.

Eight Epoch						
Bin No	Cuts	Amplitude (A)	Ratio (R)	σ_1	σ_2	χ^2/ndf
1	$1 \leq A_4 < 2$	50.15± 4.44	6.76± 0.65	1.06±0.02	0.52±0.01	81.8/58
2	$2 \leq A_4 < 3$	21.55± 5.93	10.33±2.95	1.14±0.07	0.56±0.02	47.8/45
3	$3 \leq A_4 < 4$	16.37± 4.05	8.66±2.31	1.06±0.05	0.53±0.02	39.3/45
4	$4 \leq A_4 < 5$	7.03± 1.90	15.09±4.13	1.16±0.07	0.52±0.02	37.5/40
5	$5 \leq A_4 < 6$	5.74± 2.32	14.98±6.26	1.11±0.12	0.47±0.02	24.2/34
6	$6 \leq A_4 < 7$	2.37±1.31	25.43±15.34	1.22±0.24	0.48±0.02	30.5/25
7	$7 \leq A_4 < 8$	3.07±2.45	17.31±13.62	0.95±0.21	0.46±0.03	19.5/27
8	$8 \leq A_4 < 9$	2.93± 1.77	16.61±13.04	0.93±0.15	0.41±0.02	24.1/25
9	$9 \leq A_4 < 10$	16.55± 9.16	1.43±2.21	0.55±0.05	0.36±0.06	23.2/17
10	$10 \leq A_4 < 11$	0.91± 0.80	37.27±36.48	1.37±0.76	0.40±0.03	8.2/17
11	$11 \leq A_4 < 12$	0.51± 0.49	59.27±58.69	1.62±1.46	0.37±0.03	15.2/18
12	$12 \leq A_4$	13.9± 4.9	15.39±5.59	0.72±0.06	0.33±0.01	16.6/23

Table 7.7: A list of the fit parameters for Milagro's PSF for the different A_4 bins for the eight epoch.

7.5 Flux Calculation

Fluxes from VHE gamma-ray sources typically have a power law spectrum (equation 1.1). The differential gamma-ray flux for a given source is defined as the number of photons from that source per unit area per unit energy per unit time. For a power law spectrum this is given by:

$$\frac{dN}{dE} = \phi_\circ \left(\frac{E}{E_\circ}\right)^{-\alpha} \tag{7.2}$$

where $\phi_\circ$ is the differential flux normalization, $E_\circ$ is the energy at which the flux is normalized, and α is the spectral index of the source.

It is customary to report the integral fluxes above some threshold energy, which is usually the median energy. The integral flux from a gamma-ray source is defined as the number of photons per unit area per unit time from that source, and is given by:

$$\begin{aligned} \phi &= \int_{E_t}^{E_c} \frac{dN}{dE} dE & (7.3)\\ &= \int_{E_t}^{E_c} \phi_\circ \left(\frac{E}{E_\circ}\right)^{-\alpha} dE & (7.4)\\ &= \left(\frac{\phi_\circ E_\circ}{1-\alpha}\right) \left[\left(\frac{E_c}{E_\circ}\right)^{1-\alpha} - \left(\frac{E_t}{E_\circ}\right)^{1-\alpha}\right] & (7.5) \end{aligned}$$

where E_t is the threshold energy, and E_c is some cut off energy in the spectrum of the source. In this analysis, all the fluxes are reported as integral fluxes above the median energy of this analysis which is 12 TeV, i.e. $E_t = 12$ TeV, and E_c is assumed to be 100 TeV.

To calculate the flux from a source it is necessary to take the effective area of the detector in consideration (see section 3.9). The number of events is given by:

$$N_\gamma = \int_{E_t}^{E_c} A_{eff}(E,\theta)\phi_\circ \left(\frac{E}{E_\circ}\right)^{-\alpha} dE \tag{7.6}$$

7.5.1 Flux Calculation for the A_4 Weighted Analysis Technique

To determine the flux from a gamma-ray source, the simulations are used to determine the number of Monte Carlo gamma-ray events per day as a function of declination. These numbers were obtained assuming a Crab-like spectrum of $dN/dE \propto E^{-2.62}$ and a flux at 1 TeV of 2.83×10^{-6} TeV^{-1}m^{-2}s^{-1}. This is done for all the A_4 bins in all eight epochs. This number is then multiplied by the gamma-hadron weights for each bin and the number of days in each epoch[3] and then summed to give a final total number of weighted events as a function of declination:

$$\omega(\delta) = \sum_{i=1}^{8}\sum_{j=1}^{12} N_\gamma^{ij}(\delta) \times \omega^{ij}(\gamma) \times N_{day}(i) \tag{7.7}$$

The first summation is over the number of epochs while the second summation is over the number of A_4 bins in each epoch, $N_\gamma^{ij}(\delta)$ is the number of gammas per day as a function of declination for the j'th A_4 bin in the i'th epoch. $\omega^{ij}(\gamma)$ is the gamma-hadron weight for the j'th A_4 bin in the i'th epoch, and $N_{day}(i)$ is the number of days in the i'th epoch.

This declination dependent weighted number of events, $\omega(\delta)$, is used to remove the declination dependence of the data excess map to give map in units of Crab flux:

$$\phi_c = \frac{\Delta(\delta)}{\omega(\delta)} \tag{7.8}$$

where ϕ_c is the flux in units of the Crab flux, and $\Delta(\delta)$ is the excess as a function of

[3]To correct for the instrumental dead time of $\sim$ 10%, the number of days in each epoch is multiplied by a factor of 0.9.

declination. To get the flux in units of $\mathrm{TeV}^{-1}\mathrm{m}^{-2}\mathrm{s}^{-1}\mathrm{sr}^{-1}$, a further normalization factor is needed:

$$\phi = \phi_c \times \frac{dN}{dE} d\Omega \tag{7.9}$$

The $d\Omega$ term is to give the flux in units of per steradian.

7.6 All-Sky Map

The A_4 weighted analysis technique was applied to six years of data (same as the data set mentioned in section 7.1). Figure 7.8 shows a TeV gamma-ray image of the northern hemisphere. The brightest extended region in the entire northern sky is the Cygnus Region of the Galactic plane located at roughly 300 degrees in Right Ascension and 35 degrees in Declination. The white lines show a ± 5 degree region around the Galactic plane. At each point the statistical significance of the observed excess (or deficit) is plotted.

Figure 7.7 shows the distribution of significances for the all sky map (in blue). The distribution of significances with the Crab Nebula, Markarian 421, and the Galactic Plane removed is shown in red. This distribution follows a Gaussian with a width of 0.997 and a mean of 0.001.

In the rest of this Chapter observations of known TeV gamma-ray sources will be presented. New sources that have been discovered will be discussed in the next Chapters.

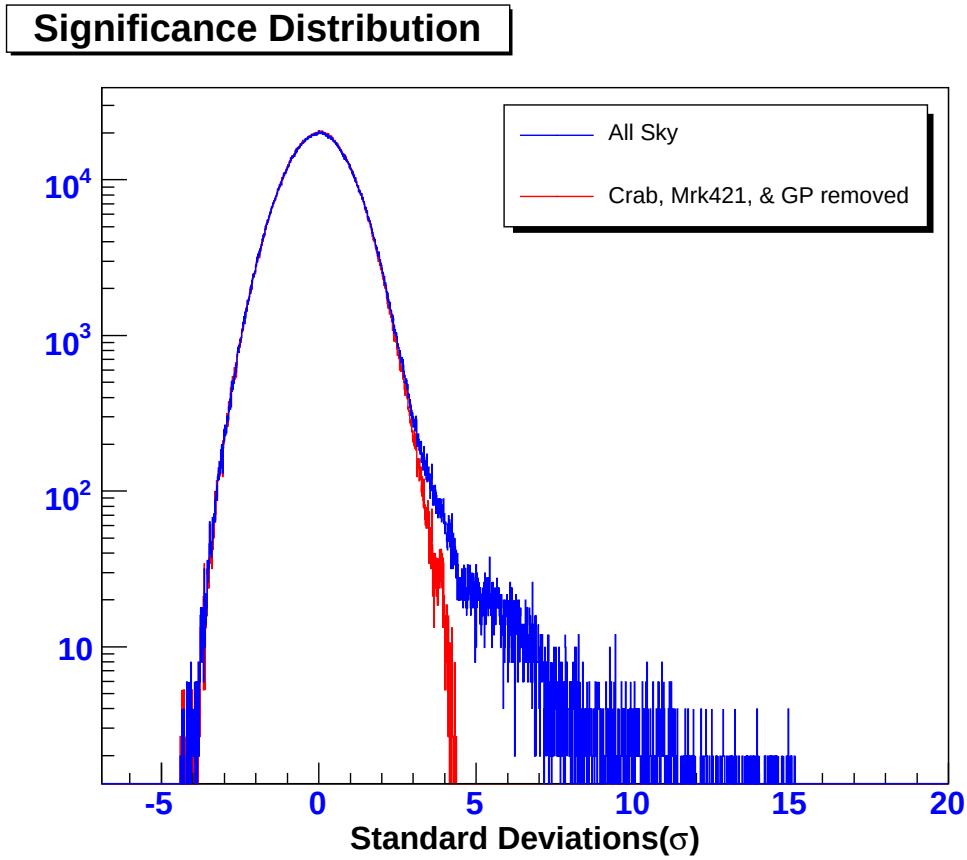

Figure 7.7: Distribution of significances.

7.6.1 Observations of the Crab Nebula

The most significant TeV gamma-ray source seen in figure 7.8 is the Crab Nebula, located at a Right Ascension of 83.63 degrees and a Declination of 22.01 degrees and visible at 15.2 standard deviations. Figure 7.9 shows a close up at the region around the Crab Nebula. The significance of the Crab in this data set is less than what one might expect by scaling the significance from the 1.7 years data set reported in section 5.4, namely $10.55 \times \sqrt{6.0/1.7} = 19.8$ standard deviations. This is due to the fact that the larger data set contains data with lower quality (no outriggers) than the 1.7 years data set.

The best fit location of the excess from the Crab Nebula is RA $= 83.60^\circ \pm 0.06^\circ_{stat}$, Dec $= 22.10^\circ \pm 0.05^\circ_{stat}$, with a Gaussian width of $\sigma = 0.38^\circ \pm 0.04^\circ_{stat}$. This is in very good agreement with the true location of the Crab Nebula[80], RA $= 83.63^\circ$, Dec $= 22.01^\circ$.

The flux from the Crab Nebula at 12 TeV is $(4.68 \pm 0.47_{stat} \pm 1.4_{sys}) \times 10^{-14}$ TeV^{-1} m^{-2}s^{-1} assuming a power law spectrum with spectral index $\alpha = -2.62$. This is consistent with the HEGRA flux at 12 TeV of [7] $(4.21 \pm 0.04_{stat} \pm 0.50_{sys}) \times 10^{-14}$ TeV^{-1}m^{-2}s^{-1}.

Although Milagro's estimate for the flux from the crab Nebula is consistent with those measured by ACTs to less than 30%, the cosmic-ray rate measured in Milagro is about 30% less than that measured by balloon experiments [30]. A conservative value of 30% for the systematic error on the flux is thus being applied in this analysis.

Table 7.8 lists the significances of the Crab Nebula for the different epochs. The first row gives the measured significance (Z), the second row gives the expected significance (Z_E), and the last row gives the deviation from the expected significance. As can be seen, there is a good agreement between the expected and measured significances in each case.

Epoch No	1	2	3	4	5	6	7	8
Significance (Z)	2.1	5.2	5.3	9.2	5.1	6.6	6.3	6.3
Expected Significance (Z_E)	2.4	4.7	4.9	8.9	4.9	6.5	6.3	6.0
$\lvert Z_E - Z\rvert / Z_E$	0.12	0.10	0.08	0.04	0.04	0.02	0.0	0.05

Table 7.8: Statistical significances of the Crab Nebula for the different epochs. The first row gives the measured significance (Z), the second row gives the expected significance (Z_E), and the last row gives the deviation from the expected significance.

7.6.2 Observations of the Active Galaxy Mrk421

One extragalactic source has been observed in this analysis. The active Galaxy Mrk421 has been observed at the level of 7.3 standard deviations in this analysis. Figure 7.10 shows a TeV gamma-ray image of the region around the active Galaxy Mrk421 for the six-year data set. The color scale is the statistical significance of the TeV gamma-ray excess at each point. The flux from Mrk421 at 12 TeV is $(3.9 \pm 0.8_{stat} \pm 1.2_{sys}) \times 10^{-14}$ TeV^{-1}m^{-2}s^{-1} assuming a power law spectrum with spectral index $\alpha = -2.62$. This amounts for 0.83 in Crab flux units. If a power law spectrum with spectral index $\alpha = -1.9$ is assumed, the flux from Mrk421 changes by $\sim 25\%$ to $(2.9 \pm 0.6_{stat} \pm 0.8_{sys}) \times 10^{-14}$ TeV^{-1}m^{-2}s^{-1}. This is the first observation of Mrk421 at such high energies.

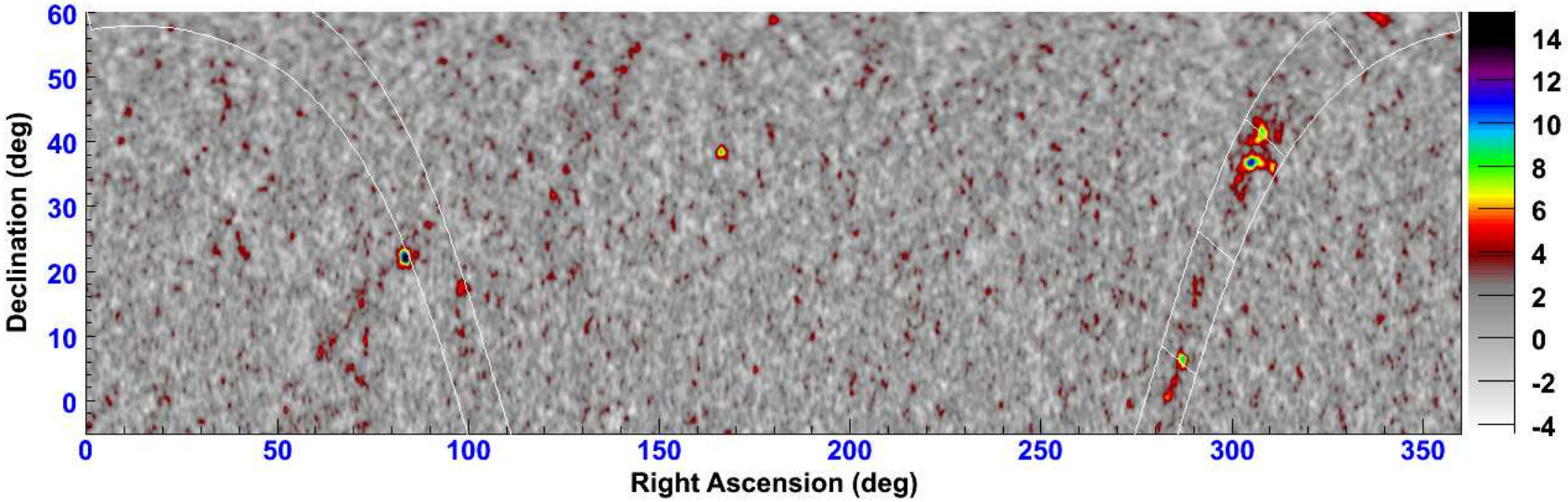

Figure 7.8: A TeV gamma-ray image of the northern hemisphere. The brightest extended region in the entire northern sky is the Cygnus Region of the Galactic plane located at roughly 300 degrees in Right Ascension and 35 degrees in Declination. The white lines show a ± 5 degree region around the Galactic plane. At each point the statistical significance of the observed excess (or deficit) is plotted. The most significant TeV gamma-ray source in the map is the Crab Nebula located at a Right Ascension of 83.6 and a Declination of 22 degrees and visible at 15.2 standard deviations.

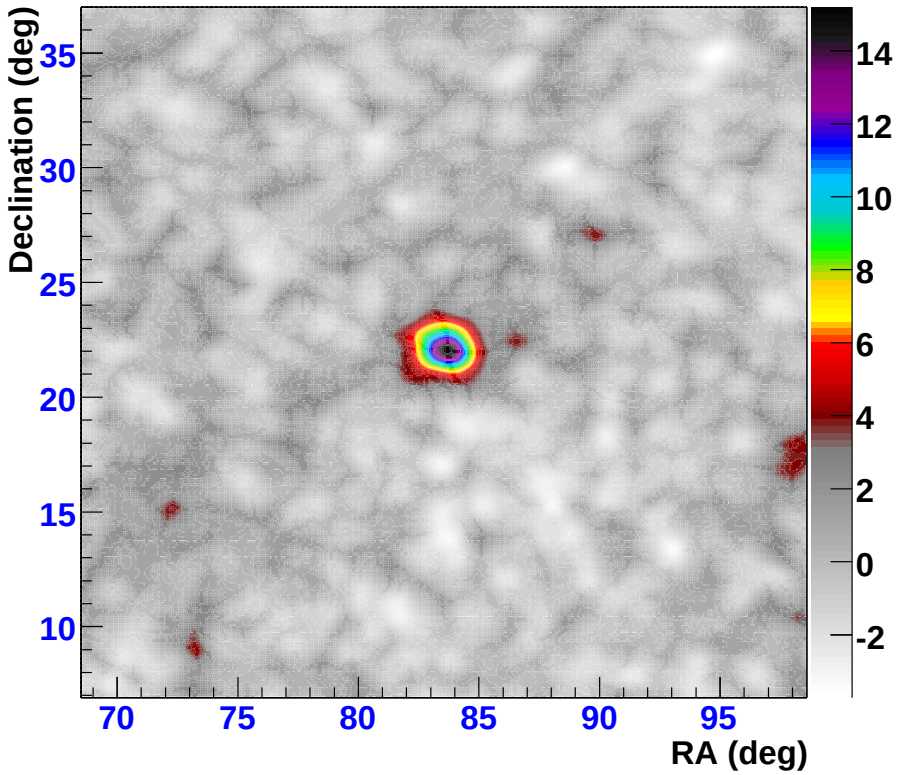

Figure 7.9: A TeV gamma-ray image of the region around the Crab nebula for the six-year data set. The color scale is the statistical significance of the TeV gamma-ray excess at each point. The significance at the location of the Crab nebula is 15.2 standard deviations. This significance is less than what one might expect by scaling the significance from the 1.7 years data set reported in section 5.4, namely $10.55 \times \sqrt{6.0/1.7} = 19.8$ standard deviations. This is due to the fact that the larger data set contains data with lower quality (no outriggers) than the 1.7 years data set.

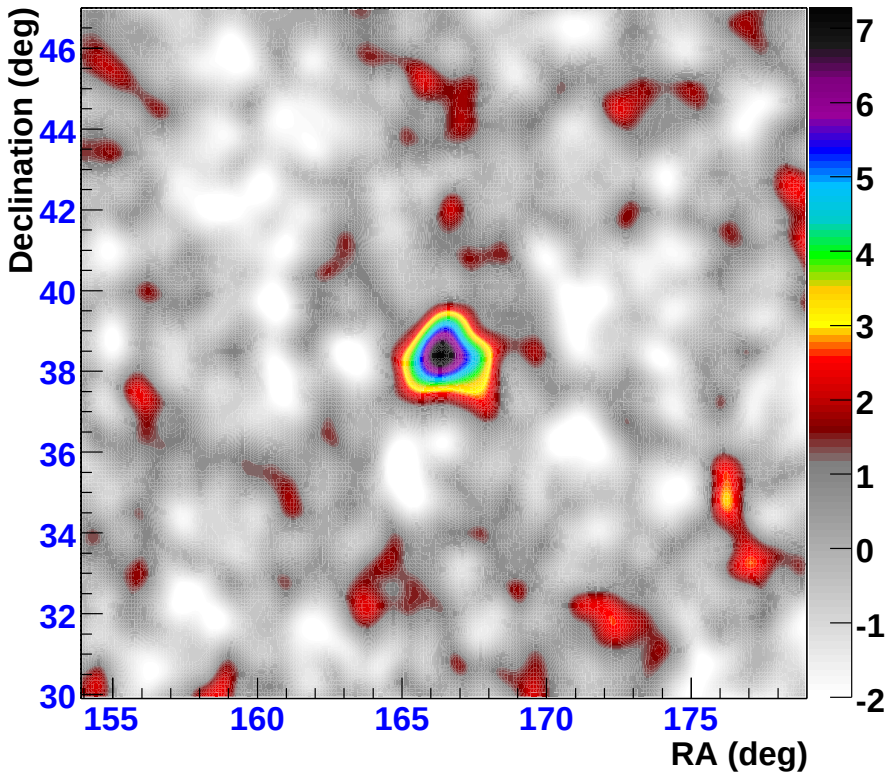

Figure 7.10: A TeV gamma-ray image of the region around the active Galaxy Mrk421 for the six-year data set. The color scale is the statistical significance of the TeV gamma-ray excess at each point. The significance at the location of Mrk421 is 7.3 standard deviations.

Chapter 8

Discovery of Localized TeV Gamma-Ray Sources in the Galactic Plane

As mentioned in the previous Chapter, the most prominent feature in the all-sky TeV gamma-ray map obtained in this analysis is the Galactic plane, which is clearly visible on the right side of figure 7.8. The same map is shown in Galactic coordinates in figure 8.1. Figure 8.2 shows a close up at the inner Galaxy visible to Milagro. This map shows a TeV gamma-ray emission from the Galactic plane in the region $l \in [30^\circ, 85^\circ]$ and $|b| < 5^\circ$. The significance of the TeV gamma-ray emission from this region ranges from 4.0 to 11.3 standard deviations. The brightest TeV emission comes from within the Cygnus region of the Galaxy defined by $l \in [65^\circ, 85^\circ]$ and $|b| < 3^\circ$. Moving to regions further away from the Galactic plane shows no significant TeV gamma-ray emission.

Emissions of TeV gamma-rays from nine regions in the Galactic plane have been observed in this work. Sources with a post-trials significance ≥ 5 standard deviations are considered as new sources. Sources with a post-trials significance < 5 and > 4

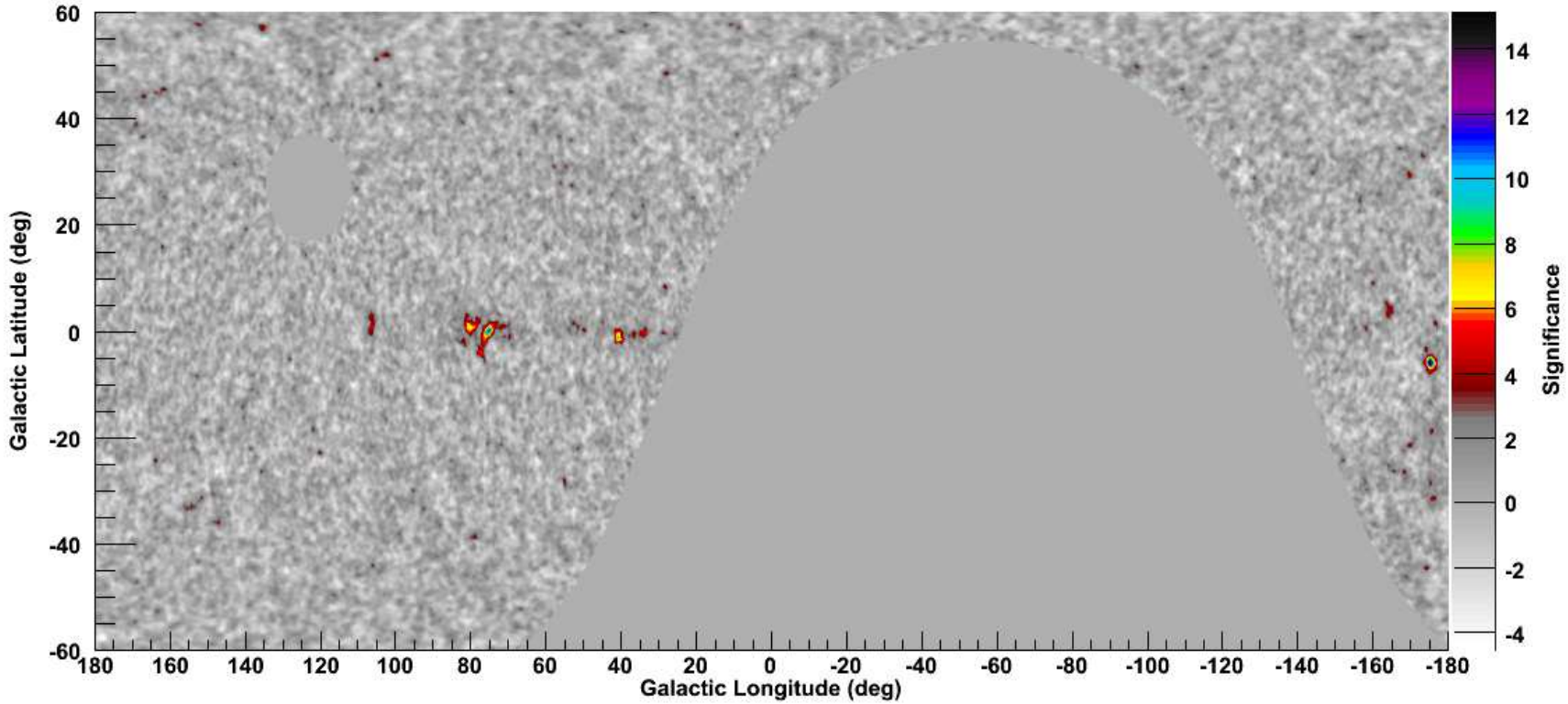

Figure 8.1: A TeV gamma-ray image of the northern hemisphere in Galactic coordinates. The large grey region is the part of the Galaxy that is obscured by the earth at the location of Milagro. The small grey region to the upper left of the figure is near the Zenith.

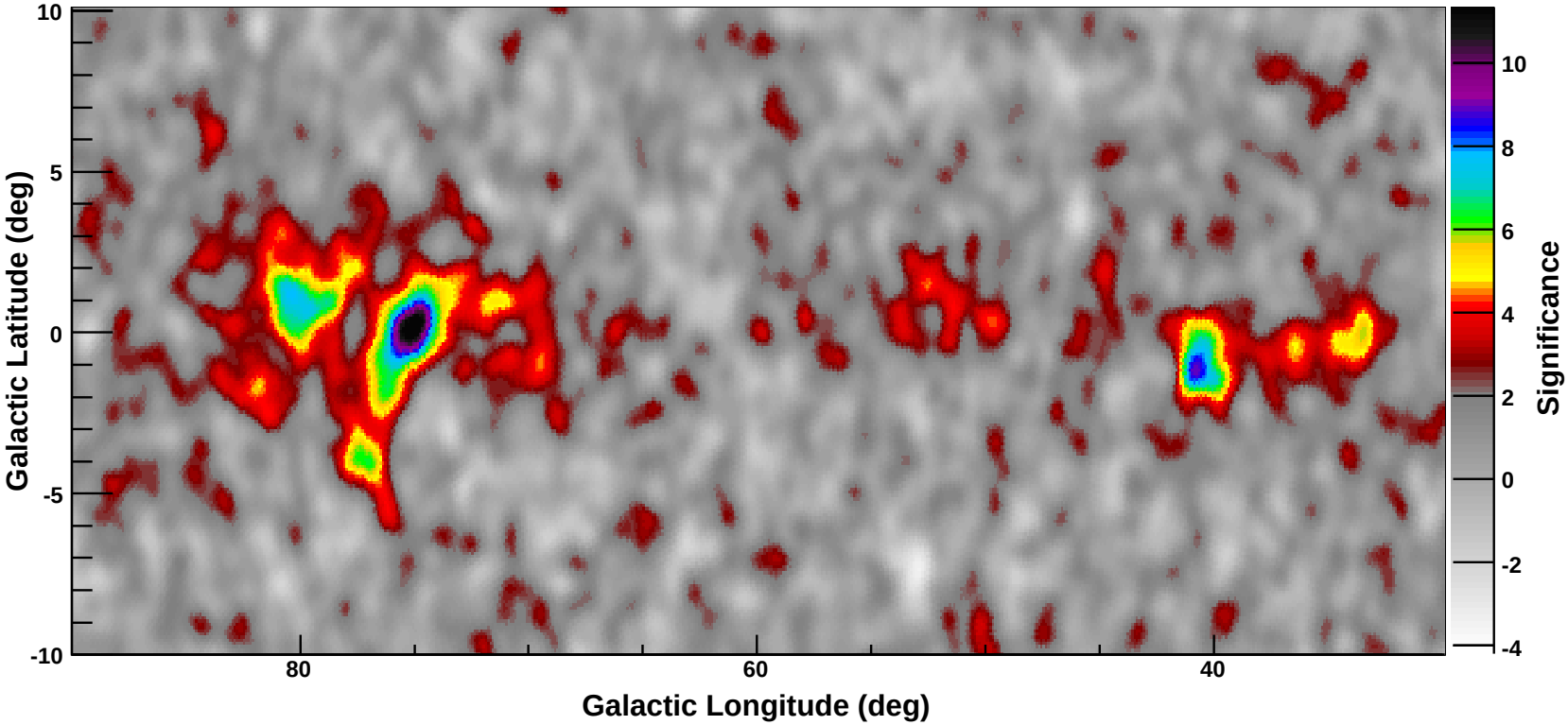

Figure 8.2: A TeV gamma-ray image of the Inner Galaxy visible to Milagro. The Galactic Center is toward the right. The Galactic Center is not visible from the location of Milagro.

standard deviations are considered as candidate sources.

8.1 Discovery of the TeV Gamma-Ray Source MGRO J2019+37

Figure 8.3 shows a close up at the Cygnus region of the Galaxy. The brightest TeV gamma-ray emission comes from Galactic Longitude 75 degrees and Galactic latitude 0.3 degrees. Observed at 11.3 standard deviations (10.2 post-trials [1]), this new TeV gamma-ray source is the second brightest source of TeV gamma-ray emission (after the Crab nebula) in the northern hemisphere. The statistical significance of this source is ~ 6 standard deviations above the diffuse TeV gamma-ray emission in the region. The new source is given the name **MGRO J2019+37**, where MGRO is for Milagro, the rest of the name gives the location of the source in equatorial coordinates; J2019 is the right ascension of the source in hour angle with reference to the J2000 epoch, and 37 is the declination of the source. This naming convention will be applied for all the newly discovered sources which will be presented in the coming sections.

8.1.1 Location of MGRO J2019+37

The location of MGRO J2019+37 is R.A.$= 304.83 \pm 0.14_{stat} \pm 0.3_{sys}$ degrees and Dec.$= 36.83 \pm 0.08_{stat} \pm 0.3_{sys}$, which, in Galactic coordinates, is equal to $l = 75.0 \pm 0.1_{stat} \pm 0.3_{sys}$ degrees and $b = 0.39 \pm 0.1_{stat} \pm 0.3_{sys}$ degrees. The systematic error is a combination of the 0.07 degree uncertainty in the location of the Crab Nebula as seen in this analysis, the uncertainties due to the unknown source morphology, and the uncertainties due to the diffuse background in the Cygnus region. The uncertainty

[1] The post-trials significance was calculated from the significance measured (pre-trials) by converting this pre-trials significance into a probability ($p_\circ$), recalculating the probability of the occurrence of one or more such events given the number of trials N_t, ($p = p_\circ \times N_t$), and converting this probability back into a significance. The number of trials for the scanned region of the Galactic plane is 95000 trials.

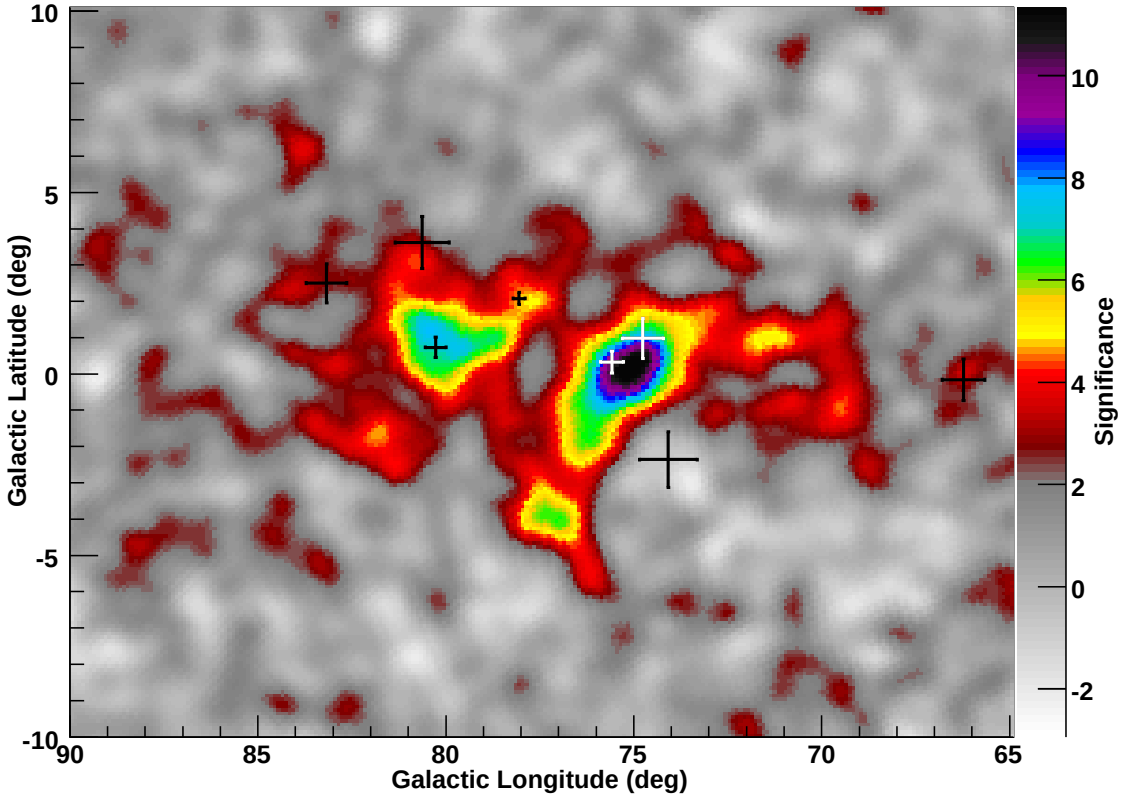

Figure 8.3: The Cygnus Region of the Galaxy as seen in TeV gamma rays. The color scale is the statistical significance of the TeV gamma-ray excess at each location. Since the Milagro exposure and sensitivity are roughly constant over the region in the figure, the statistical significance is nearly proportional to the flux from each point. The crosses show the location of EGRET sources and their corresponding location errors.

in the location of the Crab is used to adjust the absolute pointing of Milagro in this analysis [1].

A definitive understanding of this new TeV source requires further multi-wavelength observations of this source. The location of MGRO J2019+37 is consistent (within the combined location errors of EGRET and Milagro) with 2 EGRET sources (black and blue circles in figure 8.4). One of the EGRET sources (3EG J2016+3657) is coincident with the blazar-like source of unknown redshift[55], B2013+370. The location of MGRO J2019+37 is also coincident with the GeV source GeV J2020+3658 [43] which is associated with the young pulsar wind nebula [35](PWN) G75.2+0.1. An analysis of the highest energy photons (>1 GeV) observed by EGRET from this region indicates that the two EGRET sources were not resolved by EGRET. This analysis gives a median energy of 12 TeV. Given this, a blazar-like source is less likely since such high energy gamma-rays are attenuated by interactions with the extragalactic infrared background light.

8.1.2 Spatial Morphology of MGRO J2019+37

To study the spatial morphology of the newly discovered sources a subset of the data which contains the highest energy events was used. In this "high energy" data set, a cut on N_{fit} of 150 was applied. In addition, only events with $A_4 > 3.0$ were included. Using these data, the Monte Carlo predicts an angular resolution of 0.3°. An examination of the arrival directions of the higher-energy photons shows that MGRO J2019+37 is most likely an extended source or multiple unresolved sources of TeV gamma rays as seen in figures 8.4 and 8.5. Fitting the excess from the source to a circular 2-D Gaussian gives a width [2] of $\sigma = 0.32 \pm 0.12$ degrees[71]. If an elliptical 2-D Gaussian fit is used instead, the extent in the R.A. direction is ~ 2 times large than the extent in the Dec. direction. Figure 8.5 shows the radial distribution of

[2] After accounting for the width of the Crab nebula which is a point source in our PSF.

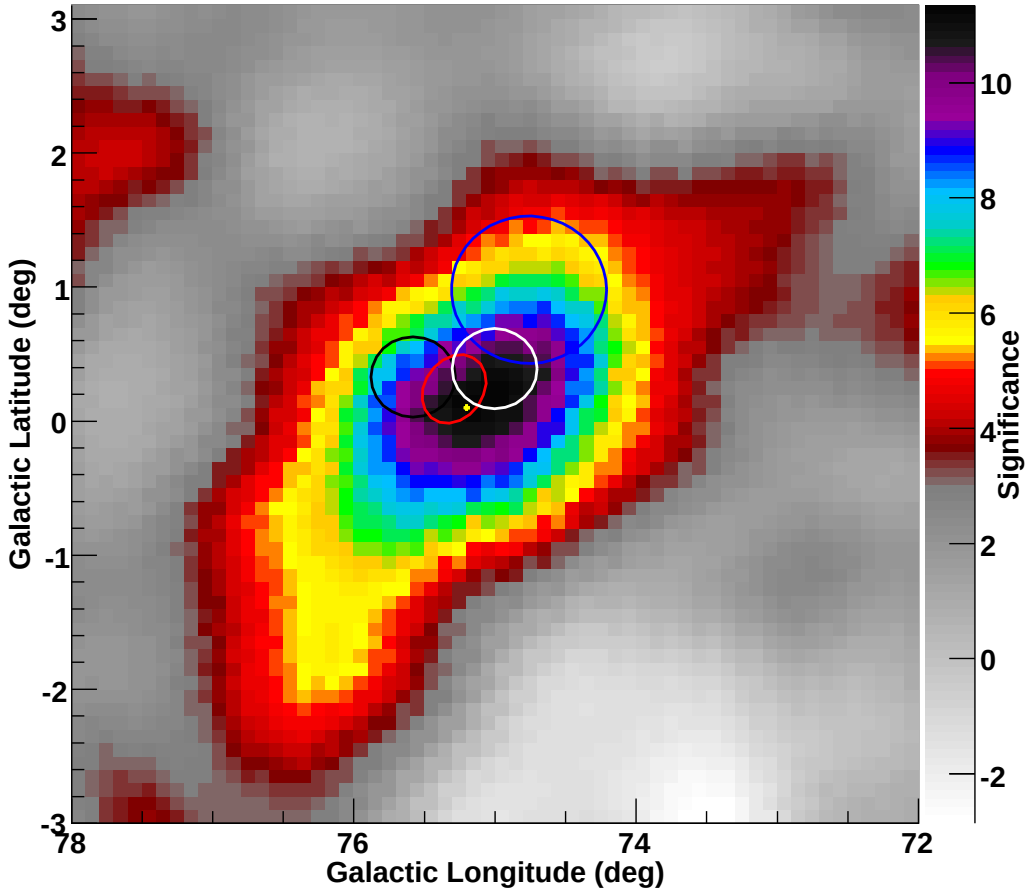

Figure 8.4: A TeV gamma-ray image of the area around the new source MGRO J2019+37. The location and location error of the source is marked by the white circle. Locations and location errors of the two EGRET source (3EGJ2016+3657 and 3EG J2021+3716) are marked by blue and black circles, respectively. The location and location error of the GeV source GeV J2020+3658 is marked by the red ellipse. This GeV source is associated with the PWN G75.2+0.1 shown in this map as a yellow dot.

excess events from the location around the Crab Nebula and MGRO J2019+37. The extent of MGRO J2019+37 is clearly visible here in comparison to the Crab Nebula.

To determine the source radius, the distance to the source should be determined. Unfortunately, Milagro's current capabilities don't allow for such a measurement and some assumptions have to be made about the source distance. The Cygnus Region lies at a distance of 1-2 kpc from the solar system. If MGRO J2019+37 lies within this region, it would have a source radius of 4-15 pc. If, on the other hand, MGRO J2019+37 is associated with the PWN G75.2+0.1, which is at a distance of 8-12 pc [60], then this source would have a source radius of 30-90 pc.

8.1.3 Flux from MGRO J2019+37

To estimate the flux from this source, the excess from a 3×3 square degree bin centered at the location of MGRO J2019+37 is used. Assuming a differential source spectrum[3] of $E^{-2.6}$, the flux from this region is given by $E^2 dN/dE = (3.49 \pm 0.47_{stat} \pm 1.05_{sys}) \times 10^{-12}$ TeV cm^{-2} s^{-1} at the median detected energy of 12 TeV.

[3]At the present time, an assumption has to be made about the spectral shape of a source. A new technique for measuring the spectral shape of a source in Milagro is being developed. See Appendix A for more details.

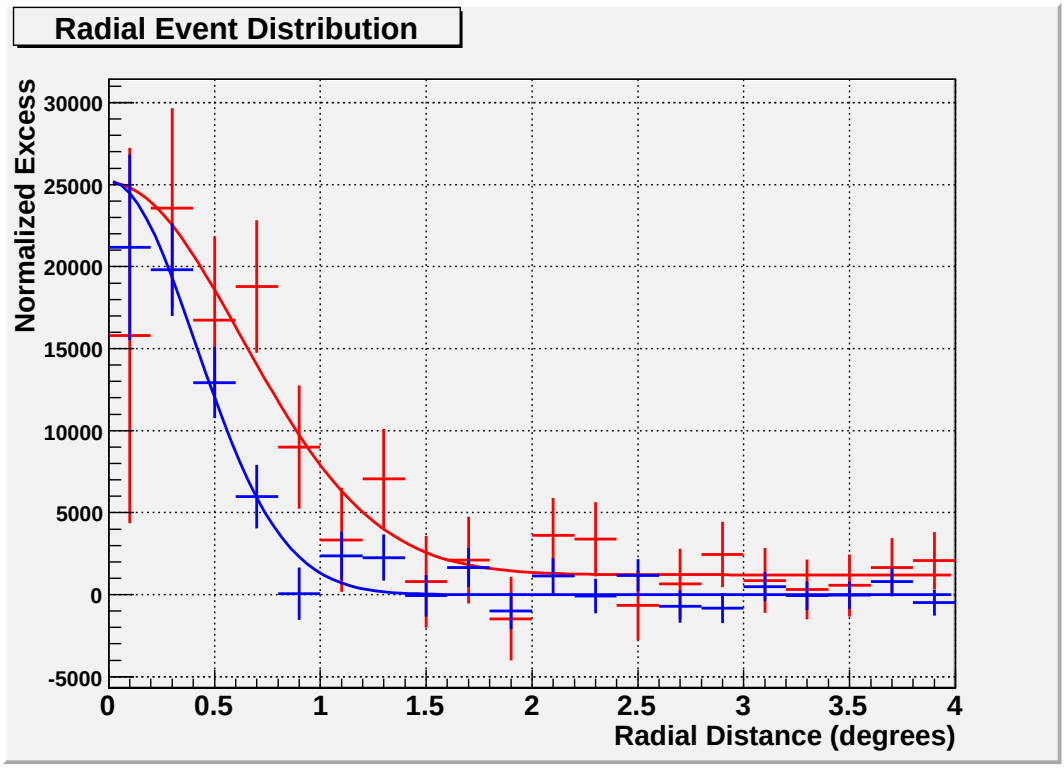

Figure 8.5: The radial distribution of excess events from the location around the Crab Nebula (blue) and MGRO J2019+37 (red). The extent of MGRO J2019+37 is clearly visible here in comparison to the Crab Nebula [1].

8.2 Discovery of the TeV Gamma-Ray Sources MGRO J2033+42 & MGRO J2031+41

Another TeV gamma-ray source has also been discovered in the Cygnus region. MGRO J2033+42 is the next brightest source in the Cygnus region after MGRO J2019+37. At 7.1 standard deviations (5.2 post-trials), this is a new source of TeV gamma-rays in this region. This source is located at $l = 80.4 \pm 0.4_{stat} \pm 0.3_{sys}$ degrees and $b = 1.2 \pm 0.3_{stat} \pm 0.3_{sys}$ degrees. MGRO J2033+42 is coincident with an EGRET source (3EG J2033+4118) and the HEGRA source TeV J2032+4130. In addition to this source, there appears to be another source at $l = 79.7 \pm 0.3_{stat} \pm 0.3_{sys}$ degrees and $b = 0.7 \pm 0.3_{stat} \pm 0.3_{sys}$. This source, MGRO J2031+41 is not coincident with any of the sources in the region including MGRO J2033+42. At 6.82 standard deviations (5.0 post-trials), this appears to be a separate source. Further detailed studies will be required to determine if this is an independent source.

Figure 8.6 shows a TeV gamma-ray image of the area around these sources. The flux from a region of 3×3 degrees centered at MGRO J2033+42 (which include MGRO J2031+41) is given by $E^2 dN/dE = (2.5 \pm 0.6_{stat} \pm 0.8_{sys}) \times 10^{-12}$ TeV cm^{-2} s^{-1} at the median detected energy of 12 TeV and assuming a differential source spectrum of $E^{-2.6}$.

The HEGRA source was detected in the energy range of 1-10 TeV with a differential photon spectral index of $-1.9 \pm 0.1_{stat} \pm 0.3_{sys}$ [6]. When extrapolated to energies at 12 TeV, the flux from this source is given by $E^2 dN/dE = (7.9 \pm 2.7_{stat}) \times 10^{-13}$ TeV cm^{-2} s^{-1}. The flux from a 3×3 square degrees area centered at the HEGRA source as measured by Milagro at 12 TeV and assuming a differential source spectrum of $E^{-1.9}$ is given by $E^2 dN/dE = (1.73 \pm 0.4_{stat} \pm 0.52_{sys}) \times 10^{-12}$ TeV cm^{-2} s^{-1} which is higher than the HEGRA flux for this source. This may be due to the additional contribution from the diffuse emission to the flux in this

region.

8.3 Discovery of the TeV Gamma-Ray Source MGRO J1909+06

Another source that has been discovered in the Galactic plane is the new TeV gamma-ray source MGRO J1909+06. This source is located outside the Cygnus region and is closer to the Galactic center. The location of this source is $l = 40.5 \pm 0.1_{stat} \pm 0.3_{sys}$ degrees and $b = -1.0 \pm 0.1_{stat} \pm 0.3_{sys}$ degrees. At 8.2 standard deviations (6.7 post-trials), this new source is the second brightest source in the part of the inner Galaxy that is visible to Milagro after MGRO J2019+37. Figure 8.7 shows a TeV image of the area around this source. The location and location error of the source is marked by the white circle. The black circle shown in the same figure marks the location and location error of the GeV source GeV J1907+0557 is marked by the black ellipse[43].

The flux from a region of 3×3 degrees around this source is given by $dN/dE = (4.1 \pm 0.9_{stat} \pm 1.2_{sys}) \times 10^{-14}$ TeV^{-1} cm^{-2} s^{-1} at the median detected energy of 12 TeV and assuming a differential source spectrum of $E^{-2.6}$.

In addition to the four discovered sources, TeV gamma-ray emission from four more sources in the Galactic plane are observed with pre-trials significances above 4.5 standard deviations. The location and the flux estimates for these sources are given in the next sections.

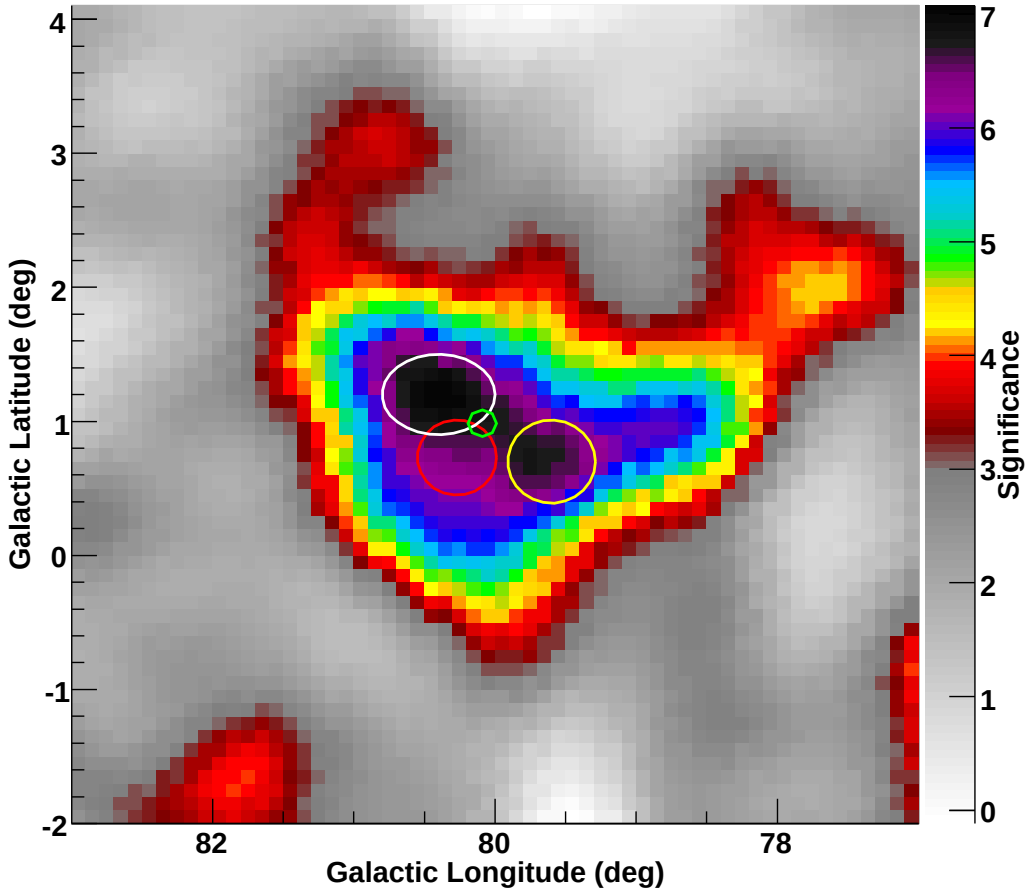

Figure 8.6: A TeV gamma-ray image of the area around the new sources MGRO J2033+42 and MGRO J2031+41. The location and location error of MGRO J2033+42 is marked by the white ellipse and the location and location error of MGRO J2031+41 is marked by the yellow circle. The Location of the EGRET source (3EG J2033+4118) is marked by the red circle, while the location of the HEGRA source (TeV J2032+4130) is marked by the green circle.

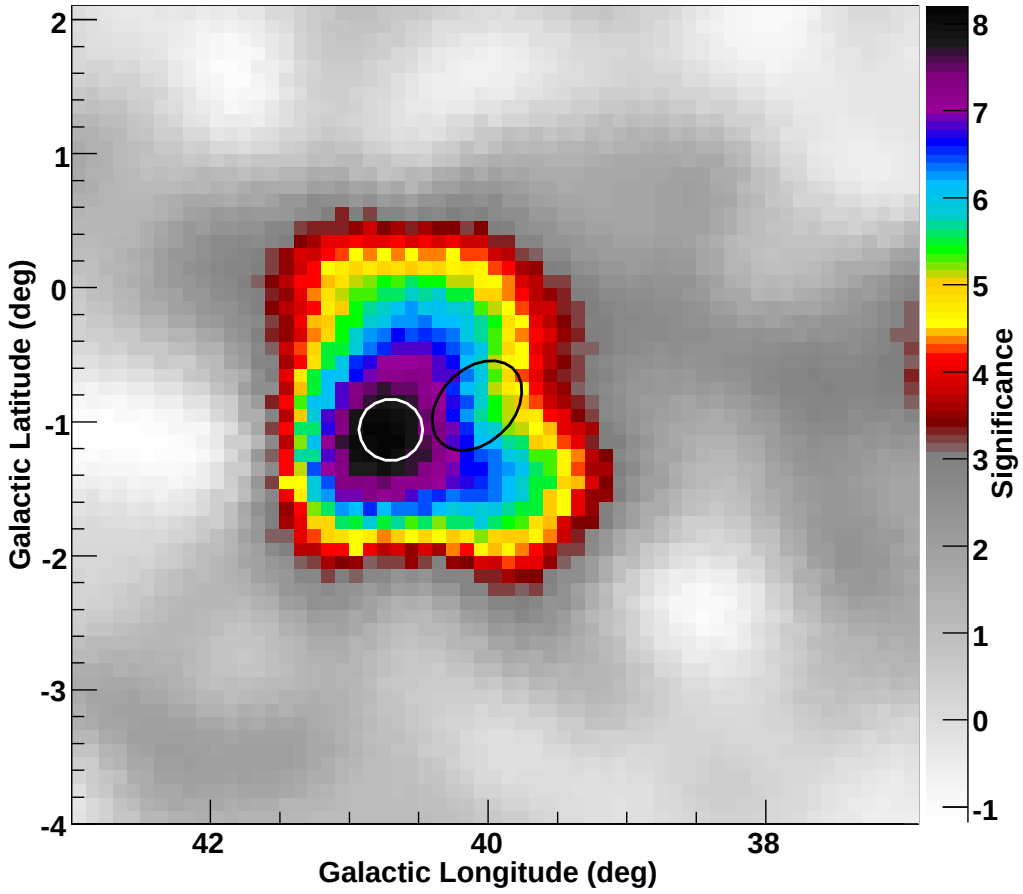

Figure 8.7: A TeV gamma-ray image of the area around the new source MGRO J1909+06. The location and location error of the source is marked by the white circle. The location and location error of the GeV source GeV J1907+0557 is marked by the black ellipse.

8.4 The TeV Gamma-Ray Source Candidate MGRO J2032+37

This TeV gamma-ray source candidate is observed at the level of 5.8 standard deviations pre-trials. A TeV gamma-ray image of the area around this source is shown in figure 8.8. The location of this source is $l = 76.3 \pm 0.1_{stat} \pm 0.3_{sys}$ degrees and $b = -1.9 \pm 0.2_{stat} \pm 0.3_{sys}$ degrees. The flux from this source is given by $dN/dE = (0.9 \pm 0.2_{stat} \pm 0.3_{sys}) \times 10^{-14}$ TeV^{-1} cm^{-2} s^{-1} at the median detected energy of 12 TeV and assuming a differential source spectrum of $E^{-2.6}$.

8.5 The TeV Gamma-Ray Source Candidate MGRO J2043+36

This TeV gamma-ray source candidate is observed at the level of 5.6 standard deviations pre-trials. A TeV gamma-ray image of the area around this source is shown in figure 8.9. The location of this source is $l = 77.2 \pm 0.2_{stat} \pm 0.3_{sys}$ degrees and $b = -4.0 \pm 0.2_{stat} \pm 0.3_{sys}$ degrees. The flux from this source is given by $dN/dE = (1.2 \pm 0.2_{stat} \pm 0.4_{sys}) \times 10^{-14}$ TeV^{-1} cm^{-2} s^{-1} at the median detected energy of 12 TeV and assuming a differential source spectrum of $E^{-2.6}$.

8.6 The TeV Gamma-Ray Source Candidates MGRO J1852+01 and MGRO J1859+03

This TeV gamma-ray source candidate is observed at the level of 5.1 standard deviations pre-trials. A TeV gamma-ray image of the area around this source is shown in figure 8.10. The location of this source is $l = 33.5 \pm 0.3_{stat} \pm 0.3_{sys}$ degrees and $b = 0.0 \pm 0.2_{stat} \pm 0.3_{sys}$ degrees and is marked by the white ellipse. The black circle in

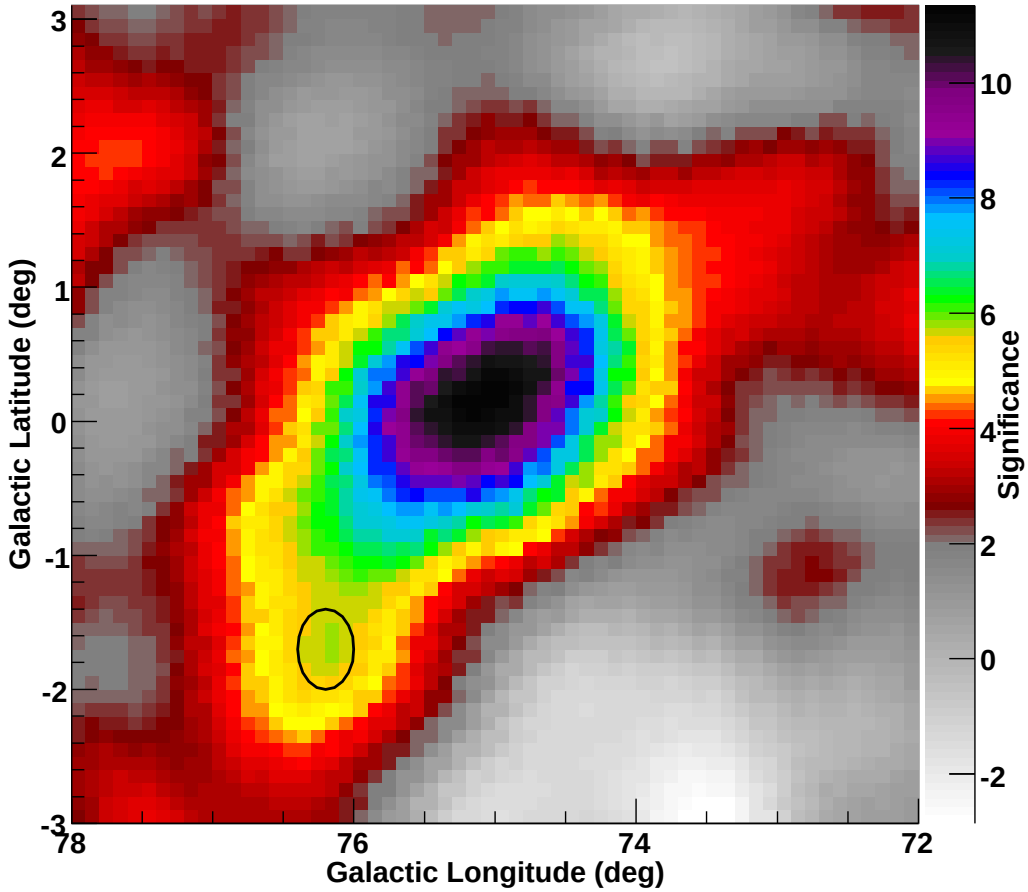

Figure 8.8: A TeV gamma-ray image of the area around the new source candidate MGRO J2032+37. The location and location error of the source is marked by the black ellipse. The black spot in the middle of the map is MGRO J2019+37.

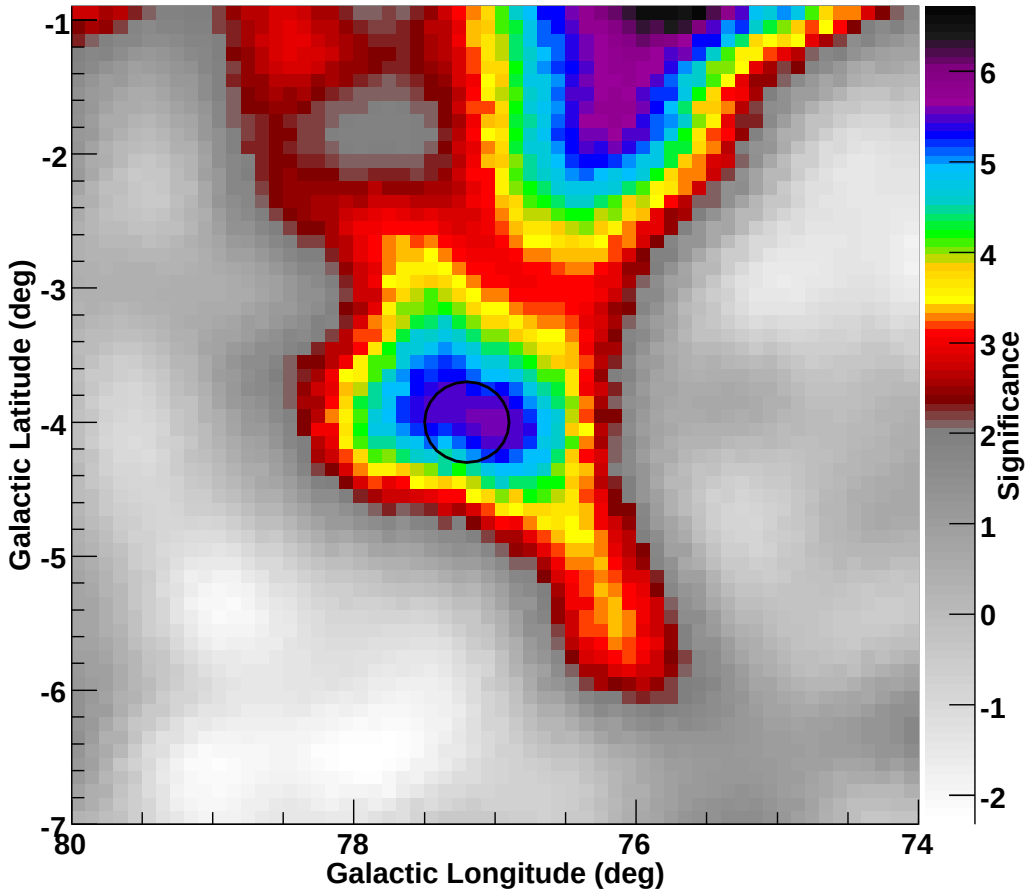

Figure 8.9: A TeV gamma-ray image of the area around the new source candidate MGRO J2043+36. The location and location error of the source is marked by the black circle.

the middle of the map marks the location and location error of the GeV sources GeV J1856+0115 [43]. In addition to MGRO J1852+01 there is another source candidate that is seen at he level of 4.1 standard deviations (pre-trials). This source candidate is given the name MGRO J1859+03 and is located at $l = 36.4 \pm 0.2_{stat} \pm 0.3_{sys}$ degrees and $b = -0.45 \pm 0.2_{stat} \pm 0.3_{sys}$.

The flux from a 3×3 squared degrees region around MGRO J1852+01 is given by $dN/dE = (5.7 \pm 1.5_{stat} \pm 1.9_{sys}) \times 10^{-14}$ TeV^{-1} cm^{-2} s^{-1} at the median detected energy of 12 TeV and assuming a differential source spectrum of $E^{-2.6}$. While the flux from a 3×3 squared degrees region around MGRO J1859+03 is given by $dN/dE = (4.6 \pm 1.2_{stat} \pm 1.4_{sys}) \times 10^{-14}$ TeV^{-1} cm^{-2} s^{-1} at the same median energy and assuming the same spectrum.

8.7 The TeV Gamma-Ray Source Candidate MGRO J2233+60

This TeV gamma-ray source candidate is observed at the level of 5.1 standard deviations pre-trials. A TeV gamma-ray image of the area around this source is shown in figure 8.11. The location of this source is $l = 106.4 \pm 0.5_{stat} \pm 0.3_{sys}$ degrees and $b = 1.7 \pm 0.8_{stat} \pm 0.3_{sys}$ degrees. The flux from this source is given by $dN/dE = (1.0 \pm 0.4_{stat} \pm 0.3_{sys}) \times 10^{-14}$ TeV^{-1} cm^{-2} s^{-1} at the median detected energy of 12 TeV and assuming a differential source spectrum of $E^{-2.6}$.

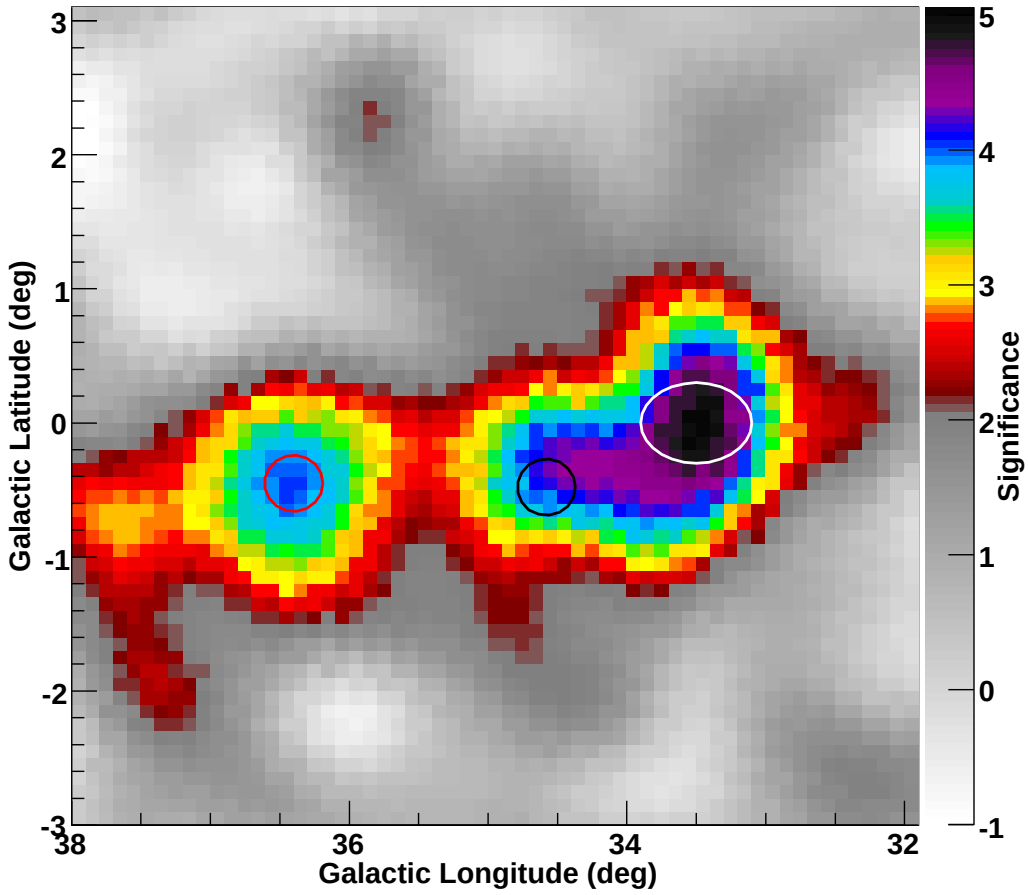

Figure 8.10: A TeV gamma-ray image of the area around the new source candidate MGRO J1852+01. The location and location error of MGRO J1852+01 is marked by the white ellipse. The location and location error of MGRO J1859+03 is marked by the red circle. The black circle in the middle of the map marks the location and location error of the GeV sources GeV J1856+0115 [43]

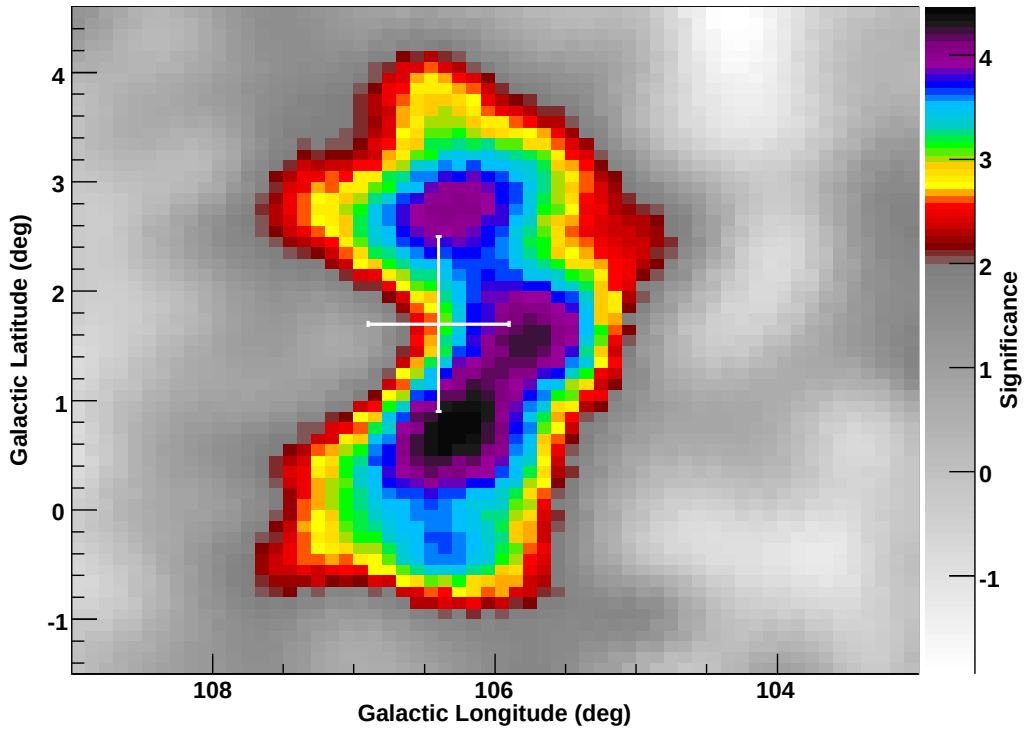

Figure 8.11: A TeV gamma-ray image of the area around the new source candidate MGRO J2033+60. The location of the source is marked by the white cross.

8.8 Milagro TeV Gamma-Ray Source Catalog

The newly discovered TeV gamma-ray sources and the candidate sources are cataloged in Table 8.1. Listed in this catalog are the names, locations (in Galactic coordinates), pre-trials significances, and fluxes for all the sources that have been observed with pre-trials significance > 4.5 standard deviations. Only sources with post-trial significances > 5.0 standard deviations are considered as sources while sources with post-trial significances < 5.0 standard deviations are considered source candidates. Figure 8.12 shows Milagro's TeV gamma-ray sources and source candidates. The numbers show the pre-trials significance for each source.

Object	Location (l, b)	Significance (std. dev.)	Flux ($\times 10^{-14}$) ($\mathrm{TeV}^{-1}\ \mathrm{cm}^{-2}\ \mathrm{s}^{-1}$)
MGRO J2019+37	$(75.1 \pm 0.1, 0.3 \pm 0.1)$	11.3	$2.4 \pm 0.4 \pm 0.8$
MGRO J1909+06	$(40.5 \pm 0.1, -1.0 \pm 0.1)$	8.2	$4.2 \pm 0.9 \pm 1.2$
MGRO J2033+42	$(80.4 \pm 0.4, 1.0 \pm 0.3)$	7.1	$1.7 \pm 0.4 \pm 0.5$
MGRO J2031+41	$(79.7 \pm 0.3, 0.7 \pm 0.3)$	6.8	
MGRO J2032+37	$(76.3 \pm 0.1, -1.9 \pm 0.2)$	5.8	$0.9 \pm 0.2 \pm 0.3$
MGRO J2043+36	$(77.2 \pm 0.2, -4.0 \pm 0.2)$	5.6	$1.2 \pm 0.2 \pm 0.4$
MGRO J1852+01	$(33.5 \pm 0.3, 0.0 \pm 0.2)$	5.1	$5.7 \pm 1.5 \pm 1.9$
MGRO J2233+60	$(106.4 \pm 0.5, 1.7 \pm 0.8)$	4.5	$1.0 \pm 0.4 \pm 0.3$

Table 8.1: Milagro TeV gamma-ray source catalog. A 0.3 degrees systematic error applies to the location of each source. The significances reported are pre-trials significances. The fluxes are given at the median energy of this analysis, 12 TeV and assuming a differential source spectrum of $E^{-2.6}$.

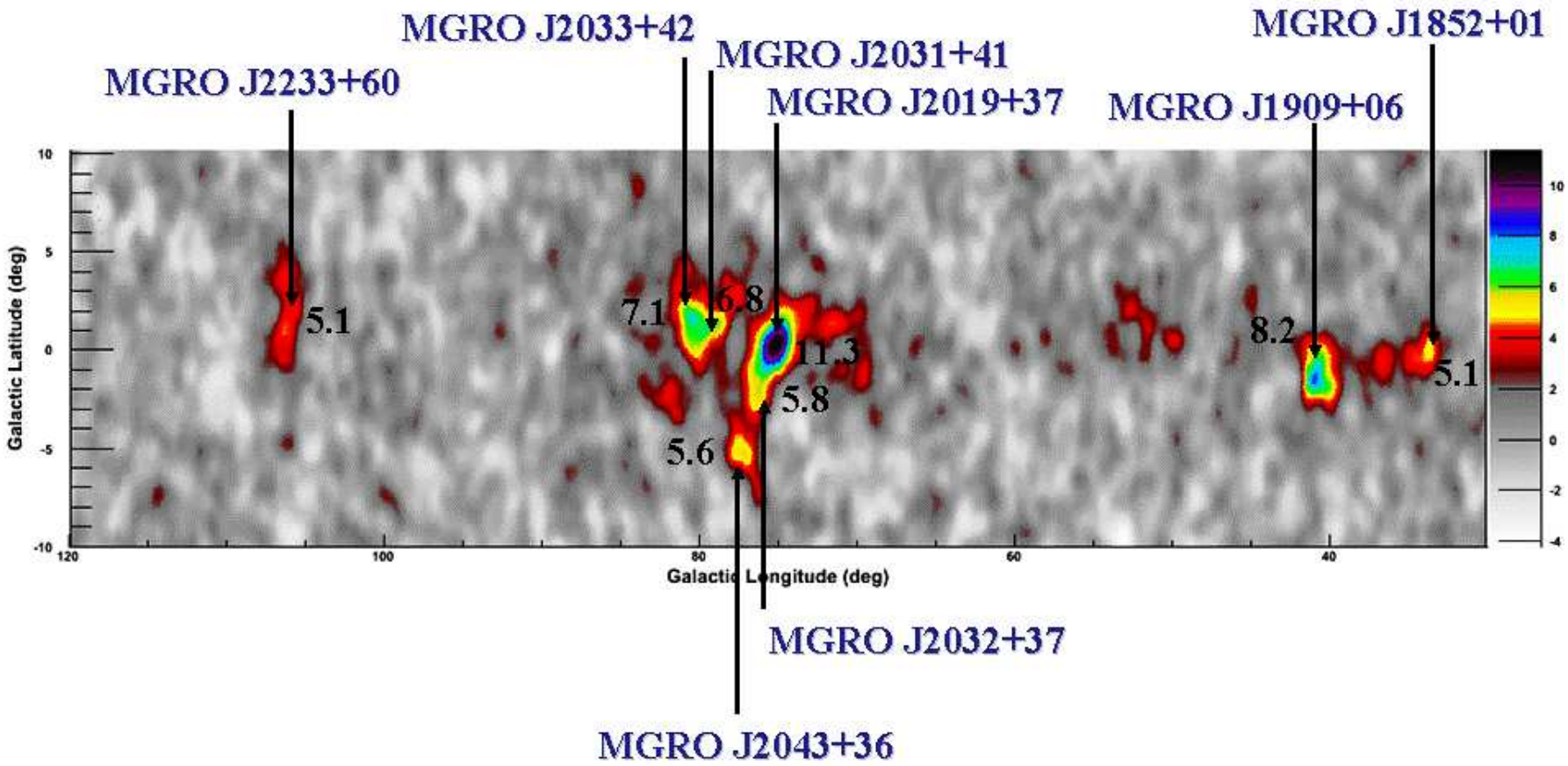

Figure 8.12: Milagro's TeV gamma-ray sources and source candidates. The numbers show the pre-trials significance for each source.

Chapter 9

Discovery of Diffuse TeV Gamma-Ray Emission From the Cygnus Region

It can be seen in figure 9.1, that in addition to the newly discovered sources in the Cygnus region, there exists a diffuse TeV gamma-ray emission from this part of the Galaxy as well. The contours in the figure show the matter density in the region. The TeV emission is correlated with the matter density with the exception of a significant deviation near the new MGRO J2019+37. This region of the Galaxy is a natural laboratory for the study of cosmic-ray origins. It contains a large column density of interstellar gas that should lead to strong emission of diffuse gamma rays. It is also the home of potential cosmic-ray acceleration sites–Wolf-Rayet stars [69], OB associations [18], and supernova remnants [29]. The Tibet Air Shower detector also recently reported an excess in the cosmic-ray flux from this region [11].

To study the diffuse emission from the Cygnus region, the contribution from the Milagro sources in the same region must first be subtracted. To do this, a 3×3 square degrees area centered at the two Milagro sources in this region, MGRO J2019+37

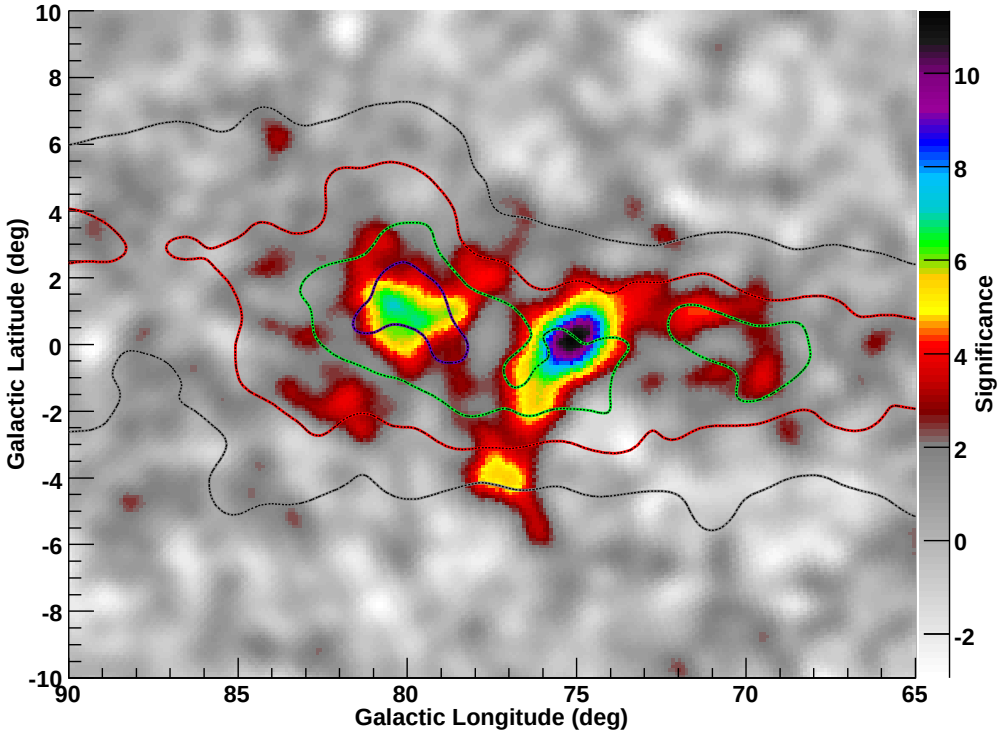

Figure 9.1: The same TeV image of the Cygnus region as in figure 8.3 but with the addition of contours showing the matter density in the region[42, 23, 46].

and MGRO J2033+42, is excluded from the flux calculations for the region defined by Galactic latitude -3.0 to 3.0 degrees and Galactic longitude 65 to 85 degrees. The flux from the remaining region at 12 TeV and assuming a differential power law spectrum of $E^{-2.6}$ is given by $dN/dE = (8.3 \pm 1.3_{stat} \pm 2.7_{sys}) \times 10^{-14}$ TeV^{-1} cm^{-2} s^{-1} which accounts for twice the flux from the Crab nebula. A change in the assumed spectral index from -2.4 to -2.8 changes the quoted flux at 12 TeV by < 10 %. In this measured flux, it is assumed that the source has no cut off in its spectrum up to 100 TeV. If there exists a cutoff in the spectrum of the source, the flux estimate will go down. The maximum factor by which the flux will go down is the case that the source has a cutoff at 12 TeV, in this case the flux will go down by a factor of 1/2. However, this is unlikely since the significance of the gamma-ray emission from this region improves when the weighted analysis is used. Taking into account that the weighting analysis gives higher weights for events with energies higher than 12 TeV (see figure 5.9), gamma-ray emission from this source is most likely to extend well beyond this energy.

In order to compare the flux value measured for the diffuse TeV gamma-ray emission from the Cygnus region, the GALPROP model is used.

9.1 The GALPROP Model

GALPROP is a computer code that is used for the calculation of Galactic cosmic-ray propagation [51] . Primary and secondary nucleons, primary and secondary electrons, secondary positrons and antiprotons, as well as gamma-rays and synchrotron radiation are included. The GALPROP model calculates the gamma-ray emissivities in every spatial grid point using the propagated spectra of cosmic-ray species, leptons and nucleons, the interstellar radiation field, and the gas densities. The gas-related components (π^0 and bremsstrahlung) of the gamma-ray sky maps are calculated us-

ing 21 cm line survey data [23] for HI and CO J = 1 to J=0 survey data for H_2, in the form of column densities for Galactocentric rings, using velocity information and a rotation curve. The cosmic-ray source distribution is based on SNR/pulsars and a variable CO-to-H_2 conversion factor. In this way, details of Galactic structure are included. Full details of the GALPROP model are given in [51].

GALPROP has two models for the propagation of cosmic-ray in the Galaxy; the "conventional" model, and the "optimized" model. The "conventional" model is tuned to have the propagated cosmic-ray particle spectra and intensities match the local direct measurements [51]. This model yields a deficit of diffuse gamma-ray emission above 1 GeV, a so-called GeV excess, observed in all directions on the sky (see Chapter 2). The "optimized" model [67] is tuned to match the EGRET diffuse emission data for the whole sky and reproduces the GeV excess by relaxing the constraints on matching the local cosmic-ray proton and electron measurements. This "optimized" model is instead based upon the secondary antiprotons in cosmic-rays and EGRET diffuse gamma-ray data. In this model the cosmic-ray intensities are significantly higher than those measured locally and the electron spectrum has been assumed to extend to well beyond 10 TeV to produce gamma rays in the Milagro energy range. The "optimized" model thus has a much larger contribution from inverse Compton scattering.

The Cygnus region is in a direction tangential to our spiral arm located at approximately the same distance from the Galactic center as the solar system. This direction is the most accurate to determine the gas distribution based on velocity information and the Galactic rotation curve. Therefore, the uncertainty in the determination of the gas distribution in this direction is minimal.

9.2 Interpretation of Results

Figure 9.2 shows the GALPROP models for the diffuse emission from the Cygnus region along with the EGRET and Milagro measurements for the same region. The Milagro measurement of the diffuse flux in the Cygnus region is a factor of $\sim$7 above predictions of the "conventional" model. The Milagro flux also exceeds the prediction of the "optimized" model, which incorporates higher cosmic-ray intensities to fit the EGRET data. Increasing the gas column density to agree with the Milagro data would violate the restrictions imposed by the EGRET data, and increasing the cosmic-ray flux at higher energies would violate constraints such as antiproton flux measurements unless the increase in cosmic-rays was local to the Cygnus region. Both the parameters of the GALPROP model and the Milagro flux measurement have large systematic uncertainties; however, the discrepancy between the model and the data likely implies the existence of an additional gamma-ray component. The spectrum of this component must be hard (for example, a differential photon spectral index of -2.3 to -2.4) in order to agree with fluxes measured by both EGRET and Milagro.

There are several possible explanations for this component: unresolved sources of TeV gamma rays, a population of high-energy electrons in the region producing an inverse Compton flux at TeV energies, or a population of cosmic-ray accelerators which is dark because the hadrons do not interact near their sources but instead with the local matter distribution. The correlation of the observed emission with the matter density can be consistent with all of these explanations if the sources are co-located with the matter. If the excess is due to inverse Compton scattered photons, then this component must be a factor of $\sim$20 higher at 12 TeV than the prediction of the conventional model. Given typical diffusion and energy-loss times of such high energy electrons, the source of these electrons must reside within the Cygnus region. Also, the proposed explanation of the GeV excess due to neutralino annihilation [24] cannot explain the Milagro high energy flux, because such a massive neutralino

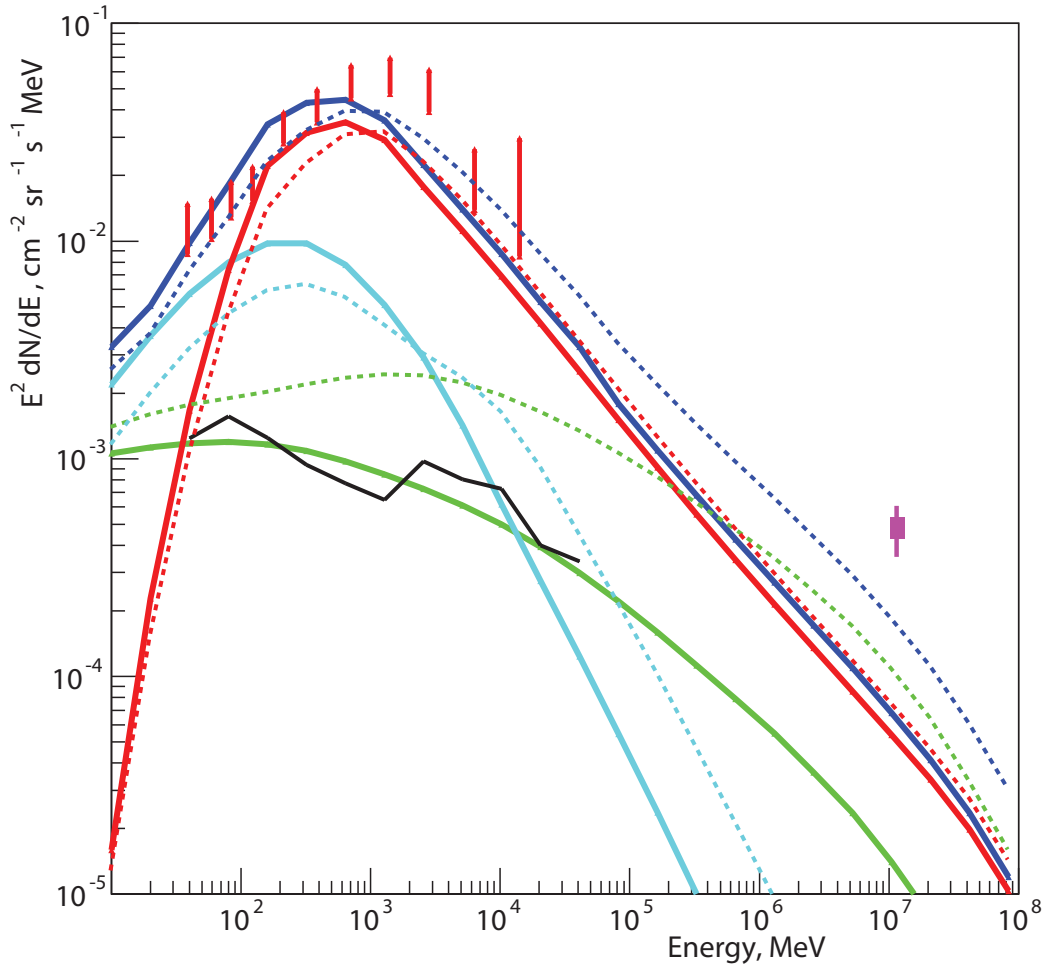

Figure 9.2: Gamma-ray spectrum of the diffuse emission from the Cygnus region of the Galactic plane. The red bars are the EGRET data, and the purple bar is the Milagro measurement with the statistical error shown as a broad line and with the systematic error shown as a narrow line. The solid lines represent the "conventional", and the dotted lines represent the "optimized" GALPROP model of Strong et al. [51]. The dark blue lines represent the total diffuse flux, the red lines represent the π^0 component, the green lines represent the inverse Compton component, the light blue lines are due to bremsstrahlung, and the black lines are due to the extragalactic background. The Milagro analysis is insensitive to isotropic emission due to the background subtraction, so the extragalactic background is not included in the Milagro energy range.

would have a much smaller number density and hence lower flux. Therefore, this Milagro observation suggests that the Cygnus region contains hard-spectrum, cosmic-ray proton or electron accelerators.

Chapter 10

Conclusions

10.1 Summary

The development of the new gamma-hadron separation variable, A_4, along with the weighted analysis technique developed elsewhere, has significantly improved the sensitivity of the Milagro detector. This new analysis resulted in the first discoveries in Milagro. Four localized sources of TeV gamma-ray emission have been discovered, three of which are in the Cygnus region of the Galaxy and one closer to the Galactic center. In addition to these localized sources, a diffuse emission of TeV gamma-rays has been discovered from the Cygnus region of the Galaxy. The localized sources have no obvious counterparts in other wavelengths and thus remain as unidentified sources. The most interesting of these localized sources is the new source MGRO J2019+37 which is the brightest TeV gamma-ray source seen by Milagro after the Crab Nebula. Unlike the other sources, MGRO J2019+37 is located at a region of low-matter density. The diffuse TeV gamma-ray emission from the Cygnus region accounts for twice that of the Crab Nebula. The flux of the diffuse emission measured by Milagro from this region exceeds predictions from the "conventional" GALPROP model by a factor of ~ 7. It also exceeds predictions from the "optimized" GALPROP

model by a factor of ~ 5. This Milagro observation suggests that the Cygnus region contains hard-spectrum proton or electron accelerators and/or unresolved sources of TeV gamma-rays in the region.

10.2 Future Directions

The obvious continuation of this work would be the addition of more data to increase the number of discovered sources. What is more important are more detailed studies of each of the discovered sources in this thesis. This includes observations at other wavelengths especially at GeV gamma-rays, X-rays, radio, and optical wave bands. Observations of these sources with ACTs should increase our understanding of these sources. The excellent angular resolution of ACTs, $< 0.1^{\circ}$, should allow for better morphological studies of these sources. The VERITAS telescope array in Arizona is the best ACT telescope suited for such studies. The fact that it is at a latitude similar to that of Milagro, $\sim 37^{\circ}$, gives similar exposures for these sources. It also gives it the maximum exposure for the Cygnus region which is located at similar declinations in the sky. At the current time, Milagro is unable to determine the spectral shape of a gamma-ray source. The determination of the spectral shape of each of the discovered sources will substantially increase our understanding of the nature of these sources. The development of such a technique has been explored which gave results for the Crab Nebula and the cosmic-ray spectra which agree with those measured by other experiments (see Appendix A). The perfection and implementation of the spectral index analysis technique given in Appendix A seems to be a natural and a necessary continuation of the work done in this thesis. One other possible continuation of this thesis work is the study of the time variability of the gamma-ray emission from the discovered sources.

Appendix A

Spectral Index Analysis Technique

One of the important parameters that should be determined for a gamma-ray air shower is its energy. An algorithm that determines the energy of an air shower based on some shower parameters like the zenith angle of the shower and the distance of the shower core from the center of the pond (core distance) is being developed. As has been mentioned earlier, the flux from celestial gamma-ray sources follows a rapidly falling power law spectrum given by:

$$\frac{dN}{dE} = \phi_\circ \left(\frac{E}{E_\circ}\right)^{-\alpha} \tag{A.1}$$

where $\phi_\circ$ is the differential flux normalization, $E_\circ$ is the energy at which the flux is normalized, and α is the spectral index of the source.

The spectral index, α of a source is a characteristic of this sources. Sources with smaller α's will emit more photons at higher energies. In this sense, the energy spectrum of a source is proportional to its spectral index α. One way to quantify the energy spectrum of a gamma-ray source will be to determine its spectral index.

In this appendix a new technique for measuring the spectral index of a γ-ray source in Milagro using A_4 is introduced. This technique makes use of the energy dependence on A_4. The spectral index of the Crab Nebula obtained with this technique is $\alpha =$

$-2.57+(0.12-0.11)^{stat}$. This value agrees with those measured by other experiments in the same energy range as Milagro.

A.1 Energy Dependence on A_4

In order to be able to measure the spectral index of a γ-ray source one needs to have a variable that is well correlated with energy, A_4 is such a variable. Figure A.1 shows the relation between the energy and A_4 for gamma Monte Carlo[1]. As can be seen in this figure, there is a very good correlation between the energy of a γ-ray event and the A_4 value of that event in the energy range 2-20 TeV.

A.2 Spectral Index Determination Technique

In order to determine the spectral index of a γ-ray source, the following steps were done:

- Eleven different gamma Monte Carlo sets were created. These data sets were simulated with different spectral indices ranging from -2.0 to -3.0 in increment of 0.1.
- Excess from the data were binned in A_4, differentially.
- Gamma MC sets were binned in A_4, differentially.
- The different gamma MC differential distributions were fit to the differential excess from the data.
- χ^2 for each of these eleven fits were calculated.
- A plot of these χ^2 values as a function of spectral index was generated.

[1]Epoch 5 is used throughout this Appendix.

- Minimum of this plot corresponds to spectral index of the source.

A.3 Crab Nebula Spectral Index Estimation

The Crab Nebula serves as a standard candle in γ-ray astronomy and a new technique is best tested on this steady source. In addition to this, the fact that this source has been well studied by many experiments in the same energy range as Milagro helps test the new technique by cross checking the results of this new technique with those of the other experiments.

Figure A.2 shows the distribution of differential excess from the Crab Nebula as a function of A_4 . The last bin in this figure contains all excess events with $A_4 \geq 12.0$, this is the reason why this bin has more events than the two previous bins. Figure A.3 shows the A_4 differential distributions of four gamma Monte Carlo sets with spectral indices -2.1, -2.3, -2.6, and -2.9. For comparison, the differential excess from the Crab (figure A.2) is shown on each of the plots.

Figure A.4 shows the distribution of the χ^2 values of the fits of the different gamma Monte Carlo sets to the Crab data as a function of the spectral index α. From this plot we see that the minimum χ^2 corresponds to a spectral index of:

$$\alpha_{crab} = -2.57 + (0.12 - 0.11)_{stat}$$

The statistical errors were obtained by fitting the distribution in figure A.4 to a quadratic function and then going up one unit in χ^2 from the minimum. As can be seen from this figure, the distribution is not symmetric around the minimum, this is why the statistical errors are not equal. In total there are 12 degrees of freedom (ndf). After the subtraction of one degree of freedom for the minimization of χ^2 with respect to α and another one for the minimization of χ^2 with respect to the scaling

factor[2], one ends up with 10 degrees of freedom. χ^2 at the minimum is equal to 13.9 this corresponds to chance probability of $\approx 18\%$

The value of α for the Crab obtained in this analysis is in good agreement with results form other experiments. Table A.1 lists Measurements of the Crab spectral index by other experiments in the same energy range as Milagro.

Tibet	$-2.62 \pm 0.17_{stat}$
HEGRA	$-2.59 \pm 0.03_{stat} \pm 0.05_{sys}$
Whipple	$-2.49 \pm 0.06_{stat} \pm 0.04_{sys}$

Table A.1: Measurements of the Crab spectral index by other experiments in the same energy range as Milagro

A.4 Cosmic Rays Spectral Index Estimation

The same technique was applied to measure the spectral index of cosmic rays. To do this, eleven different proton and helium Monte Carlo sets with different spectral indices were created. These data sets were simulated with different spectral indices ranging from -2.0 to -3.0 in increment of 0.1. The data used to measure the spectral index is the Crab off source data. The analysis proceeds in the same steps as in the one previous section.

The result for the measurement of the cosmic rays spectral index is:

$$\alpha_{cr} = -2.786 + (0.088 - 0.108)_{stat}$$

[2]The scaling factor of the i'th gamma MC distribution, S_i is defined as:

$$S_i = \frac{A_c}{A_i}\delta_i$$

where A_c and A_i are the areas under Crab differential excess and the i'th gamma MC differential distribution, respectively, and δ_i is a correction applied to S_i to minimize χ^2 of the fit of the i'th gamma MC distribution to the Crab data.

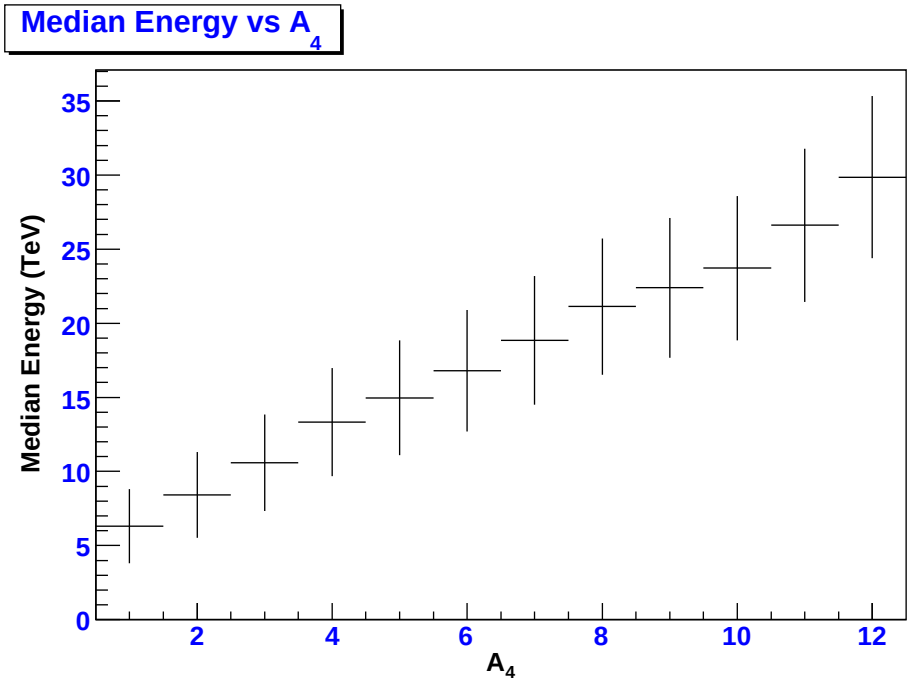

Figure A.1: Median energies of gamma-ray-initiated air showers as a function of A_4. Each point represents the median energy for gamma-ray events with an A_4 value greater than the x-axis value.

This is in good agreement with BESS measurements in the energy range 30-540 GeV:

$$\alpha_{proton} = -2.732 \pm 0.011_{stat} \pm 0.019_{sys}$$

$$\alpha_{helium} = -2.699 \pm 0.04_{stat} \pm 0.044_{sys}$$

χ^2 at the minimum is equal to 7.54 this corresponds to chance probability of $\approx 67\%$

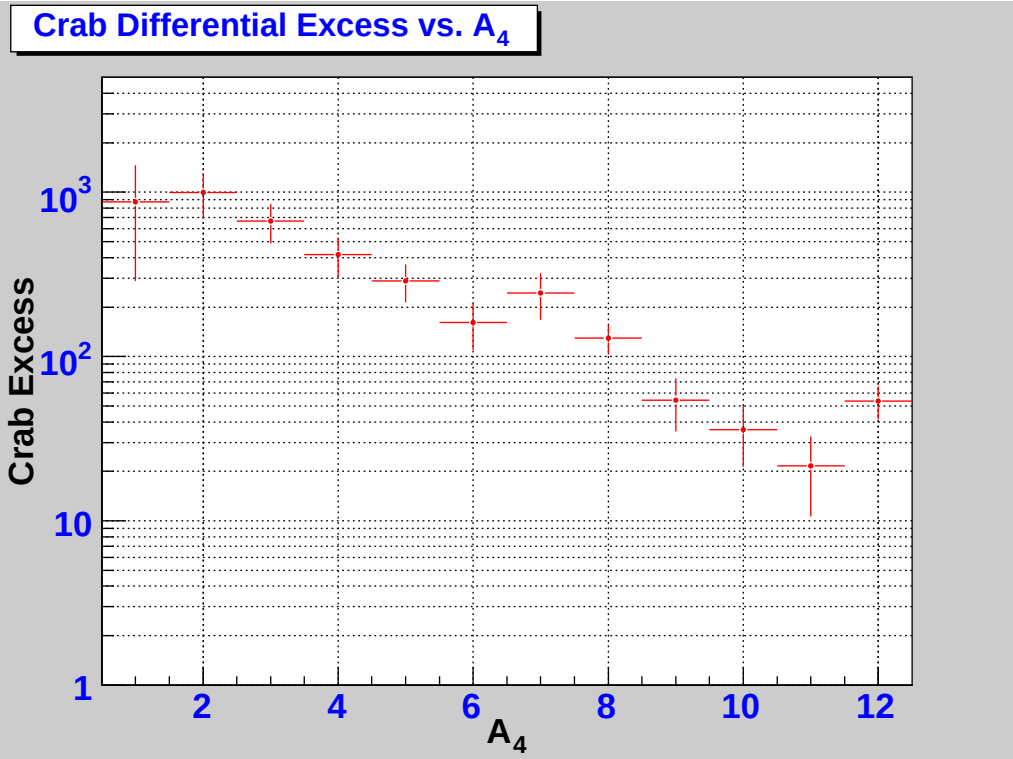

Figure A.2: Differential excess from the Crab Nebula as a function of A_4

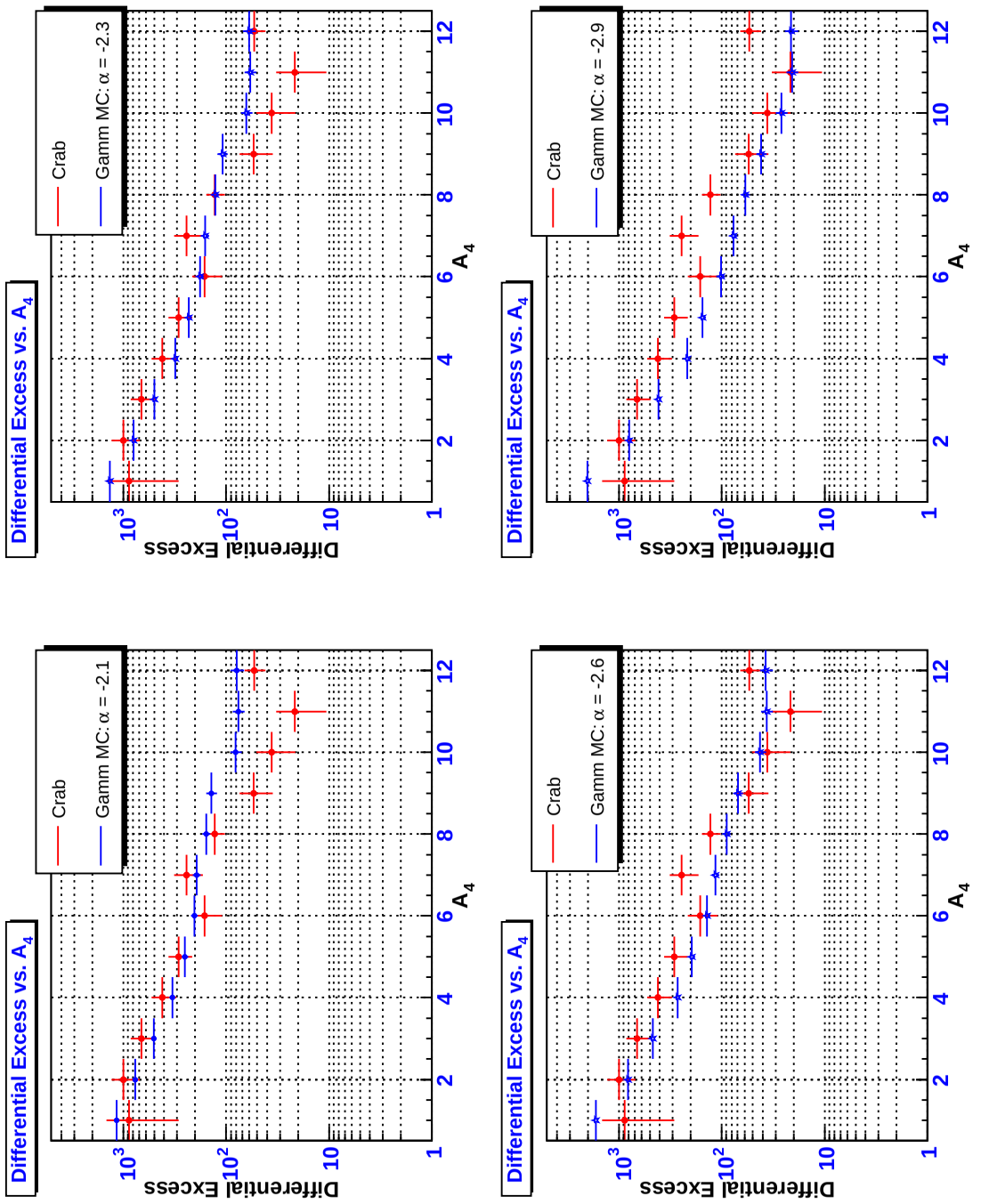

Figure A.3: A_4 differential distribution of four gamma Monte Carlo sets with spectral indices -2.1, -2.3, -2.6, and -2.9. For comparison, the differential excess from the Crab is shown on each of the plots.

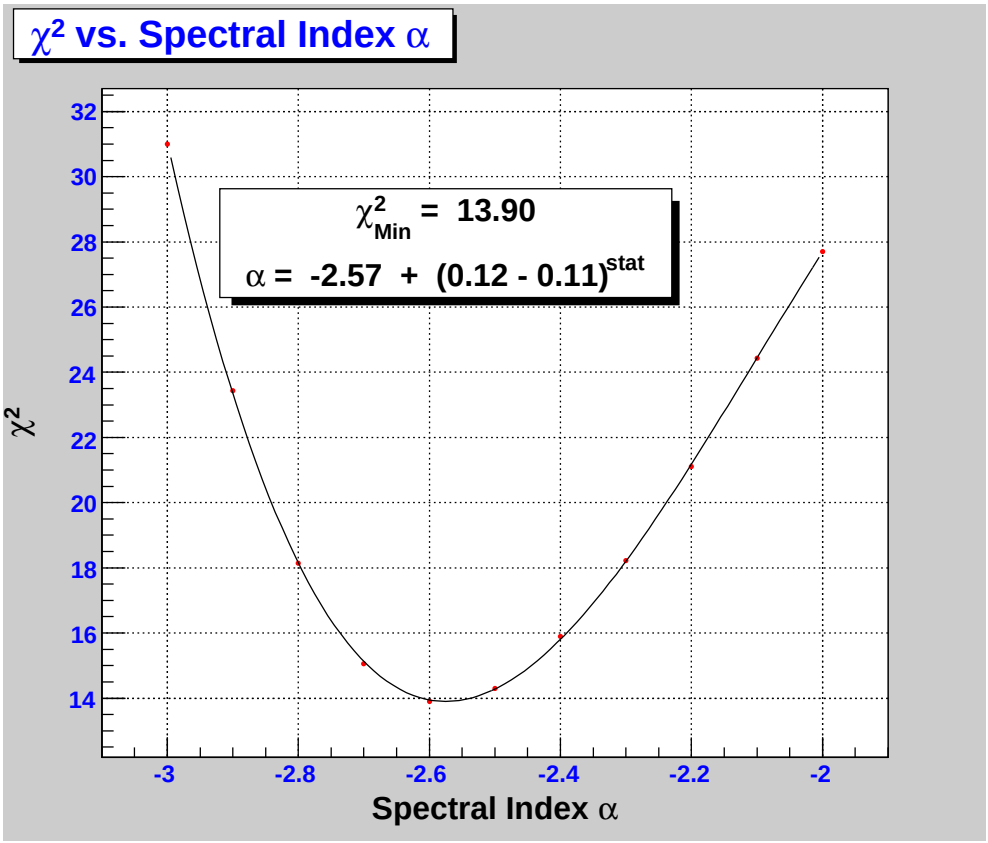

Figure A.4: Distribution of the χ^2 values of the fits of the different gamma Monte Carlo sets to the Crab data as a function of the spectral index α.

Appendix B

Detailed Plots

B.1 Δ_{angle} Distributions for Different Epochs

In this section, distributions of Δ_{angle} for different A_4 slices for each epoch are shown with the corresponding fit parameters to a 2D Gaussian function.

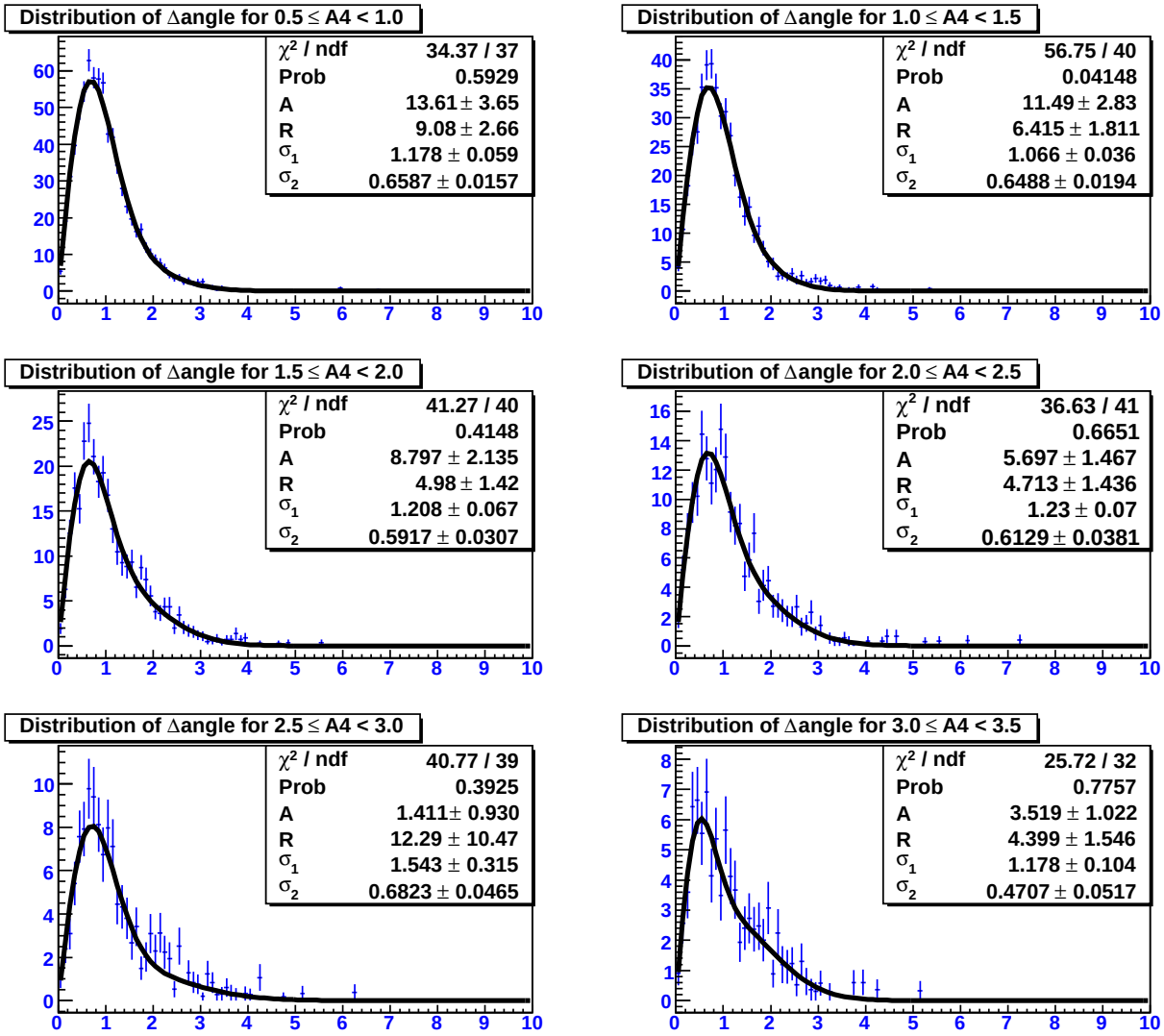

Figure B.1: Δ_{angle} distributions and the corresponding PSF fits for the first six slices in A_4 for the first epoch.

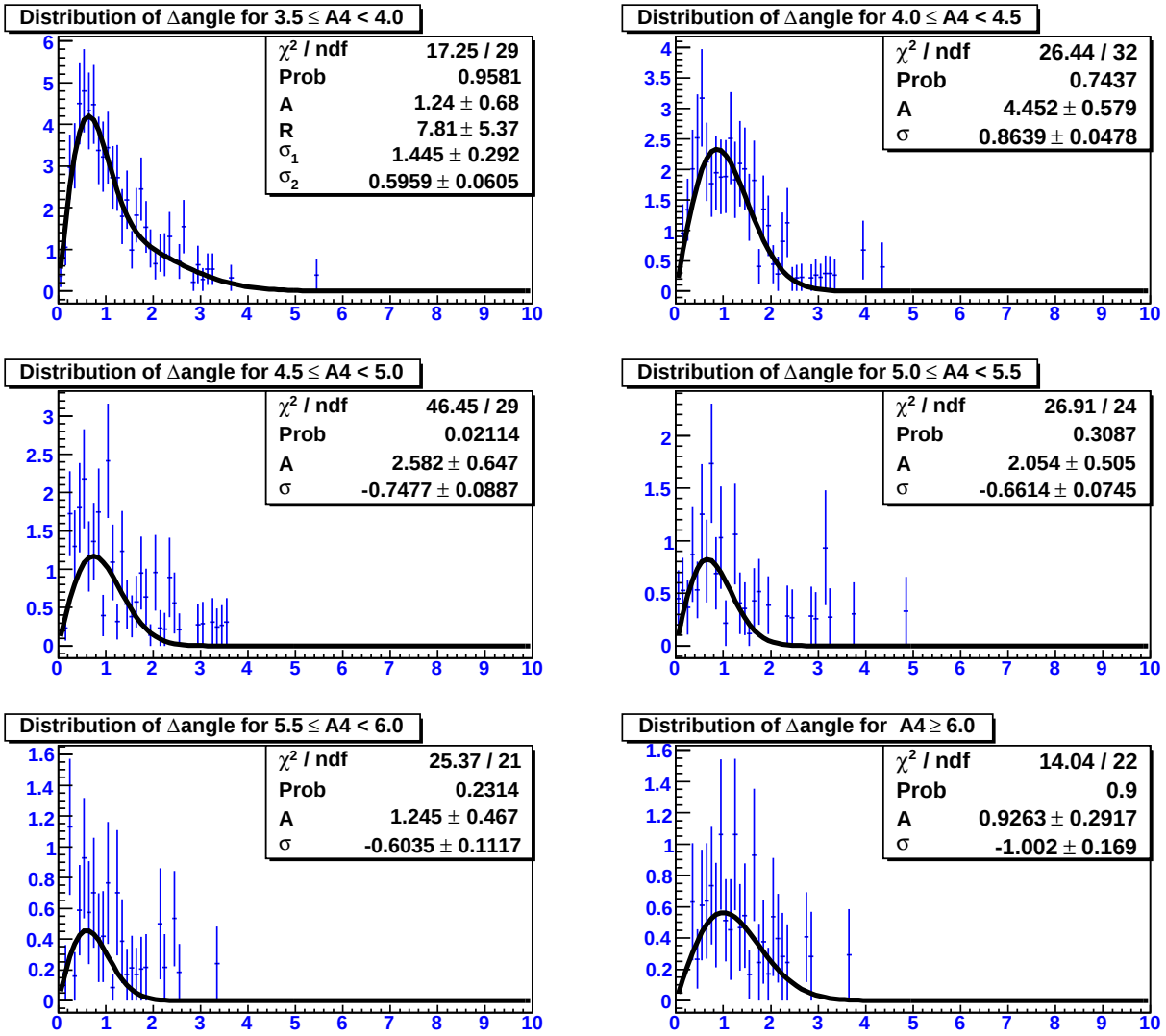

Figure B.2: Δ_{angle} distributions and the corresponding PSF fits for the last six slices in A_4 for the first epoch.

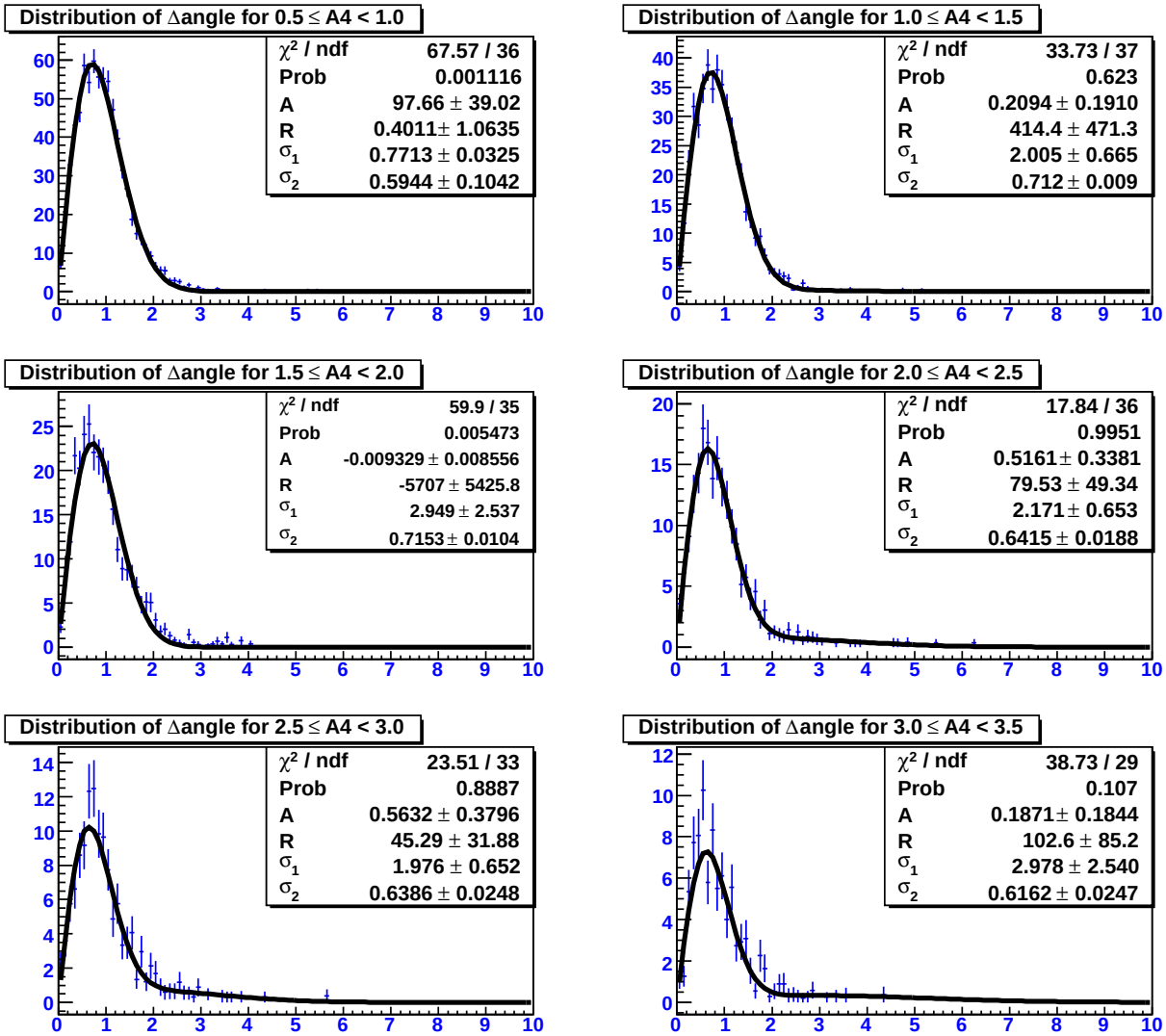

Figure B.3: Δ_{angle} distributions and the corresponding PSF fits for the first six slices in A_4 for the second epoch.

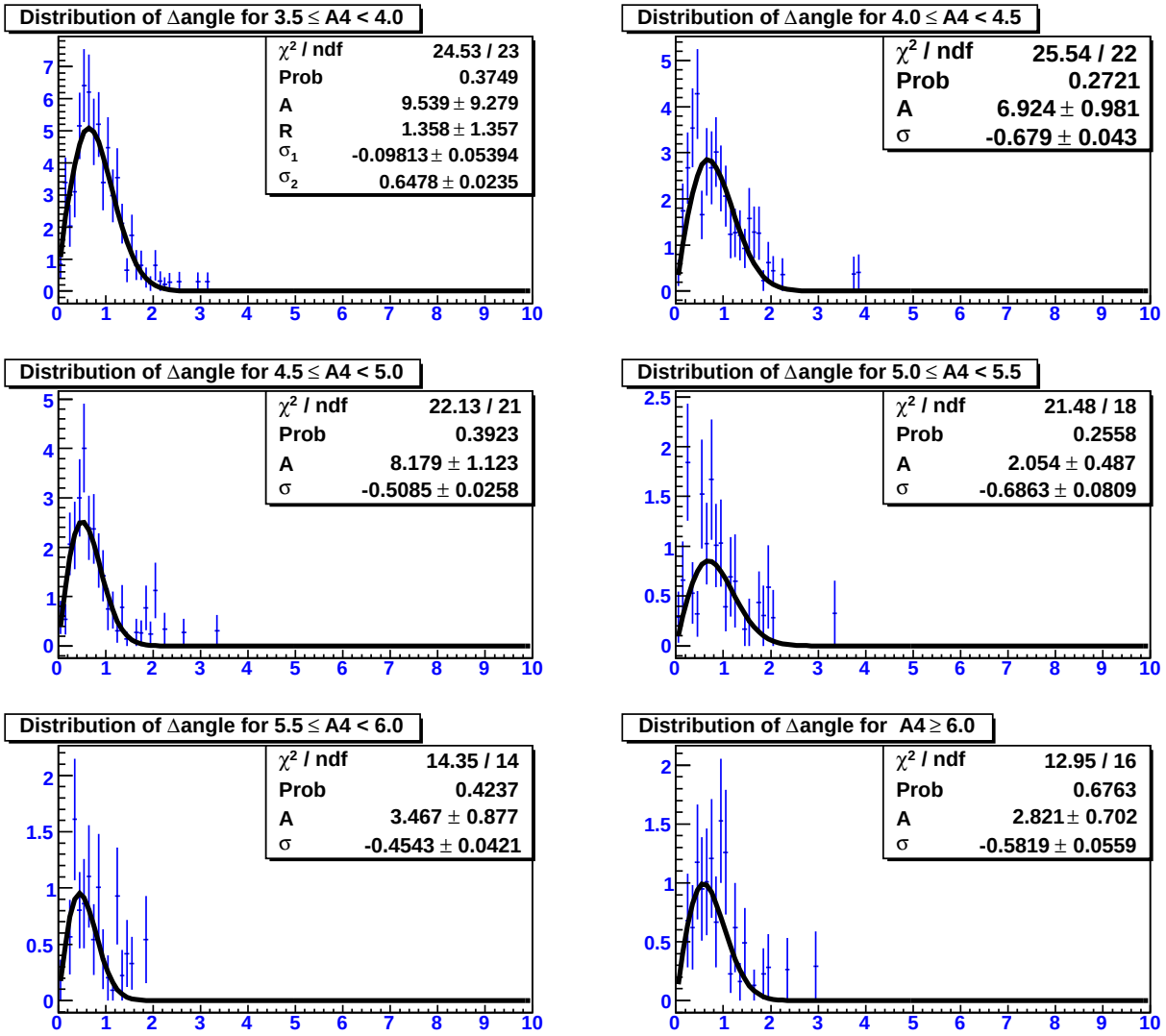

Figure B.4: Δ_{angle} distributions and the corresponding PSF fits for the last six slices in A_4 for the second epoch.

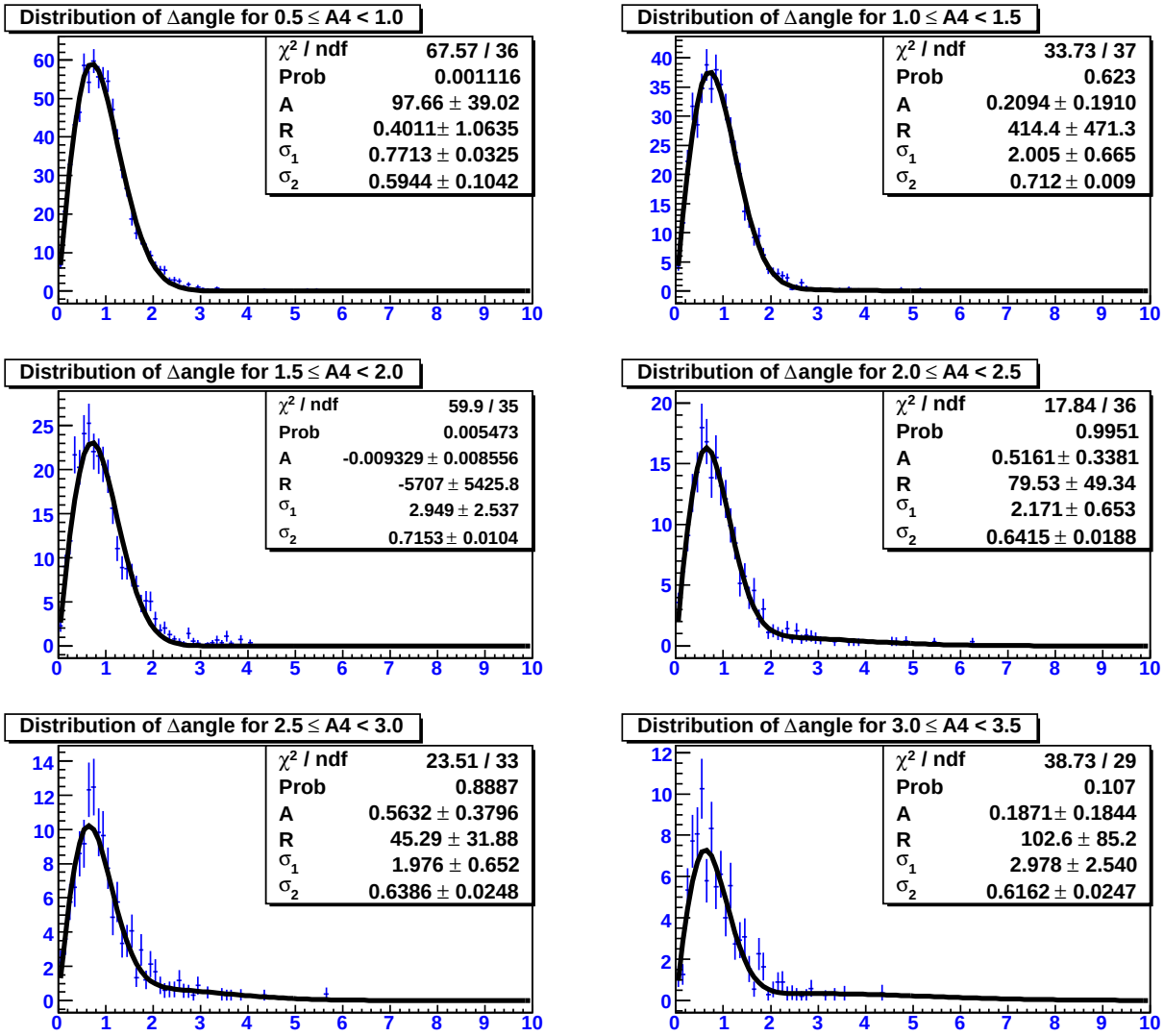

Figure B.5: Δ_{angle} distributions and the corresponding PSF fits for the first six slices in A_4 for the third epoch.

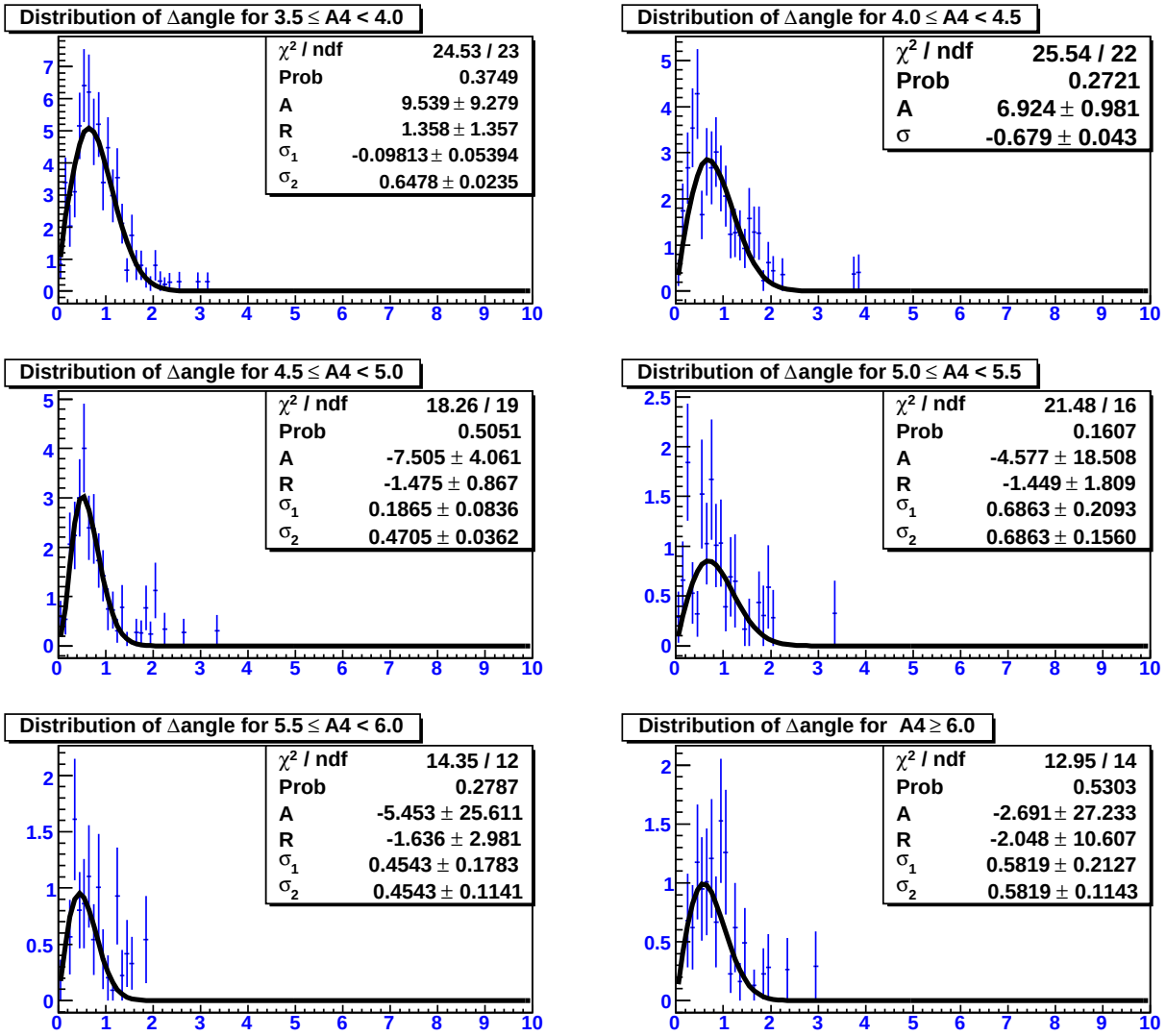

Figure B.6: Δ_{angle} distributions and the corresponding PSF fits for the last six slices in A_4 for the third epoch.

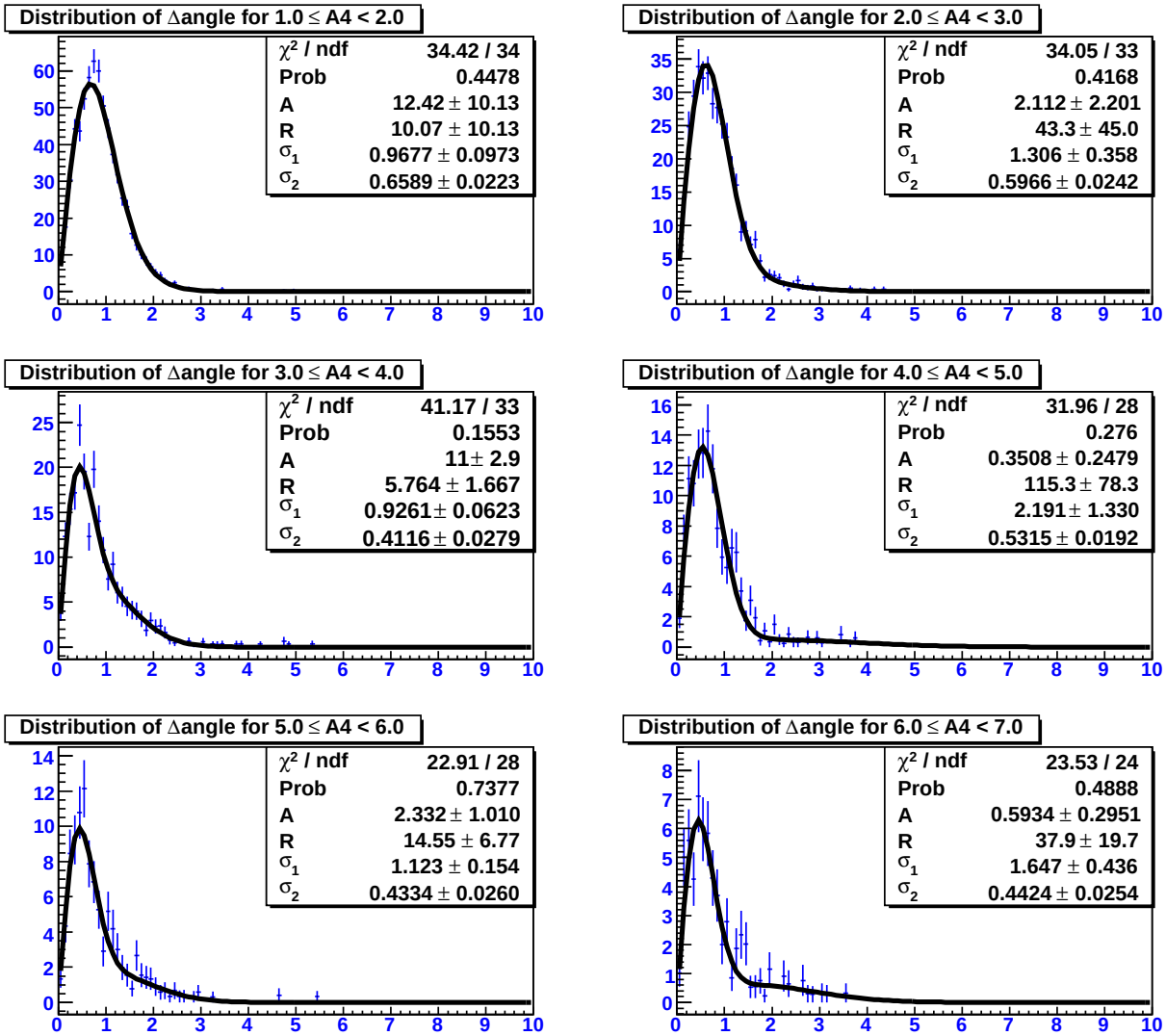

Figure B.7: Δ_{angle} distributions and the corresponding PSF fits for the first six slices in A_4 for the fourth epoch.

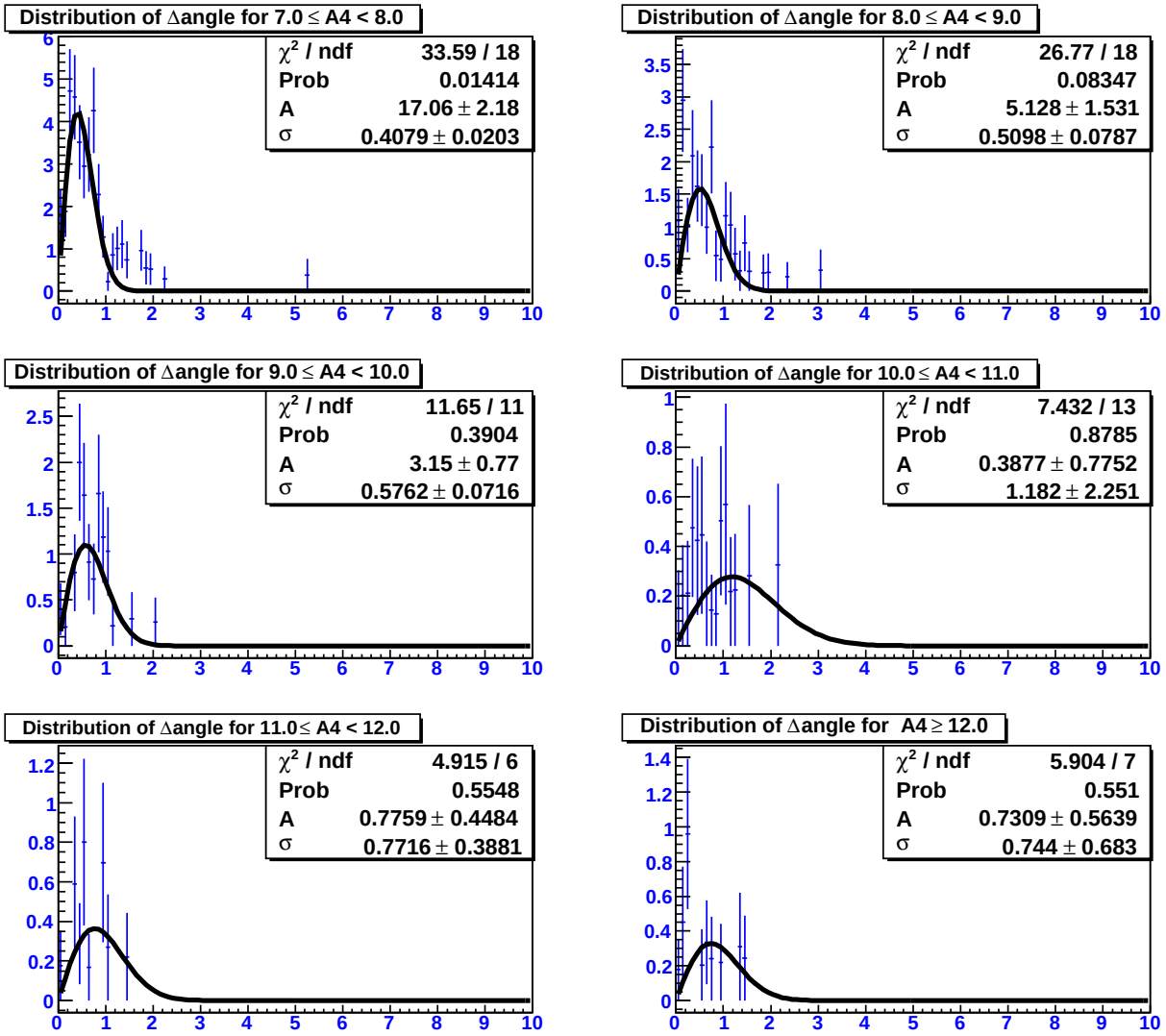

Figure B.8: Δ_{angle} distributions and the corresponding PSF fits for the last six slices in A_4 for the fourth epoch.

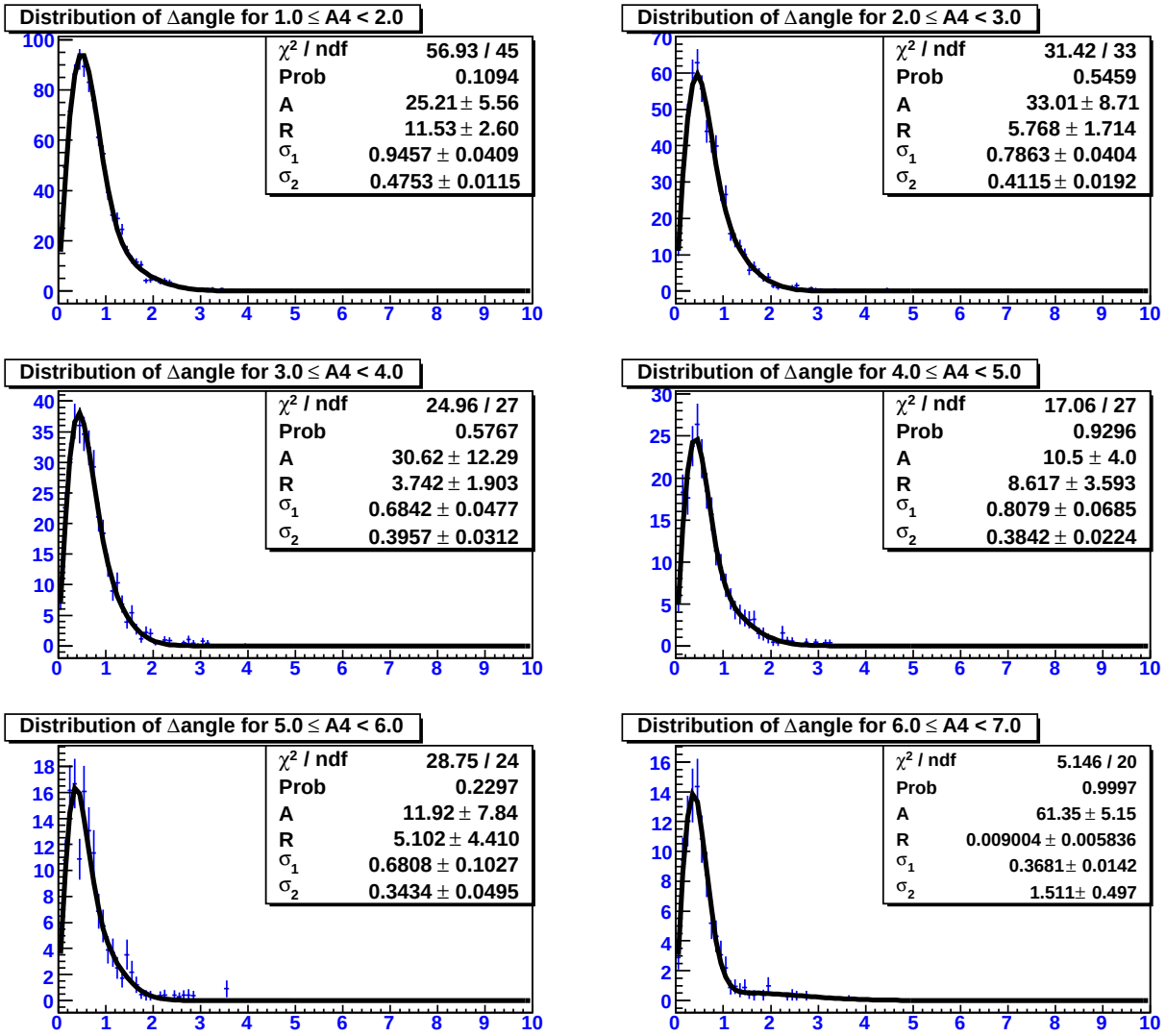

Figure B.9: Δ_{angle} distributions and the corresponding PSF fits for the first six slices in A_4 for the fifth epoch.

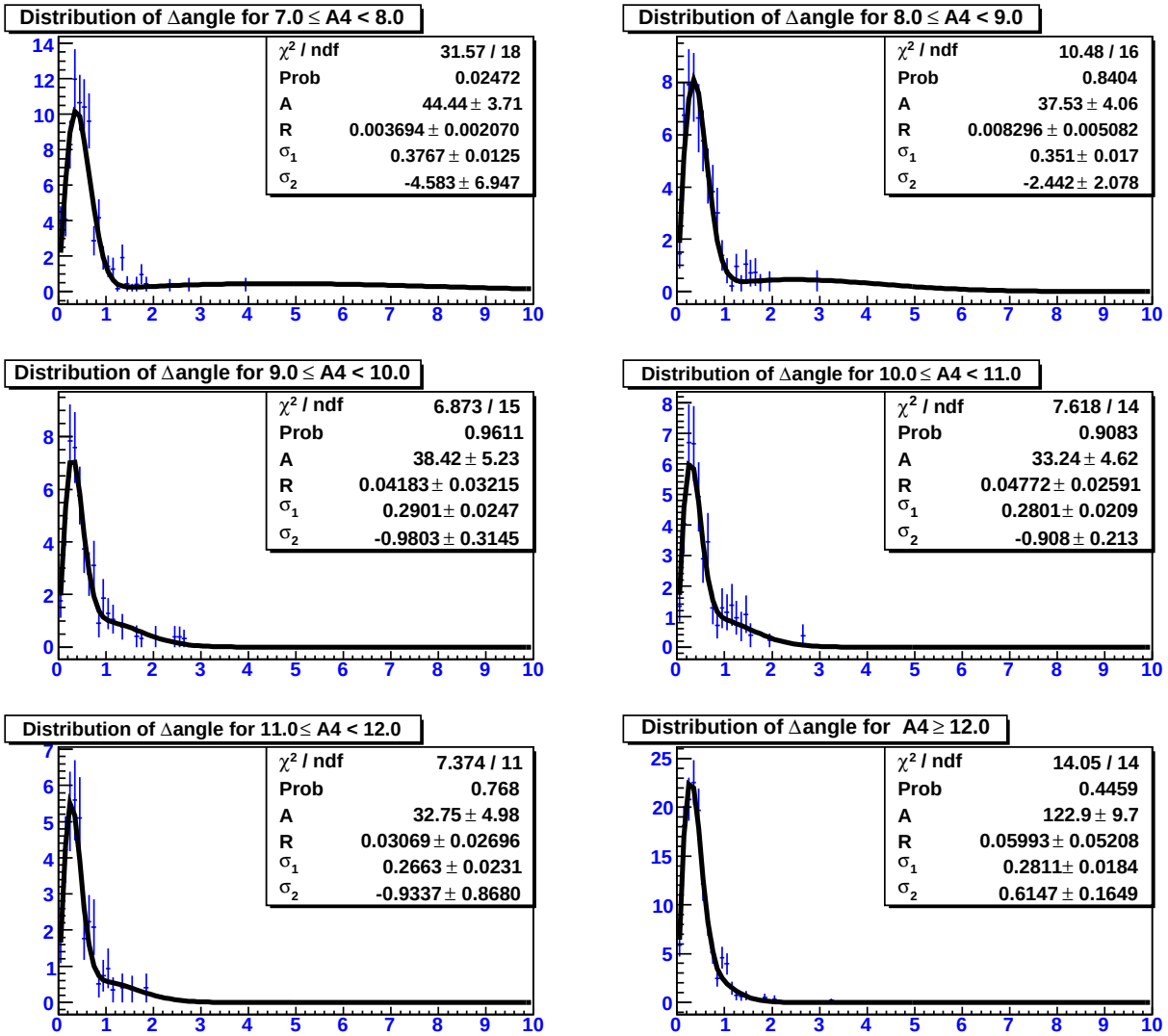

Figure B.10: Δ_{angle} distributions and the corresponding PSF fits for the last six slices in A_4 for the fifth epoch.

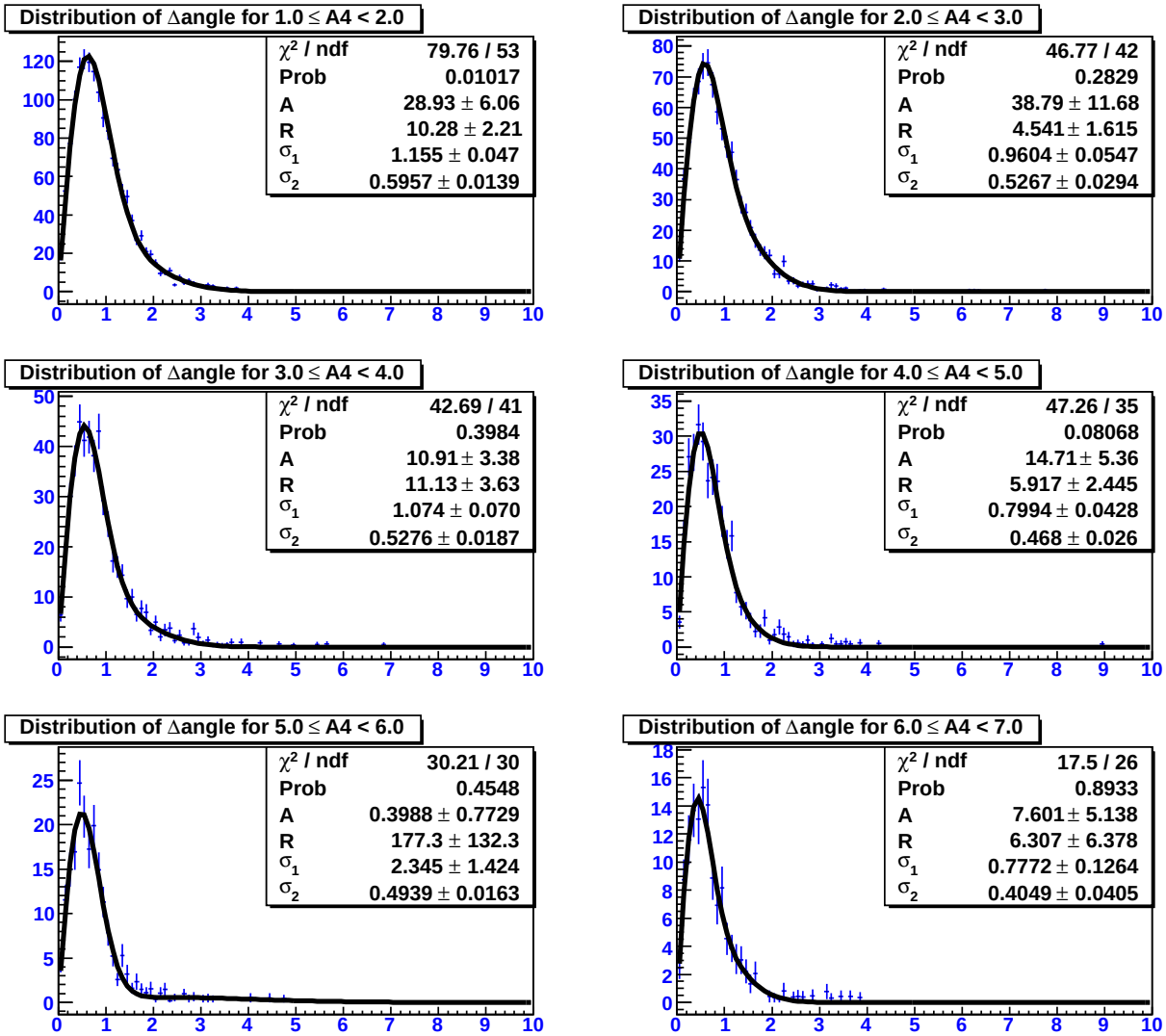

Figure B.11: Δ_{angle} distributions and the corresponding PSF fits for the first six slices in A_4 for the sixth epoch.

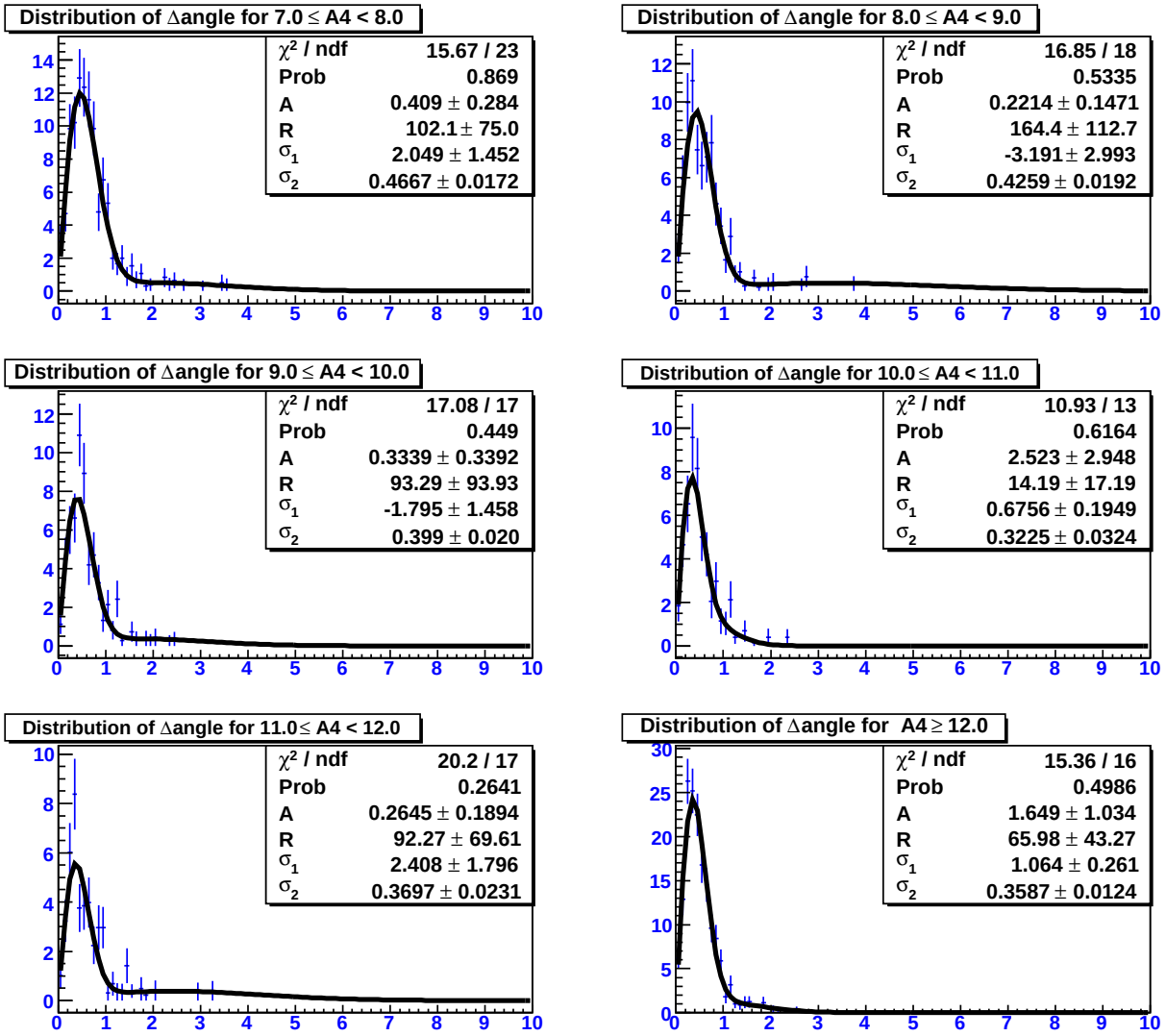

Figure B.12: Δ_{angle} distributions and the corresponding PSF fits for the last six slices in A_4 for the sixth epoch.

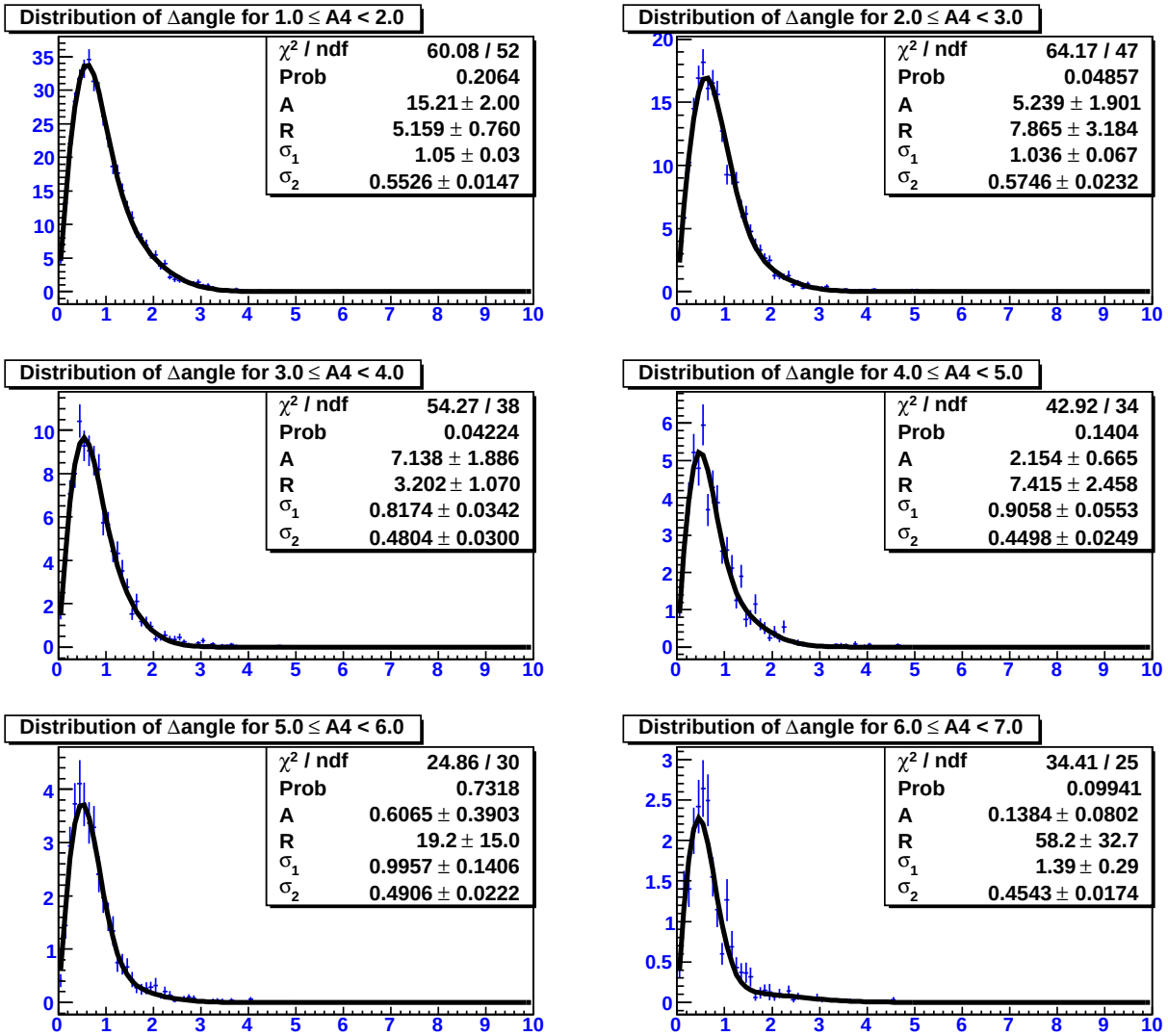

Figure B.13: Δ_{angle} distributions and the corresponding PSF fits for the first six slices in A_4 for the seventh epoch.

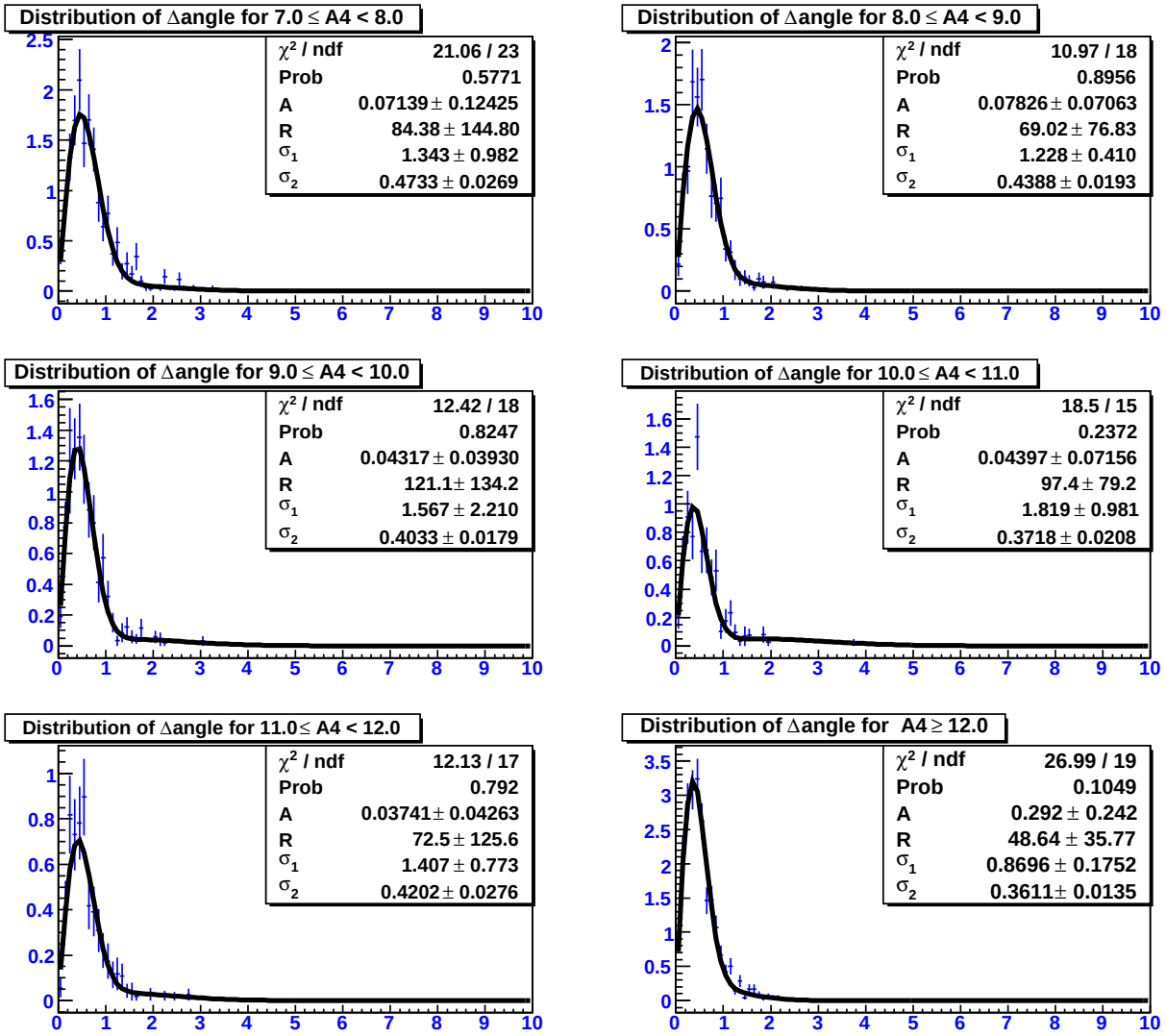

Figure B.14: Δ_{angle} distributions and the corresponding PSF fits for the last six slices in A_4 for the seventh epoch.

B.2 $\triangle_{angle}$ Distributions for Different Spectral Indices

In this section, distributions of Δ_{angle} for different A_4 slices for the eighth epochs for different spectral indices are shown with the corresponding fit parameters to a 2D Gaussian function.

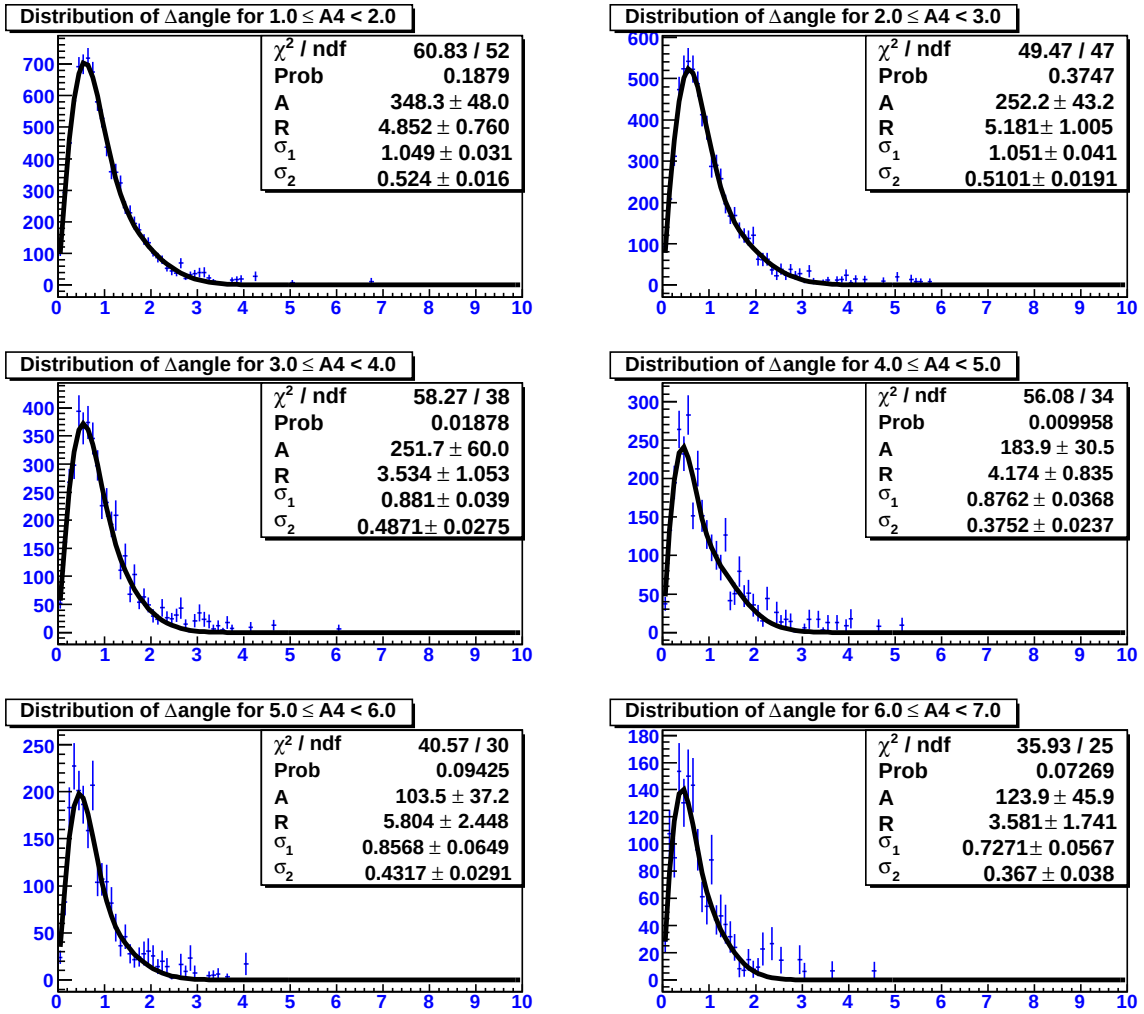

Figure B.15: Δ_{angle} distributions and the corresponding PSF fits for the first six slices in A_4 for the eighth epoch for a -2.2 spectrum.

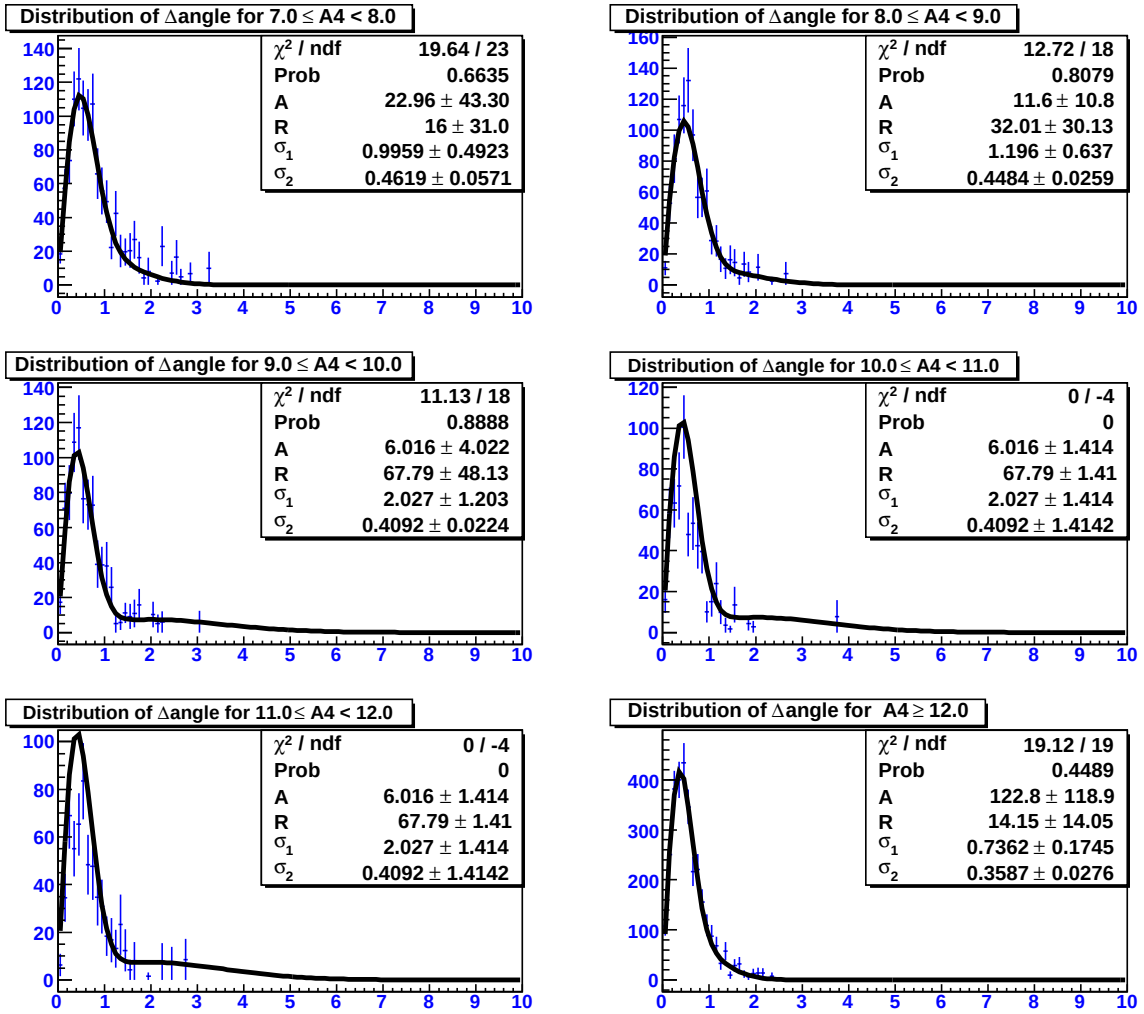

Figure B.16: Δ_{angle} distributions and the corresponding PSF fits for the last six slices in A_4 for the eighth epoch for a -2.2 spectrum.

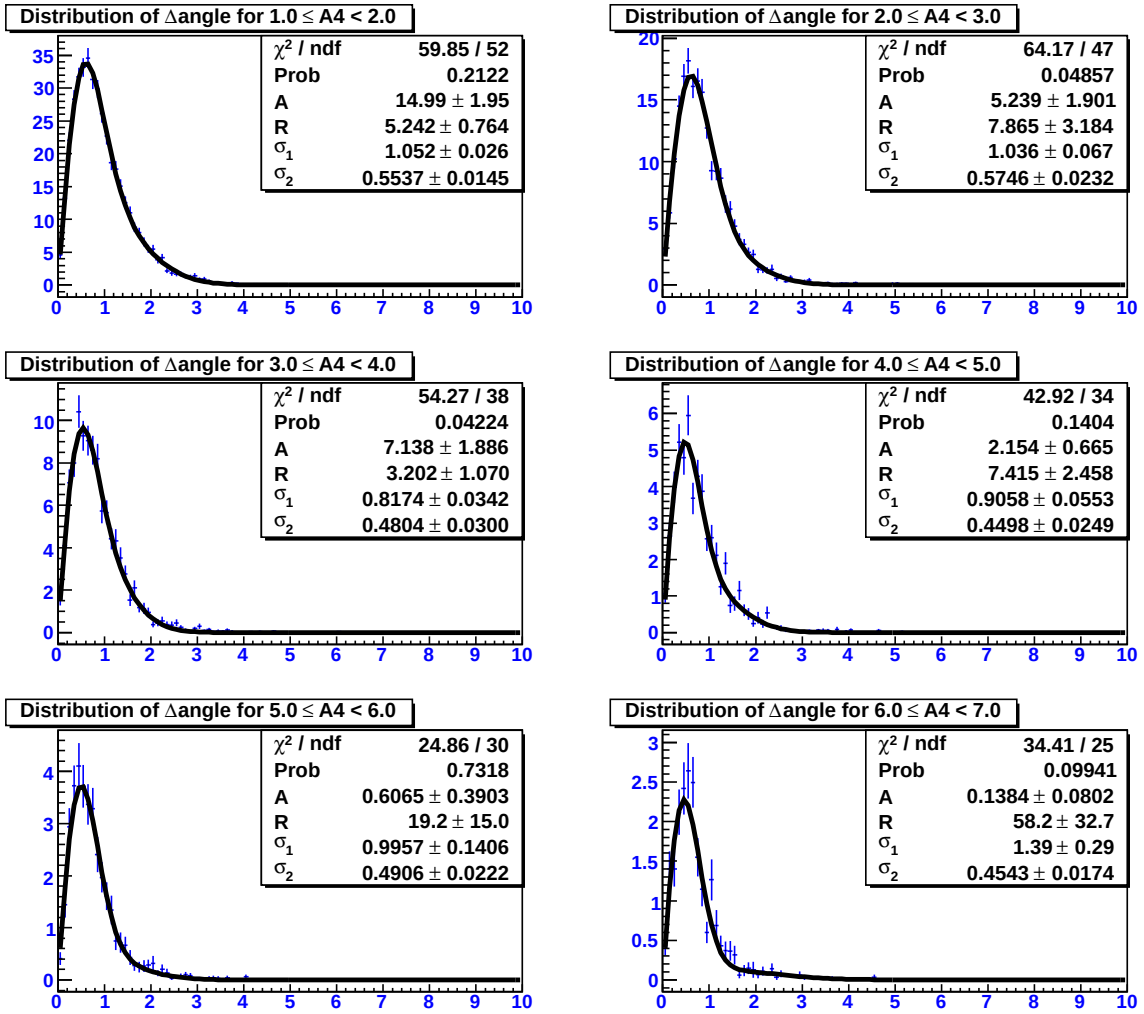

Figure B.17: Δ_{angle} distributions and the corresponding PSF fits for the first six slices in A_4 for the eighth epoch for a -3.0 spectrum.

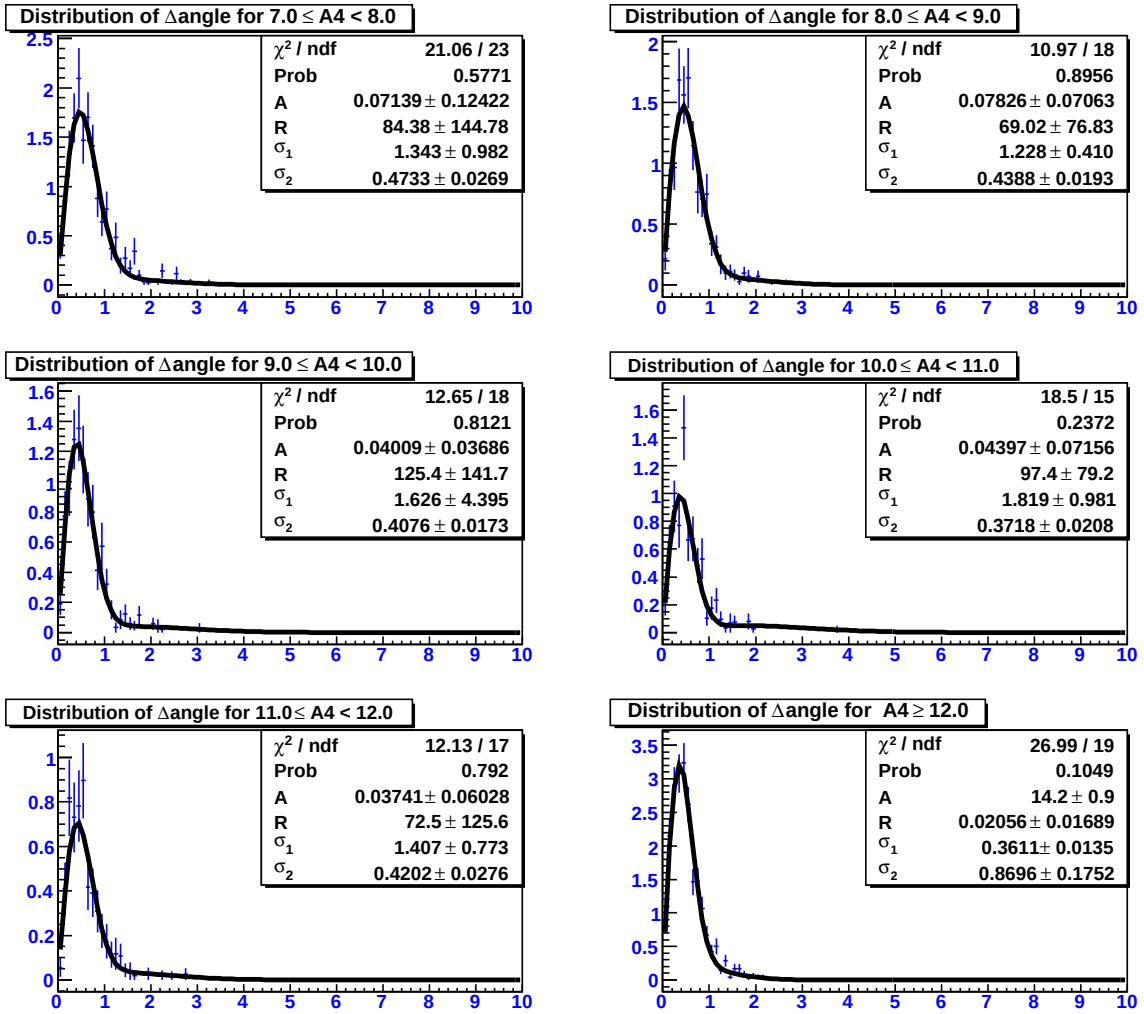

Figure B.18: Δ_{angle} distributions and the corresponding PSF fits for the last six slices in A_4 for the eighth epoch for a -3.0 spectrum.

B.3 A_4 Distributions as a function of "Dead" PMTs for different epochs

In this section, distributions of A_4 for different percentages of "dead" PMTs for cosmic-ray Monte Carlo, data, and gamma-ray Monte Carlo for each epoch are shown.

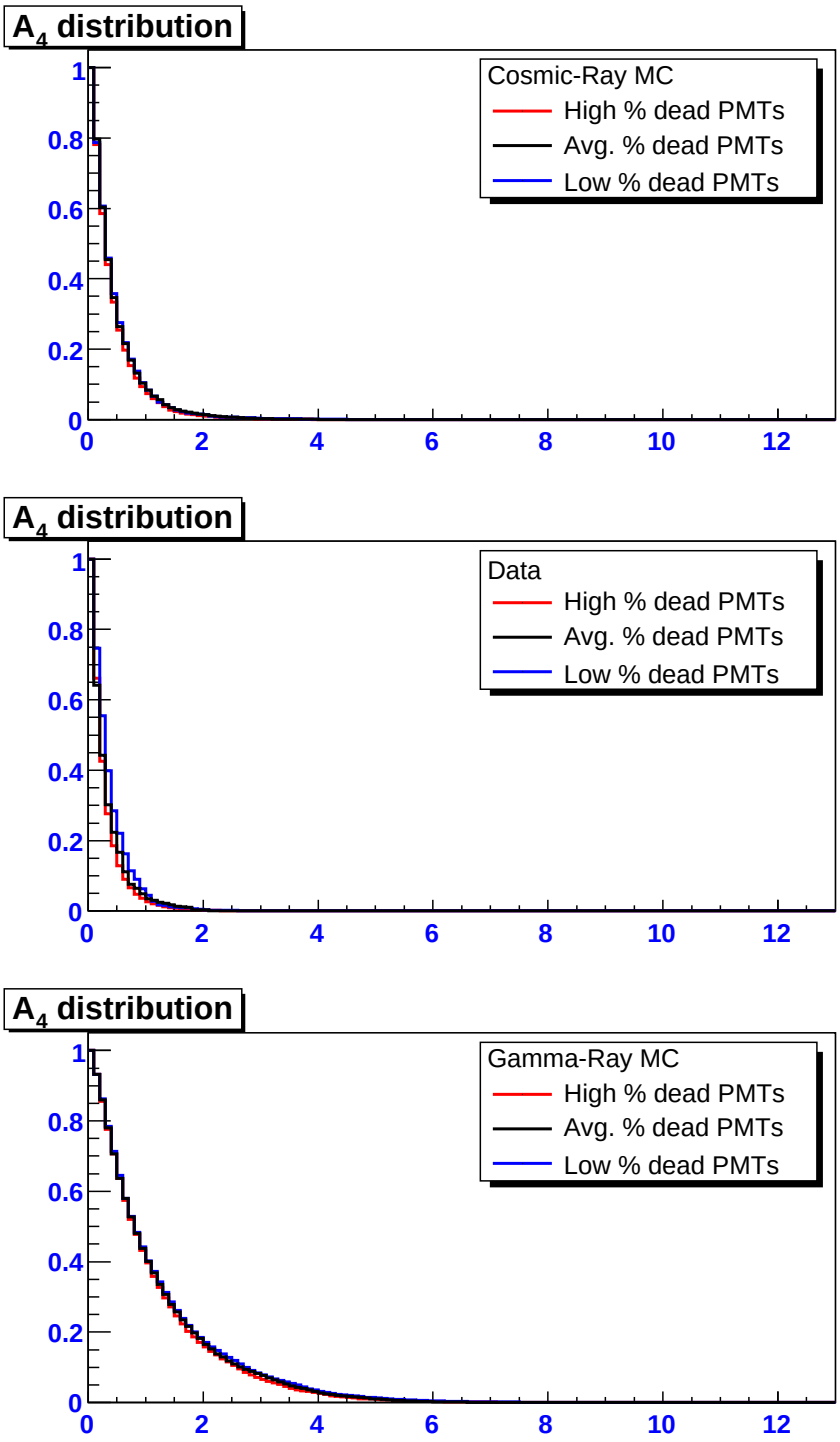

Figure B.19: Distributions of A_4 for different percentages of "dead" PMTs for cosmic-ray Monte Carlo, data, and gamma-ray Monte Carlo for the first epoch.

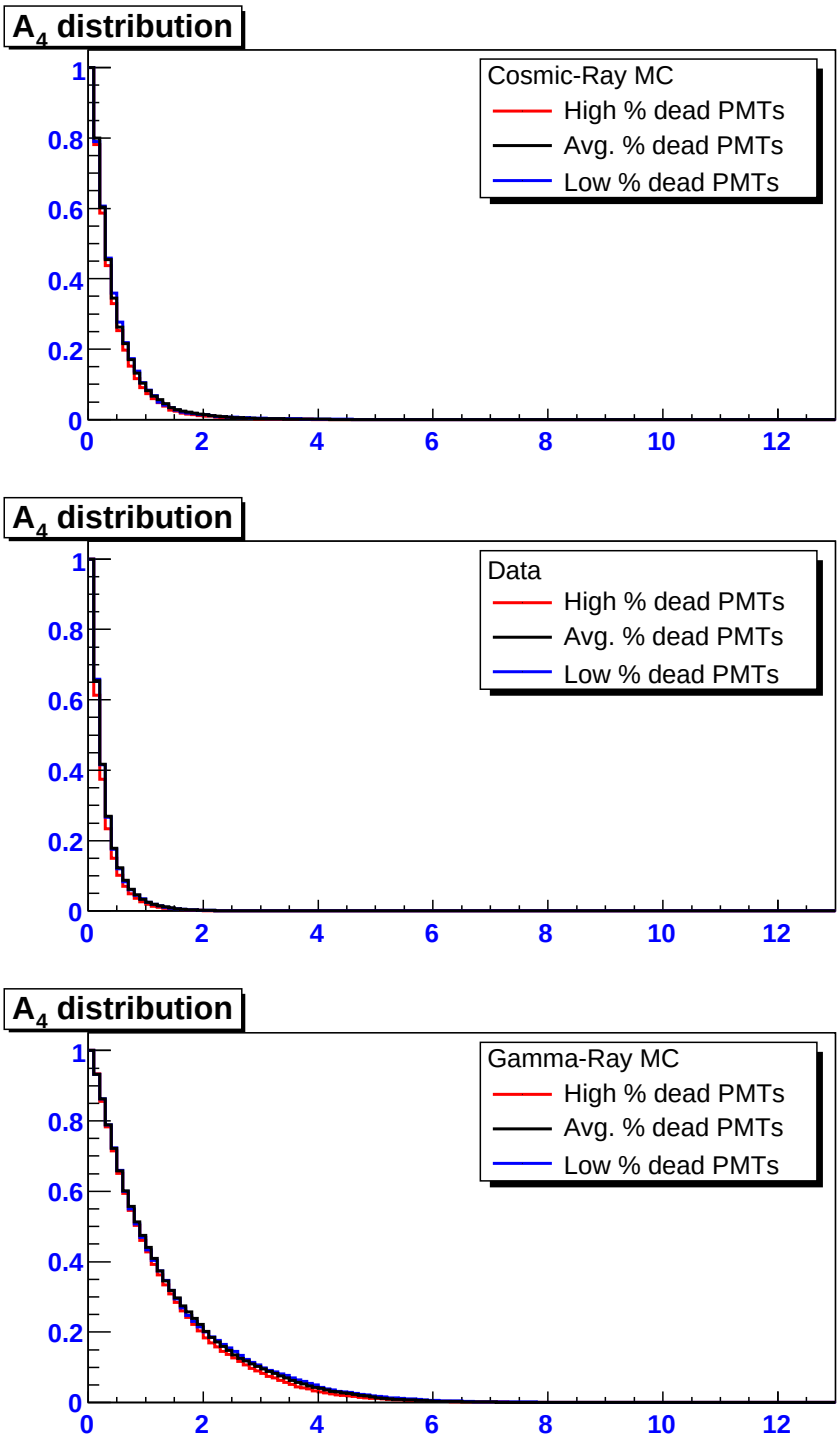

Figure B.20: Distributions of A_4 for different percentages of "dead" PMTs for cosmic-ray Monte Carlo, data, and gamma-ray Monte Carlo for the second epoch.

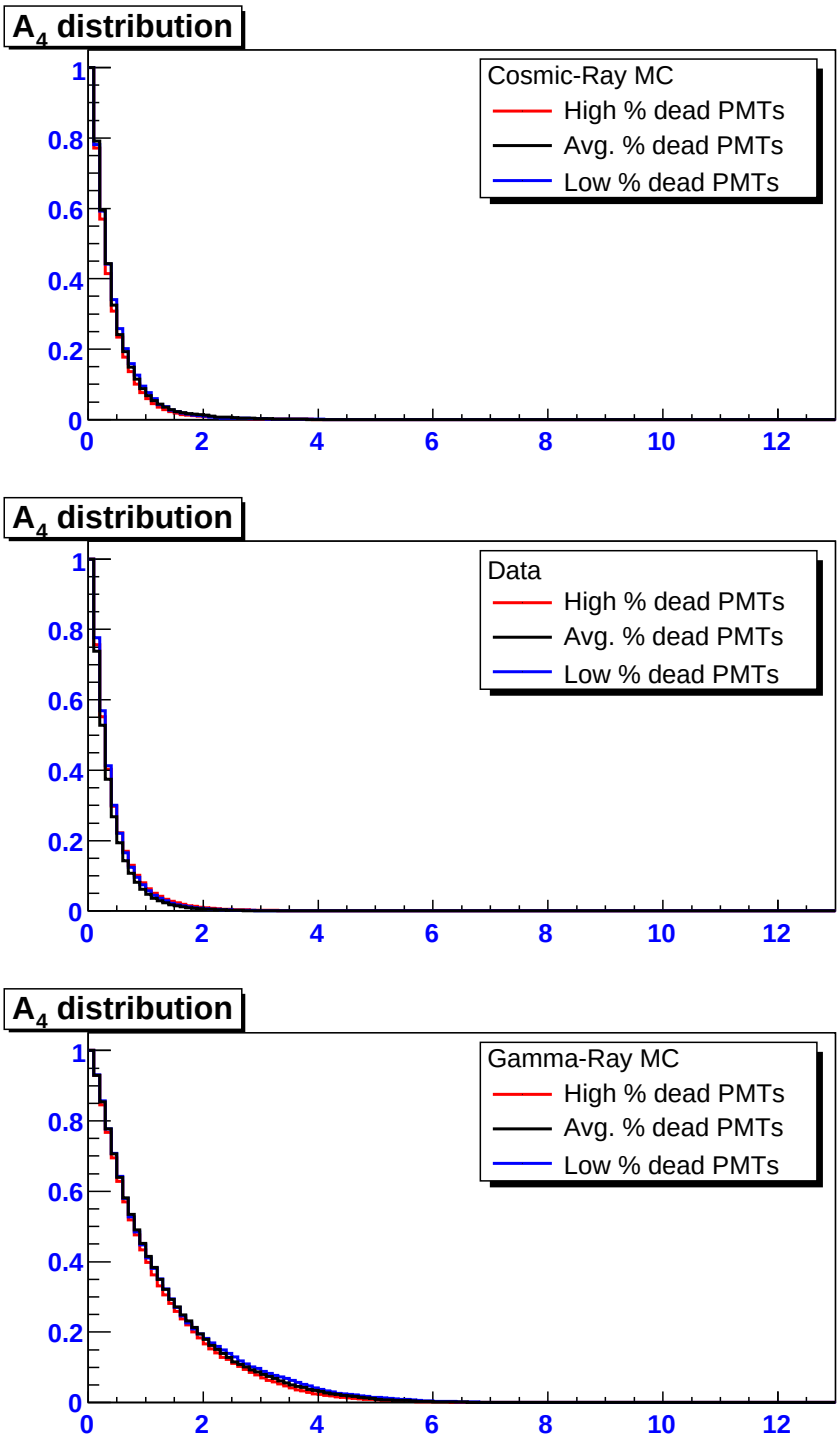

Figure B.21: Distributions of A_4 for different percentages of "dead" PMTs for cosmic-ray Monte Carlo, data, and gamma-ray Monte Carlo for the third epoch.

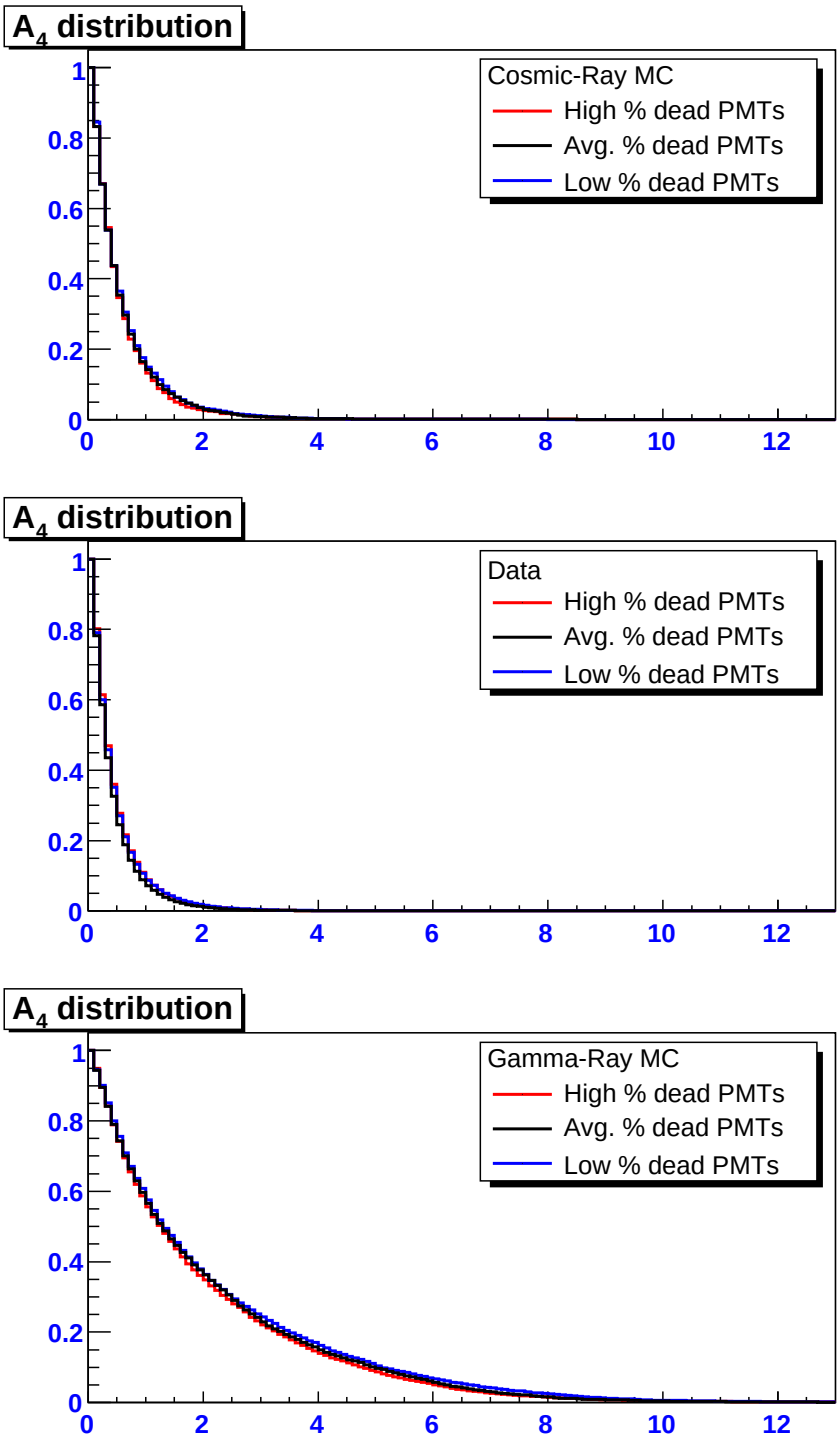

Figure B.22: Distributions of A_4 for different percentages of "dead" PMTs for cosmic-ray Monte Carlo, data, and gamma-ray Monte Carlo for the fourth epoch.

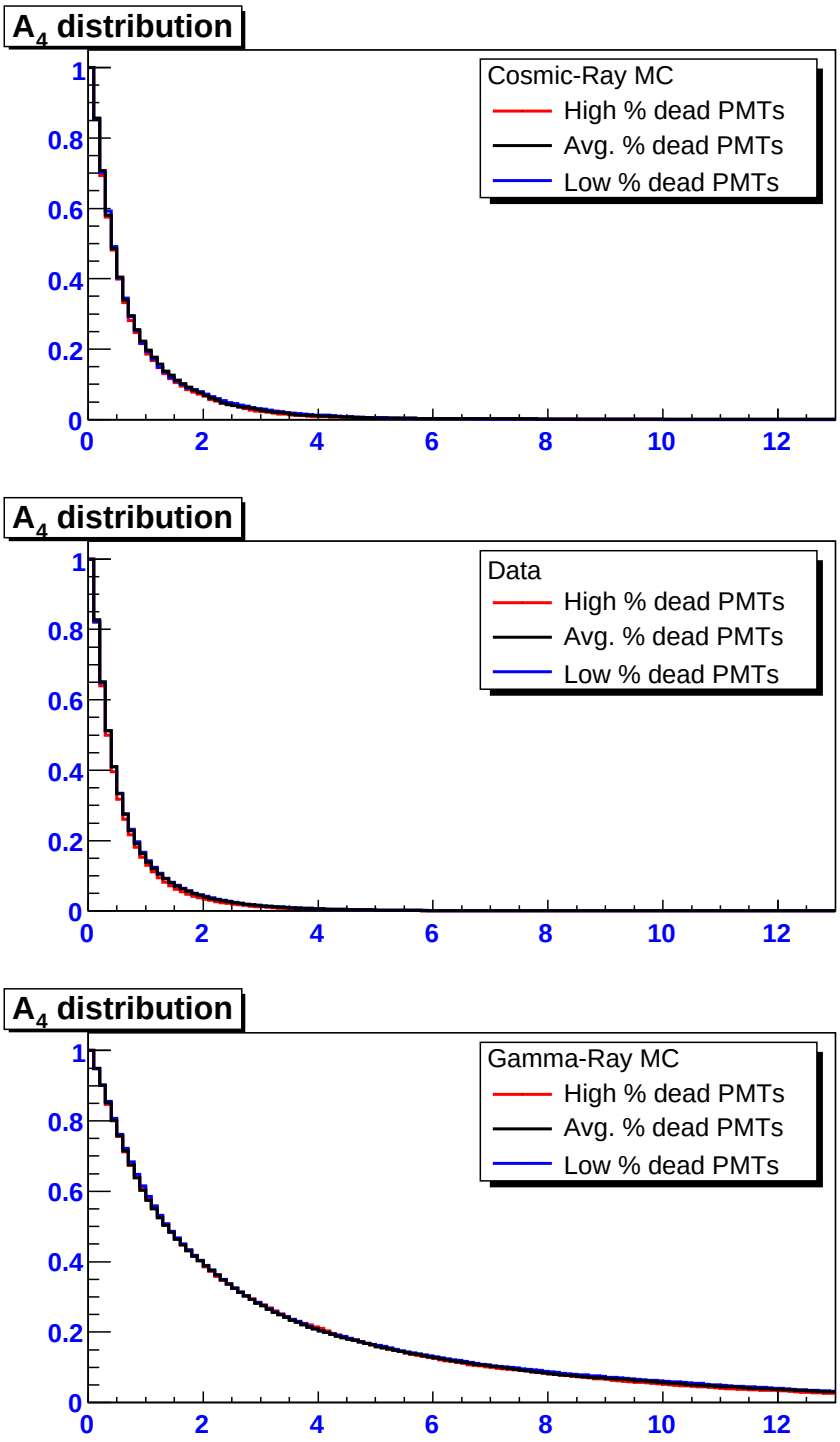

Figure B.23: Distributions of A_4 for different percentages of "dead" PMTs for cosmic-ray Monte Carlo, data, and gamma-ray Monte Carlo for the fifth epoch.

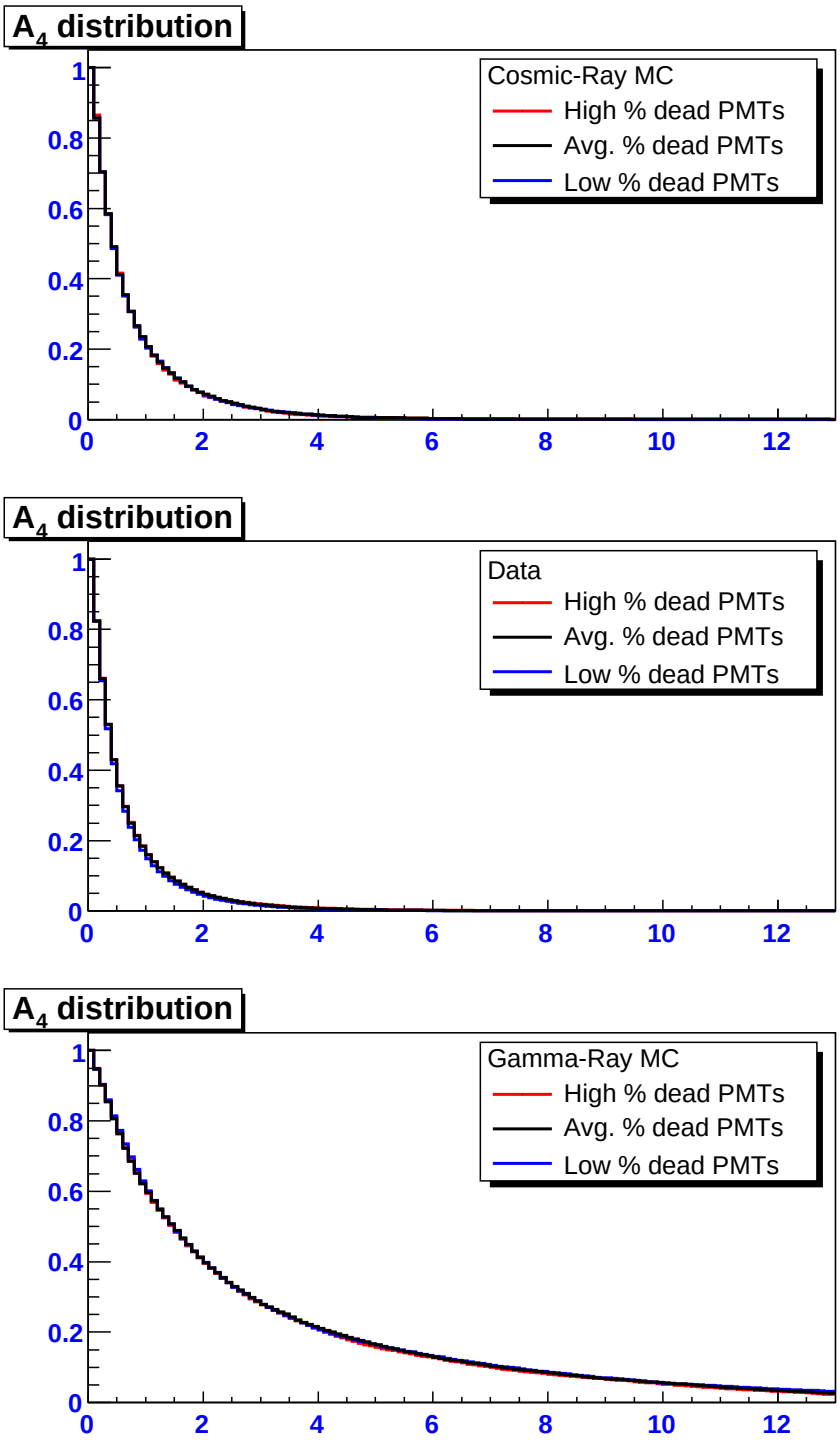

Figure B.24: Distributions of A_4 for different percentages of "dead" PMTs for cosmic-ray Monte Carlo, data, and gamma-ray Monte Carlo for the sixth epoch.

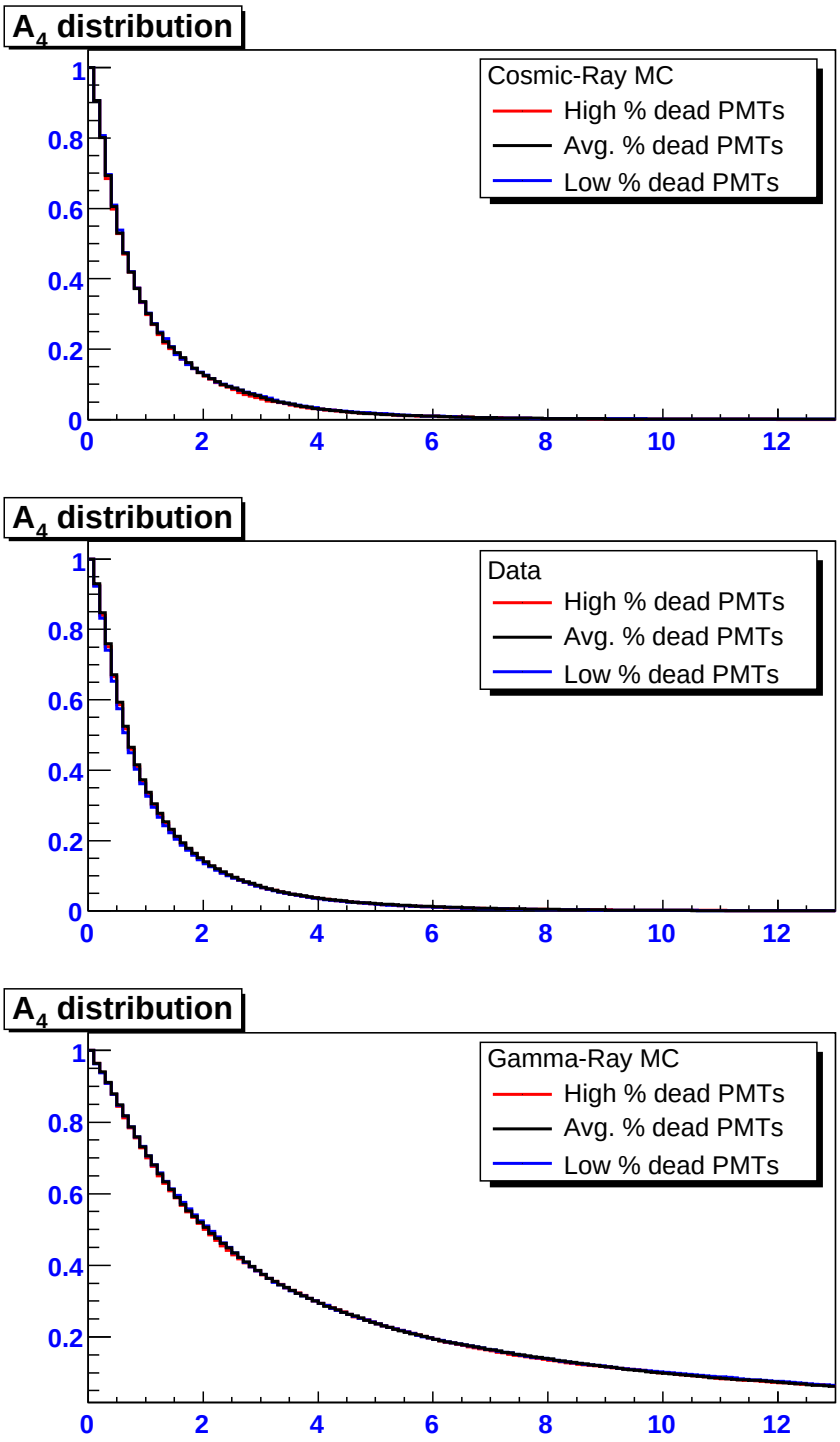

Figure B.25: Distributions of A_4 for different percentages of "dead" PMTs for cosmic-ray Monte Carlo, data, and gamma-ray Monte Carlo for the seventh epoch.

Appendix C

Detailed Tables

In this Appendix are detailed tables of the PSF fit parameters for different A_4 slices in each epoch.

First Epoch						
Bin No	Cuts	Amplitude (A)	Ratio (R)	σ_1	σ_2	χ^2/ndf
1	$0.5 \leq A_4 < 1.0$	13.61± 73.65	9.08±2.66	1.18±0.06	0.66±0.02	34.4/37
2	$1.0 \leq A_4 < 1.5$	11.49± 2.83	6.42±1.81	1.06±0.04	0.65±0.02	65.8/40
3	$1.5 \leq A_4 < 2.0$	8.80 ± 2.13	4.98±1.42	1.21±0.07	0.59±0.03	41.3/40
4	$2.0 \leq A_4 < 2.5$	5.69± 1.47	4.71±1.44	1.23±0.07	0.61±0.04	36.6/41
5	$2.5 \leq A_4 < 3.0$	1.41± 0.93	12.29±10.47	1.54±0.32	0.68±0.05	40.8/39
6	$3.0 \leq A_4 < 3.5$	3.52± 1.02	4.39±1.55	1.18±0.10	0.46±0.05	25.7/32
7	$3.5 \leq A_4 < 4.0$	1.24± 0.68	7.81±5.37	1.45±0.29	0.59±0.06	17.3/29
8	$4.0 \leq A_4 < 4.5$	4.45± 0.58		0.86±0.05		26.4/32
9	$4.5 \leq A_4 < 5.0$	2.58± 0.65		0.75±0.08		46.5/29
10	$5.0 \leq A_4 < 5.5$	0.2.05± 0.50		0.66±0.07		26.9/24
11	$5.5 \leq A_4 < 6.0$	1.25± 0.47		0.60±0.11		25.4/21
12	$6.0 \leq A_4$	0.93± 0.29		1.00±0.17		14.0/22

Table C.1: A list of the fit parameters for Milagro's PSF for the different A_4 bins for the first epoch.

Second Epoch						
Bin N$\underline{o}$	Cuts	Amplitude (A)	Ratio (R)	σ_1	σ_2	χ^2/ndf
1	$0.5 \leq A_4 < 1.0$	97.66± 39.02	0.40±1.06	0.77±0.03	0.59±0.10	65.6/36
2	$1.0 \leq A_4 < 1.5$	0.21± 0.19	414.4±471.3	2.00±0.67	0.71±0.01	33.7/37
3	$1.5 \leq A_4 < 2.0$	0.01 ± 0.01	5707.00±5425.80	2.95±2.54	0.72±0.01	60.0/35
4	$2.0 \leq A_4 < 2.5$	0.52± 0.34	79.53±49.34	2.17±0.65	0.64±0.02	17.8/36
5	$2.5 \leq A_4 < 3.0$	0.56± 0.38	45.29±31.88	1.98±0.65	0.64±0.03	23.5/33
6	$3.0 \leq A_4 < 3.5$	0.19± 0.18	102.6±85.20	2.98±2.54	0.62±0.03	38.7/29
7	$3.5 \leq A_4 < 4.0$	9.54± 9.28	1.36±1.35	0.10±0.05	0.65±0.02	24.5/23
8	$4.0 \leq A_4 < 4.5$	6.92± 0.98		0.69±0.04		25.4/22
9	$4.5 \leq A_4 < 5.0$	8.18± 1.12		0.51±0.03		22.1/21
10	$5.0 \leq A_4 < 5.5$	2.05± 0.49		0.68±0.08		21.5/18
11	$5.5 \leq A_4 < 6.0$	3.47 ± 0.88		0.45±0.04		14.4/14
12	$6.0 \leq A_4$	2.82± 0.70		0.58±0.06		12.9/16

Table C.2: A list of the fit parameters for Milagro's PSF for the different A_4 bins for the second epoch.

Third Epoch						
Bin No	Cuts	Amplitude (A)	Ratio (R)	σ_1	σ_2	χ^2/ndf
1	$0.5 \leq A_4 < 1.0$	97.66± 39.02	0.40±1.06	0.77±0.03	0.59±0.10	65.6/36
2	$1.0 \leq A_4 < 1.5$	0.21± 0.19	414.4±471.3	2.00±0.67	0.71±0.01	33.7/37
3	$1.5 \leq A_4 < 2.0$	0.01 ± 0.01	5707.00±5425.80	2.95±2.54	0.72±0.01	60.0/35
4	$2.0 \leq A_4 < 2.5$	0.52± 0.34	79.53±49.34	2.17±0.65	0.64±0.02	17.8/36
5	$2.5 \leq A_4 < 3.0$	0.56± 0.38	45.29±31.88	1.98±0.65	0.64±0.03	23.5/33
6	$3.0 \leq A_4 < 3.5$	0.19± 0.18	102.6±85.20	2.98±2.54	0.62±0.03	38.7/29
7	$3.5 \leq A_4 < 4.0$	9.54± 9.28	1.36±1.35	0.10±0.05	0.65±0.02	24.5/23
8	$4.0 \leq A_4 < 4.5$	6.92± 0.98		0.69±0.04		25.4/22
9	$4.5 \leq A_4 < 5.0$	8.18± 1.12		0.51±0.03		22.1/21
10	$5.0 \leq A_4 < 5.5$	2.05± 0.49		0.68±0.08		21.5/18
11	$5.5 \leq A_4 < 6.0$	3.47 ± 0.88		0.45±0.04		14.4/14
12	$6.0 \leq A_4$	2.82± 0.70		0.58±0.06		12.9/16

Table C.3: A list of the fit parameters for Milagro's PSF for the different A_4 bins for the third epoch.

Fourth Epoch						
Bin No	Cuts	Amplitude (A)	Ratio (R)	σ_1	σ_2	χ^2/ndf
1	$1 \leq A_4 < 2$	12.42± 10.13	10.07±10.13	0.97±0.09	0.66±0.02	34.4/34
2	$2 \leq A_4 < 3$	2.11± 2.2	43.30±45.0	1.31±0.36	0.59±0.02	34.1/33
3	$3 \leq A_4 < 4$	11.0± 2.90	5.76±1.67	0.93±0.06	0.41±0.03	41.2/33
4	$4 \leq A_4 < 5$	0.35± 0.25	115.3±78.3	2.19±1.33	0.53±0.02	31.9/28
5	$5 \leq A_4 < 6$	2.33± 1.01	14.55±6.77	1.12±0.15	0.43±0.03	22.9/28
6	$6 \leq A_4 < 7$	0.59± 0.29	37.9±19.7	1.65±0.44	0.44±0.03	23.5/24
7	$7 \leq A_4 < 8$	17.06±2.18		0.41±0.02		33.6/18
8	$8 \leq A_4 < 9$	5.13± 1.53		0.51±0.08		26.8/18
9	$9 \leq A_4 < 10$	3.15± 0.77		0.58±0.07		11.7/11
10	$10 \leq A_4 < 11$	0.39± 0.77		1.18±2.25		7.4/13
11	$11 \leq A_4 < 12$	0.78± 0.45		0.77±0.39		4.9/6
12	$12 \leq A_4$	0.73± 0.56		0.74±0.68		5.9/7

Table C.4: A list of the fit parameters for Milagro's PSF for the different A_4 bins for the fourth epoch.

Fifth Epoch						
Bin No	Cuts	Amplitude (A)	Ratio (R)	σ_1	σ_2	χ^2/ndf
1	$1 \leq A_4 < 2$	25.21± 5.56	11.53± 2.6	0.95±0.04	0.47±0.01	56.9/45
2	$2 \leq A_4 < 3$	33.01± 8.71	5.77±1.71	0.79±0.04	0.41±0.02	31.4/33
3	$3 \leq A_4 < 4$	30.62± 12.29	3.74±1.9	0.68±0.05	0.39±0.03	24.9/27
4	$4 \leq A_4 < 5$	10.5± 4.0	8.62±3.59	0.81±0.07	0.38±0.02	17.1/27
5	$5 \leq A_4 < 6$	11.92± 7.84	5.1±4.41	0.68±0.10	0.34±0.05	28.8/24
6	$6 \leq A_4 < 7$	61.35± 5.15	0.01±0.005	0.37±0.01	1.51±0.49	5.2/20
7	$7 \leq A_4 < 8$	44.44±3.71	0.003±0.002	0.37±0.01	-4.58±6.95	31.57/18
8	$8 \leq A_4 < 9$	37.53± 4.06	0.001±0.005	0.35±0.01	-2.44±2.08	10.5/16
9	$9 \leq A_4 < 10$	38.42± 5.23	0.04±0.03	0.29±0.03	-0.98±0.31	6.9/15
10	$10 \leq A_4 < 11$	122.9± 9.7	0.05±0.03	0.28±0.02	-0.9±0.21	7.6/14
11	$11 \leq A_4 < 12$	32.75± 4.98	0.03±0.02	0.27±0.02	-0.93±0.87	7.4/11
12	$12 \leq A_4$	122.9± 9.7	0.06±0.05	0.28±0.02	0.62±0.16	14.1/14

Table C.5: A list of the fit parameters for Milagro's PSF for the different A_4 bins for the fifth epoch.

Sixth Epoch						
Bin No	Cuts	Amplitude (A)	Ratio (R)	σ_1	σ_2	χ^2/ndf
1	$1 \leq A_4 < 2$	28.93± 6.06	10.28± 2.21	1.16±0.05	0.59±0.01	79.9/53
2	$2 \leq A_4 < 3$	38.79± 11.68	4.54±1.61	0.96±0.05	0.52±0.03	46.8/42
3	$3 \leq A_4 < 4$	10.91± 3.38	11.13±3.63	1.07±0.07	0.53±0.02	42.7/41
4	$4 \leq A_4 < 5$	14.71± 5.36	5.92±2.45	0.79±0.04	0.47±0.03	47.3/35
5	$5 \leq A_4 < 6$	0.40± 0.77	177.3±132.3	2.34±1.42	0.49±0.02	30.2/30
6	$6 \leq A_4 < 7$	7.60± 5.14	6.31±6.38	0.78±0.13	0.41±0.04	17.5/26
7	$7 \leq A_4 < 8$	0.41±0.3	102.1±75.0	2.05±1.45	0.47±0.02	15.7/23
8	$8 \leq A_4 < 9$	0.22± 0.15	164.4±112.7	-3.19±2.99	0.43±0.02	16.9/18
9	$9 \leq A_4 < 10$	0.33± 0.33	93.29±93.3	-1.79±1.46	0.39±0.02	17.1/17
10	$10 \leq A_4 < 11$	2.52± 2.95	14.19±17.19	0.68±0.19	0.32±0.03	10.9/13
11	$11 \leq A_4 < 12$	0.26± 0.19	92.27±69.61	2.41±1.79	0.37±0.02	20.2/17
12	$12 \leq A_4$	1.65± 1.03	65.98±43.27	1.06±0.26	0.36±0.01	15.4/16

Table C.6: A list of the fit parameters for Milagro's PSF for the different A_4 bins for the sixth epoch.

Seventh Epoch						
Bin No	Cuts	Amplitude (A)	Ratio (R)	σ_1	σ_2	χ^2/ndf
1	$1 \leq A_4 < 2$	59.4± 7.2	5.39±0.73	1.06±0.03	0.54±0.01	24.9/16
2	$2 \leq A_4 < 3$	33.42± 8.09	6.06±1.64	1.04±0.05	0.54±0.02	27.5/21
3	$3 \leq A_4 < 4$	37.64± 8.63	3.32±0.95	0.85±0.03	0.48±0.03	27.5/12
4	$4 \leq A_4 < 5$	15.42± 3.58	6.37±1.60	0.93±0.05	0.43±0.02	19.0/12
5	$5 \leq A_4 < 6$	7.18± 3.29	10.33±5.51	0.92±0.09	0.47±0.02	12.0/11
6	$6 \leq A_4 < 7$	4.39± 3.49	12.49±10.24	0.91±0.16	0.43±0.03	14.0/10
7	$7 \leq A_4 < 8$	0.98± 1.99	42.55±86.05	1.28±1.24	0.48±0.04	10.5/10
8	$8 \leq A_4 < 9$	0.86± 0.76	46.62±53.13	1.23±0.59	0.44±0.02	3.84/8
9	$9 \leq A_4 < 10$	0.56± 0.38	72.40±56.2	1.65±1.25	0.41±0.02	10.3/10
10	$10 \leq A_4 < 11$	0.32± 0.20	106.60±91.4	-2.32±5.20	0.38±0.02	14.4/7
11	$11 \leq A_4 < 12$	0.32± 0.57	68.18±108.96	-1.71±2.12	0.44±0.02	6.8/7
12	$12 \leq A_4$	5.10± 5.70	27.24±24.75	0.81±0.20	0.36±0.02	17.0/11

Table C.7: A list of the fit parameters for Milagro's PSF for the different A_4 bins for the seventh epoch.

Bibliography

[1] Abdo, A. A., *et al.*, 2007, ApJL 658, L33.

[2] Abdo, A. A., New Gamma-Hadron Separation Technique and Variables in Milagro.
Milagro Collaboration Memorandum (2005).

[3] Abdo, A. A., A_4, Milagro's New Gamma-Hadron Separation Variable and Spectral Index Estimator
Milagro Collaboration Memorandum (2006).

[4] Abdo, A. A. *et al.* In preparation.

[5] F.A. Aharonian and A.M. Atoyan, astro-ph/0009009, 2000.

[6] Aharonian, F. A. *et al.*, 2005, A&A, **431**, 197.

[7] Aharonian, F. A. *et al.*, Astrophys. J. **614**, 897 (2004)

[8] Aid, S., *et al.*, 1995, Z. Phys. C 69, 27.

[9] Alexandreas, D.E. *et al.*, Nucl. Instr. and Meth. **A328**, 570(1993).

[10] Amenomori, M. *et al.*, Phys. Rev. Lett **93**, 061101 (2004).

[11] Amenomori, M. *et al.*, 2006, Science, **314**, 439.

[12] Arnon Dar, Shlomo Dado, and A De Rujula, ApJ. **646** (2006) L21

[13] Atkins. R.A. *et al.*, Nucl. Instrum. Meth. **A449** (2000) 478-499.

[14] Atkins, R.A., *et al.*, 2003, ApJ, **595**, 803.

[15] E.G. Berezhko and H.J. Volk, Astrophysical Journal, **540**, 923-929, 2000.

[16] G. Bignami *et al.*, Astrophys. J. **232**, 649 (1979); D. Kazanas & J.P. Protheroe, Nature, 302, 228 (1983); F.W. Stecker & M.H. Salamon, Astrophys. J. **464**, 600 (1996).

[17] H. Bloemen, Annual Review Astronomy and Astrophysics, **27**, 469-516, 1989.

[18] Bochkarev, N. G. and Sitnik, T. G., 1985, Astrophys. Space Sci., **108**, 237.

[19] A. Borione *et al.*, Astrophysical Journal, **493**, 175, 1998.

[20] Sabrina Casanova, Brenda L. Dingus, arXiv:astro-ph/0609306 v1

[21] Chardonnet, P., *et al.*, Astrophysical Journal, **454**, 774, 1995

[22] K.S. Cheng (Editor), G.E. Romero (Editor), Cosmic Gamma-Ray Sources. (Springer, 2004).

[23] Dame, T. M., D. Hartmann, and P. Thaddeus, Astrophys. J., **547**, 792, 2001.

[24] de Boer, W., Sander, C., Zhukov1,V., Gladyshev, A.V., and Kazakov, D. I., 2005, A&A, **444**, 51.

[25] Digel, S.W., I. A. Grenier, A. Heithausen, S. D. Hunter, and P. Thaddeus, Astrophys. J., **463**, 609, 1996.

[26] Digel, S. W., E. Aprile, S. D. Hunter, R. Mukherjee, and F. Xu, Astrophys. J., **520**, 196, 1999.

[27] Digel, S. W., I. A. Grenier, S. D. Hunter, T. M. Dame, and P. Thaddeus, Astrophys. J., **555**, 12, 2001.

[28] Gralewicz, P.,Wdowczyk, J.,Wolfendale, A.W., & Zhang, L. 1997, A&A, 318, 925

[29] Green, D. A., 2004, Bull. Astron. Soc. India, 32,**325**.

[30] Haino, S. *et al.*, Phys. Lett. B **594**, 35 (2004) [arXiv:astro-ph/0403704].

[31] Hartman, R.C. *et al.*, Astrophysical Journal, **230**, 597-606, 1979.

[32] Hartman, R. C., *et al.* 1999, ApJS, **123**, 79

[33] Hays, E., Milagro Collaboration Memorandum (2001).

[34] E. Hays, A Search for TeV Emission from Active Galaxies using the Milagro Observatory. PhD Thesis, University of Maryland.

[35] Hessels, J. W. T, *et al.*, 2004, ApJ, **612**, 389.

[36] J.A Hinton, Ph.D. thesis, University of Leeds (1998).

[37] Hoffman *et al.*, Rev. Mod. Phys., Vol. **71**, No. 4, July 1999.

[38] Hunter, S. D., S. W. Digel, E. J. de Geus, and G. Kanbach, Astrophys. J., **436**, 216, 1994.

[39] Hunter, S.D., *et al.*, Astrophysical Journal, **481**, 205, 1997.

[40] James B., Michael M., Galactic Astronomy. Princeton University Press 1998. ISBN-10: 0691025657.

[41] Jones, F. C., and D. C. Ellison, Spa. Sci. Rev., **58**, 259, 1991.

[42] Kalberla, P. M. W., Burton, W. B., Hartmann, D., Arnal, E. M., Bajaja, E., Morras, R., & Poppel, W. G. L. 2005, A&A, **440**, 775

[43] R. C. Lamb and D. J. Macomb, Astrophysical Journal, **488**, 872, 1997.

[44] F.Lebrun *et al.*, Astrophysical Journal, **274**, 231, 1983.

[45] M. Leonor, Search for a TeV Component of Gamma-Ray Bursts using the Milagrito Detector. PhD Thesis, University if California Irvine

[46] Leung, H. O., & Thaddeus, P. 1992, ApJ,**81**, 267

[47] Li, T.P. and Ma, Y.Q., 1983, ApJ, **272**, 317.

[48] Linnemann, J., Weighting for Bins of a Hadron Identification or Energy Variable. Milagro Collaboration Memorandum.

[49] McEnery, J. E., Moskalenko, I. V., Ormes J. F.
Cosmic Gamma-Ray Sources, eds. K.S. Cheng & G.E. Romero (Dordrecht: Kluwer), Astrophysics and Space Science Library v.304, Chapter 15, pp.361-395 (2004)

[50] Mori, M. 1997, ApJ, **478**, 225

[51] Moskalenko, I. V., A. W. Strong, and O. Reimer, Astron. Astrophys., **338**, L75, 1998.

[52] Moskalenko, I. V. and A. W. Strong, AIP Conf.Proc. 801 (2005) 57-62.

[53] Moskalenko, I. *et al.*,
To appear in proceedings of 7th UCLA symposium on Sources and Detection of Dark Matter and Dark Energy in the Universe (Marina del Rey, Feb 22-24, 2006); Nuclear Physics B, in press

[54] Moskalenko, *et al.*, ApJ Letters, in press.

[55] Mukherjee, R., *et al.*, 2000, ApJ., **542**, 740.

[56] R. Ong, Physics Reports, 305, 93, 1998.

[57] M. Pohl and J.A. Esposito, Astrophysical Journal, **507**, 327, 1998.

[58] Ptuskin, V.S., *et al.*, 2006, Ap J, **642**, 902.

[59] P.T. Reynolds *et al.*, Astrophysical Journal, **404**, 206, 1993.

[60] Roberts, M. S. E., Hessels, J. W. T., Ransom, S. M., and Kaspi, V. M., 2002, ApJ Lett, **577**, L19.

[61] Schonfelder, V., (Editor), The Universe in Gamma Rays. (Springer, 2001).

[62] Shapiro, S. L., and S. A. Teukolsky, 1983, *Black Holes, White Dwarfs, and Neutron Stars: The Physics of Compact Objects* (Wiley, New York).

[63] Smith, A., A Weighting Analysis of Crab Data.
Milagro Collaboration Memorandum.

[64] Andrew Smith, University of Maryland, private communication.

[65] Sreekumar, P., *et al.*, Phys. Rev. Lett., **70**, 127, 1993.

[66] Strong, A. W., I. V. Moskalenko, and O. Reimer, Astrophys. J., **537**, 763, 2000.;

[67] Strong, A. W., Moskalenko, I.V., and Reimer, O., 2004, ApJ, **613**, 962.

[68] M.Urban *et al.*, Phys. Lett. B, **293**, 149, 1992.

[69] van der Hucht, K. A., 2001, New Astron. Rev., **45**, 135.

[70] Vlasios Vasileiou, A study on the stability of the Milagro data and its agreement with the MC from epoch to epoch. Milagro Collaboration Memorandum (2006).

[71] Gary Walker, Source Extent and Location of the Cygnus Hot Spot. Milagro Collaboration Memorandum (2006).

[72] Weekes, T., Very High Energy Gamma-Ray Astronomy.
(Taylor & Francis, 2003).

[73] *http://heasarc.gsfc.nasa.gov/docs/cgro/images/epo/news/*

[74] *http://www.ast.leeds.ac.uk/∼caw/pic_base/pic.html*

[75] *http://cossc.gsfc.nasa.gov/docs/cgro/images/egret/*

[76] *http://crab0.astr.nthu.edu.tw/ hchang/ga1/ch02-02.htm*

[77] *http://www.shef.ac.uk/physics/people/vdhillon/teaching/phy105/*

[78] *http://www-ik.fzk.de/corsika/*

[79] *http://geant4.web.cern.ch/geant4/*

[80] The NASA/IPAC extragalactic database
http://nedwww.ipac.caltech.edu/forms/byname.html

[81] *http://www.astr.ua.edu/ay102/Lab9/Lab_9_Coord.html*